INVESTIGATION OF MULTILAYERED SURFACE ACOUSTIC WAVE DEVICES FOR GAS SENSING APPLICATIONS

EMPLOYING PIEZOELECTRIC INTERMEDIATE AND NANOCRYSTALLINE METAL OXIDE SENSITIVE LAYERS

A thesis submitted in fulfilment of the requirements for the degree of Doctor of Philosophy

By

Samuel James Ippolito

B.Eng. (Hons)

SCHOOL OF ELECTRICAL AND COMPUTER ENGINEERING
SCIENCE, ENGINEERING AND TECHNOLOGY PORTFOLIO
RMIT UNIVERSITY
MELBOURNE, AUSTRALIA
JUNE, 2006

[This page is left blank intentionally.]

DECLARATION

Date: **June, 2006**

Author: **Samuel James Ippolito**

Title: **Investigation of Multilayered Surface Acoustic Wave Devices for Gas Sensing Applications**

Employing piezoelectric intermediate and nanocrystalline metal oxide sensitive layers

Department: **School of Electrical and Computer Engineering**

I certify that except where due acknowledgement has been made, the work is that of the author alone; the work has not been submitted previously, in whole or in part, to qualify for any other academic award; the content of the thesis is the result of work which has been carried out since the official commencement date of the approved research program; and, any editorial work, paid or unpaid, carried out by a third party is acknowledged.

_____

Signature of Author

_____

Date

[This page is left blank intentionally.]

Contents

List of Tables

List of Figures

[This page is left blank intentionally.]

Acknowledgments

First and foremost, I would like to thank my supervisors Prof. Wojtek Wlodarski and Dr. Kourosh Kalantar-Zadeh for their encouragement, consideration and invaluable assistance that enabled me to experience a great deal of success throughout my PhD research program.

I wish to thank my close university friends and colleagues Mr. Glenn Matthews, Mr. David Powell, Mr. Sasikaran Kandasamy, Mr. Andreas Perentos, Mr. Vijay Sivan, Mr. Alexandru Fechete, Mr. Paul Hubbard, Mrs. Lilin Li, Mr. Bin Rong, Mr. Abu Sadek, Miss. Joy Tan and Mrs. Rashidah Arsat for their help and providing a friendly and energetic atmosphere for conducting research. I would like to pass on my special thanks to Dr. Adrian Trinchi, Dr. Kosmas Galatsis and Dr. Anthony Holland for their support and encouragement. My thanks extends to the academic and administrative members of the School of Electrical and Computer Engineering, headed by Prof. Irena Cosic, at RMIT University. I am especially grateful to the technical and MMTC staff of the school for their help, with special thanks to Mr. Bob Kealy and Mr. David Welch for their assistance with the gas chamber.

My gratitude goes to members of the Gas Sensor Laboratory at the University of Brescia, Italy. A special thanks to Prof. Giorgio Sberveglieri for providing the opportunity to work with his team and experience the northern Italian culture, Prof. Guido Faglia, Dr. Elisabetta Commini, Dr. Matteo Pardo and Mr. Andrea Ponzoni for their collaboration, hospitality and friendship. I would also like to thank Prof. George Kiriakidis from the University of Crete in Greece for his collaboration and deposition of the indium oxide sensitive layers.

I thank the Cooperative Research Centre (CRC) for Microtechnology, Australia for awarding me a PhD scholarship and providing financial support for international travel and much of my research expenditure. I also wish to pass my gratitude to the IEEE UFFC society for providing financial assistance to attend the 2003 IEEE International Ultrasonics Symposium.

I would also like to take this opportunity to express my sincerest love to my parents, sister,

extended family and close friends for their love, support and understanding. I thank them all for putting up with me, especially during my undergraduate and postgraduate endeavours.

Samuel J. Ippolito

Abstract

In this thesis, the author proposes and develops novel multilayered Surface Acoustic Wave (SAW) devices with unique attributes for gas sensing applications. The design, simulation, fabrication and gas sensing performance of three multilayered SAW structures has been undertaken. The investigated structures are based on two substrates having high electromechanical coupling coefficient: lithium niobate ($LiNbO_3$) and lithium tantalate ($LiTaO_3$), with a piezoelectric zinc oxide (ZnO) intermediate layer. Sensitivity towards target gas analytes is provided by thin film indium oxide (InO_x) or tungsten trioxide (WO_3). The high performance of the gas sensors is achieved by adjusting the intermediate ZnO layer thickness. Sensitivity calculations, undertaken with perturbation theory illustrate how the intermediate ZnO layer can be employed to modify the velocity-permittivity product of the supported SAW modes, resulting in highly sensitive conductometric SAW gas sensors.

The work contained within this thesis addresses a broad spectrum of issues relating to multilayered SAW gas sensors. Topics include finite-element modelling, perturbation theory, micro-fabrication, metal oxide deposition, material characterisation and experiential evaluation of the layered SAW sensors towards nitrogen dioxide (NO_2), hydrogen (H_2) and ethanol gas phase analytes. The development of two-dimensional (2D) and three-dimensional (3D) finite-element models provides a deep insight and understanding of acoustic wave propagation in layered anisotropic media, whilst also illustrating that the entire surface of the device can and should be used as the active sensing area. Additionally, the unique and distinctive surface morphology of the layered structures are examined by Scanning Electron Microscopy (SEM) and Atomic Force Microscopy (AFM). The crystalline structure and orientation of the ZnO and WO_3 layers are also examined by X-ray Diffraction Spectroscopy (XRD). The novel multilayered SAW structures are shown to be highly sensitive, capable of sensing NO_2 and ethanol concentration levels in the parts-per-billion and parts-per-million range, respectively, and H_2 concentrations below 1.00% in air. The addition of platinum or gold catalyst activator layers on the WO_3 sensitive layer is shown to improve sensitivity and dynamic performance, with response magnitudes up to 50 times larger than bare WO_3. The gas sensing performance of the investigated structures provide strong evidence that high sensitivity can be achieved utilising multilayered SAW structures for conductometric gas sensing applications.

[This page is left blank intentionally.]

Chapter 1

Introduction

The purpose of this chapter is to provide a general framework and introduction for the work presented in this PhD thesis. This chapter is divided into four sections, addressing the research motivations, objectives, the author's achievements and thesis organisation.

1.1 Motivation

A sensor can be defined as a device which provides a "usable output in response to a specified measurand" [1]. Typically the output is an electrical signal, whereas the measurand can be defined as a physical, chemical or biochemical quantity. In order to convert a measurand into a usable output signal, at least one transduction principle is invoked during the sensing process. Lion proposed that transduction methods can be classified into one or more of the following categories: chemical, mechanical, electrical, radiant, magnetic and thermal [2]. One subdivision of the mechanical category includes sensors based on propagating acoustic waves in piezoelectric media. Surface Acoustic Wave (SAW) devices offer attractive characteristics for the development of physical, chemical and bio-sensors and have been utilised in gas sensing applications for more than 25 years [3]. SAW devices can be designed to offer high sensitivity with reasonably large dynamic range and good linearity, making them extremely suitable for precision applications at parts-per-million (ppm) and parts-per-billion (ppb) concentration levels.

The SAW family of devices include: Shear Horizontal Surface Acoustic Wave (SH-SAW), Leaky-SAW (LSAW or Pseudo-SAW), Surface Skimming Bulk Wave (SSBW), Bleustein Gulyaev (BG) wave, Love and Rayleigh wave. Major advantages of SAW based sensors include: single sided planar structure, the ability to interact directly with the sensing

medium, high sensitivity, low hysteresis, small size, direct frequency output signal and low power consumption [4]. Furthermore, work by various research groups have demonstrated the feasibility of remote sensing via wireless SAW technology [5]. This will allow SAW devices to cater for specialised distant or spatial sensing applications, which is not possible with most of the currently available technologies.

In recent times, there has been significant interest in the development of layered SAW devices that support SH-SAW and Love modes for liquid phase sensing applications. Emphasis has been placed on developing novel sensors for viscosity measurement [6–8], liquid identification [9–11] and biosensing [12–17]. However to date, limited work has reported the sensing applications of *multi*layered SAW devices specifically for gas phase analysis.

Layered SAW devices, generally have a higher mass sensitivity when compared to non-layered structures, due to the increase in acoustic energy confinement [18]. The utilisation of an intermediate or guiding layer, formed from thin films of silicon dioxide (SiO_2) or zinc oxide (ZnO), may increase acoustic confinement at the device surface. For the work presented in this thesis, the author proposes a novel multilayered SAW structure with unique capabilities for gas sensing applications. The utilisation of a high electromechanical coupling coefficient (K^2) substrates such as lithium niobate ($LiNbO_3$) or lithium tantalate ($LiTaO_3$) is combined with a piezoelectric intermediate ZnO layer. A separate metal oxide layer, deposited over the ZnO, is utilised as a gas sensitive layer.

The gas sensing performance of the proposed multilayered SAW devices presented in this thesis are encouraging. It is hoped that this research will lead to the commercialisation of highly sensitive gas sensors that can replace less sensitive acoustic or optical devices in existing commercial systems. The novel layered configurations investigated here exhibit higher electromechanical coupling coefficients than many SAW devices previously presented in the literature. Additionally, the proposed multilayered SAW devices can be fabricated with similar or lower cost than many current SAW and optical gas sensors.

1.1.1 Gas Sensor Applications

A vast array of gas sensor applications exist, from monitoring emissions in industry to the determination of toxic environments in confined spaces. Industry currently employ many varieties of gas sensing systems for monitoring and controlling emissions from their processes. Applications exist in the steel, aluminium, mineral, automotive, medical,

agricultural, aroma and food industries.

Analytical instruments based on optical spectroscopy and electrochemistry are widely used in the scientific community. These instruments give precise analytical data, however are costly, slow, cumbersome and require highly qualified personnel to operate. Current trends are to improve low cost, solid state gas sensor performance in order to obtain high linearity, sensitivity, selectivity and long term stability [19].

The only practical way to monitor air quality or provide a means to alert a human of potential danger is by direct gas sensing. A gas sensor can form part of an early warning system, notifying the appropriate authorities or provide the feedback signals to a process control system. To achieve this, a gas sensor system must be capable of accurate and stable in-situ real time measurements. Environmental factors such as operating temperature, vibration, mechanical shock, chemical poisoning, as well as various device characteristics (accuracy, resolution, physical size and cost) must also be taken into consideration.

The potential of commercialisation of SAW based sensor systems for organic gas detection, industry process control, qualitative composition determination of ternary gas mixtures as well as qualitative discrimination of typical complex gas mixtures arising from raw food products in different states of spoilage are of prime interest [20].

1.1.2 Applications Pertaining to this Research

In each specific application, stringent requirements are demanded from the sensing system and more precisely, the sensor itself. The aim is to achieve accurate and stable monitoring of the analyte under consideration. Remedial action, as a result of monitoring pollutants, can significantly influence the quality of human life and the surrounding environment. To demonstrate the dynamic performance of the proposed layered SAW structures, H_2, NO_2 and ethanol (CH_3CH_2OH) are employed by the author as target gas/vapour analytes. The sensing applications and environmental or human physiological effects of the gas analytes are highlighted below:

- *Hydrogen* (H_2) is a colourless, odourless gas which has a large flame propagation velocity. Due to its small molecular size, it can penetrate into metals causing corrosion, affecting properties such as strength and durability. There is a demand for accurate monitoring of hydrogen gas concentration less than 4.65:93.9 vol.% in air, as it is explosive [21]. Important applications of hydrogen sensing include:

fire warning systems, leak detection, environmental contamination monitoring and during biomedical procedures.

- *Nitrogen dioxide* (NO_2) is a reddish brown, highly reactive gas that is formed in the ambient air through the oxidation of nitric oxide (NO). The major sources of NO_x emissions are high temperature combustion processes, such as those occurring in automobiles and power plants. NO_2 and NO are gaseous pollutants yielding both short and long term health effects on humans, particularly persons suffering form asthma or bronchitis. At relatively high concentrations NO_2 causes inflammation of the airways and may irritate the lungs, while also lowering the resistance to respiratory infections. Irritation of the skin and eyes is also common. Airborne NO_2 transforms to form gaseous nitric acid and toxic organic nitrates, which play a major role in atmospheric reactions, producing ground-level ozone – a major component of smog. The detection of low-levels of pollutants such as NO and NO_2 has enormous potential for commercial applications in the fields of environmental protection and health care.
- *Ethanol* (CH_3CH_2OH) is a component of many alcoholic drinks and in its vapour phase falls under the category of a volatile organic compound (VOC). It is a clear, colourless vapour with a distinct odour. In humans, ethanol is known to affect the central nervous system and brain. As it is one of the most used and widespread alcohols, it has significant commercial applications.

1.2 Objectives

The aim of this research program is to develop novel conductivity based layered SAW sensors by utilising high electromechanical coupling coefficient substrates such as $LiTaO_3$ and $LiNbO_3$. Each device will employ an intermediate ZnO layer and a metal oxide sensitive layer to form a multilayered structure. Thin films of metal oxide, such as InO_x and WO_3 will be employed to provide sensitivity towards the chosen gas analytes. The novel layered configurations will be shown to be highly sensitive, capable of sensing ppb and ppm levels of NO_2 and ethanol, respectively, and H_2 concentrations below 1.00% in air. To investigate the feasibility of the proposed novel layered SAW configurations, this research program has the following main objectives:

- To study SAW propagation in anisotropic layered media via the finite-element method. Both 2 and 3D simulations will be employed to gain a deeper understanding

of the complexities associated with acoustic wave propagation in layered structures; and ultimately to aid the design of layered SAW structures for sensing applications.

- To investigate the additional degree of freedom provided by the intermediate layer thickness and attempt to maximise device sensitivity for conductivity based gas sensing applications. This shall be achieved by matching the velocity-permittivity product of the SAW mode to the conductivity of the metal oxide sensitive layer.
- To design a low noise, high gain RF amplifier, test chamber and housing assembly.
- To design, fabricate and develop novel layered SAW devices for monitoring H_2, NO_2 and ethanol gas/vapour concentrations in air. Each device will be investigated subject to different operating temperatures between room-temperature (22°C) and 300°C to determine the region of maximum response magnitude.
- To comprehensively investigate the material characteristics and surface morphology of the ZnO intermediate, InO_x and WO_3 sensitive layers.
- To investigate the potential of Rayleigh and SH-SAW modes supported in multilayered SAW structures for conductivity based gas sensing applications.

Commercially available finite-element modelling software (ANSYS 5.7) will be used to investigate and develop a deeper understanding of acoustic wave propagation principles in piezoelectric layered media. The information established will be used to justify the proposed structure for gas sensing applications.

Furthermore, the surface morphology of the ZnO intermediate and sensitive layers will be examined by Scanning Electron Microscopy (SEM) and Atomic Force Microscopy (AFM). Additionally, X-ray Diffraction Spectroscopy (XRD) will be employed to examine layer crystallinity. It is envisaged that the material characterisations combined with the gas sensing experimental results will assist with the fundamental understanding of the sensing mechanism. Furthermore, modifications to the WO_3 sensitive layer, via the addition of platinum (Pt) and gold (Au) catalyst activator layers will be implemented to potentially improve the sensor sensitivity and dynamic performance. The electrical conductivity of the sensitive layers will be shown to lie within the range of maximum sensitivity of the SAW delay line. This will enable the device to detect small changes in conductivity caused by the interaction between the sensitive layer and the low concentration analyte gas.

1.3 Outcomes and Author's Achievements

Based on a critical review of literature, the author made an informed decision to investigate novel multilayered SAW structures employing a intermediate ZnO and metal oxide sensitive layers. As a result, this PhD research program has lead to many novel outcomes and contributions to the body of knowledge in the field of conductometric SAW based gas sensors. To the best of the author's knowledge, there have been no reports published in the public domain on InO_x/ZnO/XY $LiNbO_3$, InO_x/ZnO/XZ $LiNbO_3$ or WO_3/ZnO/36° YX $LiTaO_3$ structures and the author is the first to propose them for gas sensing applications.

Additionally, it is to the best knowledge of the author this is the first time a 3D finite-element analysis of ZnO/XY $LiNbO_3$ layered SAW structures has been conducted. A significant contribution has been made by the author in the field of 3D finite-element simulation of layered SAW devices. Through the use of simulation, a better understanding of the acoustic wave propagation characteristics in layered SAW media has been achieved, which was then applied to conductivity-based gas sensing applications. Simulation results reveal that the entire surface of the device should be used as the active sensing area and that a layered structural configuration provides a higher sensitivity towards conductivity based interactions than non-layered counterparts. As a direct result of this work, one colleague and three known independent research groups are currently progressing on the authors contributions at the time of writing this PhD thesis.

Experimental gas sensing results conducted by the author demonstrate the gas sensing performance of the InO_x/ZnO/XY $LiNbO_3$, InO_x/ZnO/XZ $LiNbO_3$ and WO_3/ZnO/36° YX $LiTaO_3$ layered SAW structures towards different H_2, NO_2 and ethanol concentrations in air. The utilisation of 0.1, 0.5, 1.0 and 2.0 µm thick ZnO intermediate layers on the ZnO/36° YX $LiTaO_3$ structure experimentally demonstrate that intermediate layer thickness can be optimised to tailor the velocity-permittivity product of the propagating SAW mode, thus improving sensitivity. Furthermore, catalyst activated WO_3 sensitive layers are investigated by adding thin, non-continuous layers of Pt or Au. Results presented show that a Au catalyst activated WO_3 sensitive layer produces frequency shifts up to 755 kHz towards 1.00% H_2 in air, for a layered SAW structure with a centre frequency of ∼165.3 MHz. For the same H_2 concentration, non-catalyst activated layered SAW sensor are shown to achieve frequency shifts between 25.8 and 514.7 kHz. With respect to NO_2 and ethanol gas sensing, frequency shifts up to 91

and 119 kHz are shown towards concentrations of 8.5 and 500 ppm, respectively. Overall, results presented provide strong evidence that high sensitivity can be achieved utilising a layered SAW structure with both Rayleigh and SH-SAW modes for conductometric gas sensing applications.

Material characterisation of the intermediate ZnO layer by AFM and SEM show that there is a significant difference in surface morphology between the metallised and non-metallised regions of the $LiNbO_3$ and $LiTaO_3$ substrates. XRD characterisation of the WO_3 and ZnO layers grown on $LiTaO_3$ confirms that the ZnO grows mostly with the *c*-axis parallel to the substrate surface, whereas on the metallised region it grows normal to the surface. Due to the novel layered configuration, the InO_x and WO_3 sensitive layers acquire a unique surface morphology. Surface characterisation confirms that the underlying morphology of the intermediate ZnO layer highly influences the growth of the successive InO_x or WO_3 sensitive layer. Results presented indicate that the surface morphology of the InO_x/ZnO/X-cut $LiNbO_3$ and WO_3/ZnO/36° Y-cut $LiTaO_3$ structures exhibit very different characteristics when compared to non-layered structures. For example, the RMS surface roughness of the InO_x layer on silicon substrate was observed to be 0.610 nm. In comparison, the same 40 nm thick InO_x film deposited over the layered SAW structure was observed to exhibit a roughness of 10.12 and 27.03 nm for the non-metallised and metallised regions, respectively. Additionally, thermal treatment causes the average grain size of the ZnO layer to increase when deposited on both the $LiNbO_3$ and $LiTaO_3$ substrates. Conversely, the grain size of the WO_3 decreases with thermal treatment, however an increase in surface roughness from 13.5 to 16 nm was observed at the device surface. In the case of the InO_x film, an increase in both the RMS roughness and surface feature size are shown to occur in both the metallised and non-metallised regions of the layered SAW structure.

In addition to the above achievements, the author designed and fabricated the layered SAW sensors using various micro fabrication and vacuum deposition techniques. Furthermore, to test the performance of the designed layered SAW sensors, a custom built gas calibration system was also developed by the author. The layered SAW gas calibration system consisted of computer controlled mass flow controllers, teflon gas chamber and amplifier assembly, which were thermally and electrically shielded. The design of the RF amplifier circuit was also undertaken by the author.

The author successfully fulfilled these objectives by developing highly sensitive,

conductivity based multilayered SAW sensors for gas sensing applications. From these accomplishments there have been several key outcomes, the results of which have been published in several refereed journals and presented during international conferences. In addition, a provisional patent was lodged by the candidate's supervisors and funding body (CRC for MicroTechnolgy, Australia). The author's achievement include:

1. Co-author of a chapter in the *Encyclopedia of Sensors*.
2. Eight first author and six co-authored refereed journal publications.
3. Seven first author and seven co-authored publications in international conference proceedings.
4. Co-author of one provisional patent regarding layered SAW structures for sensing applications.

A full list of publications by the author can be found in Appendix C. Additionally, during his research candidature, the author was fortunate enough to personally attend and presented *four* oral and *two* poster research communications at:

- IEEE Conference on Optoelectronic and Microelectronic Materials and Devices 2002, Sydney, Australia, 11–13th of December.
  - "A Layered SAW Based NO_2 Sensor with a Copper Phthalocyanine Selective Layer."
  - "A Finite Element Approach for 3-Dimensional Simulation of Layered Acoustic Wave Transducers."
- Society for Optical Engineering (SPIE) International Symposium on Smart Structures, Devices, and Systems 2002, Melbourne, Australia, 16–18th of December
  - "Finite-Element Analysis for Simulation of Layered SAW Devices with XY $LiNbO_3$ Substrate."
- IEEE Ultrasonics Symposium 2003, Hawaii, USA, 5–8th of October
  - "A 3-Dimensional Finite-Element Approach for Simulating Acoustic Wave Propagation in Layered SAW Devices."
- Eurosensors 2004, Rome, Italy, 13–15th of September
  - "Highly Sensitive Layered $ZnO/LiNbO_3$ SAW Device with InO_x Selective Layer for NO_2 and H_2 Gas Sensing."

- IEEE Sensors 2004, Vienna, Austria, 24–27th of October.
  - "The Study of InO_x/ZnO/XZ $LiNbO_3$ Layered SAW Devices for Ozone Sensing."

During the research candidature, the author was also involved in two Master of Engineering (Microelectronics) programs as a technical advisor. In both cases, guidance and collaboration between the author and the Master candidates lead to a successful completion of their minor thesis [22, 23]. Furthermore, during a three month international trip in 2004 the author was invited to undertake a research program at the University of Brescia in northern Italy. Work was conducted at the Gas Sensor Laboratory, headed by Prof. G. Sberveglieri.

1.4 Thesis Organisation

This thesis is structured to provide a logical progression of the research conducted by the author. It shows the progression from finite-element simulations to perturbation theory and fabrication to microstructural characterisation, finally resulting in the successful experimental evaluation of the proposed *multi*layered SAW structures. To communicate this investigation, this thesis contains nine chapters, 3 appendices and one list of references.

It commences with this chapter, which addresses the author's motivation for undertaking research in the field of layered SAW devices. It outlines the research objectives and provides a summary of the contributions pertained as a direct result of this PhD research program. In the second chapter, the author's research rationale is presented. To justify the author's proposed multilayered SAW structures, an introduction and review relevant to current *state-of-the-art* SAW based gas sensors and metal oxide gas sensitive layers is discussed. Chapter 3 is dedicated towards 2D and 3D finite-element modelling of a layered SAW structure, with experimental verification. Results in this chapter provided the platform for further investigation of layered SAW devices employing a ZnO intermediate layer. Chapter 4 expands on the ideas and results obtained via the finite-element work to adapt the multilayered SAW structure for gas sensing applications. Sensitivity calculations for layered structures are approximated via perturbation theory, illustrating how the intermediate ZnO layer can be tailored to modify the velocity-permittivity product of the supported SAW modes. Chapter 5 describes the techniques employed to fabricated the layered SAW sensors. Techniques such as: metallisation layer deposition,

photolithography, thin film deposition and wire bonding are discussed. A summary of all the investigated layered SAW structures is also provided. Chapter 6 focuses on the results obtained from the material characterisation of the ZnO intermediate and InO_x and WO_3 sensitive layers. A comprehensive investigation into the effect of prolonged elevated operating temperature (300°C for 24+ hours) on the ZnO and WO_3 surface morphology is presented. Chapter 7 describes the measurement system for the layered SAW gas sensing experiments. Both phase and frequency measurement techniques employed to detect the change in SAW velocity during the gas sensing experiments are discussed. Chapter 8 investigates the gas sensing performance of the InO_x/ZnO/XY $LiNbO_3$, InO_x/ZnO/XZ $LiNbO_3$ and WO_3/ZnO/36° YX $LiTaO_3$ layered SAW sensors. The dynamic response of each sensor is presented towards different analyte gas species. Furthermore, the role of operating temperature and relative humidity conditions are discussed. The significant effect of Pt and Au catalyst activated WO_3 on dynamic performance is also presented. Finally, Chapter 9 presents the conclusions and suggests possible future work.

Chapter 2

Research Rationale

The previous chapter outlined the motivation and objectives of this research. The purpose of this chapter is to illustrate the author's rationale for proposing a *multi*layered SAW structure for gas sensing applications. This chapter also directs the reader to relevant publications used by the author to develop the underlying principles of the layered SAW structures proposed in this thesis.

From the outset of this research program, it was the author's intention to develop highly sensitive gas sensors employing novel multilayered SAW structures. The utilisation of substrate materials with high electromechanical coupling coefficient (K^2), combined with a piezoelectric guiding layer and a dedicated chemically sensitive layer was envisaged to fulfill this goal. The proposed novel multilayered *sensitive-layer*/ZnO/*substrate* structural configuration was the result – forming the foundations for the next generation of SAW based gas sensors.

The subsequent chapters of this thesis will investigate the benefits and unique features of this multilayered structure in depth. However, the general details, background knowledge and structural advantages will be detailed herein.

Section 2.1 summaries SAW technology and introduces the current trends in conventional SAW based gas sensors. A discussion of SAW perturbations regarding mass and conductivity sensing mechanisms is also presented.

Section 2.2 presents the novel multilayered SAW structure developed by the author. The discussion includes a list of advantages related to the proposed multilayered structure and provides a brief background of metal oxide sensitive layers.

Section 2.3 provides a summary of this chapter.

2.1 SAW Based Gas Sensors

SAW devices have been used for many diverse applications, ranging from mobile and wireless communication, the physical sensing of viscosity, pressure, gas flow to the chemical sensing of biological, ionic, molecular and vapour concentrations [24]. With operating frequencies of SAW devices ranging between approximately 10 MHz to 2 GHz, they can be tailored to suit many applications. Significant contributions in literature have detailed the history and fundamental theory of SAW devices [25–27]. Currently, the most common commercial applications for SAW devices are in the electronics and telecommunication industries, which include: bandpass filters, ladder filters, resonators, delay lines, convolvers and radar pulse compression filters. A good historical account of the development of SAW device for applications in electronics has been compiled by Morgan [28] and Hickernell [29].

As previously mentioned, there are several advantages of employing a SAW device as a chemical sensor, which include: planar structure compatible with integrated circuit technology, the ability of the device to interact directly with the sensing medium, high sensitivity to surface perturbations, good linearity, low hysteresis, direct frequency output signal and low power consumption [4]. Figure 2.1 shows the layout of a basic 2-port delay-line SAW device with uniform single electrode interdigital transducers (IDTs) forming the input and output ports. The IDTs consist of thin metal electrodes (also refereed to as fingers) of equal width and spacing. For sensing applications, a constant finger overlap or aperture W is generally utilised.

The application of an alternating voltage to the input IDT results in the electrodes becoming alternatively positive or negatively polarised, creating an electric field between

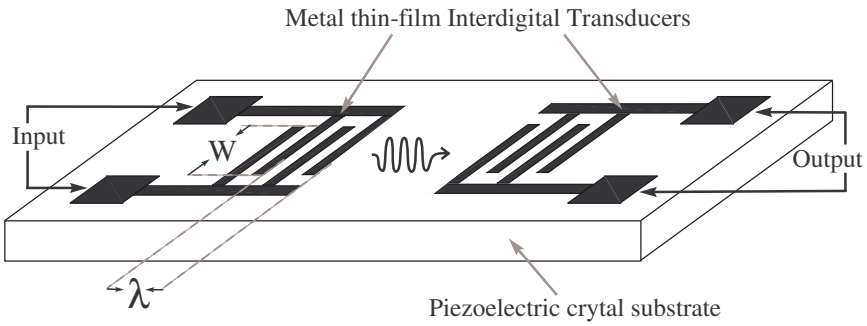

Figure 2.1: Basic layout of a 2-port SAW device.

them. The field distribution induces strains in the piezoelectric substrate resulting in the generation of acoustic (mechanical) waves. Generation of acoustic waves will be strongest at frequencies where the acoustic wavelength (λ) is close to the IDT period. These mechanical waves propagate away form the input IDT in both directions at velocity v_0. The mechanical wave energy is then transformed back into an electrical energy at the output IDT [24].

To ensure that the acoustic waves interfere constructively for an applied sinusoid voltage, the distance between two adjacent fingers should be equal to half the acoustic wavelength λ, as shown in figure 2.1. In the frequency domain, the IDT has a bandpass filter response. At the synchronous or centre frequency f_0, the transducer efficiency in converting electrical energy to acoustical energy, and vice versa, is maximised. The centre frequency is related to the period λ_0 of the IDT and v_0:

$$f_0 = \frac{v_0}{\lambda_0} \tag{2.1}$$

The combination of material properties and the IDT geometry determine the frequency response of the SAW device. The fundamental equations describing mechanical wave propagation in piezoelectric media are detailed in [24, 30–33]. The propagation of acoustic waves in piezoelectric materials is governed by two coupled systems of equations: the mechanical equations of motion and Maxwell's equation for the electric behaviour, which form the *piezoelectric constitutive equations* [31].

The acoustic properties of commonly employed materials have been investigated in depth. The extensive and detailed material parameters compiled by the likes of Slobodnik and Auld [33, 34] are essential to any model of acoustic wave propagation in isotropic and anisotropic media. Additionally, Hickernell [35] also provides a thorough review of thin film materials for SAW devices, however it primarily focuses on signal processing applications.

SAW devices based on layered structures are increasingly used for chemical sensing applications in liquid and gas phases. Adding a chemically sensitive layer to the device surface dramatically affects the acoustic wave propagation and inevitably changes the device's frequency response characteristics. Unfortunately, a layer deposited on the active surface also considerably complicates most device analysis, thus requiring more advanced modelling techniques.

The realisation and explicit design of SAW structures for well defined applications has been greatly facilitated by recent advances in the modelling of SAW propagation and newly developed fabrication techniques. Current fabrication and modelling techniques have enabled the utilisation of non-standard materials in SAW structures, when compared to the more mainstream semiconductor materials employed in commercial foundries. Increasingly, in the field of sensor technology, different combinations of materials forming new acoustic based structures have been increasingly investigated for their potential chemical sensing properties and characteristics [36]. The choice of piezoelectric substrate crystal orientations and the associated chemically sensitive layers have been investigated by different research groups to determine the type of supported SAW propagation modes, their temperature stability, sensitivity towards mechanical or electrical perturbations and effect on overall device characteristics.

2.1.1 SAW Perturbations

The basic principle in a SAW based gas sensor is the detection of small deviations in acoustic wave propagation characteristics, which are caused by perturbations on the active surface of the device. The most common technique is measuring the deviation in propagation velocity of the surface wave as a change in resonant frequency of the device [37]. However, perturbations affecting acoustic phase velocity can be attributed to by many factors, each of which represents a potential sensor response [38]:

- T – Temperature
- E – Electric Field
- c – Stiffness
- ρ – Density
- μ – Shear elastic modulus
- ε – Permittivity
- σ – Conductivity (electrical)
- η – Viscosity
- p – Pressure
- m – Mass

These interactions change the boundary conditions, producing a measurable shift in the propagating SAW mode's phase velocity. Equation (2.2) illustrates the change in acoustic phase velocity as a result of possible external perturbations, under the assumption that the perturbations are small and linearly combined:

$$\frac{\Delta v}{v_0} \cong \frac{1}{V_p}\left(\frac{\delta v}{\delta T}\Delta T + \frac{\delta v}{\delta \varepsilon}\Delta \varepsilon + \frac{\delta v}{\delta E}\Delta E + \frac{\delta v}{\delta \sigma}\Delta \sigma + \frac{\delta v}{\delta m}\Delta m + \frac{\delta v}{\delta p}\Delta p + \ldots\right) \quad (2.2)$$

Since acoustic wave devices use piezoelectric materials for the excitation and the detection of acoustic waves, the nature of almost all the parameters involved with sensor applications

concerns either mechanical or electrical perturbations. Furthermore, the temperature dependance of each parameter and the overall temperature coefficient of the structure must also be considered. Therefore, the sensor response may be due to a combination of the above parameters.

2.1.2 Conventional SAW Gas Sensor

A typical SAW based sensor consists of a 2-port SAW delay line with a thin film of gas sensitive material deposited onto the active surface of the device. For gas sensing applications, the thin film of material should be chemically sensitive to a specific gas analyte. The sensing mechanism involves the physicochemical interaction between the analyte gas and the sensitive layer. The response of the sensor is derived from the measurable shift in the SAW mode's phase velocity, due to the perturbations described by equation (2.2). Generally, the sensitive layer is deposited between the input and output IDT electrodes. Figure 2.2 shows the layout of a conventional SAW gas sensing structure.

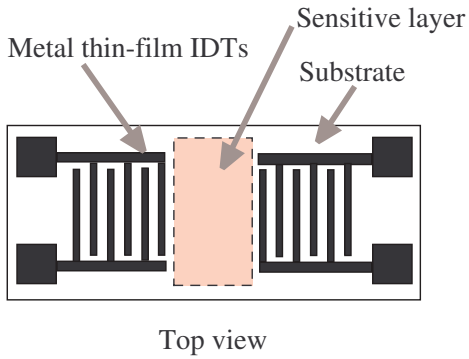

Figure 2.2: Conventional SAW gas sensor structure.

The operation of a SAW gas sensor is based on the detection of small perturbation caused by the interaction between the analyte gas and the sensitive layer. The chemical reaction between the analyte gas and the sensitive layer disturbers the surface boundary conditions of the device (see section 2.1.1), resulting in a change in the acoustic phase velocity of the propagating SAW. The two most common methods used to measure change in SAW velocity are via phase and frequency measurement techniques [39]. The frequency measurement technique is a convenient method of interpreting the sensing interaction. By measuring the resonant frequency of the device, it can be related to the change in

acoustic phase velocity (assuming negligible dispersion) by:

$$\frac{\Delta f}{f_0} \cong \kappa \frac{\Delta v}{v_0} \quad , \tag{2.3}$$

where κ is the fraction of the centre-to-centre distance between input and output IDT affected by the perturbation [38]. Similarly, the device's transfer function or velocity can be measured by several attenuation and phase measurement techniques [40–42]. In all cases, the measured quantities should ideally correlate to the relative concentration of the gas analyte.

The first application of a SAW device as a gas sensor was reported by Wohltjen and Dessy in 1979 [43]. In their paper, they investigated the operation of a $LiNbO_3$ based SAW device operating as a gas detector. Following their work, a variety of SAW sensors were developed for sensing sulphur dioxide (SO_2) [44], hydrogen (H_2) [45, 46], water, carbon dioxide (CO) [47], hydrogen sulphide (H_2S) [48], nitrogen oxide (NO) [49, 50], organophosphorous compounds [51] as well as many others. The mechanism of operation for SAW based vapour sensors has also been extensively investigated [52]. Comprehensive surveys detailing the developments of SAW sensors were then completed by D'Amico et al. [53] in 1989, Ballantine and Wohltjen [54] in 1989 and Grate et al. [44, 55] in 1993. Since then, several other reviews of acoustic wave gas sensor technology has been completed by Martin et al. [56] in 1996, Cheeke and Wang [57] in 1999, Vellekoop [58] in 1998, Drafts [59] and Anisimkin et al. [60] in 2001.

As described in section 2.1.1, perturbations affecting acoustic phase velocity can be attributed to by many factors. In regards to multi-component measurands, the use of a controlled experimental laboratory setup or environmental conditions may eliminate unwanted responses or external environmental influences. However, the use of sensor arrays, containing several different device structures, each with their own signature response characteristics has be widely investigated as a possible solution. Early investigations by groups including D'Amico and Verona [53], Ballantine and Wohltjen [54] and Grate et al. [44] reported that through the use of an array of sensors and the careful selection of the type of sensors system implemented (according to the working environment), the selectivity, sensitivity and reproducibility of the overall sensing system may be enhanced. However, more recently, pattern recognition techniques have been commonly employed to enhance the information obtained from a sensor array through intelligent data processing [61–63].

2.1.3 Sensing Mechanisms

For the development of a chemical SAW sensor, it is vitally important to understand the predominate sensing mechanism occurring during the interaction between the sensitive layer and the analyte gas. The most commonly employed sensing mechanism in SAW sensors is gravimetric, whereby a mass adsorbed on the structure causes a change in wave velocity. Typically used for liquid phase analysis, mass absorption mechanisms have been employed for gas phase volatile organic compound (VOC) sensing applications. Other common mechanisms include inducing changes in the sensitive layers' density, viscosity, conductivity or permittivity. For example, measurement of the elastic properties of palladium (Pd) thin films and their dependance upon H_2 adsorbtion have been widely investigated [46, 64]. The sensing mechanisms that occur due to the change in boundary conditions caused by the interaction listed in section 2.1.1 are well known [36]. For the purpose of the following discussion, only mass and conductivity (electrical) based sensing mechanisms, with a bias towards layered structures for gas phase analysis will be considered.

2.1.3.1 Mass Based Gas Sensing

As the acoustic radiation from a SAW device into the surrounding gas media is negligible, Rayleigh waves are commonly employed for gas phase sensing applications. Rayleigh waves have a particle displacement normal to the substrate surface and a component in the propagation direction. They are strongly guided by the substrate surface and highly sensitive towards mass perturbations. However, the mass sensitivity of a Love wave can be greater than that of a Rayleigh wave, typically due to a thin guiding layer providing higher acoustic wave confinement at the device surface when compared to the non-layered Rayleigh wave structures [18, 37]. The layered structure of Love mode devices only supports a pure SH-SAW polarisation, thus particle displacements is perpendicular to the surface plane of the device. The guiding layer is typically formed from a thin film of silicon dioxide (SiO_2) and more recently zinc oxide (ZnO). Predominately reported for liquid phase analysis, Love modes can only exist if the shear velocity in the guiding layer is less than the shear velocity in the substrate [9].

The mass sensitivity of a Love mode sensor is mainly determined by the thickness of the guiding layer and its operating frequency. Experimental studies on Love mode devices based on SiO_2/ST-cut quartz have investigated the mass sensitivity, velocity,

insertion loss, oscillation frequency stability and temperature coefficient as a function of guiding layer thickness [65]. Love mode sensors are advantageous for gravimetric sensing applications such as organic vapours absorbed by a thin polymer film. For example, Jakoby et al. [66] demonstrated that a Love wave device employing a polymer sensitive layer was highly suitable for vapour sensing applications. Furthermore, Zimmermann et al. [67] successfully applied a Love wave device for the detection of organophosphorous vapours, and achieved approximately 10 times the sensitivity of a Rayleigh wave sensor operating at a similar frequency.

Additionally, a novel application of a layered SAW device was presented by Penza et al. [68], where a SiO_2 layer on ST quartz was employed for the gravimetric detection of organic vapours absorbed on a sensitive layer consisting of carbon nanotubes. In this case the SiO_2 layer also prevented the electrical shorting of the IDT fingers by the conductive nanotube sensitive layer and also isolated the IDTs from exposure to the analyte. Du and Harding [14] also studied multilayered structures employing polymethyl-methacrylate PMMA/SiO_2/quartz. The structures were observed to exhibit higher sensitivity when compared to devices having only the SiO_2 or PMMA layers. Harding [69] further demonstrated that the acoustic properties of a SiO_2 guiding layer can be modified by introducing CF_4 gas during the deposition process. This was shown to reduce the propagation velocity in the guiding layer, resulting in an increase in mass sensitivity. Although the application of this work was for liquid phase analysis, it clearly demonstrates that there are significant sensitivity advantages of layered SAW structures when compared to their non-layered counterparts [18]. Recently, Chang et al. [70] completed a study of Love modes in ZnO/quartz and ZnO/$LiTaO_3$ structures and the preferred orientation of doped ZnO films on the 36° YX $LiTaO_3$ substrates [71] for application in both gas and liquid media.

2.1.3.2 Conductivity Based Gas Sensing

When a SAW propagates in piezoelectric media, it generates a layer of bound charge which accompanies the mechanical wave [32]. This phenomenon is typically referred to as the 'acoustoelectric effect', which is related to the electromechanical coupling coefficient (K^2) of the piezoelectric materials employed in the SAW device structure. In conductometric gas sensing applications, the interaction of the analyte gas molecules with the sensitive layer perturbs the electrical boundary condition at the surface of the device. As a result, the velocity and attenuation of the propagating electromechanical wave is influenced by

surface interactions. Generally, the larger the K^2 of the structure, the more the acoustic wave velocity is influenced by the conductivity changes at the surface of the device.

Ricco and Martin [72] first reported SAW sensors based on the conductometric sensing mechanism, using a non-layered device. Later, Niewenhuizen et al. [73] developed a layered device employing a silicon nitride Si_3N_4/ZnO/SiO_2/Si structure with copper phthalocyanine sensitive layer for NO_2 detection. This structure allows acoustic waves to be generated in a non-piezoelectric silicon substrate, with a view towards integrating the sensor with standard IC fabrication technologies. The silicon nitride acts as a passivation layer, preventing interaction with the reference delay line. In 2002, Jakubik et al. [74–76] introduced a bi-layered structure targeting H_2, using metal free phthalocyanine and copper phthalocyanine intermediate layers with a palladium sensitive layer. The bi-layered structure was used in an attempt to increase the sensitivity towards the analyte gas, by matching the operating region of the SAW device to the conductivity of the palladium sensitive layer.

The thickness of the intermediate layer can be optimised to match the operating point of the SAW to the conductivity of the sensitive layer – thereby increasing the sensitivity of the device towards conductivity changes at the surface. Currently, the dielectric materials employed to form a layered or bi-layered structure include: SiO_2, Si_3N_4, phthalocyanine and various polymers. It is also well known that on weak piezoelectric substrate, such as ST-cut quartz (K^2= 0.11%), an increase in K^2 at the surface of the device can be achieved via the deposition of a piezoelectric guiding layer, such as ZnO [37]. This is due to K^2 of the piezoelectric ZnO layer and the accompanying electric field of the propagating SAW extending out of the substrate and interacting with the adjacent piezoelectric ZnO layer.

2.2 Proposed Layered SAW Gas Sensor Structure

As previously mentioned, conventional SAW gas sensors consists of a piezoelectric substrate patterned with IDTs on the surface of the device with a gas sensitive layer deposited in between input and output ports. Work conducted by Kalantar-zadeh et al. demonstrated that by utilising a SiO_2/ST-cut quartz structure with a TiO_2 sensitive layer deposited over the entire surface of a device, a remarkably high sensitivity towards oxygen can be achieved [77]. This structure utilised the SiO_2 as an intermediate dielectric layer, sandwiching the IDTs between the substrate and SiO_2 whilst isolating the IDT electrodes from the analyte gas. Further work conducted by Kalantar-zadeh et al. demonstrated

that by utilising a ZnO layer, device sensitivity is greatly improved over SiO_2 layered and non-layered structures [16–18]. The replacement of the SiO_2 dielectric layer with the ZnO piezoelectric layer had the added benefit of providing sensitivity towards oxygen and propane analytes directly, whilst also isolating the IDTs from the sensing environment.

On review of table 2.1 and considering previous experimental results obtained by the author employing an intermediate SiO_2 layer with a copper phthalocyanine sensitive layer [78], it is postulated that significant improvements in sensitivity can be achieved by combining high K^2 substrates in a layered structural configuration with a piezoelectric intermediate layer and dedicated sensitive layer. The basis of the proposed structure centred on the multilayered SAW structures developed by Kalantar-zadeh for oxygen sensing and the ZnO/$LiTaO_3$ structure employed by Shoji et al. [86]. By using a piezoelectric ZnO intermediate layer on high K^2 substrates (between 3 and 5.5%), such as X-cut $LiNbO_3$ and 36°Y-cut $LiTaO_3$, it is believed that significant improvements in conductometric sensitivity at the surface of the device would be achieved.

Figure 2.3 shows the author's proposed structure, where the sensitive layer is shown to cover the entire surface of the device. The structure increases the sensitive layer interaction area and effectively sets the fractional scalar κ in equation (2.3) to unity. The requirements of the intermediate and sensitive layers are separate and typically cannot be satisfied by a single material. Therefore, by employing different materials to form the intermediate and sensitive layer, the functionality of each layer remains separate. The proposed design allows the appropriate materials to be selected, according to the individual requirements of the intermediate and sensitive layers.

A good intermediate layer material should be homogeneous and have low acoustic loss. The layer should also have the appropriate dielectric properties to electrically isolate the

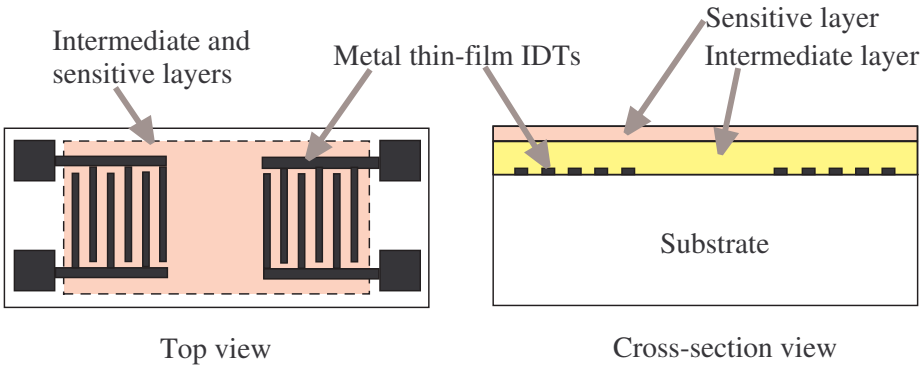

Figure 2.3: Proposed layered SAW structure.

Table 2.1: SAW base gas sensor device comparison.

Device type	Sensitive layer	Structure	Analyte gas	Operating frequency (MHz)	Frequency shift	Reference
SAW	WO_3:Ru	24° rotated Y-cut quartz	3ppm of NO	261	50kHz	[79]
SAW	Doped WO_3	YZ $LiNbO_3$	30ppm of H_2S	60	10kHz	[80]
SAW	WO_3:Au	YZ $LiNbO_3$	100ppm of H_2S	38.15	5kHz	[48]
SAW	Langmuir blodgett films	-	1.4ppm of NO_2	600	8Hz*	[50]
SAW	lead phthalocyanine	YZ $LiNbO_3$	10ppm of NO_2	110	154Hz*	[72]
SAW	catalysed lead phthalocyanine	YZ $LiNbO_3$	10ppm of NO_2	110	330Hz*	[72]
SAW	tetra-4-tert butyl silicon phthalocyanine dichloride	ST quartz	100ppm of NO_2	98.6	420Hz	[81]
SAW	lead phthalocyanine	YZ $LiNbO_3$	3.1ppm of NO_2	∼43MHz	9.5kHz*	[82]
SAW	WO_3	27°-quartz	10ppm of H_2S	260MHz	4kHz*	[83]
SAW	WO_3	YZ $LiNbO_3$	27ppm of H_2S	60MHz	9.9kHz*	[80]
SAW	Pt/WO_3	langasite	1000ppm of H_2	167.14MHz	6kHz*	[84]
Layered SAW	TiO_2	SiO_2/ST quartz	10000ppm 100ppm of O_2	63.04	45kHz 3kHz	[77]
Layered SAW	ZnO	ZnO/90°rotated ST quartz	50ppm of O_2	90	11kHz	[85]
Layered SAW	ZnO	ZnO/90°rotated ST quartz	100ppm of C_3H_8	90 90	11kHz 18kHz	[85]
Layered SAW	Palladium	copper phthalocyanine/YZ $LiNbO_3$	2% of H_2	–	1kHz*	[74]
Layered SAW	Palladium	phthalocyanine/ YZ $LiNbO_3$	2% of H_2	–	5kHz*	[75]
Layered SAW	copper phthalocyanine	SiO_2/90°rotated ST quartz	1ppm of NO_2	100	1.4kHz	[78]

* Interpreted or calculated from information provided

IDTs from the sensitive layer and in the case of a Love mode device, it should have an acoustic velocity less than that of the substrate. Its function is to guide the acoustic wave, provide high acoustic confinement at the substrate surface and increase sensitivity by using its dielectric properties to match the SAW mode to the conductivity of the sensitive layer. The last requirement will be explained in detail in Chapter 4. Conversely, a good sensitive layer should have a high surface to volume ratio or be porous, and in the case of polycrystalline films, should have many grain boundaries with a small average

grain size. Therefore, if a good sensitive layer material was utilised as a guiding layer, it would most likely produce acoustic scattering – resulting in attenuation of the propagating wave. Hence, the material properties and acoustic characteristics of a intermediate and sensitive layers are contradictory.

To the best of the authors knowledge, the proposed multilayered *sensitive-layer*/ZnO/*substrate* structural configuration has not previously been reported on for gas sensing applications. Furthermore, due to the high K^2 of the chosen $LiNbO_3$ and $LiTaO_3$ substrate orientations, it is anticipated that the supported Rayleigh and SH-SAW modes would be highly sensitive to electrical (permittivity and conductivity) perturbations at the device surface.

2.2.1 Advantages of Layered SAW Structure

The proposed multilayered SAW structure has several advantages over the conventional SAW structure presented in section 2.1.2:

- Increases acoustic energy confinement at the surface of the device.
- Increases K^2 of the structure, resulting in lower insertion loss and allowing the device design to be physically smaller.
- Increases mass and conductometric sensitivity of the structure.
- Reduces the centre-to-centre distance, due to the intermediate layer isolating the IDTs from the sensitive layer – thus, resulting in device being physically smaller.
- Matches the conductivity of a selective layer to the propagating SAW mode by optimising the intermediate layer thickness – thus, optimising the conductometric sensitivity of the device.
- Shields the IDT electrodes from harsh gas or liquid environment, which may improve both short and long term stability of the device.
- Shields the IDT electrodes from highly conductive selective layer, such as: carbon nanotubes or metal catalyst activated layers.
- Provides a sensor platform with electrode-free sensing surfaces, which may be suitable for conductive or corrosive environments [87].
- Adds a degree of freedom to control sensitive layer properties such as orientation and the size of crystallites, which may assist in tailoring material properties for the

particular application.

- Provides the ability to design structures that support different acoustic modes (e.g. Rayleigh and SH-SAW) in a single device.
- Allows structures that support SH-SAW propagation have the possibility to be employed in both gas and liquid phase analysis applications.

Furthermore, the cost of fabrication may be reduced as the intermediate and sensitive layer can cover the entire surface of the device – removing the need to shadow mask or pattern the sensitive layer in between the IDT ports, which is required in conventional SAW sensors.

Additionally, the layered configuration results in the sensitive layer acquiring a unique surface morphology. The underlying morphology of the intermediate ZnO layer is anticipated to influence the growth and formation of the sensitive layer, affecting grain size and surface area. A comprehensive investigation of the surface morphology of the intermediate and sensitive layers is presented in Chapter 6.

2.2.2 Metal Oxide Sensitive Layer

Metal oxide based gas sensors have been widely used for detecting a range of flammable and toxic gases in air. Compared to the organic and other semiconducting based sensitive layers, the metal oxide counterparts have been more successfully employed in sensing devices towards many gas analytes such as CO, CO_2, H_2, H_2O, NH_3, SO_x, NO_x, etc. with varying degree of commercial success [88]. The report of Sieyama et al. [89] in 1962, gave rise to significant development and commercialisation of semiconducting metal oxide based gas sensors. Since then, the steady state and dynamic gas sensing characteristics of metal oxide gas sensors, as exemplified by the Taguchi gas sensor, have been comprehensively studied [90].

The adsorption or reaction of a gas on the surface of a semiconducting metal oxide material induces a change in the electrical resistance of the material, which depends on gas the concentration [91]. Many review articles of semiconductor metal oxides materials for sensing applications exist in the literature [88, 91–96]. As previously mentioned, Ricco and Martin [72] first reported SAW based sensors employing a conductometric sensing mechanism. Since then it has been widely recognised that the acoustoelectric phenomena occurring in SAW devices is suitable for conductometric gas sensing applications. The

addition of noble metal catalysts has been used in metal oxide based gas sensors to increase both selectivity and sensitivity [97]. The metal components are used to strengthen interaction between the sensitive layer and the analyte gas. They are also known to reduce the response and recovery time of the sensor [97]. A thorough account of the relevant literature detailing the gas sensing mechanisms of metal oxides has been compiled by Trinchi [98].

Metal oxide sensitive layers have been selected due to their stable chemical and thermal properties. Considering that the metal oxide films are already fully oxidised when produced, they are one of the best candidates for gas sensing applications [4]. Another advantage associated with metal oxide films is that by varying the deposition parameters during the fabrication process, the possibility of 'tailoring' the layer selectivity and sensitivity towards specific gas species is possible. Galatsis [19], demonstrated that newly developed metal oxide binary-compounds were shown to be highly selective towards different analyte gases. Although this work does not concern binary-compounds, the high sensitivity and good stability of metal oxides make them an ideal candidate for SAW devices employing the acoustoelectric effect as the primary sensing mechanism. For the purpose of the work conducted during this research program, the author chose to individually focus on tungsten trioxide (WO_3) and indium oxide (InO_x) as gas sensitive layers. Further discussion regarding the sensitive layer material selection is presented in Chapter 4, section 4.2.3 and 4.3.3.

2.3 Summary

From the outset of this research program, it was the author's intention to develop a highly sensitive gas sensors using novel multilayered SAW structures. In this chapter, the author presented a discussion of 2-port SAW delay line technology with an emphasis towards gas sensing applications. The operating principles concerning conventional SAW based gas sensors was presented, highlighting the mass and conductivity based sensing mechanisms. The author's rationale for proposing a multilayered SAW structure for gas sensing applications was then presented. The author referred to the SAW literature to methodically direct the reader to relevant publications to develop the underlying principles of the proposed multilayered SAW structure. The chapter then concluded by identifying a list of advantages associated with the proposed layered SAW structure and discussed some of the relevant literature, concerning metal oxide sensitive layers.

It is envisaged that the utilisation of high electromechanical coupling coefficient (K^2) substrate materials, such as $LiNbO_3$ and $LiTaO_3$, combined with a ZnO piezoelectric guiding layer and dedicated metal oxide sensitive layer, will fulfill the objectives outlined in Chapter 1, section 1.2. The proceeding chapters of this thesis will investigate the benefits and unique features of the multilayered *sensitive-layer*/ZnO/*substrate* structural configuration in depth.

[This page is left blank intentionally.]

Chapter 3

Finite-Element Modelling with Experimental Verification

Much work has been devoted to analytical and numerical modelling techniques for SAW devices. Finite-element modelling is a very powerful tool for understanding acoustic wave propagation in complex layered media. Modelling can be employed to either understanding acoustic wave generation and detection in anisotropic layered media or to help design structures such as transducers, reflectors and couplers in a bid to obtain the desired frequency response characteristics. While transducer design is a major concern for the design of signal processing components, sensor design places much greater emphasis on understanding acoustic wave behaviour in layered media [37].

In recent years, computer simulation has become an important tool in SAW transducer design. Such simulation partly replaces time-consuming and expensive experimental work [99]. A balanced combination of computer simulation and experimental work is generally considered to lead to an efficient design process. In the case of layered SAW structures, different anisotropic material configurations have dramatic effects on the device behaviour and frequency response characteristics. To gain a better understanding of the acoustic wave propagation in a layered SAW device for conductivity-based gas sensing applications, a finite-element method is proposed and presented.

This chapter collates and summarises the findings of the author, which have been published in peer review proceedings between the years 2002 and 2004 and presented at several international conferences. Direct full-scale, two-dimensional (2D) [100] and three-dimensional (3D) [101–103] finite-element models for the analysis of the electromechanical phenomena occurring in layered SAW device structures are presented. To the best of the authors knowledge, it is the first time a full 3D finite-element model of a layered SAW device with experimental verification has been presented. The modelling

was accomplished by utilising a commercial available finite-element software package, ANSYS 5.7. As a result, other research groups have been able to progress on the authors contribution [104, 105], citing the work presented here. Furthermore, the author has co-authored new work involving finite-element modelling of acoustic flexural plate wave (FPW) devices [106], which will not be discussed here.

In this chapter, the author presents a layered SAW transducer structure, with suitable geometric parameters for 2D and 3D finite-element analysis. The structure employs both a piezoelectric substrate and piezoelectric layer, which supports complex acoustic wave propagation. The structural parameters were chosen to exploit the full capabilities of both 2D and 3D finite-element analysis. Although the author successfully analysed the layered structure by 2D finite-element method, results presented justify the author's argument that a full scale 3D analysis technique is required for accurate analysis of SAW propagation in layered structures consisting of anisotropic materials.

Section 3.1 introduces finite-element modelling concepts for piezoelectric media, detailing some of the method's advantages. Also the basic steps involved in applying finite-element transient analysis to a piezoelectric problem is described.

Section 3.2 describes the theory for coupled mode analysis using the finite-element method. The approach concentrates on piezoelectric material analysis, detailing the initial conditions and the algorithm used by ANSYS.

Section 3.3 outlines the implemented layered SAW transducer structure, suitable for 2D and 3D finite-element analysis in ANSYS. Using the same structural parameters, the experimental transfer function of the layered SAW transducer is presented, against which the performance of the finite-element model is verified. Furthermore, the computer platform specifications are detailed.

In section 3.4 the results of the 2D finite-element model are presented. Results include the displacement contour plots for both the layered and non-layered SAW device structure, a voltage contour plot and depth profile comparison. The outcomes of the 2D analysis demonstrate that the layered structure has a higher sensitivity than its non-layered counterpart. Finally, the performance of the 2D model is compared against both the layered and non-layered experimental data. Inadequacies of the 2D model are highlighted, indicating that the neglected shear-horizontal displacement component contributes significantly to analysis error.

Section 3.5 details the extension of the 2D model to a full scale 3D finite-element model. Results presented clearly identify the requirement for a full 3D analysis method. The depth profile of the layered structure demonstrates the importance of considering all 3 displacement components in the x, y and z-directions. The extended model enables the investigation of phenomena such as beam steering and diffraction effects (in both the layered and non-layered SAW structures), which were not obtainable by the present 2D analysis method. In addition, contour plots of displacement in the time domain are presented to illustrate the mechanical effect of the receiving IDT and the effect of electromagnetic feed-through is investigated. Furthermore, the frequency response generated by the finite-element simulation is compared to experimental results, showing good agreement. Finally, simulations were conducted to determine the device configuration for maximum conductivity based sensing applications.

Section 3.6 discusses some of the disadvantages and limitations with the finite-element method, and finally the chapter concludes in section 3.7 with a detailed summary of the findings presented in this chapter.

3.1 SAW Finite-Element modelling

For more than twenty years, the finite-element method has been successfully applied to predict the behavioural parameters of ultrasonic transducers [99, 107–116]. Various aspects of acoustic wave propagation have also been investigated using finite-element methods [117–124]. The finite-element approach has proven to be powerful means for the analysis and design of electromechanical devices. In contrast to analytical solutions, which show the exact behaviour of a system, most numerical methods approximate a solution only at discrete points, called nodes [125]. The exact solution to many practical engineering problems by analytical methods is not always possible. The inability to obtain an exact solution may be attributed to either the complex nature of the governing differential equations, or the difficulties that arise from dealing with boundary and initial conditions. Numerical approximation methods are generally used to deal with problems that fall into this category. The finite-element method is a numerical procedure that can be utilised to obtain solutions to a large class of engineering problems [125].

Most commonly used models for simulating the mechanical and electrical behaviour of piezoelectric transducers introduce simplifications and assumptions that are often invalid for actual designs [109]. Second order effects such as backscattering, diffraction and

mechanical loading are simplified or neglected by many other analysis techniques [28, 122]. Often a combination of various techniques are required to model different aspects of a SAW device [118]. The geometric structure and anisotropic material properties used in SAW devices often demand a full 3D description.

Although most methods address specific design requirements, many are unable to accurately predict SAW device characteristics when second order effects become significant at high-frequencies [24]. Furthermore, SAW modes such as Leaky Surface Acoustic Wave (LSAW), Surface-Skimming Bulk Wave (SSBW) and Surface Transverse Wave (STW) are also beyond the scope of most of analytical methods [24].

In earlier papers dealing with the finite-element analysis of piezoelectric devices, only small segments of the device were considered. As computing power has increased, it is now possible to perform a complete full-scale 3D analysis on a layered SAW device and compare the calculated transfer function to that of a measured device. Full-scale finite-element models have been presented for Lamb wave delay lines [123] and non-layered SAW device [118, 121, 122]. However, to the best of the authors knowledge, none have attempted full scale, multi-layered piezoelectric structures with displacement in x, y and z-axis, as presented in this chapter.

The fundamental equations that govern piezoelectric media, encompassing the relationship between stress, strain and electric field a set of partial differential equations. To theoretically analyse SAW propagation in a layered structure, it is necessary to solve these equations including the imposed boundary conditions. This chapter will extend these concepts with emphasis of solving the piezoelectric constitutive equation using the finite-element method, which will be discussed in section 3.2.

Basic Steps in the Finite-Element Method

The first step in a finite-element procedure is discretisation. This process divides the medium of interest into number of smaller subregions that comprise of elements and nodes. The nodes are points at the intersection of the element boundaries. The finite-element method uses an integral formulation at each point to create a system of algebraic equations. An approximate continuous function is assumed to represent the solution for each element. The complete solution is then generated by connecting or assembling the individual solutions, allowing for continuity at the interelemental boundaries [125].

In general, there are three approaches to formulating finite-element problems: a) direct formulation; b) minimum total potential energy formulation; and c) weighted residual formulation [125]. Regardless of how the finite-element model is formulated the analysis consist of the following three phases of implementation:

1. **Preprocessing Phase**
    - The discretisation of the problem – subdivide the problem into regions that can be represented by nodes and elements.
    - The selection of the appropriate shape functions to represent the physical behaviour of the elements. In ANSYS, this is done by selecting the element type which is responsible for the approximate continuous function representing the solution for each element.
    - The assembly of the elements – constructing the global stiffness matrix to represent the entire problem.
    - The application of the boundary and initial conditions (i.e. mechanical or electrical loading).
2. **Solution Phase**
    - To solve the set of algebraic equations simultaneously to obtain nodal results.
3. **Postprocessing Phase**
    - The extraction of the important information such as displacement and electric potential. In the case of a transient analysis the required nodal results are extracted for each time-step iteration.

Further postprocessing can be done with third-party software after the solution to the problem has been calculated. With regards to the work presented in this thesis, the extraction of data and manipulation by Matlab routines is required.

3.2 Finite-Element Approach for Coupled Mode

The finite-element theory for the transient analysis of a layered SAW device in ANSYS is summarised in this section. This summary provides a consistent background necessary for undertaking a coupled-field transient analysis using the finite-element method.

Variational principles are employed to develop the finite-element equations used by ANSYS [126]. The piezoelectric constitutive are used by ANSYS in the following form:

$$\begin{Bmatrix} \mathbf{T} \\ \mathbf{D} \end{Bmatrix} = \begin{bmatrix} [c] & [e] \\ [e]^T & -[\varepsilon] \end{bmatrix} \begin{Bmatrix} \mathbf{S} \\ -\mathbf{E} \end{Bmatrix} \quad , \tag{3.1}$$

where $\mathbf{T}$ is the stress vector, $\mathbf{D}$ is the electric flux density vector, $\mathbf{S}$ is the strain vector, $\mathbf{E}$ is the electric field vector, $[\varepsilon]$ is the dielectric matrix under constant mechanical strain and $[c]$ is the elastic stiffness coefficient matrix evaluated under constant electric field. It should be noted that ANSYS uses a convention for the stress matrix $[e]$ and its transpose $[e]^T$, which differs from the more common convention (e.g. Auld [33]), as shown below [126]:

$$[e] = \begin{array}{c} \\ x \\ y \\ z \\ xy \\ yz \\ xz \end{array} \begin{array}{c} \begin{array}{ccc} x & y & z \end{array} \\ \begin{bmatrix} e_{11} & e_{21} & e_{31} \\ e_{12} & e_{22} & e_{32} \\ e_{13} & e_{23} & e_{33} \\ e_{16} & e_{26} & e_{36} \\ e_{14} & e_{24} & e_{34} \\ e_{15} & e_{25} & e_{35} \end{bmatrix} \end{array} \quad . \tag{3.2}$$

The stiffness matrix piezoelectric constants transformed for direct input into the ANSYS software package for materials used throughout this chapter can be found in Appendix A.

The finite-element discretisation is performed by establishing nodal solution variables and element shape functions over an element domain which approximate the solution. The nodal variables are assigned to discrete elements [126]. The displacement within the element domain in the x, y, z-directions is:

$$\mathbf{u}_c = [N^u]^T \mathbf{u}_{node} \quad , \tag{3.3}$$

where $\mathbf{u}_{node}$ is the vector of nodal displacements:

$$\mathbf{u}_{node} = \{U_{x_1}\, U_{y_1}\, U_{z_1}\, \ldots\, U_{x_n}\, U_{y_n}\, U_{z_n}\}^T \quad , \tag{3.4}$$

and $[N^u]^T$ is the transpose of the displacement shape functions:

$$[N^u]^T = \begin{bmatrix} N_1 & 0 & 0 & & N_n & 0 & 0 \\ 0 & N_1 & 0 & \dots & 0 & N_n & 0 \\ 0 & 0 & N_1 & \dots & 0 & 0 & N_n \end{bmatrix} \quad , \tag{3.5}$$

and, subscript n refers to the number of nodes in the element.

The electrical potential V_c, within each element domain can be written as:

$$V_c = [\mathbf{N}^V]^T \mathbf{V}_{node} \quad , \tag{3.6}$$

where $\mathbf{V}$ is the vector of nodal electric potential:

$$\mathbf{V}_{node} = \begin{Bmatrix} V_1 \\ V_2 \\ \vdots \\ V_n \end{Bmatrix} \quad . \tag{3.7}$$

$[\mathbf{N}^V]^T$ is the transpose of electrical potential shape function:

$$[\mathbf{N}^V]^T = \{N_1 \; N_2 \; \dots N_k\} \quad , \tag{3.8}$$

where N_k is the shape function for node k.

The strain $\mathbf{S}$, and electric field $\mathbf{E}$, are related to the displacement and electric potentials, respectively by the following two equations:

$$\mathbf{S} = [B_u]\,\mathbf{u} \quad , \tag{3.9}$$

$$\mathbf{E} = -[B_V]\,\mathbf{V} \quad . \tag{3.10}$$

$[B_u]$ and $[B_V]$ are in the format utilised by ANSYS [126], which are the rearrangement of

∇_s and ∇ notations in the literature, and can be shown as:

$$[B_u] = \begin{bmatrix} \frac{\partial}{\partial x} & 0 & 0 \\ 0 & \frac{\partial}{\partial y} & 0 \\ 0 & 0 & \frac{\partial}{\partial z} \\ \frac{\partial}{\partial y} & \frac{\partial}{\partial x} & 0 \\ 0 & \frac{\partial}{\partial z} & \frac{\partial}{\partial y} \\ \frac{\partial}{\partial z} & 0 & \frac{\partial}{\partial x} \end{bmatrix} \quad , \tag{3.11}$$

$$[B_V] = \begin{Bmatrix} \frac{\partial}{\partial x} \\ \frac{\partial}{\partial y} \\ \frac{\partial}{\partial z} \end{Bmatrix} [\mathbf{N}^V]^T \quad . \tag{3.12}$$

Finally, after the application of the variational principle and finite-element discretisation, the coupled finite-element matrix equation derived for a single element model is:

$$\begin{bmatrix} [M] & [0] \\ [0] & [0] \end{bmatrix} \begin{Bmatrix} \ddot{\mathbf{u}}_{node} \\ \ddot{\mathbf{V}}_{node} \end{Bmatrix} + \begin{bmatrix} [C] & [0] \\ [0] & [0] \end{bmatrix} \begin{Bmatrix} \dot{\mathbf{u}}_{node} \\ \dot{\mathbf{V}}_{node} \end{Bmatrix} + \begin{bmatrix} [K] & [K^Z] \\ [K^Z]^T & [K^d] \end{bmatrix} \begin{Bmatrix} \mathbf{u}_{node} \\ \mathbf{V}_{node} \end{Bmatrix} = \begin{Bmatrix} \mathbf{F} \\ \mathbf{L} \end{Bmatrix} \quad , \tag{3.13}$$

where a dot above a variable denotes a time derivative. The right side of equation (3.13) contains the structural load vector $\mathbf{F}$ and the electrical load vector $\mathbf{L}$. The structural load vector is the vector of nodal, surface and body forces while electrical load vector is the applied nodal charge vector. The remaining constants for the structure are defined as:
structural mass :

$$[M] = \int_{vol} \rho \, [N^u] \, [N^u]^T \, \mathrm{d}(vol) \quad , \tag{3.14}$$

where ρ is mass density,

structural stiffness:

$$[K] = \int_{vol} [B_u]^T \, [C] \, [B_u] \, \mathrm{d}(vol) \quad , \tag{3.15}$$

dielectric conductivity:

$$[K^d] = - \int_{vol} [B_V]^T \, [\varepsilon] \, [B_V] \, \mathrm{d}(vol) \quad , \tag{3.16}$$

and the piezoelectric coupling matrix:

$$[K^z] = \int_{vol} [B_u]^T [e] [B_V] \, \mathrm{d}(vol) \qquad . \tag{3.17}$$

3.3 Layered SAW Transducer Problem Definition

The aim of using the finite-element method is to gain a deeper understanding of SAW propagation characteristics in layered media. To achieve this aim, a practical layered SAW transducer structure, with suitable parameters for 2D and 3D finite-element analysis is presented. Using the same structural parameters, the layered SAW transducer was fabricated via conventional photolithographic methods so that the results of the 2D and 3D finite-element models presented in the subsequent sections could be verified experimentally.

3.3.1 Model Constraints

The main constraining factors, caused by licensing and computational time limitations of the finite-element model, is the number of nodes and time steps used to model a structure. The larger the structure, the more nodes required during the discretisation process and the longer the computation time. Therefore, the layered SAW structure was required to have geometric dimensions suitable for both 2D and 3D finite-element methods.

3.3.2 Fabricated Device for Model Verification

Figure 3.1(a) shows the photolithographic mask pattern of the fabricated 2-port delay line, layered SAW device specifically developed for this work. Figure 3.1(b) shows an optical micrograph of the fabricated device, complete with piezoelectric ZnO layer (indicated by the dark region). The device has two electrode finger pairs in each input and output IDT port. The IDTs were formed by patterning a thin film comprising of Ti, Ni and Au, with a total thickness of 1000 Å, on a X-cut, Y-propagation $LiNbO_3$ substrate. A periodicity of λ_0=40 µm and aperture width of 200 µm were used. The edge-to-edge IDT separation is $2\frac{1}{4}\lambda_0$ or 90 µm. The photolithographic fabrication process used to fabricate the device is discussed separately in Chapter 5, section 5.1.

A 3 µm thick ZnO layer was deposited over the device by RF magnetron sputtering.

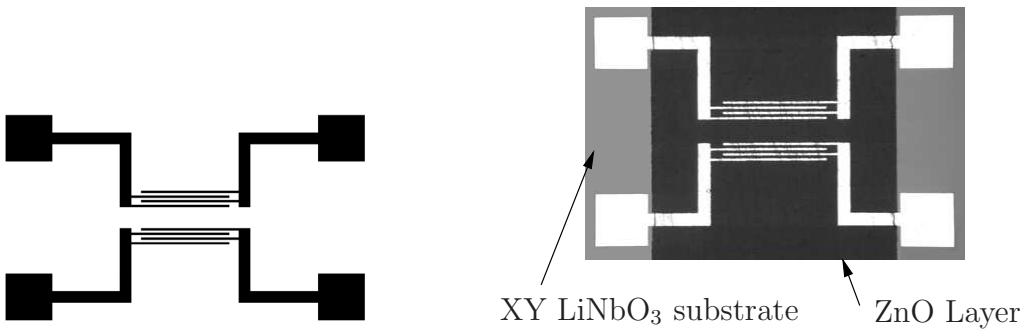

(a) Photolithographic pattern. (b) Fabricated layered SAW.

Figure 3.1: Photolithographic pattern and optical micrograph image of the fabricated layered SAW device used for the 2 and 3D finite-element model verification.

Details of this process can be found in section 5.3. The layer thickness was chosen to satisfy two conditions. The first was so that the structure achieved a maximum electromechanical coupling coefficient (K^2), for the 40 µm wavelength in accordance to the theory presented in [18]. The second condition was determined by the limitations imposed by the modelling software during the discretisation process. The geometry of the 3 µm thick ZnO layer was found to satisfy the upper nodal limit of the 3D finite-element model (see section 3.5 for further detail).

The experimental frequency responses is shown in figure 3.2, against which the performance of the finite-element models, detailed in subsequent sections, is verified. The response of the SAW device with and without the 3 µm ZnO layer is shown. The frequency responses were measured using a 50Ω vector network analyser (Anritru 37369A) equipped with picoprobe manipulators.

3.3.3 ANSYS Platform and Initial Conditions

Utilising a readily available commercial software package, ANSYS version 5.7, all finite-element simulations presented herein were performed under the academic licensing agreement. This agreement enabled all multiphysics capabilities which includes the coupled field solvers. However, the agreement limited the number of nodes to a maximum of 128,000. The implication of these limitations are discussed in sections 3.4 and 3.5.

The ANSYS software was installed on a Window 2000 operating system with a Pentium 4 processor and 768 MB of RAM. The processor speed was 1.6 GHz. Two hard disk drives were installed using separate IDE controllers in the machine. The operating system and ANSYS software were installed on the primary hard drive. The second hard drive was

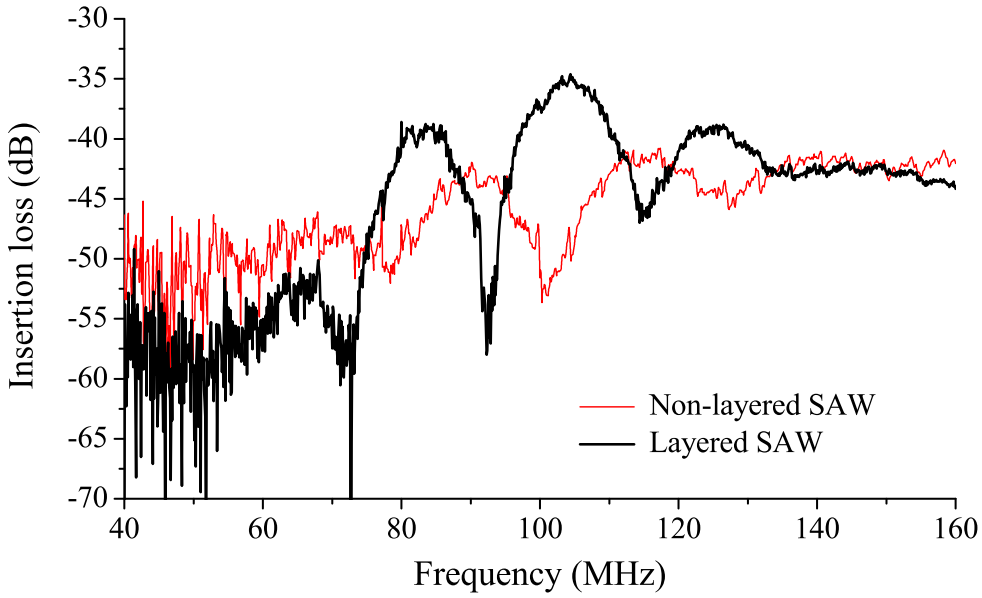

Figure 3.2: Measured frequency response of SAW device in figure 3.1(b) with and without 3 µm ZnO dielectric layer.

120 GB in size and used solely for storing and conducting finite-element simulations. Typical simulation time ranged from 4 hours for 2D and upwards of 2 days for the 3D structures.

3.3.3.1 Transient Analysis

All finite-element simulations performed were conducted using a transient dynamic analysis. This technique is used to determine the dynamic response of a structure in the time-domain. It is particulary suitable for the analysis of time-varying displacements, strains, stresses and forces present in a structure as a result of an applied load ($\mathbf{L}$), thus making it a very powerful tool for the analysis of propagating acoustic and electromagnetic waves.

3.3.3.2 Initial Conditions and Excitation Function

The initial displacement $\mathbf{u}_0$, initial velocity $\dot{\mathbf{u}}_0$ and initial acceleration $\ddot{\mathbf{u}}_0$ are all set to zero. A Dirac delta impulse function is used as the initial condition to excite the structure. However, since the Dirac delta function has an infinite amplitude and infinitesimal duration, it must be approximated in a computer simulation. A scaled rectangular approximation was chosen. The impulse function is applied on the nodes forming the

input electrodes, which can be represented as:

$$V_i = \begin{cases} \frac{1}{S_T}\,, & \text{if} \quad 0 < t \leq S_T \\ 0\,, & \text{if} \quad t > S_T \end{cases} \quad , \tag{3.18}$$

where S_T is the substep time interval, t is time and V_i is the applied signal. All other DOF for all other nodes are essential set to zero.

3.4 2D Layered SAW Simulations

A 2D finite-element model was prepared using the same specification as described in section 3.3. Figure 3.3 illustrates the 2D structural description prepared in ANSYS. As the analysis in this section is 2D, displacement in the z-direction of the structure is neglected. Therefore the simulation would be suitable for Rayleigh mode analysis, however would not be able to properly handle a SH-SAW. Nonetheless, results presented yield a useful insight into the propagation of acoustic waves in layered media.

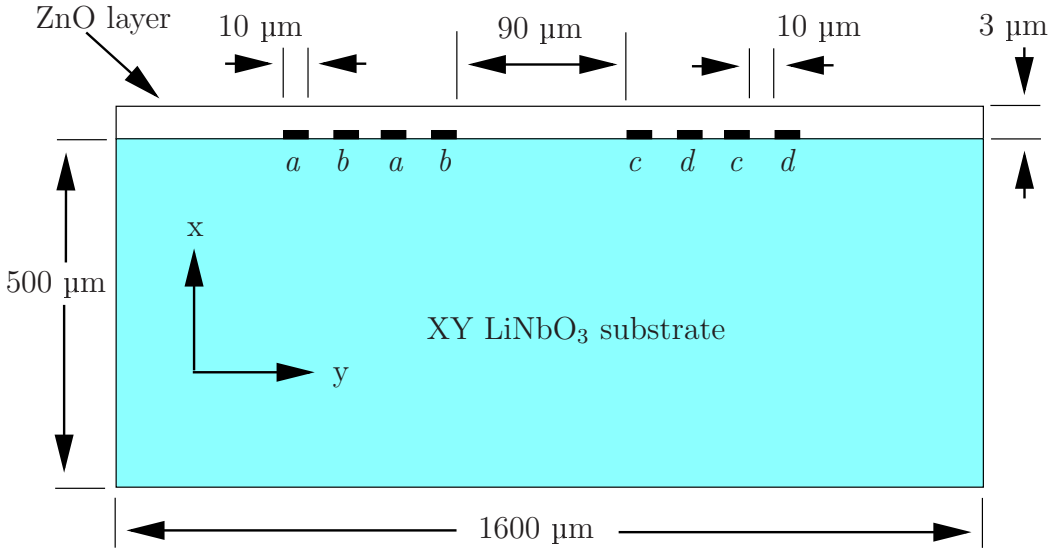

Figure 3.3: Schematic of layered SAW structure description used in 2D finite-element model.

Two separate structures were defined. The first was a non-layered substrate with only the IDTs, whilst the second was a layered structure, with IDTs and a 3 µm thick ZnO layer defined on the substrate surface. The substrate geometry for both structures was kept constant, with a length of 1600 µm and depth of 500 µm. The depth of the structure was chosen to correspond with the thickness of wafers used in the fabricated SAW devices.

A tradeoff between the number of nodes required and acoustic reflection occurring at boundaries of the structure determined the defined length of the simulated structures. 1600 µm was found to be sufficiently large enough for 200 ns long transient simulations.

3.4.1 2D Discretisation and Initial Conditions

Two-dimensional solutions are represented by plane segments. During the discretisation process, the PLANE13 element type was chosen to represent the elements in the model due to its coupled field capabilities. Each element comprises of 4 nodes with 3 degrees of freedom (DOF) enabled. These being 2 DOF for displacement, u_x and u_y and a third for voltage V. Figure 3.4 shows the mesh created underneath the IDT electrode region of the structure. The area representing the XY $LiNbO_3$ substrate consists of approximately 45,000 nodes forming over 90,000 elements. An additional 2,000 nodes represent the ZnO layer. The mesh was created so that the highest density of nodes was directly under the location of the IDTs and in the centre of the structure. To simplify the finite-element model for computational purposes, the IDT electrodes were defined as infinitesimally thin massless conductors. The IDT electrode fingers were represented as sets of coupled nodes on the substrate surface, each coupled by the voltage DOF. Thus, the IDTs were modelled only as boundary conditions, not as separate elements. A total of 4 coupled sets were

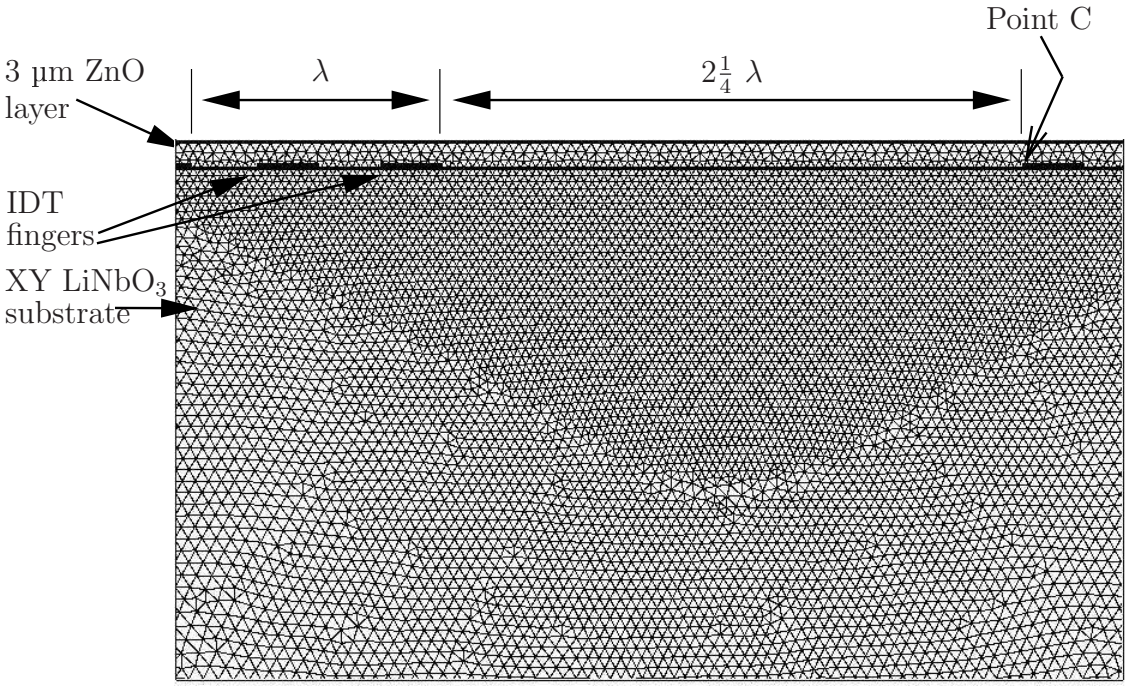

Figure 3.4: 2D mesh with 3 µm ZnO layer. Approximately 45,000 nodes forming over 90,000 elements for the substrate alone. Sufficient for modelling frequencies up to and below 100 MHz.

defined to represent the IDT fingers. These being coupled sets: a, b, c and d as shown in figure 3.3.

In general, the constitutive equations need to be solved together with Maxwell's equations for the electric field in the medium that surrounds the substrate material. Typically air or vacuum is assumed. The medium around the substrate would also require discretisation and hence, be resolved to a system of nodes and elements – resulting in increased computer resources and computation time. As the dielectric constants of the surrounding medium, such as air or vacuum are much smaller than those of the XY $LiNbO_3$ substrates, it was deemed unnecessary to discretise the surrounding medium. Studies by Xu [118], have shown that the difference between finite-element models when the surrounding medium is taken into consideration and when only the substrate is considered are negligible.

Initial Conditions

The excitation of the structure was provided by the impulse function V_i, as defined in equation (3.18). The impulse function was applied to the coupled set b. Coupled sets a and c were set to 0 volts. This effectively grounded every alternating IDT electrode finger on the substrate surface. No initial condition was defined for output coupled set d.

3.4.2 Acoustic Displacement

A transient analysis of the structures was performed for a simulation time of 200 ns. A substep time interval (S_T) of 1 ns was used. Firstly, the structure was simulated without coupled sets c and d defined. Figure 3.5 shows the displacement for the u_x and u_y of a node for both the blank and layered structures. The location of the node was approximately 90 µm away from the transmitting IDT port, which is the location of the first electrode of the receiving IDT port (point C in figure 3.4).

Both the u_x and u_y show little displacement until approximately $t = 23$ ns into the simulation – the time taken for the propagating wave to reach this location. The wave velocity is shown to be less in the layered structure when compared to the non-layered structure. It can also be seen that u_x has a larger displacement than the u_y in both the layered and non-layered simulations, showing that displacement normal to the surface is dominant.

Figure 3.6 illustrates the displacement contours of the propagating acoustic wave at

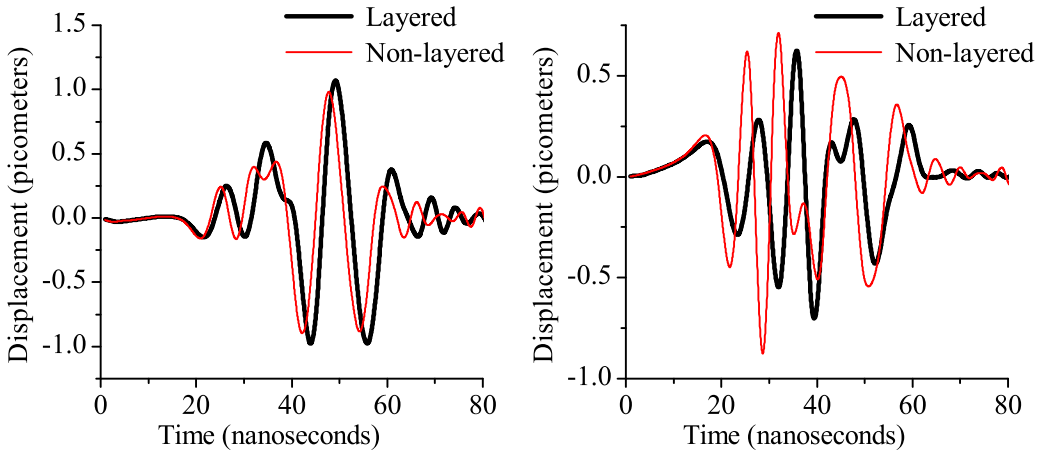

(a) Displacement in u_x.

(b) Displacement in u_y.

Figure 3.5: 2D Displacement at point C shown in figure 3.4.

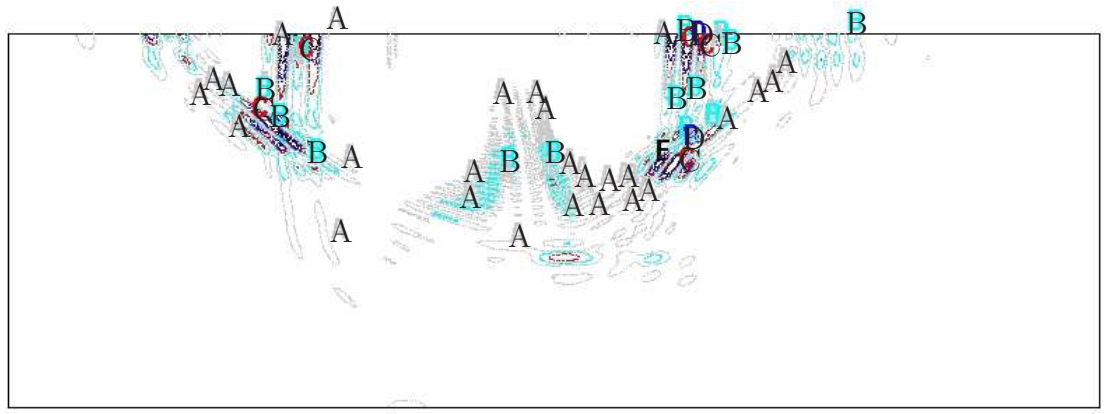

(a) Non layered structure.

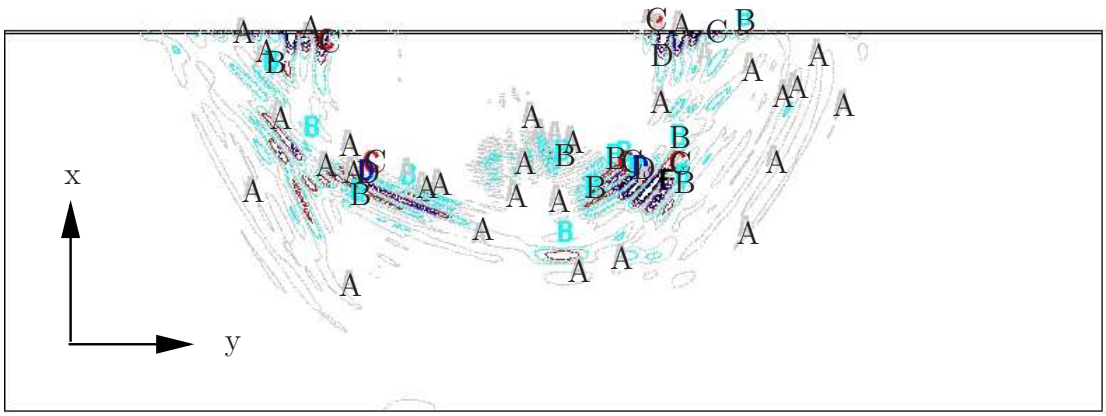

(b) Layered structure.

Figure 3.6: 2D displacement contours plots at $t = 80$ ns.

t = 80 ns. The contours show regions of constant magnitude of particle displacement. The contour plots clearly illustrate that the majority of the acoustical displacement starts at the input IDT and propagates into the depth of the substrate. This is an indication that the model handles second-order effects such as bulk-wave interference.

A comparison between the layered and non-layered contour plots reveals that the acoustical energy is more confined to the surface in the layered structure. The acoustic wave is shown to have propagated past the receiving IDT electrode finger after t = 80 ns.

3.4.3 Voltage Contours

Figure 3.7 illustrates a voltage contour plot directly under the transmitting IDT port of the layered structure at t = 9 ns. It can be seen that the electrical potential accompanying the acoustic wave also propagates into the depth and along the surface of the substrate. The electric potential associated with the propagating SAW near the surface of the substrate can be seen on the upper left and right corners of the image. For conductivity based gas sensing applications, the physicochemical interaction between the analyte gas and the device surface disrupts the boundary conditions by interacting with the electric field accompanying the propagating SAW. By inspection of the piezoelectric constitutive

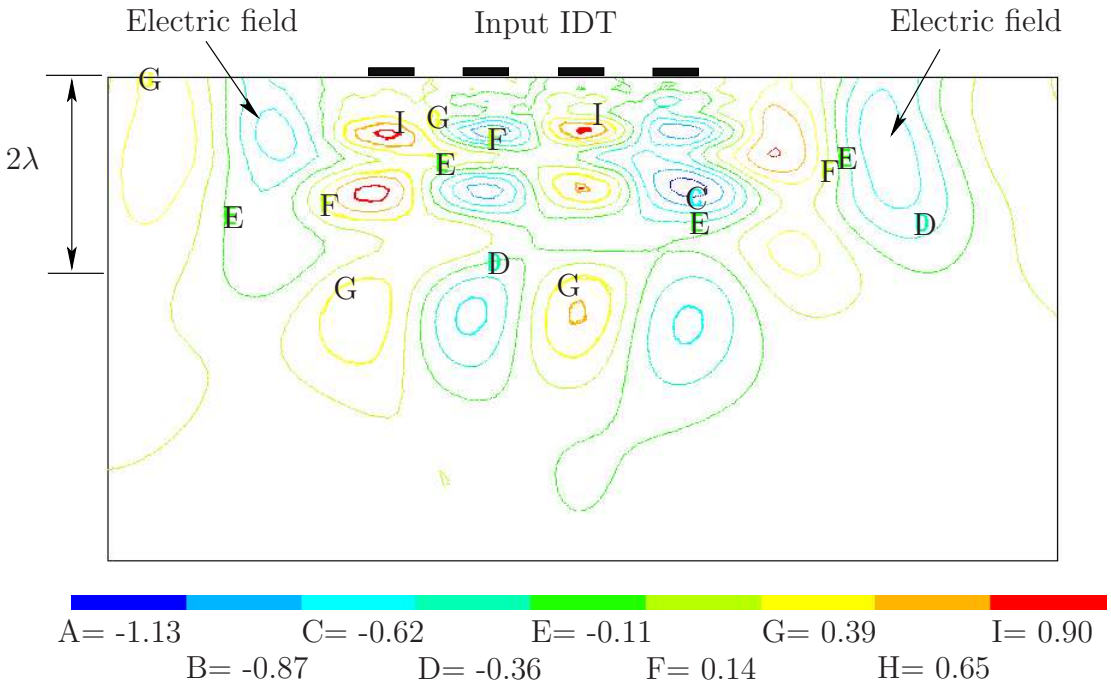

Figure 3.7: Magnified 2D voltage contour plot at t = 9 ns. Approximately 120 µm depth in x-axis is shown.

equations (equation 3.1), perturbation of the electrical boundary conditions causes a shift in the acoustic phase velocity.

3.4.4 Depth Profiles

A further analysis of the simulation results was conducted to determine the acoustic field profiles in the depth of the substrate. Using the same location as for the displacement profiles (approximately 90 µm away from the transmitting IDT port), nodes into the depth of the substrate, at point C in figure 3.4, were analysed. Figure 3.8(a) shows the normalised acoustic displacement as a function of depth into the substrate in both the x and y-directions, for the layered and non-layered structures. On review of the results, it is clear that the acoustic displacement is predominantly concentrated at the surface of the substrate. The largest displacement is normal to the surface of the structure. Additionally, the acoustic displacement attenuates into the depth of the structure. The latter observations agree with the findings in the literature [117, 127].

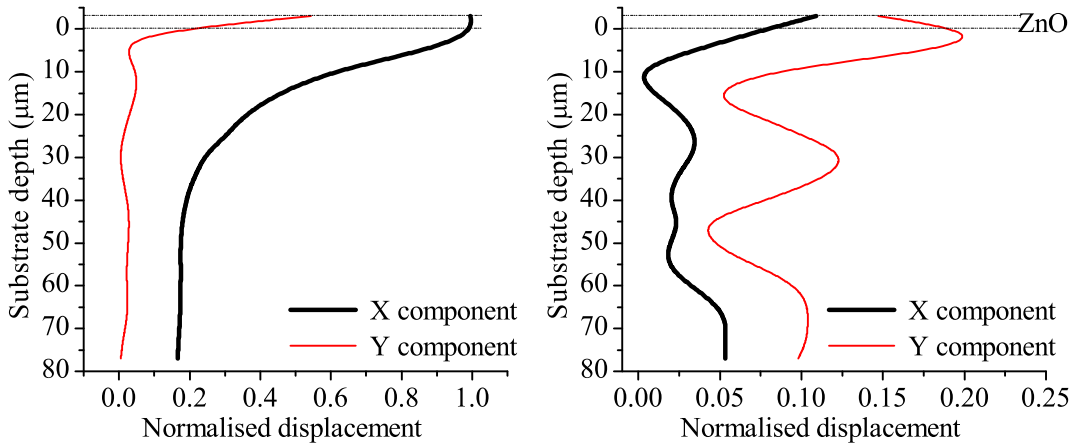

(a) Fundamental frequency.

(b) 2^{nd} harmonic frequency.

Figure 3.8: 2D depth profile calculated in the depth of the x-axis at point C shown in figure 3.4.

Figure 3.8(b) shows the normalised acoustic displacement of the 2^{nd} harmonic frequency into the depth of the substrate for both the x and y-directions in the layered structure. The 2^{nd} harmonic field profile shows a larger y-displacement component than x. The unaccounted for z-displacement component could possibly contribution to this unexpected result.

3.4.5 2D Finite-Element Model Verification

The simulated impulse response $h(t)$ is calculated by exciting the structure with the impulse function V_i, as defined in equation (3.18). The frequency responses of the simulated SAW device structures were obtained by taking a Fast Fourier Transform (FFT) of the voltage impulse response $h(t)$ produced at nodes which form the output IDT electrodes (coupled set d in figure 3.3).

The impulse response was detected by the open output IDT fingers (coupled set d) directly in the form of particle displacements and voltage potential. A Matlab script was written to extract data and perform the FFT for both the non-layered and layered structures.

To verify the validity of the 2D finite-element transient simulation, the frequency response generated from the simulation data is compared against the measured frequency response of the device presented in figure 3.1(b).

3.4.5.1 Non-Layered Structure

Figure 3.9 shows the measured and calculated frequency response of the non-layered SAW device. The measured and simulated results are in good agreement for frequencies between 80 and 100 MHz. The location of nulls and peaks of the lobes coincide, especially for the main centre lobe, which is generated predominantly by the normal displacement (x-component). Above 100 MHz the nulls and peak of the side lobes differ by approximately

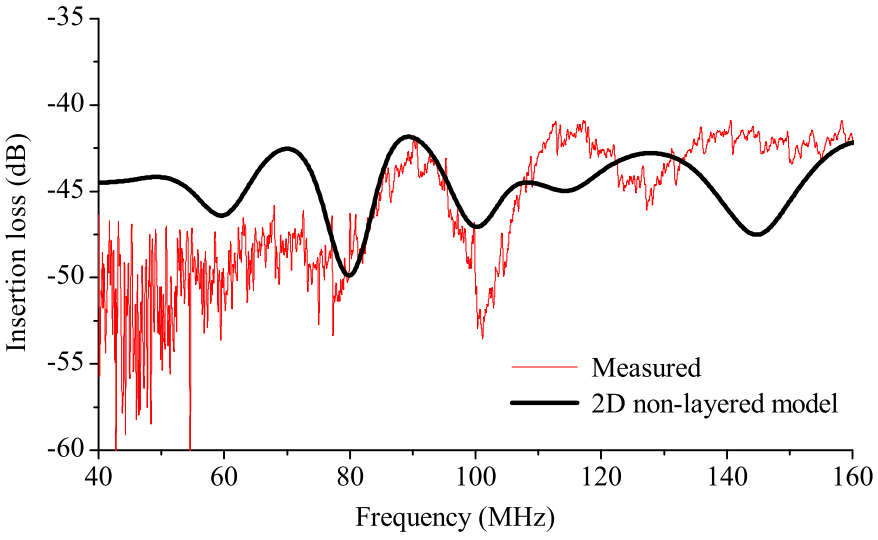

Figure 3.9: Comparison of measured and 2D simulated frequency response for non-layered XY $LiNbO_3$ structure.

10 MHz. The deviation between the simulation and measured frequency responses can be attributed to the neglected z-displacement components, which contributes to the Leaky acoustic mode of the substrate present between 100 and 120 MHz. Insufficient node density and simulation time (being limited to $t = 200$ ns) also contributed simulation inaccuracies. A higher node density and/or smaller substep time interval (S_T) is required to resolve frequency components above 100 MHz. Also, as the simulation is only calculated for 200 ns, bulk wave backscattering effects are not fully accounted for.

3.4.5.2 Layered Structure

Figure 3.10 shows the simulated and measured results of layered structure employing a 3 µm ZnO layer. A third simulation was conducted with a 5 µm thick ZnO layer for comparison. The results of the layered structure show agreement between the simulated and measured data. Again, for the same reasons as the non-layered structure, frequency components above 100 MHz appeared to not be resolved correctly. The calculated response of the layered structure (below 100 MHz) appears to follow the measured response, depicting the same lobe peaks and nulls with the correct bandwidth. However, the frequency response generated by the simulation appears to shift relative the measured response by 3 MHz. By increasing the ZnO layer thickness to 5 µm in the simulation, a direct change in operating frequency is observed. The finite-element model correctly predicts a decrease in operating frequency with increased ZnO thickness, however it is unable to match the frequency response of the fabricated device.

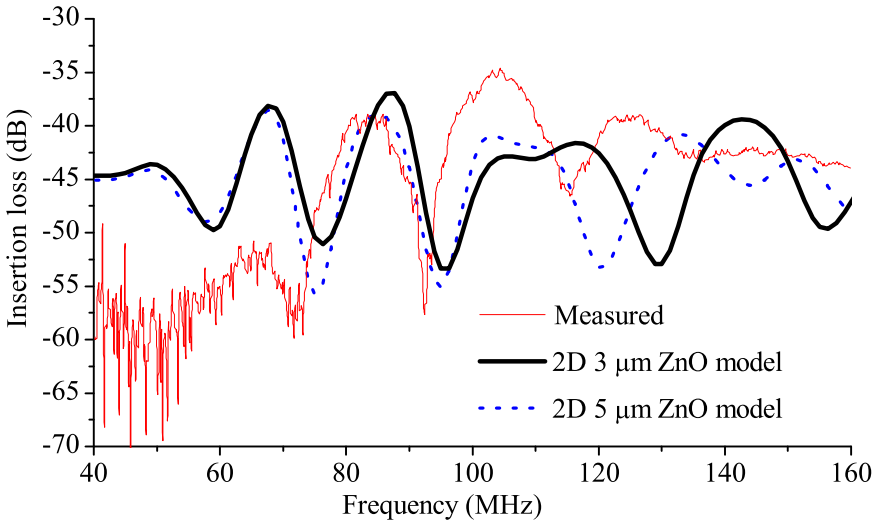

Figure 3.10: Comparison of measured and 2D simulated frequency response for layered ZnO/XY $LiNbO_3$ structure.

3.4.5.3 Comparison of Layered and Non-Layered Structure

A comparison between figures 3.9 and 3.10 reveals that the insertion loss for the structures with the ZnO guiding layer is lower than that of the non-layered SAW structure for both simulated and measured data. The simulated data also shows that the displacement is higher at the surface in the layered structure. This can be attributed to the layer confining the wave at the device's surface.

Due to these observations and the depth profile results presented above (section 3.4.4), it is suggested that the shear component of displacement is of vital importance. The 2D model is unable to handle displacement in the z-direction, which suggests that a 3D model would provide a much more accurate solution. In the subsequent section 3.5, a 3D model of this structure is presented for further investigation.

3.5 3D Layered SAW Simulations

A 3D structural definition of the layered SAW device was prepared using the same specifications described in section 3.3. Figure 3.11 illustrates the 3D description prepared in ANSYS, which includes the full 200 µm acoustic aperture width of the SAW device.

The structure was defined as a 2-port SAW delay line, with the substrate geometry being 430 µm in length (x), 500 µm depth (y) and 400 µm width (z-axis). Two electrode finger pairs in each IDT port were defined at the surface of an X-cut, Y-propagation $LiNbO_3$ substrate, forming the transmitting and receiving ports. A periodicity of 40 µm and an acoustic aperture width of 200 µm were used for each IDT. Similar to the 2D structure, the depth of the 3D structure was maintained at 500 µm. The 400 µm width of the structure allows 100 µm clearance on either side of the 200 µm acoustic aperture. The 3 µm thick ZnO layer was defined over the whole surface of the structure. This sandwiched the IDT finger pairs between the substrate and the ZnO layer, as in the 2D structure.

3.5.1 3D Discretisation and Initial Conditions

Triangular elements are widely used in finite-element modelling for their suitability for modelling complex boundaries. For the 3D model, the tetrahedral, SOLID98 element was used with 4 DOF. Three DOF provided longitudinal (u_x), normal (u_y) and shear horizontal (u_z) displacement components. The fourth DOF was voltage. A tetrahedral element shape was selected so the model could be created with the highest density of

nodes concentrated at the surface, to a depth of several wavelengths and throughout the centre of the structure. Figure 3.12 illustrates the resultant 3D mesh. The volume representing the XY $LiNbO_3$ substrate consists of approximately 100,000 nodes forming over 72,000 elements. An additional 20,000 nodes represent the 3 µm thick ZnO layer. The line divisions used to mesh the model were chosen to result in the 3D finite-element model satisfying the upper nodal limit of the ANSYS software licence agreement.

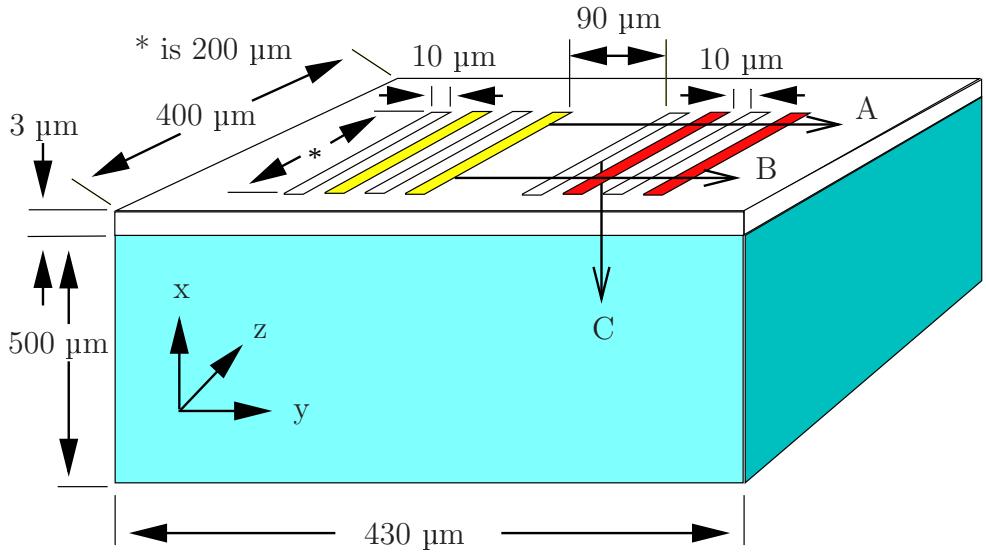

Figure 3.11: Schematic of layered SAW structure description used in 3D finite-element model.

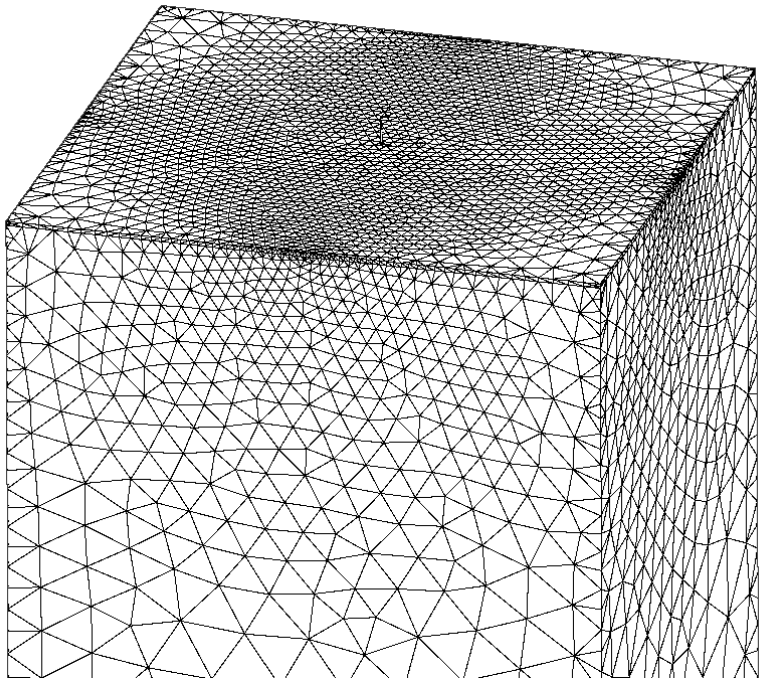

Figure 3.12: 3D finite-element model mesh with 3 µm ZnO layer.

To simplify the finite-element model, as in the 2D structure, the IDT electrode fingers were defined as infinitesimally thin mass-less conductors. Using the same method, 4 coupled sets were defined to represent the IDT electrode fingers. This being coupled sets: a, b, c and d as shown in the 2D schematic (figure 3.3). This simplification was required as the node limit, restricted by the software licence was satisfied. As a consequence, the second order effects produced by the electrode mass were disregarded, however they need not be if computer and licence resources permit. Xu [122] has studied the effects of electrode mass using the finite-element method, concluding that the method is most suitable for analysing second order effects regarding electrode perturbation. The analysis showed that for electrodes of fixed thickness, the second order effects on the frequency response become increasingly significant as the device geometry is scaled down to have centre frequencies above 1 GHz.

3.5.1.1 Initial Conditions

Similar to the 2D models, the excitation of the 3D structure was provided by the impulse function V_i, as defined in equation (3.18). The impulse function was applied to the coupled set b. Coupled sets a and c were set to 0 volts. No initial condition was defined for output coupled set d.

A transient analysis of the 3D structure was performed for a simulation time, t =100 ns. A substep time interval of 1 ns was used.

3.5.2 Acoustic Displacement

Unlike the 2D finite-element models, the 3D models consider all 3 displacement components, in the x, y and z-directions. For a general case employing anisotropic materials such as the XY $LiNbO_3$ and ZnO, an accurate solution requires all 3 displacement components to be considered.

Figure 3.13 illustrates contour plots at selected times for both a non-layered and layered 3D structure. The plots were calculated by ANSYS's summation function of the x, y and z-displacement components. The contour plots were generated from a top view, looking directly on to the active surface of the device (normal to the x-axis) at time, t = 20, 50 and 60 ns from top to bottom, respectively.

A comparison between contour plots for the layered and non-layered structures shown in

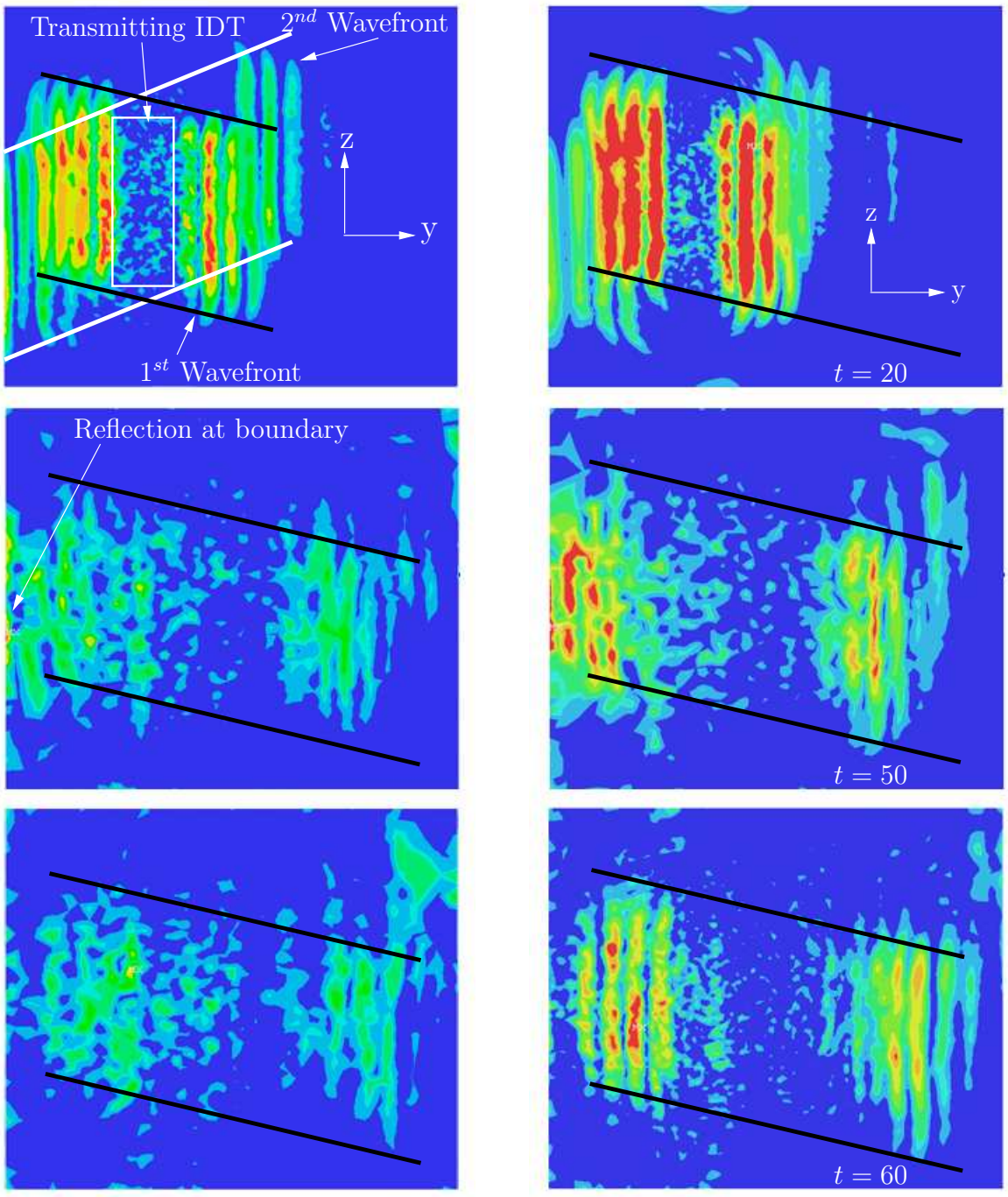

(a) Non-layered structure.

(b) Layered structure.

Figure 3.13: Top view of acoustic contour plots in time. *Top*: $t = 20$ ns. *Middle*: $t = 50$ ns. *Bottom*: $t = 60$ ns. Note how the wave propagates at a slightly alterant offset angles along the y-axis.

figure 3.13 reveal that the ZnO/XY $LiNbO_3$ structure has a higher acoustic displacement at the surface. In plots $t = 50$ and 60 ns, there is a higher displacement present in the location of the receiving IDT in the layered structure. The series of contour plots clearly illustrates that the ZnO layer plays a critical role in confining the acoustic energy to the surface of the structure.

3.5.2.1 Beam Steering

The first noticeable difference between the 2D and 3D models is the beam steering effect, or so-called acoustic beam-walkoff associated with acoustic wave propagation in anisotropic media. The 3D finite-element simulation can be used to visually conceptualise such effects.

The 3 contour plots for the non-layered structure in figure 3.13(a) shows that the acoustic energy is generated at the location of the transmitting IDT and propagates along the y-axis. At $t = 20$ ns there appears to be two distinct wavefronts propagating, suggesting dispersion is occurring. The two distinct waves will be referred to as '1^{st} wavefront' and '2^{nd} wavefront' in the text. It is also possible to see these wavefront in the layered structure at $t = 20$ ns in figure 3.13(b). The propagating wavefronts appear to travel at a slightly offset angles along the y-axis. The 2^{nd} wavefront propagates faster than the 1^{st} and appears to be comprised of higher frequency components. However it quickly attenuates by the time $t = 50$ ns. Further analysis presented in section 3.5.3, reveals that the y-component is the predominant displacement in the 2^{nd} wavefront – indicating that it is a longitudinal mode.

The 1^{st} wavefront corresponds to the predominant mode of the XY $LiNbO_3$ substrate and is present in the plot, $t = 60$ ns, for both the non-layered and layered structures. In the following section, the predominant displacement component of the 1^{st} wavefront will be shown to be in the z-direction, showing that the wave is shear-horizontally polarised. The 2D model presented in the previous section was unable to account for these features, as it neglected the z-component.

To confirm that the propagating wavefronts travel at a slightly offset angle along the y-axis, figure 3.14 plots the acoustic displacement along the paths **A** and **B**, shown in figure 3.11. Figure 3.14(a) shows the acoustic displacement calculated at 80 MHz for the z-component in the layered ZnO/XY $LiNbO_3$ structure, along the paths **A** and **B**. The 80 MHz frequency component was chosen because it was calculated to have the highest energy content in the layered structure. The intensity attenuates as the wave propagates

along the surface towards the receiving port. It is evident that the intensity calculated along the paths **A** and **B** have similar characteristics, although path **B** demonstrates overall higher energy intensity. The increase in energy intensity of path **B** shows the wave deviates or is steered as it propagates. This was first observed in the 3D contour plots presented in figure 3.13.

The deviation from the y-axis is in good agreement with literature for a XY $LiNbO_3$ substrate, which gives a value of approximately 5° [128]. The beam steering effect is a direct result of the anisotropic material properties of the substrate and the fact that the structure does not support a 'pure mode' propagation direction.

Figure 3.14(b) shows the acoustic displacement calculated for the z-component at 90 MHz in a non-layered XY $LiNbO_3$ structure along the same paths. As the acoustic phase velocity is higher in the absence of the ZnO layer, the 90 MHz frequency component was calculated to have the highest acoustic displacement in the structure. This corresponds with the 90 MHz centre frequency lobe shown in figure 3.9. Although the curves **A** and **B** show similar characteristics in both the non-layered and layered structures, it can be seen that the acoustic energy propagates more evenly in the layered structure.

In both the layered and non-layered structures, the calculated energy for the x and y-components along path **A** and **B** were significantly lower than the z-component, on average by a factor of 10 for each frequency component – confirming that the shear-horizontal mode is the dominant mode of propagation in the ZnO/XY $LiNbO_3$ structure.

3.5.2.2 Diffraction

A second order effect that is handled by the 3D finite-element model is diffraction. This effect is very much related to beam steering present in the substrate. Diffraction is due to finite aperture width and occurs in both isotropic and anisotropic media. Ideally, when SAWs are launched from the IDT, they should have wavefronts parallel to the fingers with a so-called 'flat wavefront' [24].

The contour plots presented in figure 3.13, at $t = 20$ ns and the data presented in figure 3.14 clearly illustrate that the launched wavefronts do not have a 'flat' front. At $t = 20$ ns in figure 3.13(b), the propagating waves can be seen to have a semi-spherical top and bottom, which is sometimes referred to as a 'banana' effect. The spherical nature is dependent on the aperture of the radiating source [24]. Diffraction can effectively

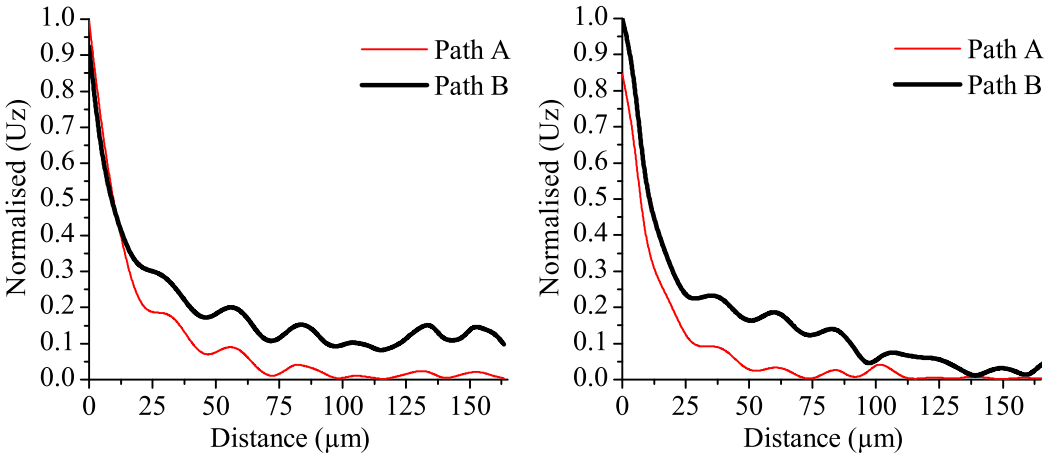

(a) Layered structure at 80 MHz.

(b) Non-layered structure at 90 MHz.

Figure 3.14: Normalised surface acoustic energy at the approximate centre frequency for both blank XY $LiNbO_3$ and ZnO/ XY $LiNbO_3$ layered SAW models, along path **A** and **B** shown in figure 3.11, for the z-component.

attenuate the SAW device frequency response. Therefore, if it is not accounted for, inaccuracies in the calculated frequency response may occur.

3.5.3 Depth Profile

In a layered SAW structure, due to the increased acoustic energy entrapment at the surface, a higher sensitivity than non-layered SAW structures is generally obtained [17]. This has been confirmed by the contour plots presented earlier. To investigate the acoustic energy concentration throughout the depth of the layered SAW structure, profiles of normalised particle displacement in depth have been calculated along path **C**, shown in figure 3.11. Figure 3.15 shows the profiles of normalised particle displacement calculated at 60 MHz, 80 MHz, 100 MHz and 120 MHz in the x, y, and z-directions.

Figure 3.15(a) shows the normalised particle displacement of the x-component in the structure's depth. The highest displacement component was found to be at 80 MHz. Unlike the results presented in the 2D depth profile, the overall magnitude of x-component displacement is smaller than the y-component.

Figure 3.15(b) shows the y-component, where the highest content is at 120 MHz. The y-component is the predominant displacement for a longitudinal mode. As the 2^{nd} wavefront in figure 3.13 at $t = 20$ ns is faster than the 1^{st}, it can be concluded that 2^{nd} wavefront is a longitudinal mode.

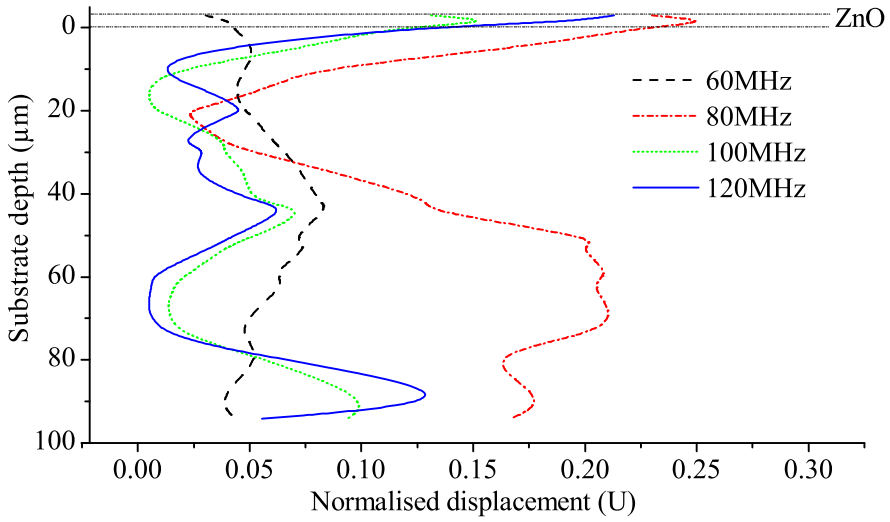

(a) X-component.

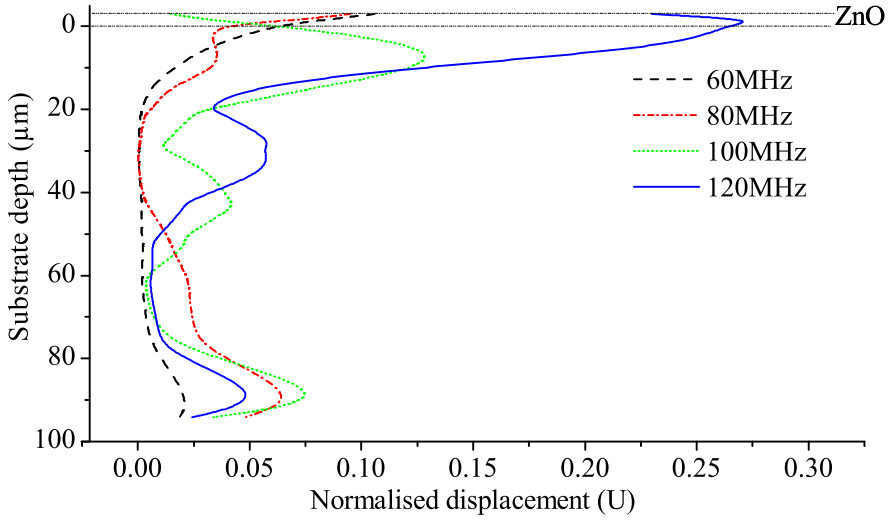

(b) Y-component.

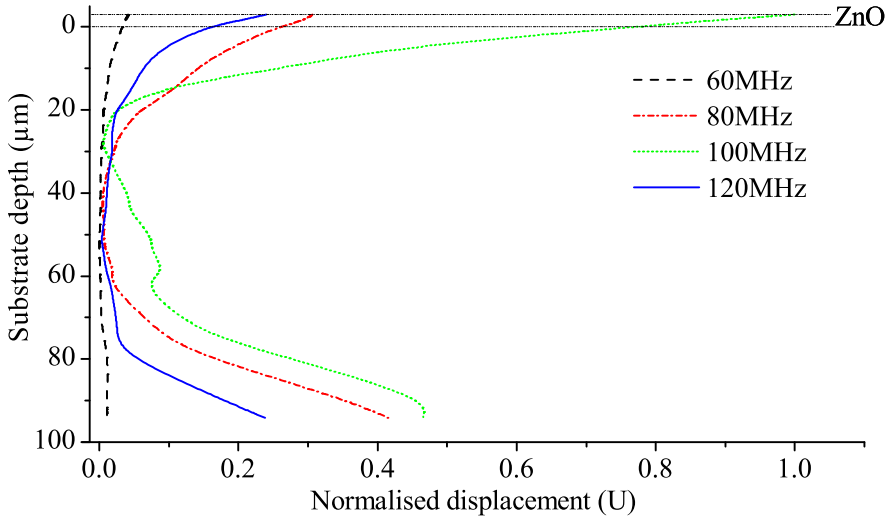

(c) Z-component.

Figure 3.15: 3D depth profile – normalised particle displacement profile of layered SAW device in x (u_x), y (u_y) and z-axis (u_z) along path **C** in in figure 3.11.

Overall, the magnitude of the x and y-components were considerably smaller than the shear z-component, which is the predominant displacement in the structure. Figure 3.15(c) shows the maximum normalised displacement is in the z-axis at 100 MHz – more than double the magnitude of any other components. This suggests that the dominant mode of acoustic propagation is mainly polarised in the shear horizontal plane, parallel to the device surface. It has also been found that such particle displacements are within 20 µm or $\frac{1}{2}$ λ of the device surface. This is much smaller than values given in the literature, which states that acoustic confinement of a SAW is within 2 λ into the depth of the substrate [24]. Therefore, significant surface energy confinement is seen in the $ZnO/LiNbO_3$ layered structure when compared to its non-layered counterparts. The high energy confinement at the surface of the device is paramount for increasing its sensitivity towards mass perturbations. Furthermore, at a depth of 60 µm the displacement appears to start increasing again. As the node density in the 3D finite-element model begins to decline at this depth, further study would be required to confirm the accuracy of results below 60 µm.

3.5.4 Electrostatic Feed-Through

The complexity of IDT effects involved in a SAW device is enough to justify the use of several different modelling approaches concurrently. The majority of modelling techniques generally introduce simplifications and assumptions that are invalid for actual designs [109]. These simplifications often predict a response that does not correspond to the experimental frequency response of the device. The 3D finite-element model presented combines both the electrostatic and mechanical coupling effects associated with a SAW device. The most important advantage of using a 3D approach is that second order effects such as backscattering, bulk wave interference, diffraction, triple-transit-interference and electromagnetic feed-through can all be taken into consideration concurrently.

Some of the most interesting second order effects that can be investigated using the finite-element method is the electromagnetic feed-though effect and triple-transit-interference. The electromagnetic feed-through can be evaluated in the electrostatic limit, by relating the direct coupling of input signal to output IDT. The triple-transit-interference is due to multiple SAW reflections between bidirectional input and output IDTs.

In order to investigate these two second order effects, firstly the layered structure was simulated without coupled sets c and d – hence, no receiving IDT was defined. A

comparison between a simulation with the receiving IDT defined was then made. Contour plots generated from a top view, looking directly on to the active surface of the device (normal to the x-axis), were generated by linear interpolation within each element from the nodal values. If two or more elements were connected to the same node, the results were averaged. Figure 3.16 shows summation of the u_x, u_y and u_z displacement components for $t = 2$ ns.

Figure 3.16(a) shows significant displacement of the substrate surface at both the transmitting and receiving IDT ports. The displacement at the receiving port can be attributed to the electromagnetic feed-through that is induced by the voltage applied to the transmitter IDT port. It was observed that the acoustic wave generated at the receiving port, although at much lower amplitude, also propagates along the y-axis, towards transmitting port causing the triple-transit-interference. Both these effects are often neglected or simplified in the majority of modelling and analytical techniques used for the analysis of SAW devices.

Figure 3.16(b) shows the contour plot where only the IDT fingers forming the transmitter port were defined. For the structure presented, approximately 20 ns was required for the acoustic wave generated by the transmitting IDT to propagate to the receiving IDT.

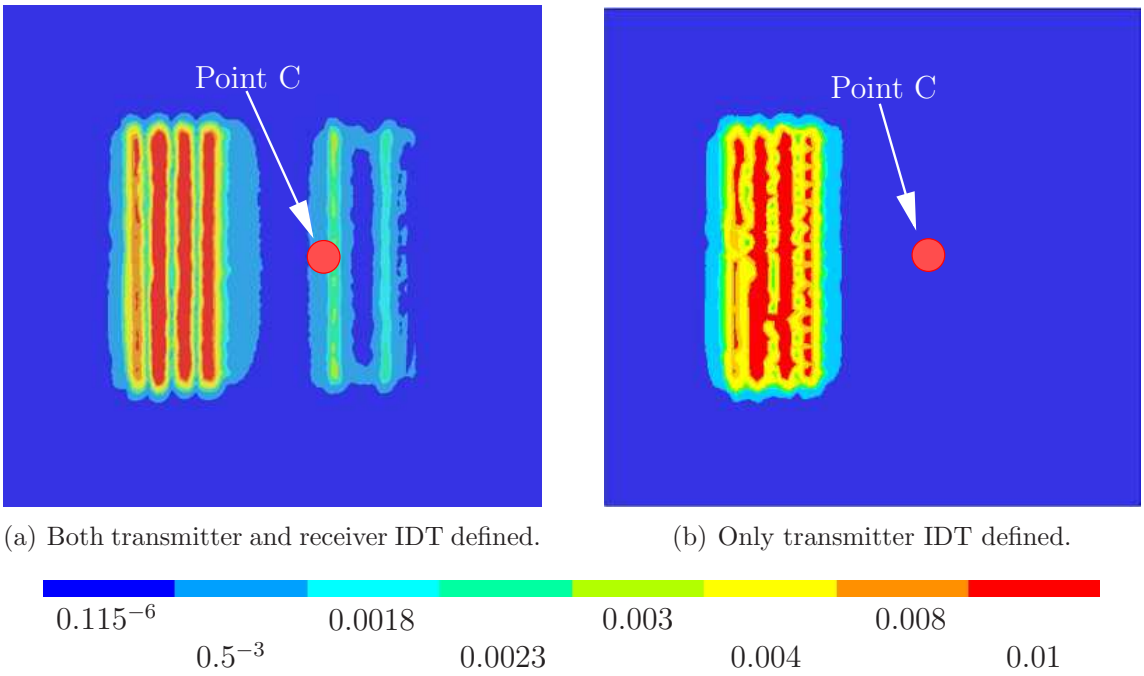

(a) Both transmitter and receiver IDT defined. (b) Only transmitter IDT defined.

Figure 3.16: SAW displacement contours at $t = 2$ ns. (a) – only transmitter is defined. (b) – both transmitter and receiver IDT ports are defined.

By choosing one of the nodes at the location of the receiving IDT, represented by point **C** in figure 3.16, a displacement curve was generated for both simulations. Figure 3.17 shows the displacement of the x, y, and z-component for the layered structure in both circumstances.

The z-component of displacement is approximately 3 times larger when compared to the x and y-components. Therefore, a shear-horizontal mode is suggested to be the predominant mode of the structure, as the z-component represents shear-horizontal displacement. It can be seen that the magnitude in the z-component generated by the electromagnetic feed-through is comparable to the magnitude of displacement generated by the input IDT. Displacement in the y-component shows minimal difference for both simulations, however there is a marginal increase in the x-component for $t \leq 20$ ns. This indicates that displacement normal to the substrate surface is also influenced by the electromagnetic feed-through.

3.5.5 3D Finite-Element Model Verification

To verify the performance of the 3D finite-element transient simulation, the simulated frequency response is compared against the measured frequency responses described in section 3.3. The comparison is shown in figure 3.18. The results of the 3D layered structure, which consider all three components of displacement, show a much improved agreement between the simulated and measured data than the 2D model. An FFT and extraction process was used, as described for the 2D structure in section 3.4.5. Due to the computational limitations, the frequency response was calculated by zero padding the time domain voltage in the FFT.

As the simulation did not model the effects of the network analyser connections or external circuit, the frequency response derived from the simulation data was adjusted (increase) to match the insertion loss of the measured SAW device. However, it is clear that the location of the nulls and lobe peaks coincide, particularly for the main centre lobes. The limitation of the finite-element model, such as the size of the structure, node density and the limited number of time steps used, inhibit the simulation's ability to accurately determine the frequency response above approximately 110 MHz.

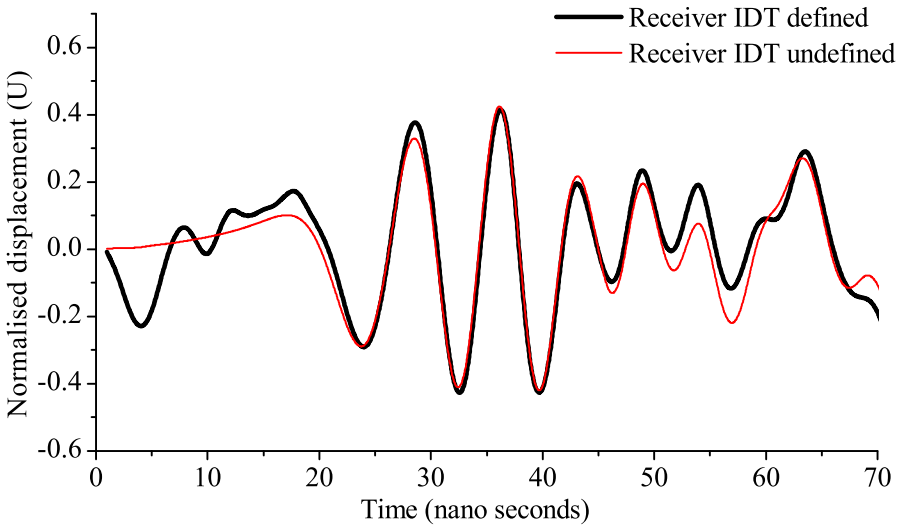

(a) X-component.

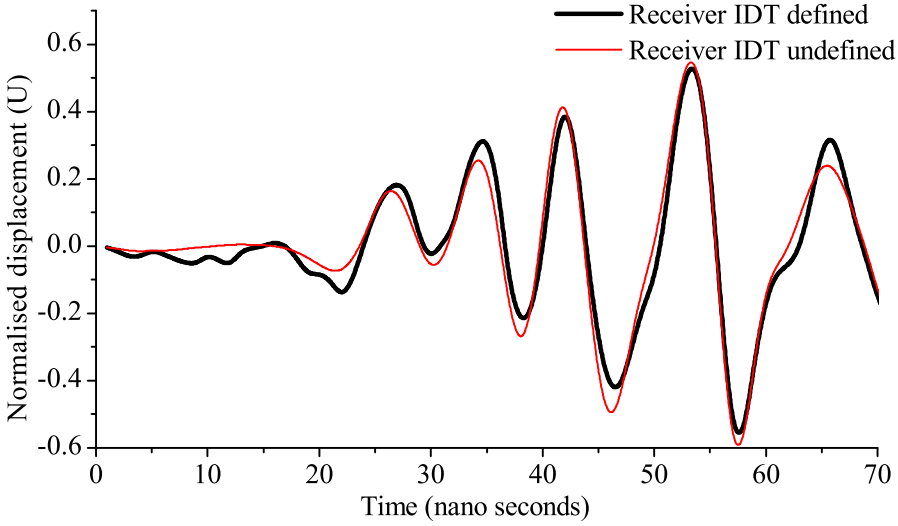

(b) Y-component.

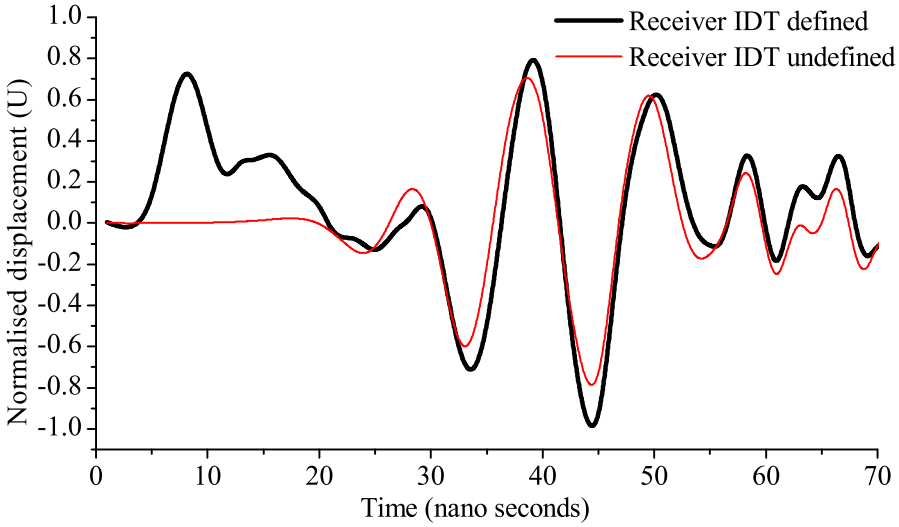

(c) Z-component.

Figure 3.17: Normalised particle displacement for x (u_x), y (u_y) and z-axis (u_z) on the substrate surface at point **C** in in figure 3.11 with and without the receiver IDT defined.

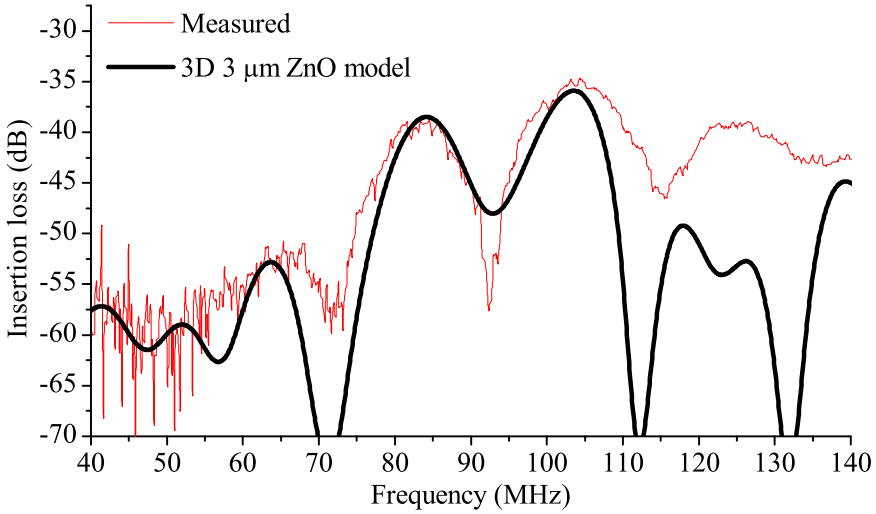

Figure 3.18: Comparison of measured and 3D simulated frequency response for layered ZnO/XY $LiNbO_3$ structure.

3.5.6 Conductometric Sensitivity

After the accuracy of the 3D finite-element transient simulation was verified, the model was used to investigate the best configuration for conductivity based sensing applications. For sensing applications, typical configuration of the device would involve placing a sensitive layer between the transmitting and receiving IDT, as described in Chapter 2, section 2.1.2. Alternatively, as the structure presented employees a ZnO layer, it is also possible to completely cover the entire surface of the device with the sensitive layer.

Two further simulations of the 3D finite-element layered structure were conducted in a bid to determine which sensitive layer configuration provided the highest sensitivity towards conductivity based interactions at the surface of the device. The results show that the proposed method of covering the entire active surface of the layered structure with the sensitive layer yield a higher conductive based sensitivity over the conventional method of employing only the space in between the IDT ports.

The effect of a gas interaction can be modelled by electrically shorting the surface of the sensing layer. The short surface condition represents a gas reaction where electrons are injected into the surface of the device, increasing the layers conductivity. Such a case could be used to mimic an interaction between H_2 gas and a n-type metal oxide sensitive layer. Coupling of the nodes at the surface of the ZnO layer by the voltage DOF created the short surface condition. This simplification was utilised so that the number of nodes in the 3D model did not need to be increased.

The first of these simulations was a partial short surface, which involved coupling only the nodes at the surface between the transmitting and receiving IDT by the voltage DOF. This situation is similar to the conventional SAW gas sensor structure depicted in Chapter 2, figure 2.2. The second simulation involved coupling all the nodes at the surface of the structure, representing the proposed layered SAW gas sensor structure (as shown in Chapter 2, figure 2.3). Figure 3.19 shows the frequency responses derived from the simulations. Curve **A** is the frequency response of the 3D model without the short surface condition. Curve **B** is the frequency response of the simulation with the short circuit between input and output IDTs, while curve **C** is that of the short circuit across the complete surface of the structure.

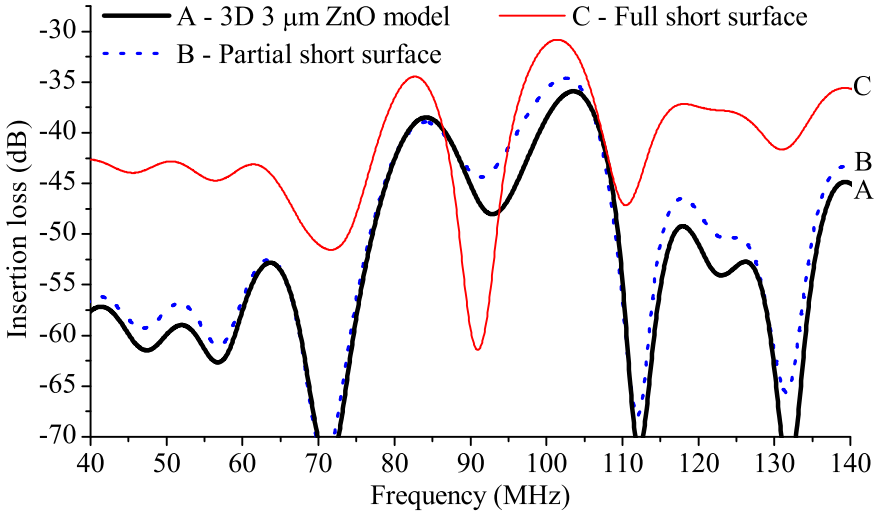

Figure 3.19: Frequency response for a ZnO/XY $LiNbO_3$ SAW device. **A** - 3D finite-element simulation result. **B** - 3D finite-element simulation result with partial short surface. **C** - 3D finite-element simulation result with full short surface.

It can be seen that the simulation with the ZnO surface completely shorted (curve **C**) resulted in the largest frequency shift, when compared to the original (curve **A**). The simulation with the partial short surface (curve **B**) shows very little variation in the frequency response when compared to curve **A**. Therefore, a device configuration utilising the entire surface of the structure as the active sensing area resulted in a larger frequency shift. Thus, the finite-element simulation predicts that this configuration would result in a device with high sensitivity towards conductivity perturbations at the device surface.

A similar process was conducted for a non-layered XY $LiNbO_3$ SAW device. However, in this case, the only configuration possible for gas sensing is to place the selective layer between the transmitting and receiving IDT ports. Obviously, covering the entire

surface with the selective layer may electrically short the IDT finger pairs. A comparison between frequency responses derived from the simulations reveal a negligible frequency shift between the models with and without the (electrical) short surface condition. The variation was significantly lower than the difference produced by the partial short surface layered structure. Therefore, confirming that a layered SAW device has a greater sensitivity over it non-layered SAW counterpart when utilising the entire surface as the active sensing region.

3.6 Limitations of the Finite-Element Model

As with all analytical and numerical modelling techniques, the finite-element model presented here has its disadvantages and limitations. A disadvantage of the finite-element method is that it cannot handle a semi-infinite medium. Therefore, the whole substrate must be exhaustively modelled. In the case of bulk wave interface this may be advantageous, otherwise the extra computational effort may not significantly influence the result. Furthermore, singularities due to discontinuities in the charge density at the edges of IDTs are also not fully handled by the presented finite-element model.

Other limitations are mostly related to the node density of the model. Higher density node structures and longer simulation times may improve accuracy, but also considerably increase computation time. Factors such as boundary reflections and the size of the model impose limitations as well.

In this work, the software licence agreement limited the number of node in each model. This imposed limitations on the model's substrate size, resulting in the travelling acoustic wave reflecting off the model boundaries back into the structure. Reflected waves were found to affect the next propagating wavefront. In figure 3.13, at $t = 50$ and 60 ns it is possible to see the launched acoustic wave reflecting from the boundary in both the non-layered and layered contour plots. Unfortunately, reflection is most certainly contributing to inaccuracies. The wave propagation may become distorted, thus producing invalid results. To avoid the reflection at the boundary, dampening elements can be used, however they need to be capable of dampening the propagating wave for all modes and displacement components. At current time, the author could not acquire such element for the ANSYS platform, so a trade-off between simulation time and model size was implement instead. Recently, a finite difference time domain technique for acoustic wave propagation in piezoelectric media has been developed for a perfectly matched layers, that

solves the issues of spurious reflections, providing the capability to simulation acoustic wave propagation in a sub-region of an infinite medium [129].

Node density of the structure was also found to be a critical component. Incorrect discretisation resulted in a model with too few nodes or nodes incorrectly distributed in the structure. It is critical that the node density be at least of the order of 10 nodes per wavelength (λ) for the highest frequency component propagating in the modelled structure. As a consequence, an extremely large number of nodes is required for the 3D model presented. However, to comply with the licensing agreement, it was only possible to maintain a node density of 10 nodes per wavelength at the surface (several wavelengths in depth) and throughout the centre of the structure. Unfortunately, for the 3D model, the node density was not sufficient at the boundaries of the model, hence excessive wave reflection existed if the simulation time exceeds more than 100 ns.

The results produced by the 3D finite-element model are in good agreement with the measured results. Increased accuracy could also be achieved by eliminating parametric discrepancies between the model and fabricated layered SAW device. Further discrepancies between simulation and measured results presented in figures 3.9, 3.10 and 3.18 could also be contributed to by uncertainties between the model and simulation definition. Table 3.1 lists some general uncertainties that lead to discrepancies between simulated and measured results. Thin films, such as the ZnO layer result in material constants which are highly dependant on the fabrication process. Furthermore, variations in substrate material constants provided by different manufactures and additional fabrication errors resulting form patterning IDTs can also contribute to discrepancies between the simulated and measured results.

Table 3.1: Uncertainties that lead to discrepancies between simulated and measured results.

Modelling uncertainties	Fabrication uncertainties
• Uncertainties in substrate material constants	• Supplier and material constants are lot dependent
• Uncertainties in ZnO material constants	• Many parameters are fabrication and process dependant
• Infinitesimally thin and massless electrodes used	• Possible irregular IDT fabrication error
• Rigid coupling interface between ZnO/substrate assumed	• Over/under etching fabrication faults
• Defect free ZnO with homogeneous thickness assumed	• repeatability of thin film deposition

3.7 Summary

Both 2D and 3D finite-element models were utilised to simulate a 2-port layered SAW delay line structure. Using commercially available finite-element software ANSYS 5.7, 2D and 3D visualisations of acoustic wave propagation in layered piezoelectric media were presented. Direct full-scale 2D and 3D models were developed for the investigation and analysis of the electromechanical phenomena occurring in layered SAW devices.

To the best of the author's knowledge, this is the first time a full 3D finite-element model of a layered SAW device has been presented with experimental verification. The models provide a powerful means of studying SAW propagation in a complex, anisotropic layered media. As a direct result of the presented work, other research groups, throughout the sensor and SAW transducer communities have expressed interest in further developing these models. Currently, extensions on the author's contribution have been published in the literature citing some of the work presented herein [104–106].

Outcomes from this research can be summarised by the following points:

- The depth profile and displacement contour plots show that the layered structure has a higher degree of acoustic energy confinement to the surface of the device when compared to its non-layered counterpart. The high energy confinement at the surface is paramount for increasing mass sensitivity of the device.
- The layered ZnO/XY $LiNbO_3$ SAW structural configuration has been shown to provide a higher sensitivity towards conductivity based surface interactions when compared to its non-layered counterpart.
- The presented model shows that the entire surface of the device should be used as the active sensing area.
- Displacement was shown to occur in the x, y and z-directions, rendering the 3D finite-element model necessary to obtain an accurate solution.
- The presented model was able to take into account both the electrostatic and mechanical effects associated with a layered SAW device, essential for understanding second order effect such as, diffraction, bulk-wave interference, triple-transit-interference and electromagnetic feed-through.

The finite-element method is most likely the only tool at present that has the potential to achieve the ultimate goal of full-scale simulation of SAW devices with high fidelity [118].

The performance of the 2D and 3D finite-element models were demonstrated by the frequency response analysis of the ZnO/XY $LiNbO_3$ layered SAW structure and comparison with experimental data. The frequency responses of the models were obtained through the FFT of the impulse response, which is obtained directly from both the 2D and 3D finite-element simulations. Results presented show that the measured and modelled frequency responses are in good agreement. Using a finite-element modelling technique is an effective way of gaining a deeper understanding of surface acoustic wave propagation in piezoelectric media and ultimately in the optimisation of SAW transducer designs.

Despite the computational requirement and difficulties involved in full-scale finite-element simulations, the cost of SAW device development may be greatly reduced by computer simulation techniques. The influence of many design parameters on the characteristics of acoustic propagation can be calculated without fabricating multiple devices, reducing the requirement for time consuming experiments. Furthermore, finite-element simulations can be easily utilised to optimise the performance of a SAW device [123].

The finite-element model may easily be extended to include the mass loading effects of the IDT electrodes and the size of the model can be increased to account for a larger number of IDT finger pairs. In addition, the finite-element model could be extended by simulating the effect of nanomaterials, with regards to their arrangement (ordered vs. random placement) and their influence on SAW propagation. Furthermore, gas interaction with the metal oxide sensitive layer could be studied, exploring the changes in structural and material properties during the operation of the sensor. With the increase in computer power in the near future, it is of the author's opinion that full 3D models of multi-layered SAW sensors will be realised. The knowledge gained by such models will aid in obtaining information essential to understanding the sensing mechanism and improving sensor design.

[This page is left blank intentionally.]

Chapter 4

Layered SAW Sensor Design

Substantial work has been conducted on the design of SAW delay line devices for filtering and signal processing applications. However, the requirements and constraints for SAW based sensors are different. Design parameters, such as the number of finger pairs, electrode widths, acoustic aperture and the distance between the IDT ports (delay path length) are similar. However, in multilayered sensing structures, the thickness of each layer is critical in obtaining the desired sensing characteristics. Material parameters and layer thickness of the intermediate and sensitive layers have been shown to significantly influence the dielectric behaviour and electromechanical coupling coefficient (K^2) of the structure [16–18] and need to be considered during the design process.

Application specific constraints are also placed on the physical properties of the gas sensor. The design should minimise the number of required fabrication steps, as well as allowing for easy deposition of the intermediate and sensitive layers. Other factors include the pad layout and the physical size of the substrate. For example, the larger the substrate area, the more thermal energy required to elevate the device to the required operating temperature.

Due to the large number of material and operation specific requirements, there is no particular method for designing SAW delay lines for chemical sensing applications. Furthermore, it is not possible to satisfy the requirements for all sensing applications with one single design process. A sensor engineer faces many challenges and decisions when designing a sensor for a given application. In most cases, the selection of materials and structural parameters results in design tradeoffs between device operating temperature, long term stability, selectivity and sensitivity.

In this chapter the author discusses a novel layered structure, employing a piezoelectric intermediate (guiding) layer and metal oxide sensitive layer. The additional degree

of freedom, provided by the intermediate layer thickness is investigated to maximise sensitivity of conductivity based gas sensors. The intermediate layer thickness is shown to directly affect the operating point of the SAW by matching the velocity-permittivity product of the SAW mode to the conductivity of the metal oxide sensitive layer. The author theoretically demonstrates that an optimised ZnO layer thickness increases the response magnitude of the structure when the velocity-permittivity of the SAW mode is optimised. A total of three SAW modes supported by the layered structures are investigated, each with different acoustic behaviour.

Section 4.1 describes the electromechanical coupling coefficient (K^2), which is used throughout the chapter during the design process of the investigated layered SAW structures.

Section 4.2 discusses the acoustic properties of both the $LiNbO_3$ and $LiTaO_3$ substrates chosen, and details some of the specific advantages of layered structures. The effect of the intermediate ZnO layer on K^2 calculated at the ZnO/substrate interface is discussed. Furthermore, the material properties of the metal oxides sensitive layer are investigated.

Section 4.3 introduces the IDT structures employed by the author. The design and optimisation of the photolithographic mask patterns are presented. Furthermore, a more rigourous method of calculating K^2 at the ZnO/substrate interface is discussed.

Section 4.4 highlights the most important advantages of using a layered structure for gas sensing applications. Perturbation theory is used to show that an optimal thickness of the ZnO intermediate layer can be chosen for maximum conductivity based sensitivity. Optimisation of the ZnO layer thickness is presented and the design tradeoffs are analysed with regards to the chosen SAW modes.

Section 4.5 details a summary of the findings presented in this chapter.

4.1 Electromechanical Coupling Coefficient (K^2)

The electromechanical coupling coefficient is a measure of efficiency in converting an applied electrical energy to mechanical energy associated with a surface acoustic wave [24, 34]. For conductivity based sensing applications, it can be thought of as a measure of interaction between electrical and mechanical fields in a piezoelectric material.

The electromechanical coupling coefficient (K^2) can be calculated by determining the

perturbated wave velocity caused by a change in the electrical boundary conditions. It can be obtained theoretically or experimentally by:

$$K^2 = 2\frac{v_f - v_m}{v_f} \quad , \tag{4.1}$$

where v_f and v_m are the free surface and metallised surface phase velocity, respectively. Theoretically, the metallised surface condition can be modelled with an infinitesimal thin, perfectly conducting layer on the device surface [24, 37], as shown in Chapter 3 section 3.5.6.

The value of K^2 will depend on the interface at which it is calculated. In non-layered devices this is the substrate surface. In layered devices it is normally the interface between the intermediate (dielectric) layer and the substrate. However, for conductivity based sensing purposes, it should be calculated at the device surface. Based on these properties it is possible to evaluate the suitability of a particular substrate and layer configuration for a given application.

4.2 Material Selection

The material properties of both the intermediate and sensitive layers greatly affect the propagation characteristics of the SAW. In the case of conductivity based sensing applications, piezoelectric materials with a high K^2 are of prime interest. As mentioned previously, the SAW devices investigated are based on multilayered structures. The materials chosen to form the device influence the permittivity properties and the K^2 of the supported SAW modes in the structure.

Material properties of the substrate predominantly determine which SAW mode(s) are supported. Different types of acoustic modes have substantially different propagation properties. The group velocity and K^2 of the supported acoustic modes are determined by the structure and layer material properties. An extensive collection of data regarding these parameters is published in the literature and textbooks [24, 32–34].

The successive layers, forming the intermediate and the metal oxide sensitive layers can also influence which type of acoustic modes are supported by the substrate. Each layer and associated thickness need to be considered during the design process. The intermediate and sensitive layers' material properties can affect the overall structural K^2

and permittivity.

The effect of prolonged elevated operating temperatures on the material properties also requires consideration. Thin film characterisation, concerning surface morphology of the associated layers and temperature effects are presented separately in Chapter 6.

4.2.1 Substrate Materials

Table 4.1 list the substrate orientations chosen by the author for investigation during this research program. Two substrate materials, $LiNbO_3$ and $LiTaO_3$ were chosen as they support different acoustic modes with a relatively high K^2. The free and metallised velocity values presented in table 4.1 were calculated by the Greens' function method presented in [130, 131] and can readily be found in textbooks [24, 33]. The values were used with equation (4.1) to calculate K^2 for each SAW mode.

The SAW modes supported by the chosen substrates have different acoustic properties. A total of three SAW modes have been chosen for investigation. Each SAW mode provides an opportunity to make comparisons, and investigate different phenomena associated with conductivity based sensitivity. In a non-layered configuration the investigated SAW modes possess different acoustic wave polarisations and wave type. The polarisations of a wave can be readily determined by examining the relative magnitudes of displacement in the depth of the substrate. The associated polarisations for each of the investigated SAW modes is listed in table 4.1.

Table 4.1: Substrate crystal cut properties calculated at $\lambda = 24$ µm.

Substrate material	Crystal cut	SAW axis	Velocity (m/s) free	Velocity (m/s) metallised	$f_{o_{\text{free}}}$	K^2	Polarisation
$LiNbO_3$	X	Y	3696.1	3639.5	154.00 MHz	3.06%	Generalised SAW
$LiNbO_3$	X	Z	3483.2	3404.2	145.13 MHz	4.54%	Rayleigh
$LiTaO_3$	36° Y	X	4226.3	4108.8	176.10 MHz	5.56%	Quasi shear-horizontal

4.2.1.1 XY $LiNbO_3$ Substrate

The X-cut Y-propagating $LiNbO_3$ substrate is an acousto-optic material, traditionally employed for developing integrated photonic devices such as Mach-Zehnder modulators [132] and acousto-optic tunable filters [133]. XY $LiNbO_3$ is advantageous to this study because it supports a single SAW mode with significate displacement in all three directions (u_x, u_y and u_z). The finite-element work presented in Chapter 3 verified that displacement

occurs in all 3-directions. Other factors such as the presence of multiple wavefronts and different acoustic behaviour with and without a ZnO layer make the substrate a particularly interesting candidate for further investigation. Furthermore, once XY $LiNbO_3$ is combined with a ZnO dielectric layer, it is shown to possess excellent sensing behaviour towards H_2 gas (see Chapter 8 section 8.2).

4.2.1.2 XZ $LiNbO_3$ Substrate

XZ $LiNbO_3$ is advantageous to this study because it has a higher K^2 than XY $LiNbO_3$. Secondly, XZ $LiNbO_3$ supports displacement normal to the surface, which is the common displacement type chosen for gas sensing applications.

4.2.1.3 36° YX $LiTaO_3$ Substrate

The 36° YX $LiTaO_3$ orientation supports both Leaky-SAW and surface skimming bulk wave (SSBW) propagation. The supported propagating wave is strongly dependent on the surface boundary conditions and metallisation. Theoretical and experimental analysis has shown that Leaky-SAW is the dominant propagation mode with metallised surface conditions, while SSBW dominate on the free surface conditions [24]. In sensing applications, 36° YX $LiTaO_3$ base devices are preferred for liquid media as the polarisation of the acoustic wave is shear horizontal (SH) – limiting acoustic radiation into the adjacent liquid. 36° YX $LiTaO_3$ was chosen to demonstrate that the SH-SAW is highly sensitive to changes in electrical boundary conditions, making it suitable for conductivity based gas sensing applications.

4.2.2 Intermediate Layer Material

The addition of a dielectric intermediate layer can increase acoustic energy confinement at the surface, isolate the IDT electrodes from the sensitive layer, influence the properties of the propagating SAW mode(s) such as velocity and temperature coefficient; and change the permittivity and K^2 of the structure. Therefore, the material properties of the dielectric layer are critical to the SAW device performance.

The layered structure presented in figure 4.1 utilises an intermediate ZnO and metal oxide sensitive layer. Each layer and associated thickness need to be considered during the design process. The ZnO layer configuration is employed to increase the device's sensitivity towards conductivity changes at the surface. The ZnO thickness can be tailored

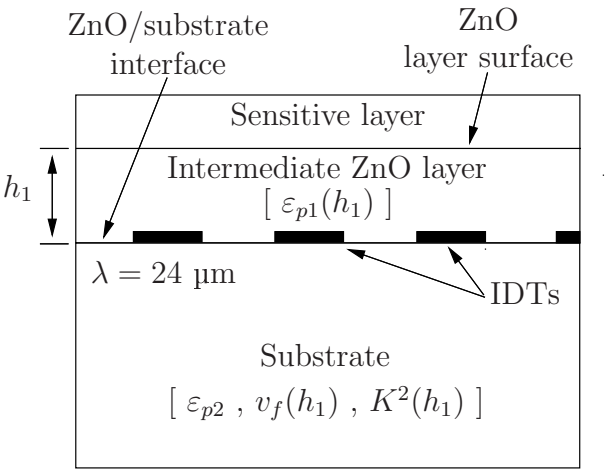

Figure 4.1: Diagrammatic cross-section of layered structure.

to match the surface sheet conductivity to the optimum operating region of the SAW device, which is discussed in the following sections.

ZnO is a well-known piezoelectric material with a hexagonal crystalline structure which is used in a range of scientific and technological applications [134]. ZnO films have a long history of being used for the excitation of SAWs on non-piezoelectric substrates. Work conducted by Kalantar-Zadeh et al. [16–18] based on ST-cut quartz substrates, showed that ZnO substantially increased device sensitivity when used in place of SiO_2. The addition of a ZnO dielectric layer onto $LiTaO_3$ and $LiNbO_3$ substrates increases the K^2 for supported SAW modes at the ZnO/substrate interface.

Figure 4.2 shows the calculated K^2 of each SAW mode presented in table 4.1 as a function of ZnO layer thickness. The necessary parameters required for the calculations were obtained by employing the methods detailed in [130, 131] and a fixed wavelength of $\lambda = 24$ µm. The K^2 at the ZnO/substrate interface is shown to increases with layer thickness for all SAW modes investigated. The maximum K^2 results at different ZnO thickness for each of the SAW modes investigated. Figure 4.2 shows that the SAW modes in ZnO/36° YX $LiTaO_3$ and ZnO/XZ $LiNbO_3$ structures exhibit a maximum K^2 for a ZnO thickness between 1 and 2.5 µm. However, the maximum K^2 for SAW mode in the ZnO/XY $LiNbO_3$ structure occurs when the ZnO film thickness is ∼4.5 µm.

The decrease in K^2 observed at larger ZnO layer thickness is due to the acoustic energy and the accompanying electric field becoming increasingly isolated from the ZnO/substrate interface. This reduces the coupling for a larger ZnO layer thickness. However, at the

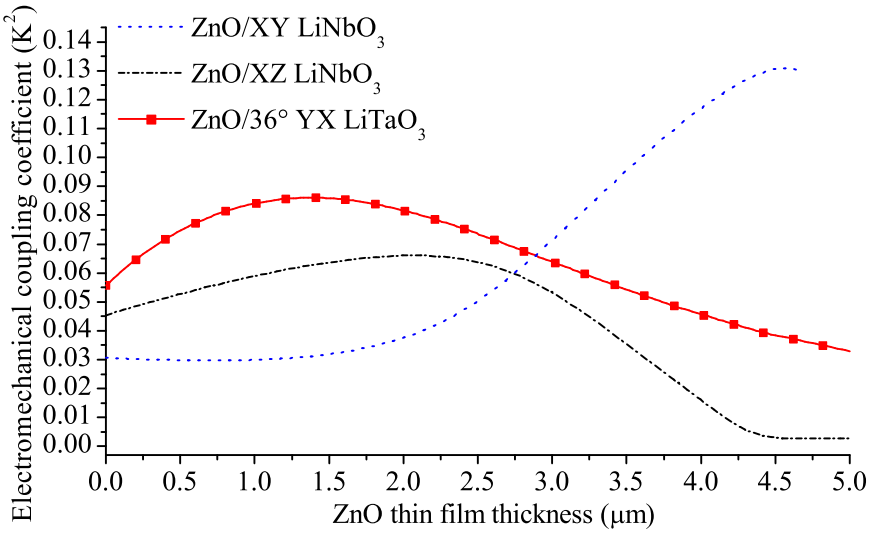

Figure 4.2: Electromechanical coupling coefficient, (K^2), calculated for a periodicity of $\lambda = 24$ µm at the substrate surface.

optimum ZnO thickness, K^2 at the ZnO/substrate interface is maximised, resulting in increased acoustic wave generation efficiency. This can be used advantageously during IDT design as the signal to noise ratio is increased, resulting in smaller layered SAW sensors with lower insertion loss.

4.2.3 Sensitive Layer Material

The change in electrical resistance caused by the adsorption of an analyte gas on the surface of a metal oxide thin film has been well documented [92, 94]. Metal oxides such as SnO_2, TiO_2, ZnO, In_2O_3, InO_x and WO_3 are well known to change their electrical properties in the presence of different gas atmospheres. Significant progress has been made to utilise the change in electrical properties to quantify the presence of specific reactive gases. Based on the reversible changes in conductivity, metal oxide thin films have been used as sensitive layers towards ethanol, benzene, H_2, O_3, NH_3, NO_2, CO, etc. [92, 94, 135–139].

ZnO is a metal oxide and has been employed as a gas sensitive layer [140–142]. Sieyama et al. first reported ZnO thin films for gas sensing applications in 1962 [89]. Since then, ZnO has been widely applied as a gas sensitive material for SAW based devices [143]. Work conducted by Kalantar-Zadeh et al. [16–18] showed that ZnO is sensitive to oxygen concentrations as low as 0.2 ppm in nitrogen gas. However, by employing ZnO for its dielectric and piezoelectric properties alone, thinner, more sensitive metal oxide films can

used to form a gas sensitive layer. It is the author's opinion that this layered structure approach provides a more sensitive and configurable SAW based sensing platform.

The thin metal oxide sensitive layers employed in the structure presented in figure 4.1 are 6 to 30 times thinner than the intermediate ZnO dielectric layer. The thin film layers provide higher sensitivity with quicker response and recovery times, when compared to the relatively thick ZnO layer. The metal oxide layers chosen for investigation during this research program are InO_x and WO_3. The sheet conductivity of the InO_x and WO_3 layers is altered when surface interactions between the layer and an oxidising or reducing gas occur. The layers were specifically chosen to provide sensitivity towards H_2 and NO_2 gases and ethanol vapour.

4.2.3.1 InO_x Sensitive Layer

Indium oxide films exhibit a change in band-gap depending upon the oxygen concentration in the film [144, 145]. Indium oxide in its stoichiometric form (In_2O_3), behaves as an insulator. In its non-stoichiometric form (InO_x) it can behave as an n-type semiconductor as a result of intrinsic defects and oxygen vacancies [146]. The oxygen vacancies in the InO_x film act as donors and hence the sample's conductivity can be changed by controlling the oxygen deficiency [147]. Kiriakidis et al. showed that InO_x films are sensitive towards both O_3 and NO_2 at operating temperatures between 50°C to 300°C [148]. For work based on the ZnO/$LiNbO_3$ structure presented in Chapter 8, two different thicknesses of InO_x, 40 and 200 nm are investigated for NO_2 and H_2 gas sensing applications.

4.2.3.2 WO_3 Sensitive Layer

The sensitivity of WO_3 films to O_3, NO_x, H_2S, H_2 and NH_3 has been widely studied in the literature [79, 149, 150]. WO_3 is an n-type semiconductor, highly sensitive towards both oxidising and reducing gases. For work based on the ZnO/36° YX $LiTaO_3$ structure presented in Chapter 8, 150 and 160 nm thick WO_3 sensitive layers are investigated for ethanol vapour and H_2 gas sensing applications, respectively. The catalyst activated Au–WO_3 and Pt–WO_3 sensitive layers, also employed on the ZnO/$LiTaO_3$ layered SAW structures, are investigated for H_2 sensing applications.

4.3 Layered SAW Gas Sensor Design

A critical aspect in developing a layered SAW gas sensor is the SAW delay line. Various publications have documented IDT design principles for SAW devices [4, 24, 32, 44, 63]. A combination of IDT and substrate parameters need to be optimised so that the acoustic mode of a device is stable over the full range of operating temperatures. This is especially important in conductivity based sensing applications, as the sensor is required to operate within a broad range of temperatures to achieve optimal sensitivity towards different gas species.

The influence of aperture width, transducer separation etc, which may also be important parameters in the design of a SAW based gas sensor can be analysed. For this purpose, design techniques based on the equivalent circuit [151, 152], P-matrix [153], Coupling of Modes (COM) [154], and Green's function [31] can be utilised as an alternative to the finite-element model to design delay line or resonator structures. Devices with desirable properties typically include low insertion loss to ensure oscillation is maintained, large phase slope to reduce frequency instability and convenient physical layout for sensing purposes [37].

Different IDT structures can be used to excite the supported acoustic modes. Chapter 2, section 2.1 introduced the relationship between SAW phase velocity (v) and wavelength (λ). Efficient transduction is accomplished when adjacent, oppositely polarised fingers are one quarter the acoustic wavelength apart [32, 44]. The spacing between the fingers of the IDTs is one of the major parameters that determines the operating frequency of the SAW device. Table 4.1 gives the calculated centre frequency f_0, for the chosen SAW modes with $\lambda = 24$ µm, using equation (2.1). It should be kept in mind that the chosen wavelength directly influence the optimum thickness required for the intermediate dielectric layer in a layered structure.

4.3.1 Interdigital Transducer (IDT) Design

Transducer bandwidth is inversely proportional to the number of IDT electrode fingers. A narrow bandwidth is desirable for oscillator applications in order to avoid spurious oscillations and improve stability [32]. The IDT pattern used for all experimental work employed a 2-port delay line structure with 64 finger pairs in each port. The high number of IDT electrode fingers create a narrow bandwidth structure with a resonate peak at the centre frequency of each device.

To decrease insertion loss, the centre-to-centre separation distance of the IDT ports employed for all experimental work was 85 λ. In a conventional SAW based sensor, such as the structure depicted in figure 2.2, the use of a small (i.e. $<$ 200 µm) centre-to-centre distance is generally not possible as it effectively limits the surface area of the sensitive layer. By using the proposed layered configuration, the ZnO intermediate layer isolates the sensitive layer from the IDTs. Therefore, the sensitive layer can cover the complete surface area of the structure (as depicted in Chapter 2, figure 2.3). This increases the active surface area of the device, whilst reducing the size of the required substrate. Furthermore, the insertion loss of the layered SAW device at the resonant centre frequency is reduced when compared to devices with larger centre-to-centre IDT spacing.

4.3.1.1 Photolithographic Pattern

Figure 4.3 shows three successive IDT design variations for the fabrication of experimental layered SAW gas sensor having a periodicity of 24 µm. Version (a) is the original design used for the preliminary experimental work. Version (b) is a dual delay line arrangement with an improved pad and bus bar layout. Version (c) is a single delay line design incorporating the improved pad and bus bar layout, which reduces the substrate size required for each sensor. Version (a) was found to introduce increased electromagnetic feed-through. The performance of version (b) and (c) were found to be approximately the same. The aperture width W, of all designs is 1250 µm, except in the case of version (b) where 3 separate aperture width designs of 1000, 1250 and 1500 µm were implemented.

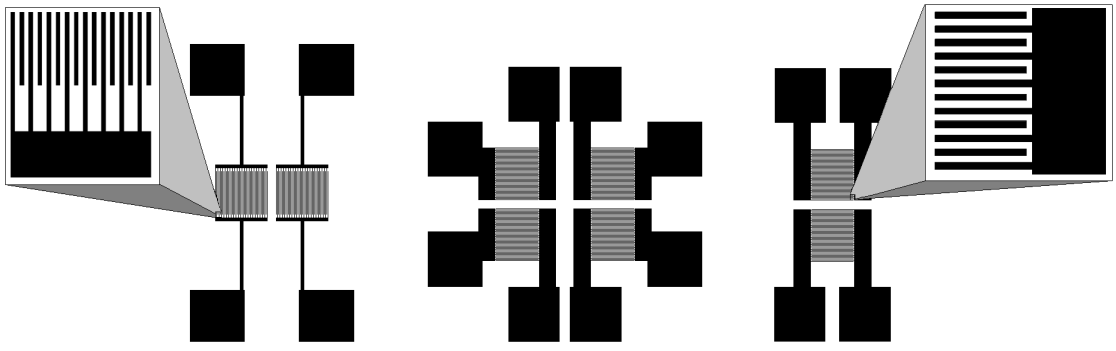

(a) Original SAW design.

(b) Dual delay line design.

(c) Single delay line design, with reduced substrate size.

Figure 4.3: Photolithographic pattern for layered SAW sensors used for gas sensing experiments.

4.3.1.2 IDT Aperture

Figure 4.4 shows 3 measured S_{21} transmission parameters employing aperture widths of 1000, 1250 and 1500 µm on 36° YX $LiTaO_3$ substrate. All measurements show a resonant centre frequency peak at approximately 174 MHz with an insertion loss of approximately 6 to 7 dB. The design with 1250 µm aperture has a lower side lobe suppression, justifying the use of the 1250 µm aperture for all gas sensing experiments.

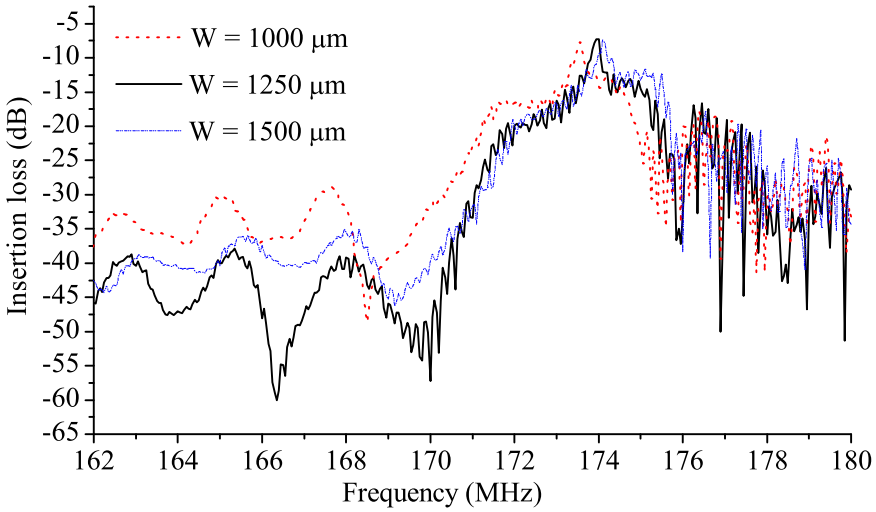

Figure 4.4: Frequency response of 36° YX $LiTaO_3$ SAW device with aperture (W) = 1000, 1250 and 1500 µm.

4.3.2 Intermediate ZnO Layer

The combination of the ZnO dielectric layer with the chosen substrate materials leads to several interesting observations for each of the SAW modes investigated. ZnO has an acoustic velocity of 2531 m/s, which is substantially lower than any of the SAW mode velocities supported by the investigated substrates. The addition of the ZnO layer affects the properties of the SAW propagation media. Properties such as phase velocity (v), electromechanical coupling (K^2), permittivity (ε_p) and polarisation (wave type) are all influenced by the layer.

As previously discussed (section 4.2.2), the maximum K^2 at the the ZnO/substrate interface, calculated for each of the SAW modes occurs at different ZnO layer thicknesses. However, there are a number of practical details which need to be accounted for in the design and operation of SAW sensors [32], particularly for layered structures.

In a layered structure higher order modes may exist, depending on the layer thickness.

The existence of higher order modes can have both positive and negative effects. Higher order modes may provide more sensitive operating frequencies, or the flexibility to choose a different operating mode (if available) with desired characteristics for the particular sensing application. However, in the case where the SAW device is the frequency determining element in an oscillator, it is usually desirable to have a single operating frequency at which the system will reliably begin oscillation [37].

A further consideration, specific to the chosen XZ $LiNbO_3$ orientation, is the possibility to change the properties of non-piezoelectric SAW modes supported by the substrate. The addition of a ZnO layer on XZ $LiNbO_3$ substrate allows a non-piezoelectric shear mode to gain a K^2 value, which is a function of increasing ZnO thickness. The K^2 of the shear mode is as much as 27 times less than the K^2 of the generalised SAW mode shown in table 4.1. The spatial frequency separation of the two distinct modes (in the frequency domain) decreases with increasing ZnO thickness. Therefore, if the layered SAW device is used as the frequency determining element in an oscillator, the possibility of 'mode hopping' is substantially increased with the addition of the ZnO layer.

4.3.2.1 Accurate Theoretical Determination of K^2

The accuracy of K^2 calculated at the ZnO/substrate interface needs to be confirmed. Using the residue of the poles in the Green's function and the inverse Greens function, the K^2 of a crystal cut were calculated separately for both free and metallised cases. The metallised case is for highly conductive layers, whilst the free case may be used to mimic low conductive layers. This method is a more rigourous alternative to equation (4.1), which was utilised to generate the K^2 curves in figure 4.2. Using established principles from [31, 155, 156] it was possible to calculate the K^2 for the free and metallised case of each of the investigated SAW modes. Using a wavelength of $\lambda = 24$ µm, the K^2 for the free surface condition is calculated by:

$$K^2_{free} = -2\ \Gamma_f\ \varepsilon_\infty \qquad . \tag{4.2}$$

Similarly, the K^2 for the metallised surface condition is calculated by:

$$K^2_{metallised} = \frac{2\ \Lambda_m}{\varepsilon_\infty} \qquad . \tag{4.3}$$

The definitions of Γ_f, Λ_m and ε_∞ can be found in [155] (equations (13), (16) and (19), respectively). For substrate orientations supporting Rayleigh modes, such as ST-quartz

and 128° YX $LiNbO_3$, the SAW mode's free and metallised K^2 values, calculated by equations (4.2) and (4.3), should be approximately equal.

Figure 4.5 shows the free and metallised K^2 values for the ZnO/XY $LiNbO_3$, ZnO/XZ $LiNbO_3$ and ZnO/36° YX $LiTaO_3$ structures. The K^2 value calculated by equation (4.1) are shown to lie in between the values produced by equations (4.2) and (4.3) for all cases. Table B.1 in Appendix B, lists the data values used to generate the curves in figure 4.5. The discrepancy between the three values illustrates how equation (4.1) poorly characterises the SAW modes. Similar discrepancies between values have been noted by Lee [157]. The K^2 of the structure is said to conform if the values obtained from equations (4.2) and (4.3) differing by no more than 1 order of magnitude. The non-conforming values are particulary evident for the ZnO/XY $LiNbO_3$ and ZnO/XZ $LiNbO_3$ structures where the ZnO thickness is above 2 µm. The ZnO/36° YX $LiTaO_3$ structure

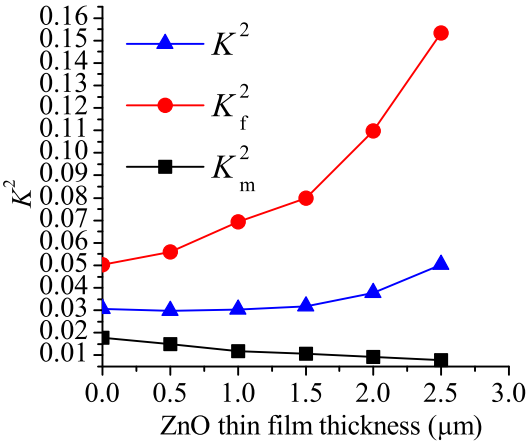

(a) ZnO/XY $LiNbO_3$.

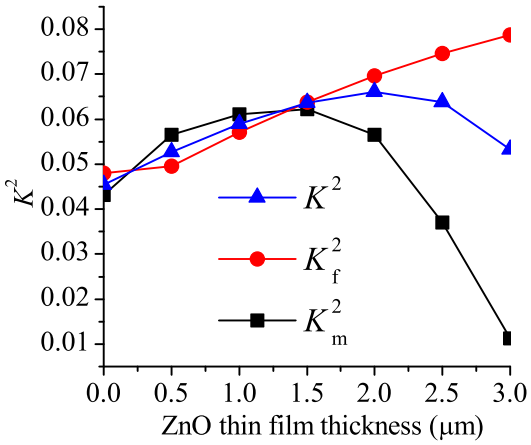

(b) ZnO/XZ $LiNbO_3$.

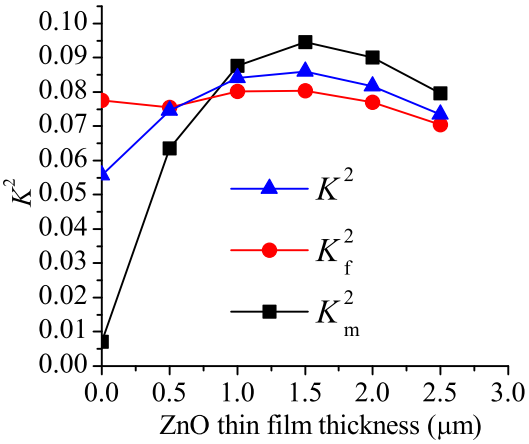

(c) ZnO/36° YX $LiTaO_3$.

Figure 4.5: Theoretical determination of K^2 at ZnO/substrate interface for $\lambda = 24$ µm.

is only shown to conform with the ZnO layer for reasons presented in section 4.2.1.3. For modes such as pseudo SAW (L-SAW) and SSBW, the propagation characteristics under free and metallised surface conditions vary strongly. Therefore, the three K^2 values are likely to differ more. On analysis of the curves present in figure 4.5, the K^2 values show best agreement for all investigated SAW modes at ZnO thicknesses between 0.5 and 1.5 µm.

4.3.3 InO_x and WO_3 Sensitive Layers

Thin films of InO_x or WO_3 metal oxide were employed as the gas sensitive layer. As stated previously, the selective layers employed are 6 to 30 times thinner than the ZnO intermediate layer. As in the case of other metal oxide sensitive layers, sensitivity is related to film thickness, which is ultimately determined by the grain size of the polycrystalline film chosen [158]. Layer thicknesses were primarily selected to provide a range of different sheet conductivities and stability at the desired elevated working temperature of the device, typically between 200 and 300°C. Preliminary work employing conductometric transducers established the desired thickness for both the InO_x [148, 159, 160] and WO_3 [161, 162]. In total, three varieties of sensitive thin film layers were used throughout this research program:

- 40 and 200 nm thick InO_x sensitive layers.
- 150 and 160 nm thick WO_3 sensitive layers.
- 160 nm thick WO_3 sensitive layer, catalyst activated by Au and Pt non-continuous films, 4 and 6 nm thick respectively.

The 40 and 200 nm thick InO_x films were employed as the sensitive layer for the $LiNbO_3$ based layered SAW sensors, while the WO_3 and catalyst activated Au–WO_3 and Pt–WO_3 sensitive layers were employed on the $LiTaO_3$ layered SAW sensors. Non-continuous platinum and gold layers were used to improve the sensitivity of the WO_3 films. Further details of the sensitive layers will be discussed in Chapters 6 and 8.

4.4 SAW Sensor Sensitivity

Apart from previously mentioned advantages, the most important aspect of using a layered structure is the ability to tailor the device for maximum conductometric sensitivity. The dielectric (ZnO) layer thickness is optimised to match the conductivity of the sensitive

layer to the permittivity-velocity product of the substrate. Therefore, the sensitive layer thickness can be tailored for maximum sensitivity towards specific gas species.

In general, the predominant sensing mechanism for conductometric SAW sensors is based on surface conductivity changes, which can be approximated by perturbation theory. Perturbation theory may be used to quantify the effect of small changes at the devices' boundary conditions due to surface interactions. As shown in Chapter 2, equation (2.2), perturbation may be due to a number of factors, each of which may cause a sensor response. Ideally, detectable changes should be dominated by the interaction between the sensitive layer and the analyte gas. In the case of oxidising and reducing gases, the interaction with metal oxide sensitive layers such WO_3 or InO_x are assumed to be solely conductometric. Therefore, the interaction of the gas molecules with the sensitive layer perturbs the electrical boundary condition at the surface of the SAW device. As a result, the velocity and attenuation of the electromechanical waves are perturbed. The change in velocity for a given SAW mode can be calculated by perturbation theory [72]:

$$\frac{\Delta v}{v} = \frac{-K^2}{2} \frac{1}{1 + \left(\frac{v_f \ \varepsilon_p(k_0)}{\sigma_{sh}} \right)^2} \quad , \tag{4.4}$$

where v_f is the free surface SAW phase velocity in the layered structure, σ_{sh} is the sheet conductivity of the layer and $\varepsilon_p(k_0)$ is the effective permittivity in the absence of the piezoelectric effect (as a function of the propagation wavenumber of the SAW, $k_0 = \frac{2\pi}{\lambda}$). Assuming that the deviation in SAW phase velocity (Δv) is related to change in device centre frequency (Δf) by the following relationship:

$$\frac{\Delta f}{f_0} \cong \frac{\Delta v}{v} \quad , \tag{4.5}$$

conductivity perturbation can be related to change in centre frequency (f_0). This is only true if the layer is sufficiently thin were dispersion effects can be safely neglected. Figure 4.6 illustrates the variation of the relative change of SAW frequency calculated for the ZnO/XZ $LiNbO_3$ structure as a function of the sheet conductivity, with $\lambda = 24$ µm and a constant ZnO thickness of 1.2 µm. To optimise the electroacoustic interaction for sensing applications, the metal oxide sensitive layer conductivity must fall within the range where the curve has a significantly large gradient. The diagrammatic explanation in figure 4.6 illustrates the assumed response of both reducing and oxidising gases, introducing opposite but equal magnitude conductivity changes. At the point of maximum sensitivity

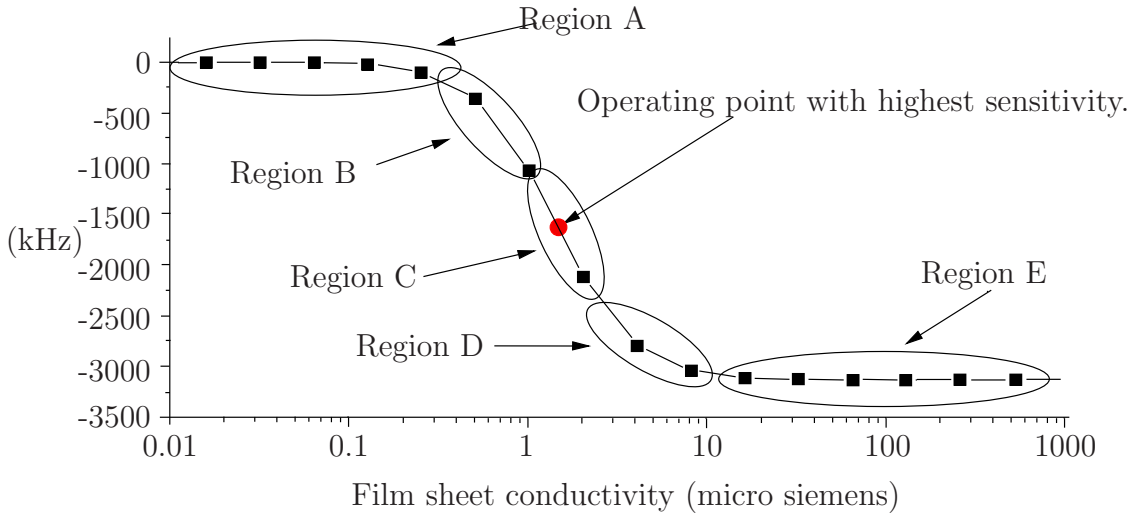

(a) Fractional change in frequency (kHz) vs. Film sheet conductivity (micro siemens).

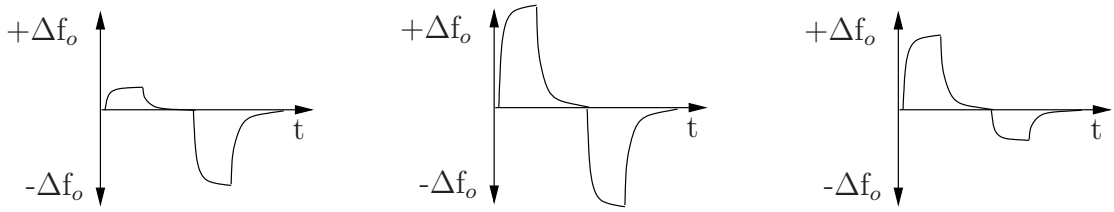

(b) Region B. (c) Region C. (d) Region D.

Figure 4.6: Fractional change in frequency vs. film sheet conductivity with diagrammatic explanation. Calculated for ZnO/XZ $LiNbO_3$ structure where $\lambda = 24$ µm and ZnO thickness is 1.2 µm. The material properties and the thickness of the intermediate and sensing layer can be tailored to determine the operating point on the curve.

(*Region C*), the frequency shifts are shown to be of opposite directions and of equal magnitude. However, *Region B* and *Region D* are shown to have non-proportional, opposing responses to the same reducing and oxidising conditions. Furthermore, in the layer conductivity ranges of *Region A* and *Region E*, little or no frequency shift would be observed.

By selecting the correct material properties and controlling parameters such as film thickness, operating temperature, deposition and annealing procedures, the electroacoustic interaction of the SAW device may be optimised for sensing applications [79]. On further analysis of equation (4.4), the point of maximum sensitivity is when the sheet conductivity of the layer is matched to the velocity-permittivity product of the SAW mode, (i.e. when $\sigma_{sh} = v_f\ \varepsilon_p(k_0)$). As shown in figure 4.1, properties of the layered structure (K^2, v_f and $\varepsilon_p(k_0)$) are functions of intermediate layer thickness

(h_1). Therefore, the sheet conductivity of the layer should be matched to the velocity-permittivity product of the SAW mode so that the layered structure operates at the point of maximum sensitivity.

4.4.1 Optimisation of ZnO Layer Thickness

As discussed previously, in the case of a layered structure, K^2 for a given SAW mode is a function of layer thickness and is calculated at a constant wavelength. To characterise surface interactions, K^2 should be calculated at the ZnO or the device surface. Utilising the same numerical approach as in section 4.2.2, figure 4.7 shows K^2 calculated as a function of ZnO thickness at the ZnO surface for each of the investigated SAW modes. The addition of the ZnO decreases K^2 at the device surface, with increasing layer thickness. This is due to the ZnO layer isolating the electric field at the device surface from the highly piezoelectric substrate.

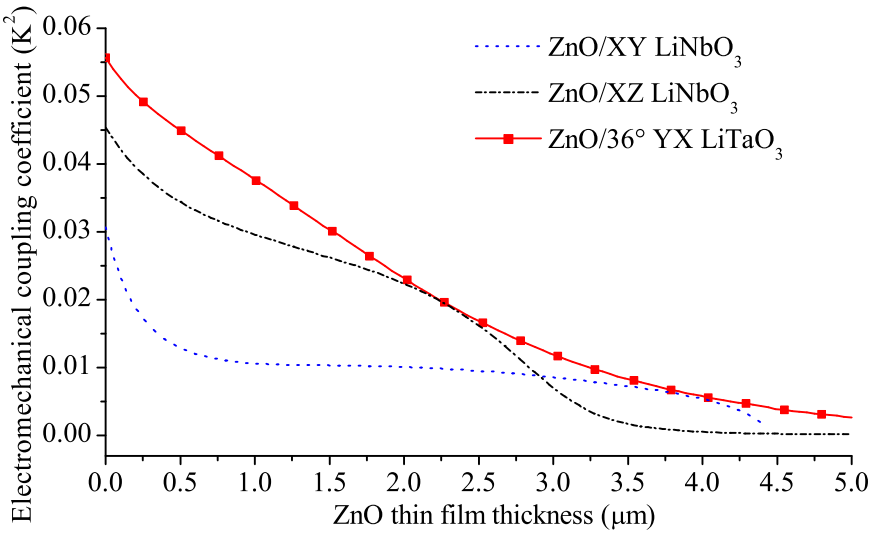

Figure 4.7: Electromechanical coupling coefficient at the active surface of the device. Calculated for $\lambda = 24$ µm.

Therefore, to appreciate the full effect of the ZnO intermediate layer with regards to maximising device sensitivity, the expression for conductivity sensitivity can be derived by taking the derivative of equation (4.4) with respects to σ_{sh} :

$$\frac{\mathrm{d}\left(\frac{\Delta v}{v}\right)}{\mathrm{d}\,\sigma_{sh}} = \frac{-K^2\,{v_f}^2\,\varepsilon_p(k_0)^2}{\left(1+\frac{{v_f}^2\,\varepsilon_p(k_0)^2}{{\sigma_{sh}}^2}\right)^2\,{\sigma_{sh}}^3} \quad . \tag{4.6}$$

Using K^2 calculated at the surface and assuming $\frac{\Delta f}{f_0} \cong \frac{\Delta v}{v}$ and a small conductivity change, equation (4.6) can be plotted as a function of both σ_{sh} and ZnO thickness. Figure 4.8 shows the sensitivity plot for the ZnO/36° YX $LiTaO_3$ structure. Similarly, figure 4.9(a) and (b) shows the sensitivity plots for both the ZnO/XY $LiNbO_3$ and ZnO/XZ $LiNbO_3$ layered structures, respectively. The 3-dimensional plots reveal that a different ZnO thickness is required to achieve optimal sensitivity over approximately the same conductivity range for each of the investigated SAW modes. The line contours illustrate the calculated regions of maximum sensitivity for ZnO layer thickness and sheet conductivity values. Table 4.2 lists the optimal ZnO layer thicknesses and conductivity ranges for each SAW mode. The broad and narrow conductivity ranges are represented by the outer and inner contours (red and dark blue contour lines in figures 4.8 and 4.9), respectively. Highest sensitivity is achieved in the region specified by the (dark blue) inner contour line. Moderate sensitivity should be possible within a region of sheet conductively spanning 2 orders of magnitude from the centre of the inner contour line – specified by the broad conductivity range encompassed by the outer (red) contour line in each plot.

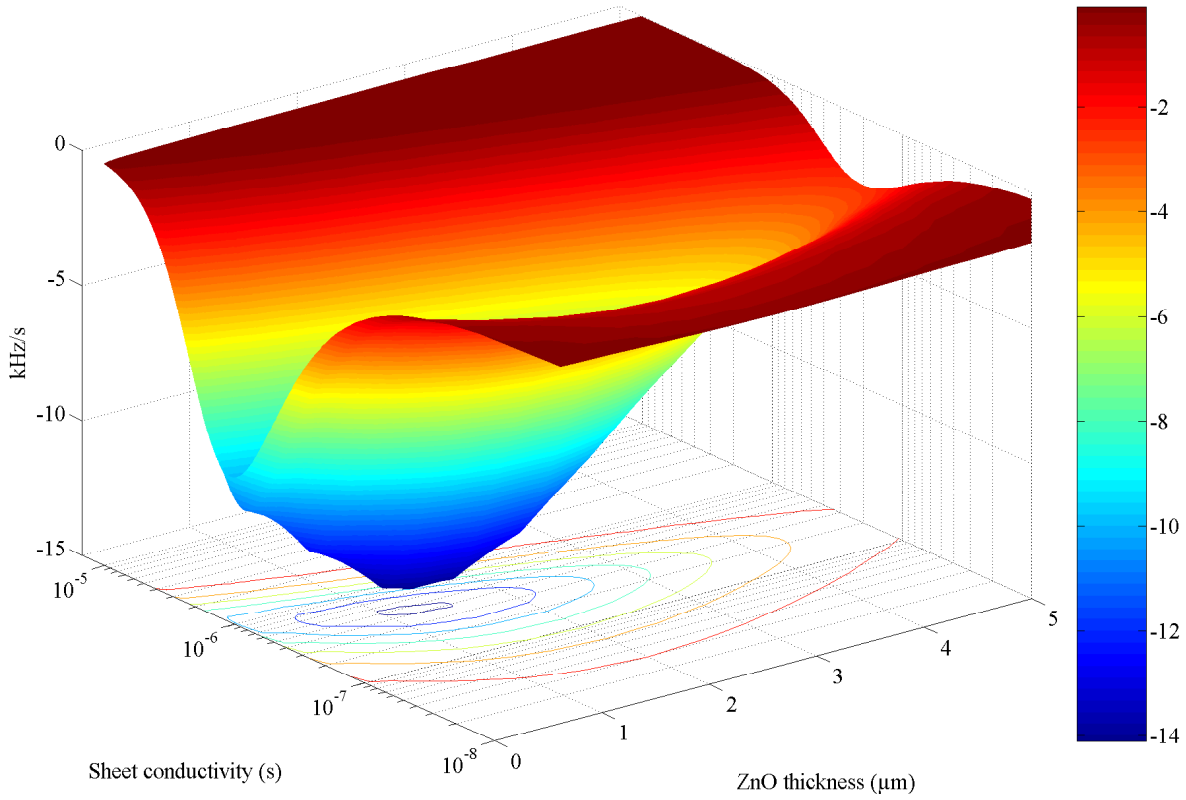

Figure 4.8: Sensitivity of ZnO/36° YX $LiTaO_3$ layered SAW structure.

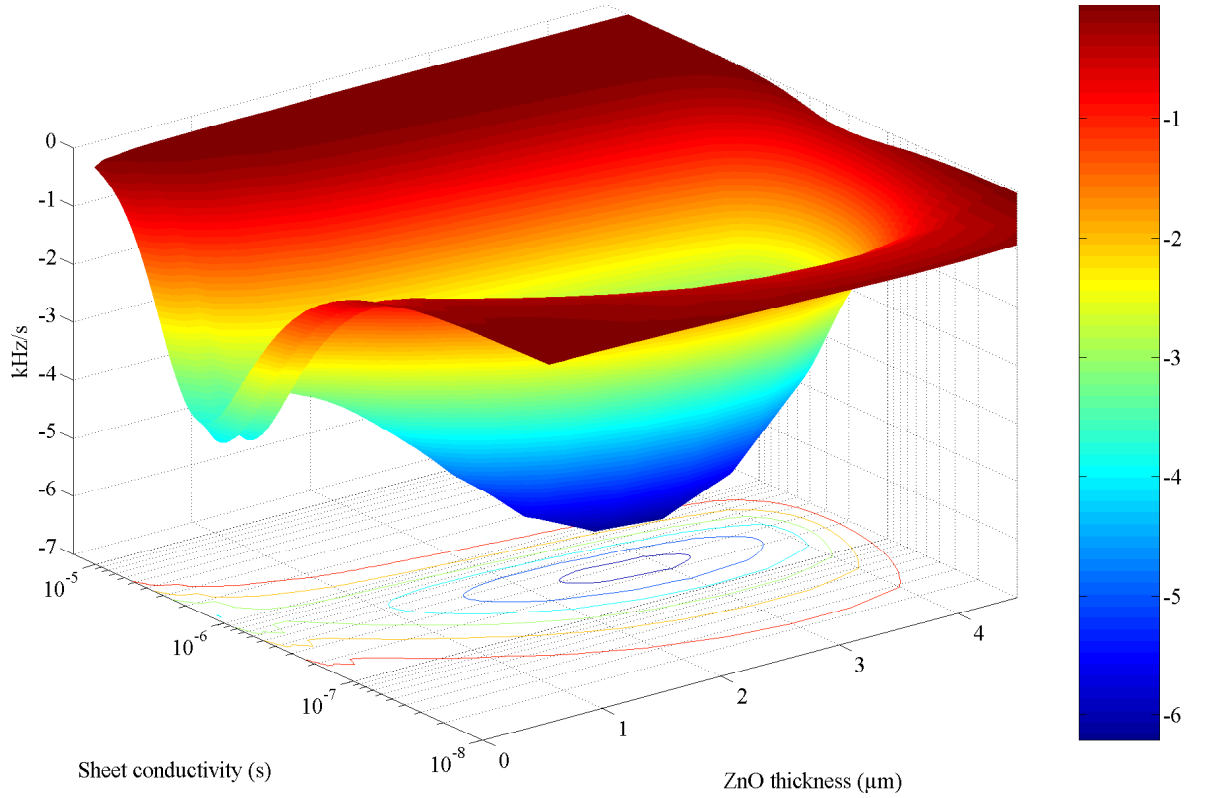

(a) ZnO/XY $LiNbO_3$

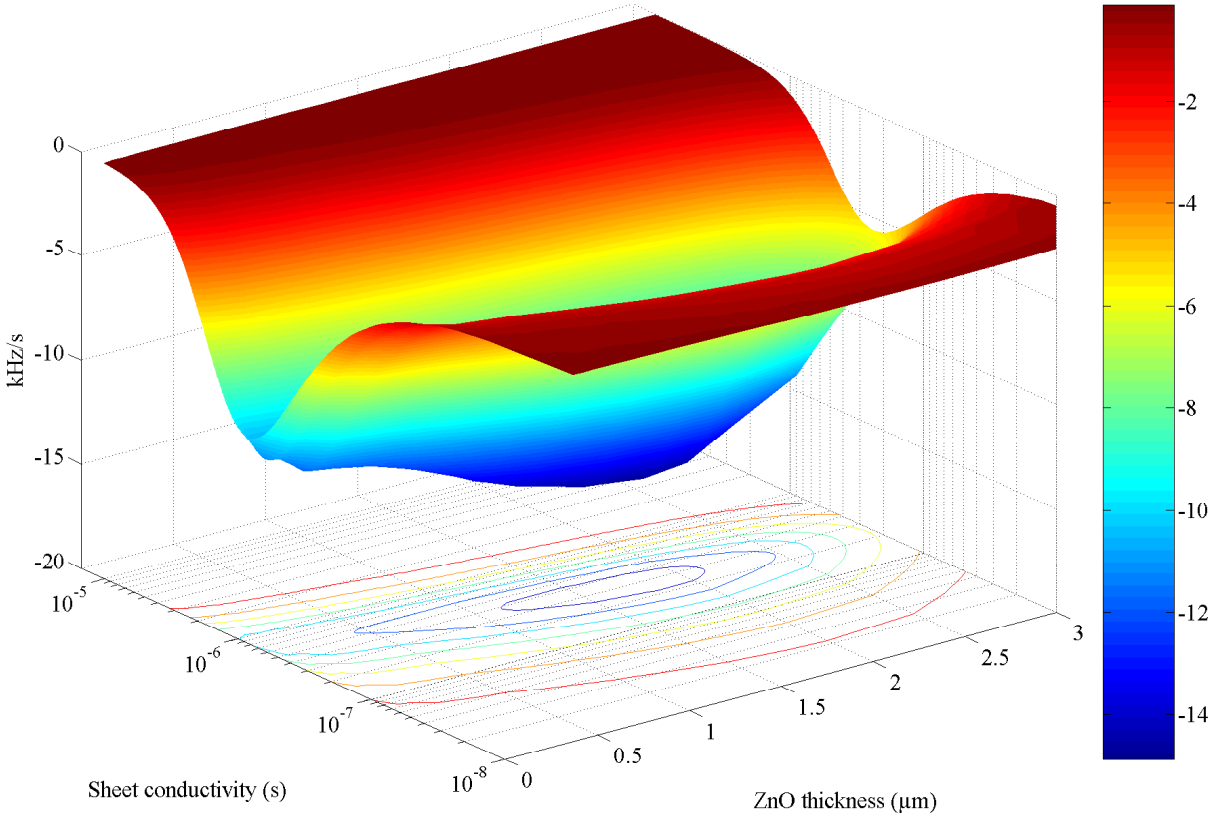

(b) ZnO/XZ $LiNbO_3$

Figure 4.9: Sensitivity of ZnO/XY $LiNbO_3$ and ZnO/XZ $LiNbO_3$ layered SAW structures.

Table 4.2: Optimal ZnO thickness and conductivity ranges for each SAW mode.

Substrate material	Crystal cut	SAW axis	Optimal ZnO thickness	Conductivity (siemens)	
				Broad range	*Narrow range*
$LiNbO_3$	X	Y	2.2 - 3.2 µm	$2e^{-8} < \sigma_{sh} < 1e^{-6}$	$1.5e^{-7} < \sigma_{sh} < 4.0e^{-7}$
$LiNbO_3$	X	Z	1.2 - 2.2 µm	$2e^{-8} < \sigma_{sh} < 1e^{-6}$	$2.0e^{-7} < \sigma_{sh} < 5.0e^{-7}$
$LiTaO_3$	36° Y	X	1.0 - 1.5 µm	$3e^{-8} < \sigma_{sh} < 2e^{-6}$	$3.5e^{-7} < \sigma_{sh} < 5.5e^{-7}$

4.4.1.1 Layered Structure Permittivity

In the derivation of equation (4.6), it is necessary to evaluate the permittivity of the layered structure $\varepsilon_p(k)$, at each ZnO thickness. The permittivity was approximated by matching the boundary conditions of the ZnO layer with the substrate by adapting the method detailed by Blϕtekjær et al. in [163]:

$$\varepsilon_p(k) = \varepsilon_{1p} \frac{\varepsilon_{1p} \tanh(k_0\, h_1) + \varepsilon_{2p}}{\varepsilon_{2p} \tanh(k_0\, h_1) + \varepsilon_{1p}} \quad , \tag{4.7}$$

where the permittivities of the ZnO layer and the semi-infinite substrate of interest are ε_{1p} and ε_{2p}, respectively. Using the same numerical method [130], ε_{1p} was calculated at different ZnO thicknesses (h_1). Table 4.3 list the different ZnO thickness permittivity values along with the substrate orientation permittivity values used in the calculations.

Table 4.3: ZnO and substrate permittivity values used in calculations.

Substrate	Substrate permittivity ε_{2p} (F/m)	ZnO thickness h_1 (μm)	ZnO permittivity ε_{1p} (F/m)
XY $LiNbO_3$	7.2099×10^{-10}	0	Substrate permittivity
		0.05	4.2320×10^{-11}
		0.06	4.7444×10^{-11}
XZ $LiNbO_3$	4.1777×10^{-10}	0.07	5.1793×10^{-11}
		0.1	6.3489×10^{-11}
		0.2	8.8170×10^{-11}
36° YX $LiTaO_3$	4.4499×10^{-10}	0.5	9.7277×10^{-11}
		1.0	9.9118×10^{-11}
		1.2	9.9778×10^{-11}
		1.5	9.9256×10^{-11}
		1.8	9.8972×10^{-11}
		2.0	9.9002×10^{-11}
		2.5	9.8973×10^{-11}
		≥ 3.0	9.8972×10^{-11}

4.4.2 Design Tradeoffs

To streamline fabrication procedures, it was only possible to deposit a single ZnO thickness for all experimental gas sensing work. Considering that an intermediate ZnO layer

thickness of 0.5 to 1.5 µm was calculated to have a high K^2 at the ZnO/substrate for all investigated SAW modes, the author decided on a 1.2 µm thick intermediate ZnO layer. The chosen intermediate layer thickness provided the best tradeoff between ZnO thickness and sensitivity for all investigated SAW modes. The 1.2 µm ZnO thickness is further justified as it satisfies the maximum sensitivity range for both the XZ $LiNbO_3$ and 36° YX $LiTaO_3$ substrate orientations, as shown in table 4.2. Additionally, preliminary gas sensing experiments using different intermediate ZnO layer thicknesses in the WO_3/ZnO/36° YX $LiTaO_3$ structure, provide evidence that ∼1.2 µm of ZnO results in maximum sensitivity. The experimental results are presented separately in Chapter 8, section 8.1. Fortunately, the 1.2 µm thick intermediate ZnO layer enables the ZnO/XY $LiNbO_3$ structure to fall within the broad range of sensitivity, yielding K^2 values of 3% at the ZnO/substrate interface and 1% at the device surface. Table 4.4 summarises the velocity, centre frequency and K^2 for the investigated SAW modes, calculated for a ZnO thickness of 1.2 µm and $\lambda = 24$ µm.

Table 4.4: Substrate crystal cuts with 1.2 µm ZnO layer, calculated at $\lambda = 24$ µm.

Substrate material	Crystal cut	SAW axis	Velocity (m/s)		$f_{o_{free}}$	K^2	
			Free	Metallised		Interface	Surface
$LiNbO_3$	X	Y	3567.5	3548.9	148.65 MHz	3.04%	1.04%
$LiNbO_3$	X	Z	3404.8	3356.8	141.87 MHz	6.11%	2.81%
$LiTaO_3$	36° Y	X	4112.1	4040.5	171.34 MHz	8.56%	3.46%

4.5 Summary

This chapter presented some of the advantages of the proposed layered SAW structures. The conductometric sensitivity of layered SAW structures was approximated using perturbation theory, illustrating that the ZnO intermediate layer modifies the velocity-permittivity product of the SAW mode. Therefore, this enabled the sensitive layer thickness to be tailored for maximum sensitivity towards specific gas analytes, leaving the ZnO layer thickness to be chosen for optimisation of the velocity-permittivity product of the structure under investigation.

Results revealed that an optimal intermediate layer thickness is required to maximise conductivity based sensitivity of a given layered SAW structure. Optimisation of ZnO layer thickness was presented and the design tradeoffs with regards to the chosen SAW modes were discussed. Outcomes from this research can be summarised by the following

points:

- The ZnO intermediate layer configuration is employed to increase the devices' sensitivity towards conductivity changes at the surface by matching the sheet conductivity of the layer to the optimum operating region of the SAW device.
- A different ZnO layer thickness is required to maximise the velocity-permittivity product for the SAW modes investigated throughout this study. Table 4.2 provides a summary.
- The 1.2 µm thick layer was shown to provide maximum conductively based sensitivity for both the ZnO/XZ $LiNbO_3$ and ZnO/36° YX $LiTaO_3$ layered structure configurations.
- The 1.2 µm thickness was further justified as it satisfies the K^2 value for the ZnO/substrate interface for all 3 SAW modes investigated. A ZnO layer thickness above 1.2 µm was shown to be of no substantial advantage with regards to increasing the ZnO/substrate K^2 values for the chosen SAW modes (see section 4.3.2.1).

The methods and results presented in this chapter could allow future work to better optimise the intermediate layer geometry and material parameters in order to match the SAW mode to the conductivity range of the sensitive layer – as opposed to the method of matching the sensitive layer to the velocity-permittivity product of the SAW mode. Therefore, adjusting the intermediate layer parameters would effectively allow the thin film sensitive layers to be solely chosen for maximum sensitivity towards specific gas analytes.

Chapter 5

Layered SAW Device Fabrication

This chapter describes the fabrication process for the layered SAW devices investigated in this thesis. There are many steps involved in the fabrication of a layered SAW device, which include: metallisation layer deposition, photolithography, thin film deposition (intermediate ZnO and metal oxide sensitive layers) and wire bonding. A defect in any fabrication stage could lead to an irreversible error that requires restarting the entire process. The fabrication processes employed by the author are outlined in sections 5.1 through to 5.4 of this chapter. In section 5.5, the frequency response of each device is presented at different stages throughout the fabrication process. Finally, the chapter concludes in section 5.6, by providing a summary of the layered SAW structures employed throughout this research program.

5.1 SAW Transducer Fabrication Process

The layered SAW transducer fabrication process was accomplished by using standard fabrication techniques such as: electron beam evaporation, photolithography, sputtering and chemical etching.

Throughout this research program the following layer SAW structures were fabricated:

- XY $LiNbO_3$ SAW devices with an IDT aperture width of 200 µm, formed from Au/Ni/Ti metallisation layers, used for verification of finite-element work presented in Chapter 3.
- XY $LiNbO_3$ SAW devices with an IDT aperture width of 1250 µm, formed from Al/Cr metallisation layers.
- XZ $LiNbO_3$ SAW devices with an IDT aperture width of 1250 µm, formed from Al/Cr metallisation layers.

- 36° YX $LiTaO_3$ SAW devices with IDT aperture widths of
  1000, 1250 and 1500 µm, formed from Al/Cr metallisation layers.

As discussed in Chapter 3, the XY $LiNbO_3$ SAW device employing the Au/Ni/Ti metallisation layers was utilised to verify the the finite-element models. Similarly, the remaining layered SAW structures, employed for the gas sensing experiments (presented separately in Chapter 8), were previously justified in Chapter 4.

The SAW transducers were fabricated by the author using cleanroom and vacuum lab facilities provided by the Microelectronics and Materials Technology Centre (MMTC) at RMIT University. The metallisation of the substrate wafers was deposited by MMTC staff using thermal evaporation. The intermediate ZnO and WO_3 sensitive layers (including Pt and Au catalytically activated WO_3 layers) were deposited by the author using chemical vacuum deposition techniques. The author also actively initiated the deposition of the InO_x sensitive layers, during a joint project with The University of Crete, in Greece. Furthermore, a WO_3 sensitive layer was also deposited during the author's research fieldwork at The University of Brescia, in Italy.

The following subsections will describe the fabrication process of the layered SAW structures, including: sample preparation, metallisation, wafer dicing, photolithography, chemical etching and deposition of both the intermediate ZnO and metal oxide sensitive layers.

5.1.1 Sample Preparation

Cleaning of the samples is a very important part of the fabrication procedure. Using class-1000 cleanroom facilities, the surface of the 75 mm (3 inch) X-cut $LiNbO_3$ and 36° Y-cut $LiTaO_3$ substrates was cleaned prior to the deposition of the metallic thin films used to form the IDTs. To obtain good edge definition of the IDTs, a uniform metallic film with high adhesion is required. To ensure adhesion of the metallic film, each wafer was de-greased in acetone for five minutes. A rinse in ethanol for a further two minutes was conducted before rinsing with deionised water. Compressed nitrogen was used to blow dry the wafer. If necessary, after inspection, further cleaning of the samples was attempted in an ultrasonic bath of acetone for 30 minutes.

To confirm that the wafer was clean, a thorough visual inspection of the wafer was conducted under a microscope. A cotton swab with methanol was used to remove any

further particle contamination.

5.1.2 Metal Thin-Film Deposition

The metal layers were deposited by a Balzers^{TM} electron beam evaporator. Two types of metallisation were used in this research program.

For the finite-element verification presented in Chapter 3, a three layer film was used to form the IDT metallisation layer. The layer composed of 500 Å of gold (Au), 300 Å of nickel (Ni) and 200 Å of titanium (Ti). The films were deposited sequentially by electron evaporation process onto the bare X-cut $LiNbO_3$ substrate. The purpose of the titanium layer is to assist with the adhesion of the Au/Ni layer to the substrate surface. The Au layer provides high conductivity while the Ni layer acts as a lattice relaxation layer in-between the Ti and Au layers. The electron beam evaporator was set at an electron beam voltage of 6keV for Ti, Ni and Cr or 11keV for Au and Al. The typical chamber base pressure before evaporation was 2×10^{-7} Torr.

An aluminium/chromium (Al/Cr) metallisation layer was utilised for all the SAW devices used in the gas sensing experiments. The double layer configuration composed of 2500 Å of Al on 300 Å of Cr. The Cr layer promotes adhesion of the Al to the substrate.

5.1.3 Wafer Dicing

After metallisation, each wafer was cut into small rectangular samples with a Tempress (model 602) dicing saw. As the dicing process is delicate, a diamond substrate blade (type 2.187-4A-30RU7) was used. Any cracked or chipped samples were rejected. During the dicing process, the surface of the wafer was protected by a thick photoresist coating to avoid damage to the metallisation layer.

5.1.4 Photolithographic Mask

The photolithographic masks were designed and fabricated to pattern the substrate samples with the IDT designs. The IDT structures, presented in figures 3.1(a) and 4.3, were implemented by writing computer scripts for Agilent ADS software in layout mode. The design files were exported in the standard GDSII stream format suitable for external mask fabrication facilities. The masks were fabricated on three and four inch rectangular quartz substrates for the photolithography process.

5.1.5 Photolithography

Photolithography is the process of transferring the design on the mask to the metal layer. The photolithography process was conducted in a class-1000 clean room environment with a constant temperature of approximately 22°C and a relative humidity of 40%. Typically, groups of 6 to 10 samples were processed at a time.

Firstly, a thin film of positive photoresist (AZ 7905) was spin coated on top of the metallised surface of the substrate. A positive photoresist is one which becomes soluble on exposure to UV light. The sample surface was flooded with photoresist and spun in a spinner at 3000 rpm for 30 seconds, resulting in a uniform layer of the photoresist with a thickness approximately 0.5 µm after soft baking the sample.

The soft baking process involved putting the sample in an oven at 90°C for 20 minutes, which hardens the photoresist to form a cured film. A Karl Suss MJB-3 mask aligner and the quartz mask were then used to transfer the pattern onto the metallised substrate samples. The cured photoresist layer was exposed to a UV light source with a wavelength of 550 nm. The exposure time was calculated so each sample received approximately 100 millijoules of UV power. Typical exposure times ranged between 8 and 15 seconds, depending on the UV power intensity.

The UV exposed samples were then developed using AZ-400 developer, diluted with deionised water (1:4). The developing time was approximately 12 to 18 seconds depending on initial solution concentration. The samples were then washed with deionised water to remove any excess developer solution. To confirm that the exposure and development processes were successful, samples were subsequently visually inspected using an optical microscope.

After developing, the pattered photoresist layer underwent a post-baking process at 110°C for 20 minute. The post-baking process was found to make the patterned photoresist layer more durable during the chemical etching process.

5.1.6 Chemical Etching

Wet chemical etching was used to remove the unwanted metallised regions (Au/Ni/Ti or Al/Cr) on the samples. The etching time was found to be very critical in defining the features of the IDTs. Over or under etching could lead to different distances between the electrode fingers forming the IDT structure, resulting in distortion of the electrical

characteristic of the device.

5.1.6.1 Au/Ni/Ti Chemical Etching

For the Au/Ni/Ti metallisation layer, the etching process started with the 500 Å thick gold layer. The gold etching solution was made by mixing 14 grams of 'Techni Strip AU' with 1 litre of deionised water. Etching time varied from sample to sample and greatly depends on the enchant solution strength. Typically, the samples were immersed for 40 to 60 seconds until a noticeable colour change occurred, indicating that the nickel layer had been exposed. The samples were then washed in deionised water to remove any excess etchant.

The nickel etchant consisted of 15 grams of ammonium persulfate, 25 ml of nitric acid (70% concentration) and 100 ml of deionised water. Each sample was immersed for approximately 30 seconds until the titanium layer was reached. The samples were then washed in deionised water to remove any excess etchant.

The titanium layer was etched with a buffered (3%) hydrofluoric (HF) acid solution. Typically the samples were immersed in the etchant for less than 20 seconds, until the substrate became visible. The samples were then washed in deionised water to remove any excess etchant and dried with compressed nitrogen gas. To confirm that the etching process was successful, the samples were visually inspected under a microscope before and after the removal of the patterned photoresist layer. The removal of the photoresist layer was accomplished by the process described in section 5.1.1.

5.1.6.2 Al/Cr Chemical Etching

For the Al/Cr metallisation layers, the aluminium layer was etched by two different methods. The first method involved heating aluminium etchant to 40°C and immersing the sample in the etchant. The etchant consisted of 80 ml of phosphoric acid, 5 ml nitric acid, 5 ml of acetic acid and 10 ml deionised water. Consistent agitation was required to avoid bubble formation on the surface of the sample. The bubbles inhibit the etchant, leaving the sample with many small under-etched circular areas. Due to the difficulty involved, another procedure was used. Using diluted AZ-400 developer (1:4), which is a potassium hydroxide based solution, the aluminium layer was found to etch evenly, without any agitation. A 3 to 5 minute duration was required to etch a 2500 Å thick aluminium layer. In the case of the latter method, the post-baking process was found to

greatly enhance the stability of the patterned photoresist once immersed into the AZ-400 solution. The samples were then washed in deionised water to remove any excess etchant.

The exposed chromium layer was etched using a solution consisting of 5 grams ceric ammonium nitrate, 4 ml nitric acid and 50 ml of deionised water. Typically the samples were immersed in the etchant for 30 seconds, until the exposed regions of the substrate became visible. To confirm that the etching process was successful the samples were visually inspected under a microscope before and after the removal of the patterned photoresist layer. The removal of the photoresist layer was accomplished by the process described in section 5.1.1.

5.2 Intermediate and Sensitive Layer Deposition Techniques

The intermediate ZnO and InO_x and WO_3 sensitive layers were deposited by sputtering techniques. Sputterer systems fall into one of two categories, dictated by the type of power supply employed. The first has a Direct Current (DC) supply, generally employed for metallic targets. The second has a radio frequency (RF) supply, which is used for insulating or ceramic targets. During the course of this research program, both DC and RF sputtering systems have been utilised by the author.

5.2.1 RF Magnetron Sputtering

RF planar magnetron sputtering is suitable for depositing both metallic and non-metallic target materials. In general, RF sputtering systems are used for the deposition of highly insulating materials such as metal oxides or ceramics. Throughout the course of this research program, both metallic and ceramic targets were used with RF magnetron sputtering technique.

All intermediate ZnO and WO_3 sensitive layers were deposited by planar RF magnetron sputtering. Two separate planar RF magnetron sputtering systems were used during the course of this research program. The first system, based at RMIT University, Melbourne, Australia, was used by the author to deposit all ZnO and the 160 nm WO_3 thin films. The second planar RF magnetron sputterer, based at The University of Brescia, was used to deposit a WO_3 sensitive layer on the 36° YX $LiTaO_3$ base devices, during the author's stay in Italy.

5.2.2 DC Sputtering

Two separate planar DC sputtering systems were used during the course of this research program. A planar DC magnetron sputter, based in Crete, Greece, was used to deposit the InO_x thin films for the X-cut $LiNbO_3$ base devices.

The second planar DC sputter was used by the author to deposit the Pt and Au catalyst activator layers on the surface of the WO_3 sensitive layers for the 36° YX $LiTaO_3$ base devices.

5.3 ZnO Intermediate Layer Deposition

The ZnO dielectric intermediate layers were deposited over the IDTs of each sample, forming the layered SAW transducer structure. Where necessary, a shadow mask was used to prevent the IDT electrical wire-bond pads from being coated during the ZnO deposition process.

5.3.1 ZnO Deposition for Finite-Element Verification

The 3 µm thick ZnO deposition, required for the verification of the finite-element work, was conducted using a RF magnetron sputterer. A 99.99% pure ZnO target was used. The sputter chamber was evacuated to 1.0×10^{-5} Torr, where a gas mixture of 40% O_2 balanced in Ar was introduced to achieve a constant working pressure of 1.0×10^{-2} Torr for the duration of the sputtering process. The sample was heated to approximately 260°C during deposition, resulting in a deposition rate of approximately 0.5 µm per hour at a RF power of 40 W. The distance of the sample from the target was 65 mm.

5.3.2 ZnO Deposition for Experimental Gas Sensors

All the layered SAW sensors used for the experimental gas sensing work were fabricated with a 1.2 µm thick ZnO layer. The ZnO layer was deposited over the patterned XY $LiNbO_3$, XZ $LiNbO_3$ and 36° YX $LiTaO_3$ samples, using a 99.99% pure ZnO target, by planar RF magnetron sputtering. The samples where heated to approximately 255°C and a constant working pressure of 1.0×10^{-2} Torr was used during deposition. The target to sample distance was fixed at 65 mm. The sputtering atmosphere consisted of 40% oxygen balanced in argon. A RF power of 120 W resulted in a deposition rate of approximately 1.2 µm per hour.

5.4 Metal Oxide Sensitive Layer Deposition

As stated previously, the materials forming the gas sensitive layers employed in this research program were InO_x and WO_3. They were deposited by DC and RF magnetron sputtering, respectively.

5.4.1 InO_x Deposition

The InO_x layer was deposited over the ZnO surface of the SAW devices using a planar DC magnetron sputterer. The InO_x sensitive layers were deposited by the collaborative researchers, headed by Prof. Kiriakidis, at The University of Crete in Greece.

Two different InO_x film thicknesses were deposited. The first group of devices were deposited with a 40 nm thick InO_x film. Similarly, using an extended deposition time, a 200 nm thick InO_x film was deposited on a second group of devices under the same deposition conditions.

Using a reactive sputtering technique, a 99.999% pure metallic indium target was employed to deposit the InO_x thin films. A 100% oxygen plasma was used at a working pressure of 1.1×10^{-2} Torr. The current and voltage was 0.15 A and 300 V, respectively. Deposition temperature was maintained between 24 and 40°C. An ex-situ thickness measurement confirmed a deposition rate of approximately 3 nm per minute.

5.4.2 WO_3 Deposition

Tungsten trioxide was deposited as the sensitive layer for SAW gas sensors fabricated using a 36° YX $LiTaO_3$ substrate. Two separate RF magnetron sputtering systems were employed for WO_3 deposition.

5.4.2.1 160 nm WO_3 Sensitive Layer

The author deposited the 160 nm thick WO_3 sensitive layers using a metallic tungsten target (99.999% pure), by planar RF magnetron sputtering. Sputtering was conducted at a working pressure of 1.0×10^{-2} Torr with 90% oxygen balanced in argon. The samples were heated to 260°C and a target to sample distance of 65 mm was used. Sputtering was conducted with a RF power of 80 W, resulting in a deposition rate of 5.3 nm per minute. Samples used for gas sensing experiments (presented in Chapter 8) were sputtered for 30 minutes, resulting in a thickness of approximately 160 nm.

5.4.2.2 150 nm WO_3 Sensitive Layer

A single WO_3 sensitive layer was deposited during the author's stay at The University of Brescia, Italy. The WO_3 sensitive layer was deposited by a planar RF magnetron sputterer using a metallic tungsten target. Sputtering was conducted with 50% oxygen balanced in argon with a working pressure of 6.2×10^{-2} Torr. A deposition temperature of 300°C and a sample to target distance of 70 mm were used. A RF power of 50 W resulted in a film thickness of 150 nm.

5.4.3 Deposition of Pt and Au Catalyst Activator Layers

Platinum and gold catalyst activator layers were deposited on the surface of several WO_3/ZnO/36° YX $LiTaO_3$ layered SAW structures which employed the 160 nm WO_3 layer. The Pt and Au catalyst layers were deposited by the author on top of the WO_3 sensitive layers via planar DC sputtering at room temperature. The thickness of the Pt and Au layers was estimated to be approximately 4 to 5 and 6 to 7 nm thick, respectively. SEM characterisation, presented separately in chapter 6 section 6.3.4, show that the films deposited are non-continuous at the specified thicknesses. In both cases, it was observed that the WO_3 surface changed in colour after the catalyst deposition. A greenish and a blackish colour was observable for the platinum and gold layers, respectively.

5.5 Layered SAW Sensor Frequency Responses

To monitor the quality of the fabrication process, the device's frequency responses were measured using a network analyser prior to the deposition of each subsequent layer. A thermal wedge wire bonder (manufactured by West Bond) was used to bond gold ribbon wire (0.01" × 0.1") to the electrical pads of each device. If the fabrication quality or the electrical characteristics were not deemed to be within the acceptable limits, the device was rejected.

Each SAW device underwent a significant change in its frequency response as a result of the ZnO and subsequent metal oxide layer depositions. The following subsections show measured frequency responses (transmission parameter, S_{21}) for each of the investigated layered SAW structures. The measurements were taken with a vector network analyser (Rohde & Schwarz ZVRE) using 50Ω calibrated leads.

5.5.1 InO_x/ZnO/XY $LiNbO_3$ Layered SAW Sensor

Figure 5.1 shows the measured S_{21} transmission parameter of an InO_x/ZnO/XY $LiNbO_3$ layered SAW sensor at 3 stages of the fabrication process. Without the ZnO layer, the SAW mode is not observed to have good frequency response characteristics due to a lack of surface trapping. The addition of the ZnO layer clearly improves the frequency response.

Without the ZnO layer, operation of the device as the frequency determining element in an oscillator circuit is limited due to the poor frequency response characteristics (see Chapter 7, section 7.2).

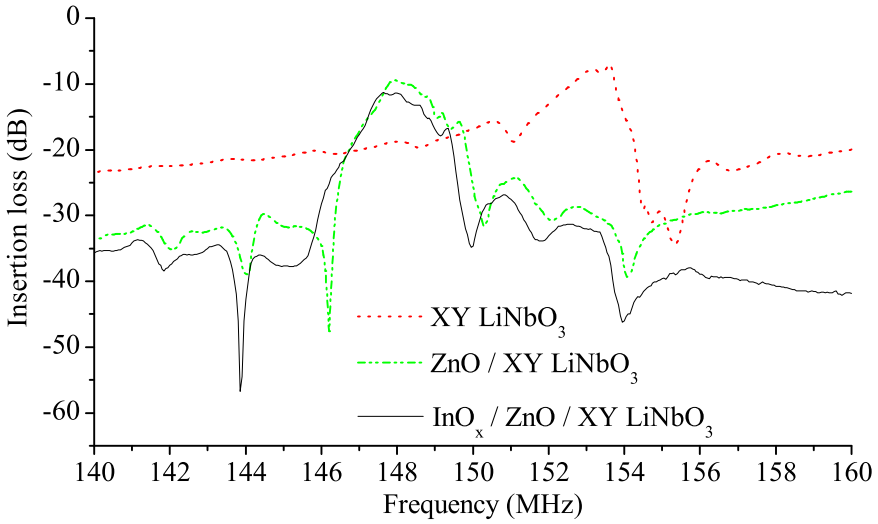

Figure 5.1: Frequency response of XY $LiNbO_3$ based layered SAW sensor throughout the fabrication process.

5.5.2 InO_x/ZnO/XZ $LiNbO_3$ Layered SAW Sensor

Figure 5.2 shows the measured S_{21} transmission parameter of an InO_x/ZnO/XY $LiNbO_3$ layered SAW sensor throughout the fabrication process. The significant difference between the frequency response of the XY and XZ $LiNbO_3$ orientations is due to the high anisotropic material properties of the $LiNbO_3$ substrate. Due to the large number of electrode finger pairs in the IDTs, the presence of sharp resonant peaks can be observed at 143.9 MHz for the non-layered device and 140.5 MHz with the ZnO intermediate layer. The resonant peaks shift to 140.1 and 139.8 MHz for the 40 and 200 nm InO_x sensitive layers, respectively.

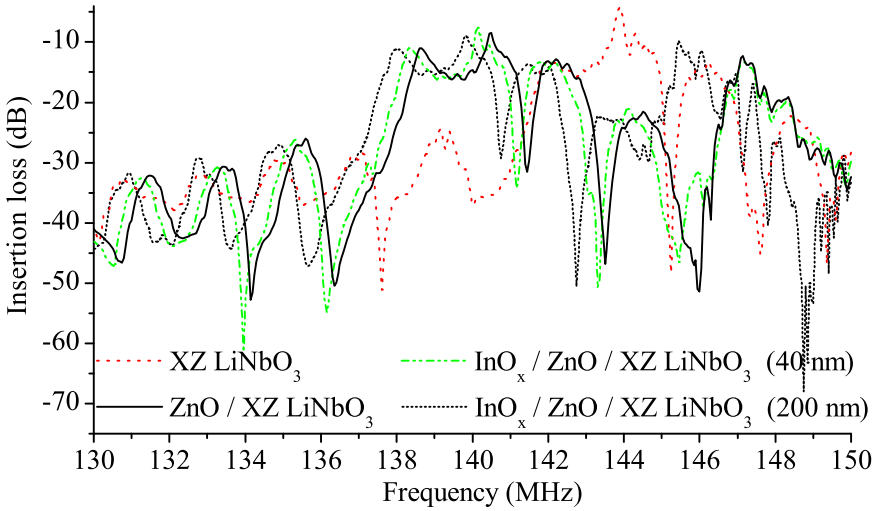

Figure 5.2: Frequency response of XZ $LiNbO_3$ based layered SAW sensor throughout the fabrication process.

5.5.3 WO_3/ZnO/36° YX $LiTaO_3$ and Pt– and Au–WO_3/ZnO/36° YX $LiTaO_3$ Layered SAW Sensors

Figure 5.3 shows the measured S_{21} transmission parameters of the Pt– and Au–WO_3/ZnO/ 36° YX $LiTaO_3$ layered SAW sensor after each major step of the fabrication process. The sharp resonant peak in the non-layered structure (174.45 MHz) is shown to significantly change once the ZnO intermediate and WO_3 sensitive layers are deposited. The deposition of the Pt and Au catalyst activator layers results in a minimum insertion loss of −10.2 and −13.6 dB at 168.53 and 168.8 MHz, respectively.

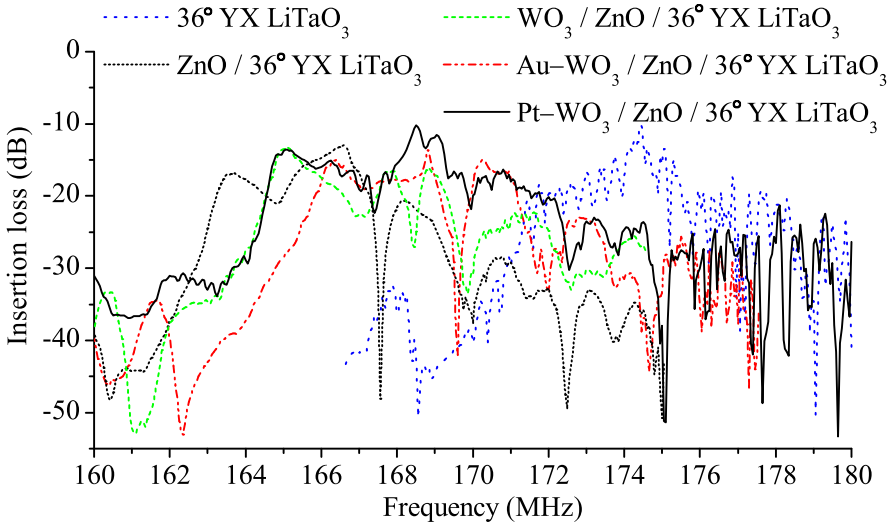

Figure 5.3: Frequency response of 36° YX $LiTaO_3$ based layered SAW sensors throughout the fabrication process employing the WO_3 and the Pt or Au catalyst activated WO_3 sensitive layers.

5.6 Summary

In this chapter, the fabrication steps of the layered SAW sensors were outlined. The steps involved in the fabrication process included: metallisation layer deposition, photolithography, thin film deposition and wire bonding. The deposition parameters of the ZnO intermediate, InO_x and WO_3 sensitive layers were presented. The intermediate ZnO and WO_3 sensitive layers were deposited by planar RF magnetron sputtering techniques. The InO_x sensitive layers were deposited by planar DC magnetron sputterer, whilst the Pt and Au catalyst layers were deposited by planar DC sputterer.

Particular emphasis was placed on the development and characterisation of key fabrication techniques to ensure that the layered SAW sensor fabrication was repeatable. The methods used helped ensure the credibility of the experimental results presented in Chapter 8. Each device was systematically inspected and tested throughout the fabrication process. A visual inspection of each device was conducted under a microscope and electrical characteristics prior to and after the deposition of each successive layer was carried out. The electrical characteristics were obtained by measuring the S_{21} transmission parameter with a vector network analyser. To ensure that only high quality layered SAW sensors were used, any devices with unsatisfactory visual and electrical characteristics were rejected.

Figure 5.4 shows a schematic cross-section for each of the different layered SAW structures fabricated during the course of this research program. Figure 5.4(a) shows the structure used for the finite-element verification presented in Chapter 3, while figures 5.4(b) through to 5.4(f) show the layered SAW structures used in the gas sensing experiments presented in Chapter 8. Material characterisation of the InO_x and WO_3 layers deposited on the ZnO/X-cut $LiNbO_3$ and ZnO/36° Y-cut $LiTaO_3$ layered structures shown in figure 5.4 will be presented in the following chapter.

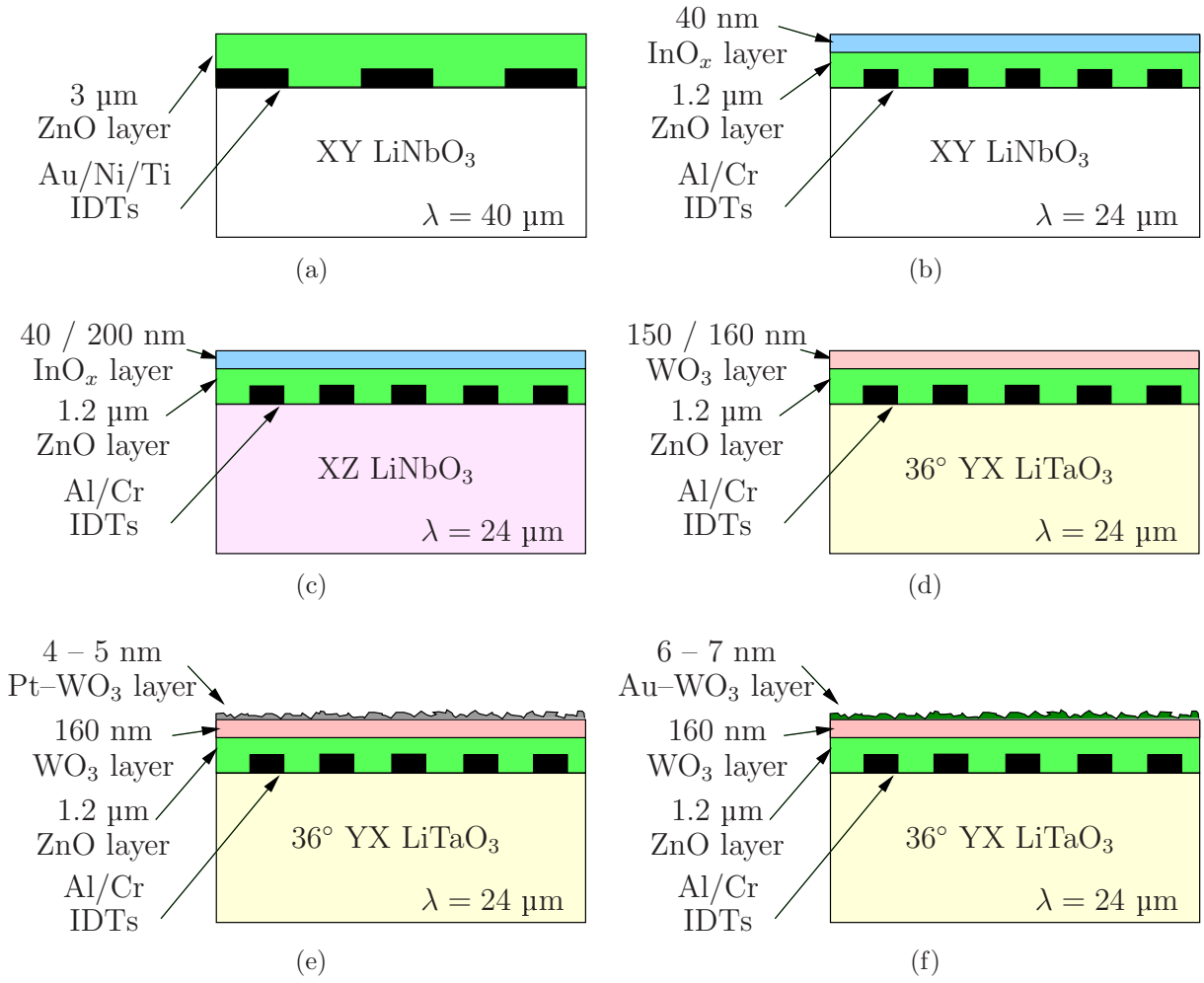

Figure 5.4: Cross-section schematic of fabricated layered SAW structures.

[This page is left blank intentionally.]

Chapter 6

Results – Thin Film Characterisation

In this chapter, the material characterisation results of the ZnO, InO_x and WO_3 thin films, which were deposited by the techniques described in Chapter 5, are presented.

Metal oxides are known to have stable chemical and thermal properties over extended periods, making them well suited for gas sensing applications [4]. During formation, the metal element undergoes an oxidation process, thus making the film less likely to be affected by irreversible oxidation due to an analyte gas. However, prolonged operation at elevated temperature may change the morphology of metal oxide thin film, which influences its interaction with gas [97, 164, 165].

As previously mentioned, the InO_x or WO_3 sensitive layer's interaction with a gas species results in a conductivity change at the metal oxide surface. The sensing performance of thin films such as InO_x and WO_3 is dependent on their morphological structure and surface characteristics. The underlying morphology of the intermediate ZnO layer greatly influences the growth of the InO_x and WO_3 sensitive layers; affecting grain size and surface area. To the best of the author's knowledge, this is the first time the surface morphology of InO_x/ZnO/X-cut $LiNbO_3$ and WO_3/ZnO/36° Y-cut $LiTaO_3$ layered structures has been investigated. Surface morphology characterisation will be presented for the intermediate ZnO layer and the InO_x and WO_3 sensitive layers at different stages of the fabrication and gas testing process.

In this chapter, the surface morphology of the layered structures is studied by various micro-characterisation techniques. These techniques include: Atomic Force Microscopy

(AFM), Scanning Electron Microscopy (SEM) and X-ray Diffraction (XRD). The chapter is structured as follows:

Section 6.1 details the surface morphology of the intermediate ZnO layer. AFM and SEM characterisation methods are used to analyse the growth of the 1.2 µm ZnO film on the metallised and non-metallised regions of both the $LiNbO_3$ and $LiTaO_3$ substrates. The effect of prolonged operation at elevated temperature (300°C for 24 hours) on the ZnO surface morphology is also discussed. Additionally, XRD characterisation of the ZnO layer grown on $LiTaO_3$ is presented.

In section 6.2 the surface morphology of the InO_x sensitive layer is discussed. AFM surface characterisation of the 40 nm thick InO_x layer deposited on both a silicon substrate and the layered ZnO/X-cut $LiNbO_3$ structure is presented. Furthermore, SEM characterisation reveals the differences between the 40 and 200 nm InO_x films employed on the layered ZnO/X-cut $LiNbO_3$ structure.

Section 6.3 investigates the surface morphology of the WO_3 sensitive layer deposited on the ZnO/36° Y-cut $LiTaO_3$ structures. Characterisation by AFM, both prior too and after thermal treatment, demonstrates that the WO_3 sensitive layer undergoes surface morphology modifications due to prolonged operation at temperatures up to 300°C. Furthermore, the addition of gold catalyst activator layers on the WO_3 sensitive layer surface is characterised by SEM, using both Secondary Electron (SE) and Backscatter Electron (BSE) detectors.

Section 6.4 provides a summary of the findings presented in this chapter.

6.1 Analysis of ZnO Intermediate Layer

The material properties of metal oxide thin films are strongly dependant on the deposition technique, and are known to vary considerably from bulk material properties [166]. For example, crystal orientation, grain size, stiffness and density are all sensitive to deposition parameters. Thus, acoustic properties of the material are directly affected by the deposition technique and associated deposition parameters. Additionally, the properties of polycrystalline thin films can be strongly influenced by the composition and orientation of the substrate on which they are grown [37].

As previously mentioned, the intermediate ZnO layer is employed to increase the devices'

sensitivity towards conductivity changes at the surface. Sputtered ZnO normally forms in the hexagonal wurtzite structure, having a 6-mm crystal symmetry with lattice constants a=3.25 Å and c=5.12 Å [18, 167]. Each zinc atom is tetrahedrally coordinated to four oxygen atoms, where the zinc d-electrons hybridise with the oxygen p-electrons. Layers occupied by zinc atoms alternate with layers occupied by oxygen atoms [167].

ZnO thin films have been prepared by many deposition techniques, such as thermal evaporation, reactive evaporation, spray pyrolysis, chemical vapour deposition and sol-gel. However, RF magnetron sputtering with Ar/O_2 gas mixture is the most widely employed technique [18]. RF sputtering of ZnO permits relatively low deposition temperature with better adhesion and higher density than other methods [168]. RF sputtered ZnO films are polycrystalline. Under certain conditions, depending on the substrate, the individual crystals grow with the crystallographic c-axis perpendicular to the substrate surface [18, 168].

The following two sections 6.1.1 and 6.1.2, investigate the surface morphology of the ZnO layer deposited on the $LiNbO_3$ and $LiTaO_3$ substrates. In each section, AFM and SEM characterisation techniques are employed to gain a deeper understanding of the surface morphology induced by the different substrates and metallised regions. Finally, XRD analysis is used to confirm the crystalline structure and orientation of the ZnO layer on the $LiTaO_3$ substrate.

6.1.1 Surface Characterisation of ZnO on X-cut $LiNbO_3$

The surface morphology of the 1.2 µm thick ZnO layer on the X-cut $LiNbO_3$ structure was investigated by AFM and SEM techniques. The ZnO forms the intermediate layer in structures (b) and (c) presented in Chapter 5, figure 5.4. No surface characterisation is presented for the 3 µm thick ZnO layer employed for structure (a) in figure 5.4.

All AFM and SEM surface characterisation of the $ZnO/LiNbO_3$ structures were conducted on samples which were thermally treated. The thermal treatment process was conducted either in a furnace at 300°C in air for 24 to 48 hours, or via the elevated operating temperature during the gas sensing experiments procedure detailed in Chapter 7, section 7.3.4. The furnace conditions were chosen to be similar to the thermal treatment experienced by each device during the gas sensing experiments.

6.1.1.1 AFM Surface Characterisation of ZnO/$LiNbO_3$ structure

The grain size and surface roughness were investigated with a Nanoscope III atomic force microscope in tapping mode. Figure 6.1(a) shows a 50 × 50 µm 3D representation of a patterned area, illustrating the different ZnO growth on the X-cut $LiNbO_3$ substrate and metallised regions. The difference in growth between the metallised and non-metallised regions is due to the substrates strong influence on the initial growth of the 1.2 µm thick ZnO intermediate layer. Figure 6.1(b) shows a 5 × 5 µm 'top view' image of the ZnO deposited on a metallised region of the sample. The rough metallic surface is represented by the bright dots within a z-range (normal to the surface) of 85 to 170 nm. The RMS surface roughnesses of the ZnO deposited on the metallised region, calculated by the AFM software, was 21.58 nm for the image in figure 6.1(b).

Figure 6.2 shows both a 3D and 2D ZnO surface representation of a non-metallised region of the sample. The ZnO surface roughness of the 1 × 1 µm 'top view' image was calculated to be 7.37 nm with a mean grain radius of 70 nm.

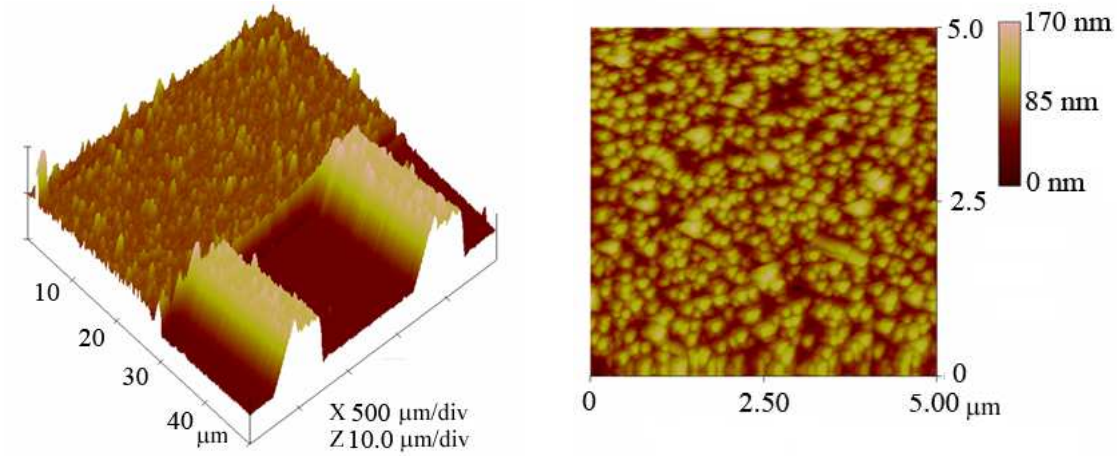

(a) Patterned area. Metallised and non-metallised regions shown

(b) Metallised region.
RMS surface roughness = 21.58 nm.

Figure 6.1: AFM surface image of 1.2 µm ZnO on X-cut $LiNbO_3$ patterned substrate.

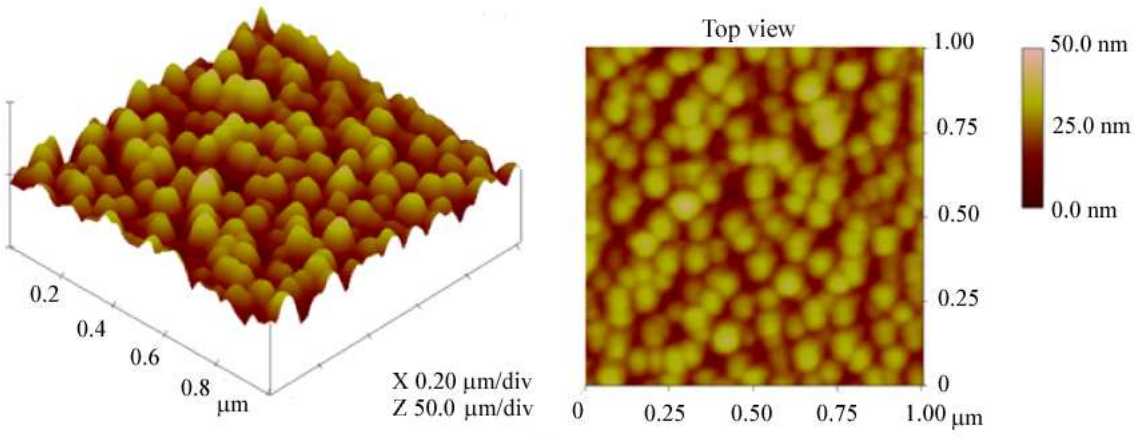

Figure 6.2: AFM surface image of 1.2 µm thick ZnO deposited on non-metallised X-cut $LiNbO_3$ substrate. A RMS surface roughness of 7.37 nm with 50 nm surface features (in the z-range) was measured.

6.1.1.2 SEM Surface Characterisation of ZnO/$LiNbO_3$ Structure

The ZnO film deposited on the X-cut $LiNbO_3$ substrate was characterised using a SEM (Philips XL-30) with an SE detector. Figure 6.3 shows a micrograph taken using a 25kV acceleration voltage with a spot size of 2.5. The upper part of the micrograph image shows the ZnO thin film deposited on the metallised (Al) region, while the lower part shows the ZnO film deposited on the non-metallised $LiNbO_3$ substrate. The SEM micrograph clearly demonstrates the size and shape of the ZnO grains to be different between the metallised and non-metallised regions of the sample. In accordance with the AFM results, the grain roughness and size appear smaller in the non-metallised region. The micrograph also

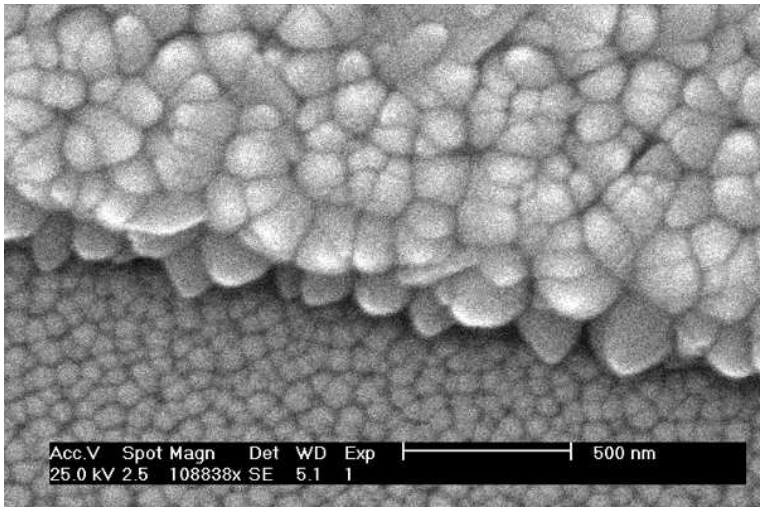

Figure 6.3: SEM Micrograph ZnO on metallised X-cut $LiNbO_3$ (top) and non-metallised region (bottom) using a secondary electron (SE) detector.

reveals that the surface structure is more homogenous and compact in the non-metallised region of the sample.

6.1.2 Surface Characterisation of ZnO on 36° Y-cut $LiTaO_3$

The surface morphology of the ZnO layer deposited on a 36° Y-cut $LiTaO_3$ substrate was investigated using AFM and SEM techniques. Additional XRD characterisation was also conducted to evaluate the crystallinity of the 1.2 µm thick ZnO layer deposited on the 36° Y-cut $LiTaO_3$ substrate. Results presented within this section directly relate to 1.2 µm thick ZnO layer employed as the intermediate layer in structures (d), (e) and (f) presented in Chapter 5, figure 5.4.

6.1.2.1 AFM Surface Characterisation of ZnO on 36° Y-cut $LiTaO_3$ Substrate

The grain size and surface roughness were investigated with a Veeco CP-Research Atomic Force Microscope (AFM) in intermittent-contact mode. Figure 6.4 shows a 40 × 40 µm 3D representation of a patterned area, illustrating the different ZnO growth on the 36° Y-cut $LiTaO_3$ substrate and metallised regions. A profile is provided to illustrate the typical fabrication uniformity of the IDTs (each 6 µm wide with 6 µm inter-finger spacing).

AFM surface characterisation of the ZnO layer was performed on two separate samples. Both samples were deposited with 1.2 µm of ZnO, however one sample was thermally treated at 300°C for 24 hours in air. Figures 6.5 and 6.6 show the AFM surface

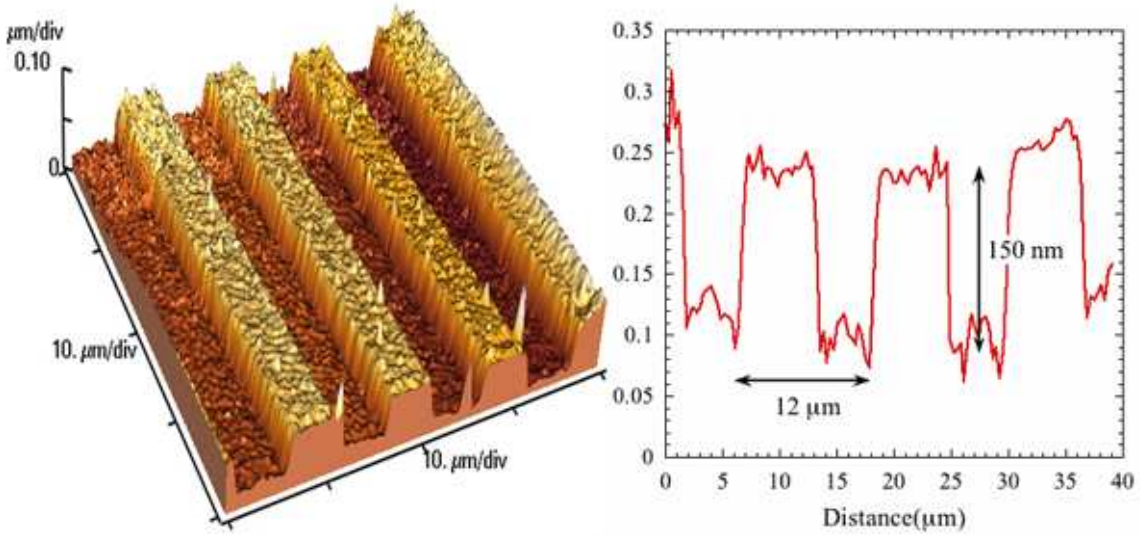

Figure 6.4: AFM surface image of ZnO/X-cut $LiNbO_3$. *Left* – 40×40 µm AFM image of 1.2 µm ZnO deposited on IDT structure. *Right* – Profile across IDTs.

characterisation results of the non-thermally treated ('as deposited') and thermally treated sample, respectively. Each figure provides a 1 × 1 µm and 2 × 2 µm 3D representations of the non-metallised and metallised (Al) regions on the samples. The 1 × 1 µm and 2 × 2 µm image sizes are provided to give the reader a clearer representation of the surface morphology for both the metallised and non-metallised regions.

The 'as deposited' ZnO layer in figure 6.5 is shown to have a slightly oblique, cross-hatched grain structure on the non-metallised region of the sample. The grain structure differs from that of the ZnO deposited on the X-cut $LiNbO_3$ substrate. XRD analysis presented in section 6.1.2.3 reveals that the ZnO grains grow with the *c*-axis parallel to the surface of the 36° Y-cut $LiTaO_3$ substrate, thus resulting in the cross-hatched structure. A rougher, less ordered grain structure is observed on the metallised region. The ZnO on the non-metallised region was calculated to have an RMS surface roughnesses of ∼18 nm in the 1 × 1 µm image (figure 6.5(c)) with a ZnO grain size of in the range of 75 - 132 nm. From figure 6.5(d), the metallised region of the same sample shows the ZnO layer has a smaller grain size in the range of 55 – 102 nm with a slightly larger RMS roughness of ∼21.5 nm.

Figure 6.6 illustrates the surface morphology of the ZnO layer after thermal treatment. The grain structure in the non-metallised region is less ordered than before thermal treatment and appears to be more like the structure in the metallised region. The grain size was found to increase to approximately 220 – 300 nm with an RMS roughness value of ∼28 nm for the non-metallised region. The metallised region shown grains with a more homogeneous size distribution with an average diameter of approximately 110 nm, with the exception of a few elongated grains approximately 450 nm long. The RMS roughness for the metallised region was ∼20 nm. All grain sizes and RMS roughness values were calculated from the 1 × 1 µm scans.

Overall, the grain structure is more ordered in the 'as deposited' sample, when compared to the thermally treated sample. The main difference observed was that the grain size increases after thermal treatment. RMS roughness is shown to greatly increases in the non-metallised regions, however slightly decreases in the metallised.

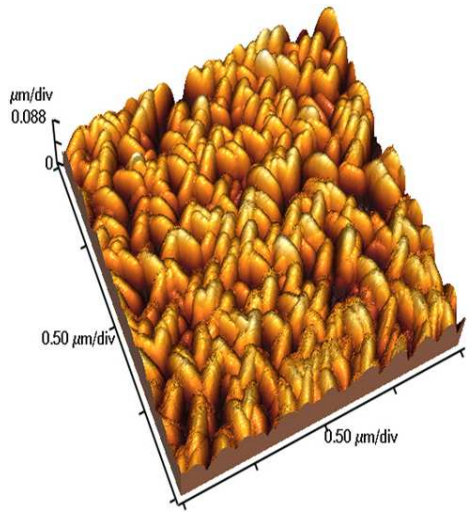

(a) 2×2 µm of ZnO on 36° Y-cut $LiTaO_3$ substrate.

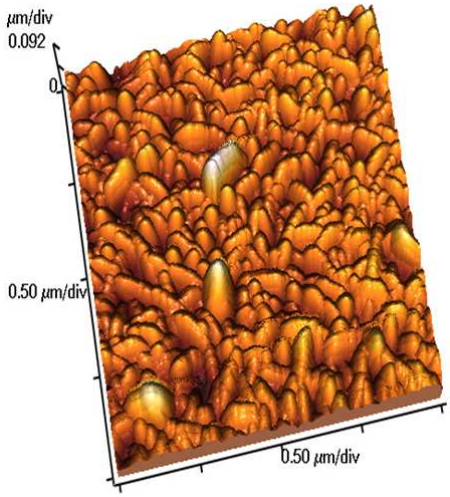

(b) 2×2 µm of ZnO on metallised 36° Y-cut $LiTaO_3$ substrate.

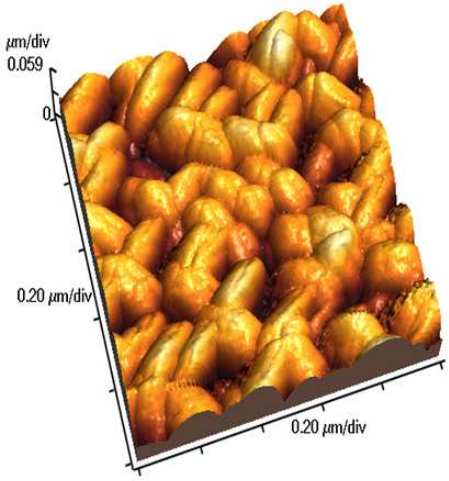

(c) 1×1 µm of ZnO on 36° Y-cut $LiTaO_3$ substrate.

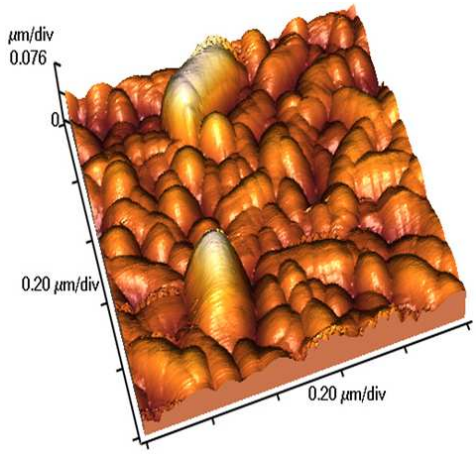

(d) 1×1 µm of ZnO on metallised 36° Y-cut $LiTaO_3$ substrate.

Figure 6.5: AFM surface image of 1.2 µm ZnO deposited on 36° Y-cut $LiTaO_3$ SAW structure – as deposited (prior to thermal treatment).

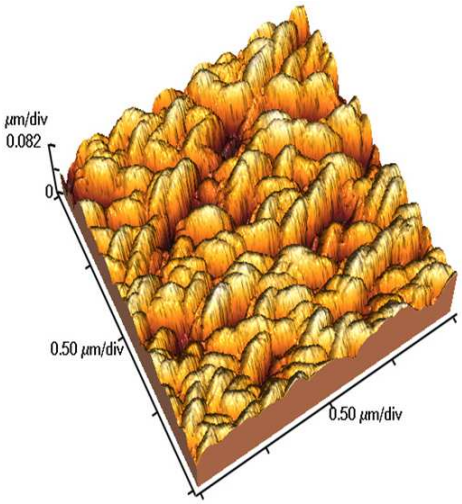

(a) 2×2 µm of ZnO on 36° Y-cut $LiTaO_3$ substrate.

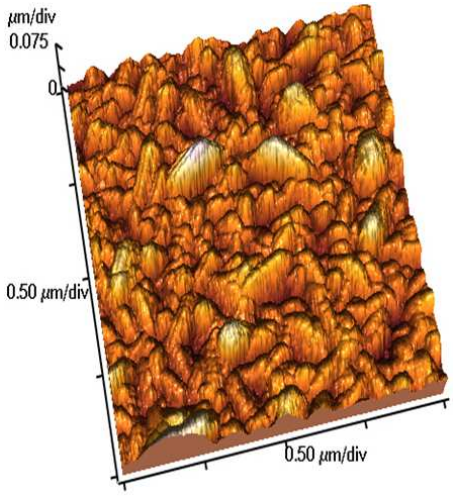

(b) 2×2 µm of ZnO on metallised 36° Y-cut $LiTaO_3$ substrate.

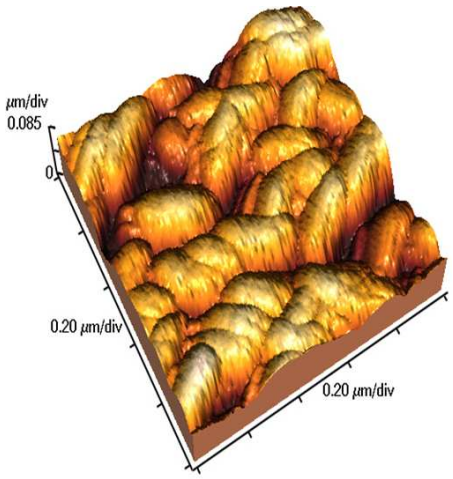

(c) 1×1 µm of ZnO on 36° Y-cut $LiTaO_3$ substrate.

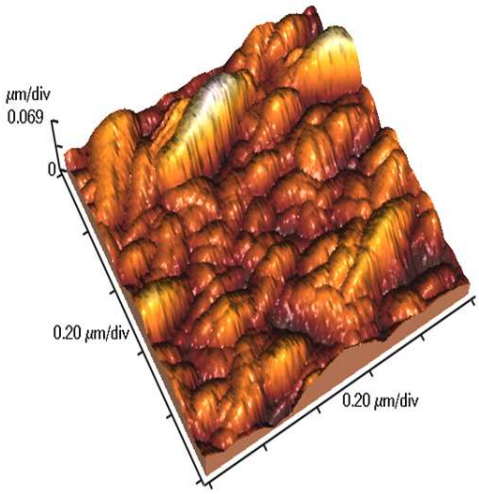

(d) 1×1 µm of ZnO on metallised 36° Y-cut $LiTaO_3$ substrate.

Figure 6.6: AFM surface image of 1.2 µm ZnO deposited on 36° Y-cut $LiTaO_3$ SAW structure – after thermal treatment (300°C for more than 24 hours).

6.1.2.2 SEM Surface Characterisation of ZnO on 36° Y-cut $LiTaO_3$ Substrate

The ZnO film deposited on the 36° Y-cut $LiTaO_3$ substrate was also micro-characterised using a SEM (Philips XL-30) with a SE detector, prior to thermal treatment. Figure 6.7 shows the SEM micrograph of the film at the edge of an IDT electrode finger, taken using a 10kV acceleration voltage with a spot size of 4.0. The analysis clearly indicates that the grain size and shape differ substantially between the metallised and non-metallised regions of the sample. The left side of the micrograph image shows the ZnO thin film deposited on the non-metallised region, while the right side shows the ZnO film deposited on the bare substrate. In accordance with the AFM results, the grain size is smaller in the metallised regions. Unlike the ZnO/$LiNbO_3$ structure, the micrograph of the ZnO/$LiTaO_3$ structure reveals that the surface is more homogenous and compact in the metallised region of the sample, when compared to the non-metallised region.

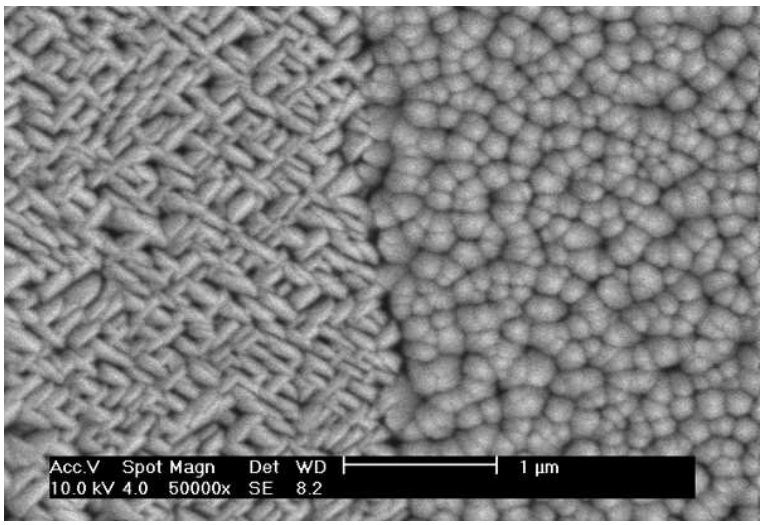

Figure 6.7: SEM Micrograph ZnO on non-metallised 36° Y-cut $LiTaO_3$ (left) and metallised region (right) using a secondary electron (SE) detector.

6.1.2.3 XRD Characterisation of ZnO/36° Y-cut $LiTaO_3$ Structure

XRD analysis was conducted on the ZnO/36° Y-cut $LiTaO_3$ structure to examine the ZnO layer crystallinity. Figure 6.8 shows the XRD pattern of the 'as deposited' ZnO/36° Y-cut $LiTaO_3$ structure. The ZnO grain growth and corresponding crystal orientation are (001) on the metallised region and (110) on the bare substrate. A strong ZnO (110) peak indicates that the *c*-axis lies in the plane of the non-metallised substrate [11, 169]. The *c*-axis growth, parallel to the substrate surface results in the slightly oblique, cross-hatched organised grain structure, which is observed in both the AFM and SEM images presented

in figure 6.5(d) and 6.7, respectively. The presence of a smaller ZnO (102) peak is shown to be dominated by the (110) peak, thus the XRD pattern confirms that the ZnO layer is mostly c-axis orientated.

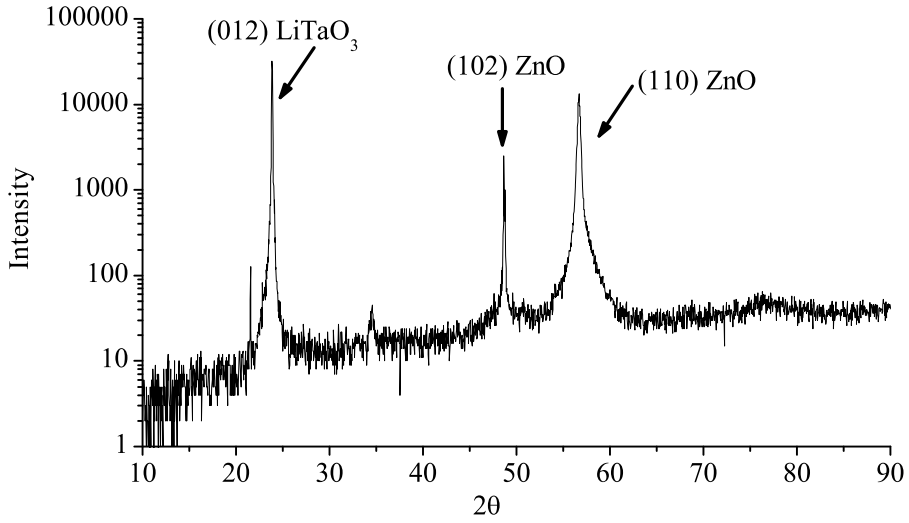

Figure 6.8: XRD pattern of ZnO deposited on 36° Y-cut $LiTaO_3$ substrate.

6.2 InO_x Sensitive Layer Surface Characterisation

The InO_x sensitive layers deposited over the $ZnO/LiNbO_3$ structure were investigated by AFM and SEM techniques. Results presented within this section relate to both the 40 and 200 nm thick InO_x films deposited over the $ZnO/LiNbO_3$ structures (b) and (c), presented in Chapter 5, figure 5.4. Additionally, AFM surface morphology characterisation of the 40 nm InO_x layer deposited on a silicon substrate is presented.

AFM and SEM surface characterisation of the $InO_x/ZnO/LiNbO_3$ structures was conducted on samples which were thermally treated, using the process described in section 6.1.1.

6.2.1 AFM Characterisation of 40 nm InO_x Film on Silicon Substrate

The surface morphology of the InO_x film was investigated with a Nanoscope III atomic force microscope in tapping mode. Figure 6.9 shows a 1 × 1 µm 3D representation of a 40 nm thick InO_x film deposited on a (100) silicon substrate. A z-range of 5 nm within a

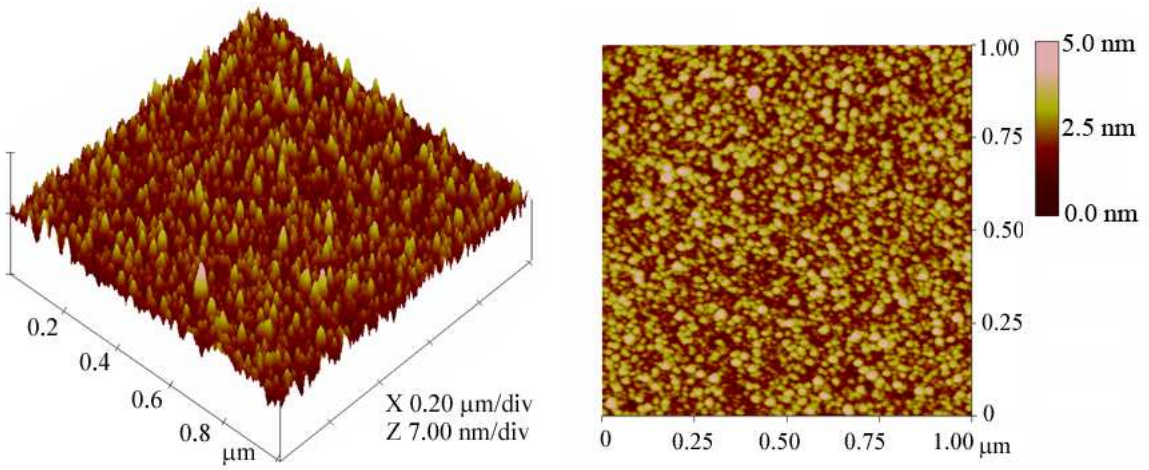

Figure 6.9: AFM surface image of 40 nm InO_x layer deposited on silicon substrate. A surface roughness (RMS) of 0.61 nm with a grain radius of 19 nm was measured.

z-scale of 7 nm is shown in the image. An RMS surface roughness of 0.610 nm and a mean grain radius of 19 nm were measured over the scan area. Further AFM characterisation of InO_x thin films deposited on silicon and Corning glass substrates can be found elsewhere [159, 160].

6.2.2 AFM Characterisation of InO_x Layer on $ZnO/LiNbO_3$ Structure

The surface morphology of the InO_x layer deposited over the $ZnO/LiNbO_3$ structure was also investigated using the same procedure as the sample deposited on silicon. Figure 6.10 illustrates a 2×2 µm 'top view' and 3D representation of the metallised region. Similarly, figure 6.11 illustrates a higher resolution 1×1 µm image of the non-metallised region of the sample. It can be seen that after the 40 nm InO_x sensitive layer is deposited, the surface morphology exhibits features with facets comparable with the underlying ZnO. It can also been seen that the InO_x growth is substantially different between the metallised and non-metallised regions, suggesting that the 40 nm InO_x film follows the underlying ZnO surface topography. The different growth of InO_x on the layered SAW structure and the silicon substrate (figure 6.9) can be directly attributed to the difference in surface roughness of the ZnO layer and the silicon substrate.

A comparison between figures 6.1(b) and 6.10 reveals that the RMS surface roughness of the metallised $ZnO/LiNbO_3$ region increases from 21.58 nm to 27.03 nm once the 40 nm InO_x film is deposited. Thus, resulting in approximately a 25% increase once the InO_x

film is deposited, when compared to the ZnO alone.

In the case of the non-metallised region of the sample, the InO_x surface roughness of 1×1 µm 'top view' image was calculated to be 10.12 nm with a mean grain radius of 70 nm. In comparison to the measured RMS roughness of 7.37 nm in figure 6.2, once the InO_x film was deposited, a roughness of 10.12 nm was observed. This is a 37% increase in RMS roughness for the non-metallised region of the sample. Furthermore, the size of the surface features, in the z-range shows an increase of approximately 25%. The increase in grain size observed was from roughly 50 nm features for the ZnO substrate before InO_x deposition to 75 nm afterwards.

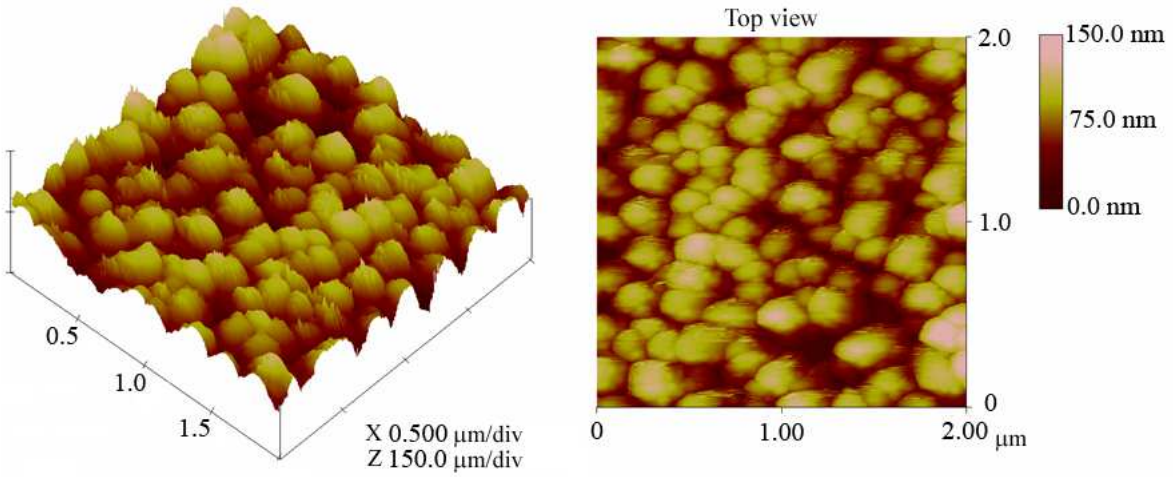

Figure 6.10: AFM surface image of 40 nm InO_x layer deposited on top of the 1.2 µm thick ZnO on metallised region of X-cut $LiNbO_3$ substrate.

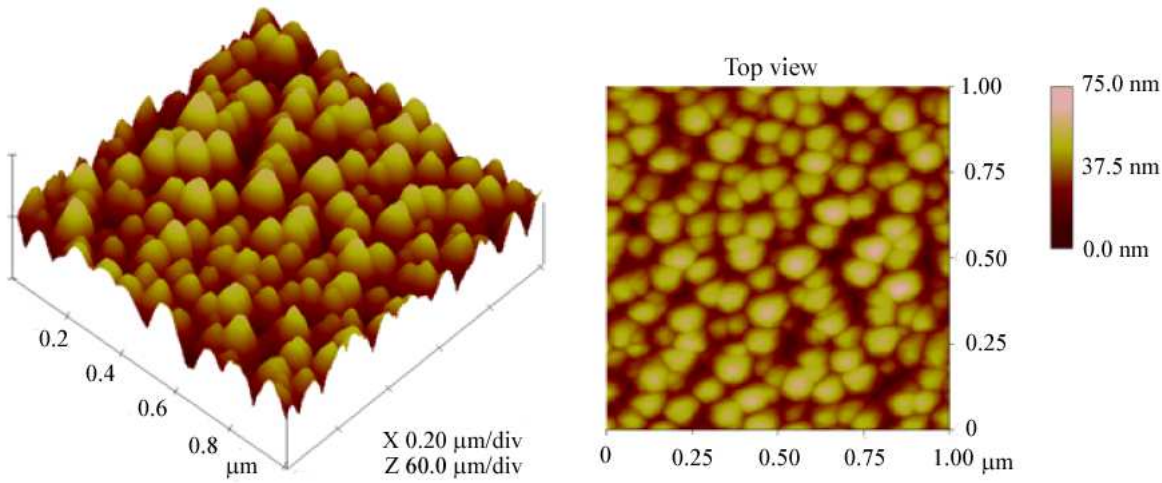

Figure 6.11: AFM surface image of 40 nm InO_x layer deposited on top of the 1.2 µm thick ZnO on non-metallised X-cut $LiNbO_3$ substrate.

After the InO_x deposition, the grain structure becomes better defined in both the metallised and non-metallised regions of the sample. This is particularly visible in the 'top view' images, suggesting an improvement in surface crystallinity of the thin films.

6.2.3 SEM Characterisation of InO_x Layer on $ZnO/LiNbO_3$ Structure

Both the 40 and 200 nm thick InO_x sensitive layers deposited on the $ZnO/LiNbO_3$ structure were micro-characterised using a SEM (Philips XL-30) with a SE detector. Figure 6.12 shows a micrograph of (a) 40 nm and (b) 200 nm InO_x layers. Both images were taken using a 25kV acceleration voltage with a spot size of 2.5. In both micrographs, the left hand side shows the InO_x layer deposited on the metallised region, while the right shows the InO_x layer deposited on the non-metallised region of the $ZnO/LiNbO_3$ sample.

The morphology of the 40 nm InO_x layer is not clearly visible. Similar to the AFM characterisation, the surface morphology exhibits feature facets comparable to the rather rough structure of the ZnO layer prior to the InO_x deposition. This is also evident when comparing figure 6.12(a) with the SEM micrograph of the $ZnO/LiNbO_3$ structure in figure 6.3. On both the metallised and non-metallised regions of the 40 nm InO_x layer, the texture of the underlying ZnO grains is still clearly distinguishable.

The micrograph of the 200 nm InO_x layer shows that the ZnO grains on the underlying structure are still visible. However the thicker, denser amorphous InO_x layer appears to

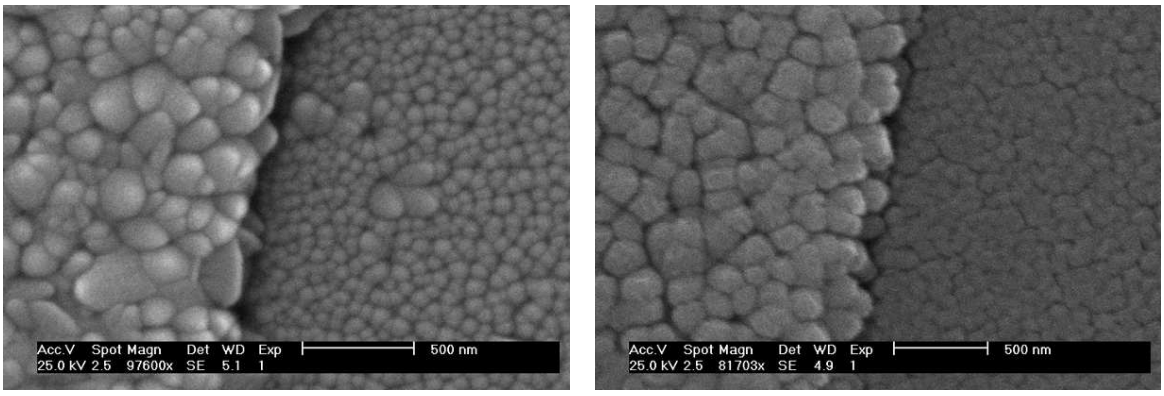

(a) 40 nm InO_x deposited. (b) 200 nm InO_x deposited.

Figure 6.12: SEM Micrograph of InO_x deposited on $ZnO/LiNbO_3$ structure. *Left side of images* – deposited over metallised $LiNbO_3$ substrate. *Right side of images* – deposited on polished $LiNbO_3$ substrate.

smoothen the texture of the device surface in the non-metallised region of the sample. By contrast, the surface topography of the metallised region appears to exhibit deeper, larger and more defined grain boundaries.

6.3 WO_3 Sensitive Layer Characterisation

In this section, the surface morphology of the 150 and 160 nm WO_3 sensitive layer is presented. The WO_3 sensitive layers deposited over the ZnO/36° Y-cut $LiTaO_3$ structure were investigated by AFM, SEM and XRD characterisation techniques. Results presented within this subsection directly relate to the 150 and 160 nm WO_3 thin films employed as the sensitive layers in structures (d), (e) and (f) in figure 5.4. Furthermore, SEM surface characterisation of the Au catalyst activator layer deposited on the surface of a WO_3/ZnO/36° Y-cut $LiTaO_3$ structure, which corresponds to structure (f) in figure 5.4 can be found in section 6.3.4.

6.3.1 AFM Characterisation of WO_3 Layer on ZnO/$LiTaO_3$ Structure

The surface morphology of the WO_3 layer was investigated with a Veeco CP-Research Atomic Force Microscope (AFM) in intermittent-contact mode. AFM surface characterisation of the WO_3/ZnO/$LiTaO_3$ structure was performed on two separate samples. For both samples, the 150 nm of WO_3 was deposited over a 1.2 µm thick intermediate ZnO layer. The second sample was thermally treated by operating at elevated temperature when exposed to gas, according to the procedure described in Chapter 7, section 7.3.4.

Figures 6.13 and 6.14 show AFM surface characterisation of the 'as deposited' and thermally treated samples, respectively. Each figure illustrates a 1 × 1 µm and 2 × 2 µm 3D representation of the non-metallised and metallised regions.

The 'as deposited' WO_3 sensitive layer in figure 6.13 shows only a marginal difference in surface morphology features between the metallised and non-metallised regions of the sample. This demonstrates that the WO_3 layer is only marginally influenced by the difference in surface morphology of the underlying ZnO layer, which can be seen by comparison with figure 6.5.

Figure 6.14 illustrates the surface morphology of the WO_3 sensitive layer after the second sample had undergone thermal treatment during the testing procedure. A noticeable difference in the WO_3 layer's surface morphology occurs between the non-metallised (c) and metallised (d) regions of the sample after thermal treatment. A more obvious change is seen when comparing the respective images in figures 6.13 and 6.14. The typical grain size decreases from 132 – 176 nm in the non-metallised region of the 'as deposited' sample to 90 – 132 nm after thermal treatment. In the non-metallised region, an RMS roughness of ∼11.5 nm and ∼12 nm were measured before and after prolonged exposure to elevated

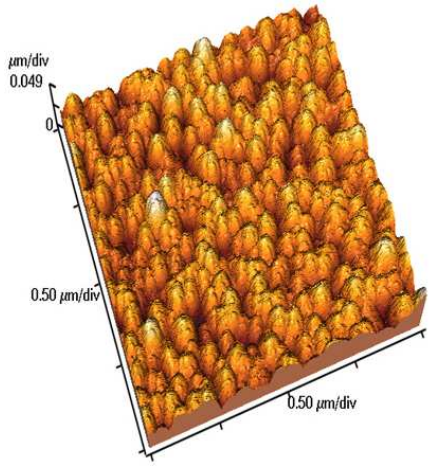

(a) 2×2 µm of WO_3 on ZnO/36° Y-cut $LiTaO_3$ structure.

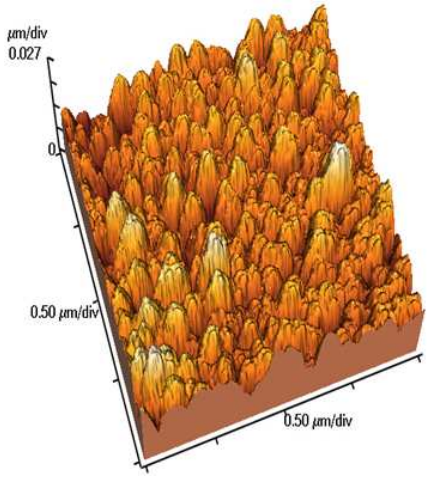

(b) 2×2 µm of WO_3 on metallised region of ZnO/36° Y-cut $LiTaO_3$ structure.

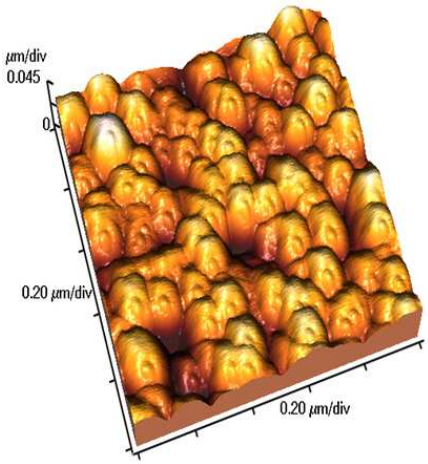

(c) 1×1 µm of WO_3 on ZnO/36° Y-cut $LiTaO_3$ structure.

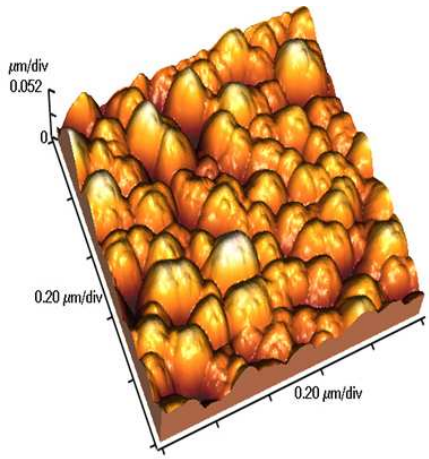

(d) 1×1 µm of WO_3 on metallised region of ZnO/36° Y-cut $LiTaO_3$ structure.

Figure 6.13: AFM surface image of 150 nm WO_3 sensing layer deposited on ZnO/36° Y-cut $LiTaO_3$ SAW device – as deposited (prior to gas testing). *Note:* ZnO intermediate layer thickness is 1.2 µm.

operating temperatures, respectively. The typical grain size in the metallised region was observed to have slightly decreased from 75 – 191 nm to 60 – 156 nm, with an RMS roughness increasing from ∼13.5 nm to ∼16 nm after thermal treatment.

Figure 6.14(c) clearly shows that the shape of the WO_3 grains become well defined after thermal treatment, with an increase in surface area when compared to figure 6.13(c). This can be observed from the change in grain shape, suggesting an improvement in surface crystallinity with continued heat exposure. Unlike the ZnO, the WO_3 decreases in overall grain size after the thermal treatment process. However, both the ZnO and WO_3 were

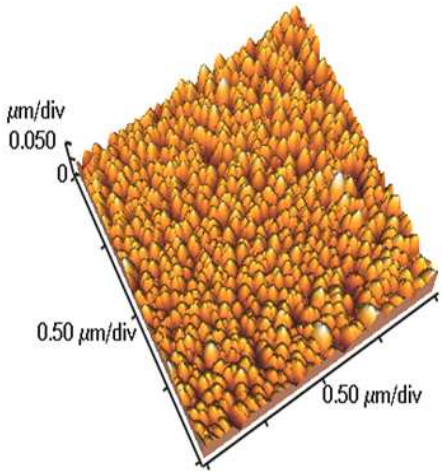

(a) 2×2 µm of WO_3 on ZnO/36° Y-cut $LiTaO_3$ structure.

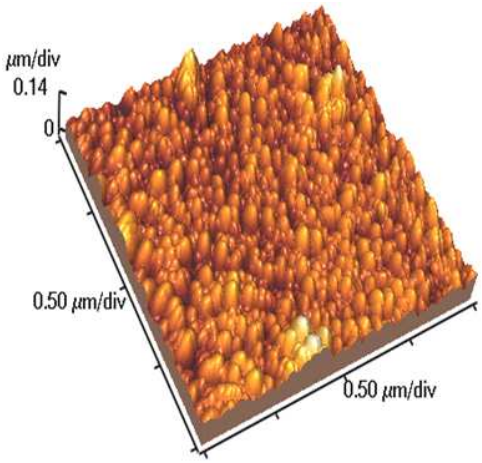

(b) 2×2 µm of WO_3 on metallised region of ZnO/36° Y-cut $LiTaO_3$ structure.

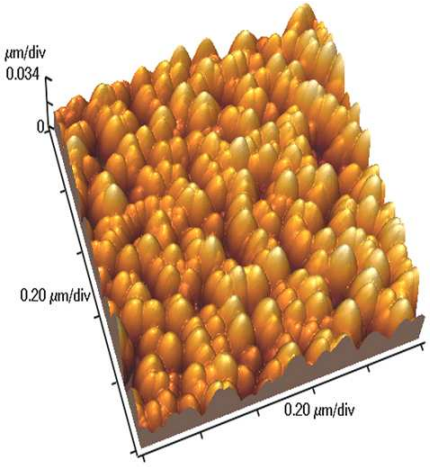

(c) 1×1 µm of WO_3 on ZnO/36° Y-cut $LiTaO_3$ structure.

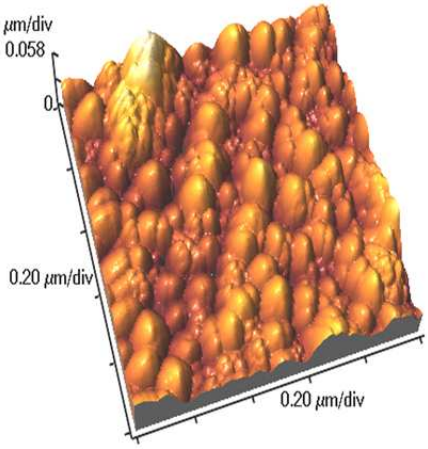

(d) 1×1 µm of WO_3 on metallised region of ZnO/36° Y-cut $LiTaO_3$ structure.

Figure 6.14: AFM surface image of 150 nm WO_3 sensing layer deposited on ZnO/36° Y-cut $LiTaO_3$ SAW device – after testing (thermal treatment). *Note:* ZnO intermediate layer thickness is 1.2 µm.

shown to generally increase in RMS roughness after thermal treatment. The exception is the metallised region of the ZnO layer, which showed a slight decrease in RMS roughness, when compared to the RMS roughness of the WO_3 after thermal treatment.

Stankova et al. [164] presented XPS and AFM results on RF sputtered WO_3 thin films, suggesting that a change in cluster size, but not the film's chemical composition, is caused by high temperature annealing. The results presented here agree with this conclusion, however complete certainty could only be verified with further analysis.

6.3.2 XRD Characterisation of WO_3/ZnO/36° Y-cut $LiTaO_3$ Structure

Figure 6.15 shows the XRD pattern of the 'as deposited' 160 nm WO_3 sensitive layer on the ZnO/36° Y-cut $LiTaO_3$ structure. Peaks are observed at angles of $2\theta = 34.5°$ and 36.5°, which were not present in the XRD pattern of the ZnO/36° Y-cut $LiTaO_3$ structure in figure 6.8. The relative intensity of the $LiTaO_3$ (012) main peak is observed to substantially increase with the deposition of the WO_3 layer. Cantalini et al. [149] were able to show the existence of a peak at $2\theta = 24°$ when WO_3 was RF sputtered. Therefore it is suggested that the $LiTaO_3$ and WO_3 peaks overlap at this position, thus resulting in the observed increase in intensity at $2\theta = 24°$.

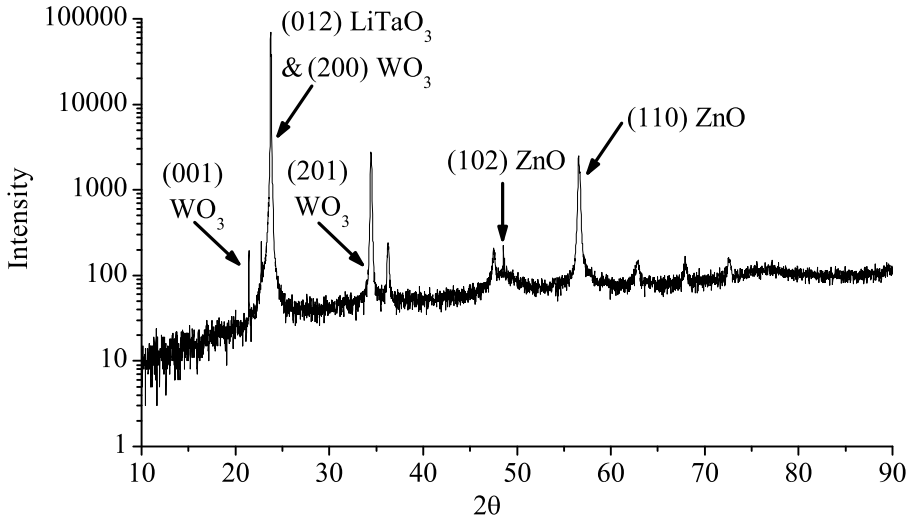

Figure 6.15: XRD pattern of WO_3 deposited on ZnO/36° Y-cut $LiTaO_3$ structure.

6.3.3 SEM Characterisation of WO_3 Layer on ZnO/$LiTaO_3$ Structure

The WO_3 sensitive layers deposited over the ZnO/36° Y-cut $LiTaO_3$ structures were characterised using two different SEMs. A Philips XL-30 with secondary electron (SE) and backscatter electron (BSE) detectors were used to characterise the 160 nm WO_3 layer. The 150 nm WO_3 layer was characterised with a JEOL 6700F FE-SEM.

Figure 6.16 shows a micrograph of the 160 nm WO_3 layer deposited over a non-metallised ZnO/36° Y-cut $LiTaO_3$ structure, prior to thermal treatment. The image was taken using a 20kV acceleration voltage, with a BSE detector and spot size of 1.5. The micrograph illustrates the underlying ZnO grain boundaries, which are partially visible through the 160 nm WO_3 sensitive layer. The ZnO is shown to have the oblique, cross-hatched grain structure as previously mentioned in section 6.1.2. The partial visibility of the ZnO grain boundaries is due to the BSE detector resolving grain boundaries at a penetration depth of approximately 1 µm, due to the high 20kV acceleration voltage. The sparsely spaced ZnO crystals appearing in the image are assumed to be the ZnO grains protruding through the much thinner WO_3 layer. Thus, it can be concluded that the underlying ZnO layer is of non-uniform thickness. This is further supported by the AFM characterisation of the ZnO layer presented in section 6.1.2.1. The WO_3 thin film does not appear to follow the same grain structure as the underlying ZnO. Instead the WO_3 forms grains that appear to have smaller spherical boundaries than the cylindrical boundaries of the ZnO, irrespective of the ZnO surface morphology. The dark areas around the ZnO grains highlight the porosity of the ZnO film layer. This suggests that the ZnO is less densely arranged when compared to the WO_3 film.

A second sample was prepared with a WO_3 layer 6 times as thick (approximately 960 nm), by extending the deposition time to 3 hours. It was also deposited over the ZnO/36° Y-cut $LiTaO_3$ structure with a 1.2 µm thick ZnO intermediate layer. Figure 6.17 shows a SEM micrograph of a cleaved sample using a 20kV acceleration voltage, with a SE detector and a spot size of 3.0. The sample was cleaved to reveal a cross section of the layers. It clearly shows the WO_3 and ZnO layers deposited on a $LiTaO_3$ substrate. The ZnO is shown to grow with clear grain boundaries forming columnar structures perpendicular to the surface of the substrate. A similar columnar structure was also observed by Kalantar-Zadeh [18]. Unfortunately, the grain boundaries of the ∼960 nm WO_3 layer are not clearly visible. This is due to the fact that the WO_3 layer is more densely packed when compared

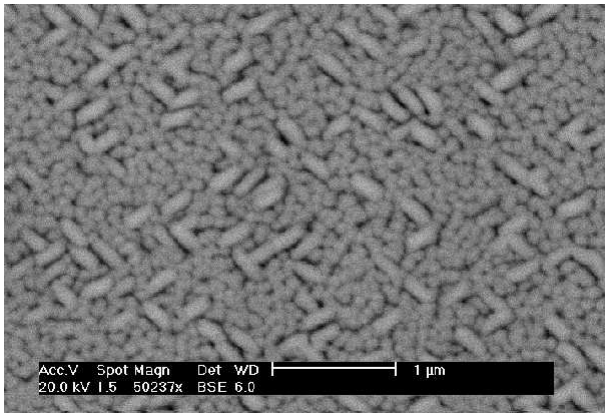

Figure 6.16: SEM Micrograph of WO_3 (160 nm) on ZnO (1.2 µm) on $LiTaO_3$ substrate using BSE detector.

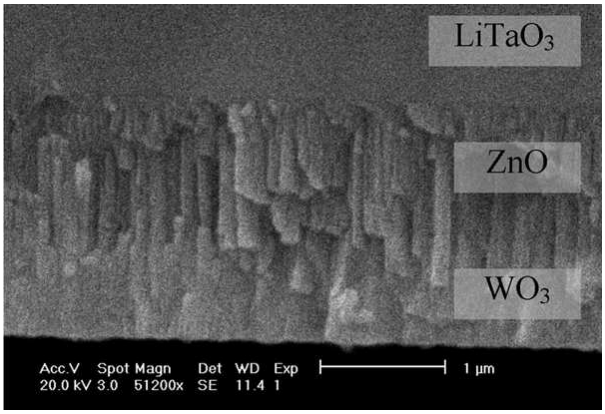

Figure 6.17: Cross sectional SEM micrograph of WO_3 (960 nm) and ZnO (1.2 µm) layer on a $LiTaO_3$ substrate using SE detector.

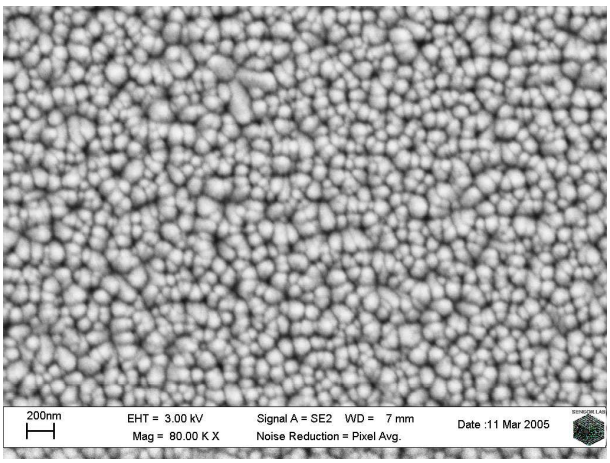

(a) Before thermal treatment.

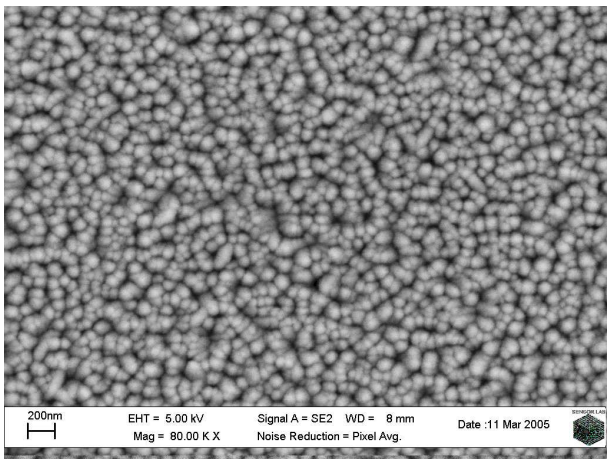

(b) After thermal treatment.

Figure 6.18: SEM Micrograph of non-metallised region 150 nm WO_3 sensing layer deposited on ZnO/36° Y-cut $LiTaO_3$ structure.

to the ZnO layer.

Figure 6.18 shows a micrograph of the 150 nm WO_3 layer deposited over the metallised region of the ZnO/36° Y-cut $LiTaO_3$ structure. Micrographs (a) and (b) were taken prior to and after thermal treatment of the sample, respectively. Acceleration voltage of 3kV and 5kV were used for micrograph (a) and (b), respectively. The SEM micrographs confirm that the WO_3 grain size decreased after exposure to elevated temperature of 300°C for a prolonged period of time during testing procedure. The WO_3 appears to grow in columnar structure on top of the ZnO in a more densely packed fashion than the underlying ZnO film.

6.3.4 SEM Characterisation of WO_3 with Au Catalyst Activator Layer

To improve the gas sensing properties of the WO_3, a metal catalyst activator layer (composing of either Pt or Au) was deposited by planar DC sputterer on top of the WO_3/ZnO/36° Y-cut $LiTaO_3$ structure. It is well known that a metal catalyst loaded on top of a metal oxide surface can significantly improve the performance of a solid-state gas sensor [91, 170, 171]. As mentioned previously in Chapter 5, section 5.4.3, a 6 to 7 nm thick, non-continuous film of Au was deposited on top of the 160 nm WO_3 sensitive layer. The catalyst activated Au–WO_3 sensitive layer, employed on the ZnO/36° Y-cut $LiTaO_3$ structure was characterised using a Philips XL-30 SEM with both SE and BSE detectors. The sample was thermally treated before characterisation. The aggregation effect of the Au layer deposited on WO_3 film is illustrated in the SEM micrographs presented in figure 6.19. The gold particles on the surface produced high contrast dots and can easily be seen as small bright regions on top of the underlying WO_3 structure. Micrographs (b) and (c) were taken using a 20kV acceleration voltage and a spot size of 1.5 and 1.2, respectively. The metallised region of the sample is shown in micrograph (b), while the non-metallised region is shown in (c). As the BSE detector provides information on both sample composition and surface morphology, the surface morphology information obtained needed to be confirmed by a secondary method. Micrograph (a) in figure 6.19, taken with the SE detector confirms that the BSE image (b) is correctly depicting the sample surface in the metallised region of the sample. Micrograph (a) was taken with an acceleration voltage of 20kV and a spot size of 1.5, using the SE detector at the same location. It should be noted that the feature on the left hand side of figures 6.19(a) and (b) was used to focus the microscope and is not considered in the discussion.

The micrographs in figure 6.19 confirm the presence of the gold as a non-continuous film, since the image shows bright dots distributed over the entire surface of the sample. The underlying surface morphology of the ZnO shown in micrographs (c) and (b) appear similar to the micrographs shown in figures 6.16 and 6.18(b), respectively. Attempts were made to characterise the Pt–WO_3 structure, however difficulty was experienced in gaining a focused image due to charging of the sample.

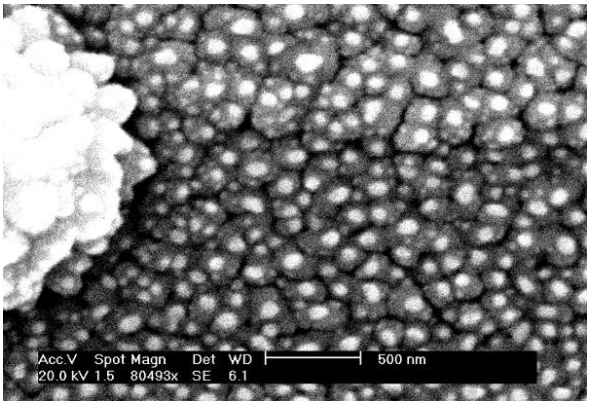

(a) Au-WO_3 on metallised region, taken with SE detector.

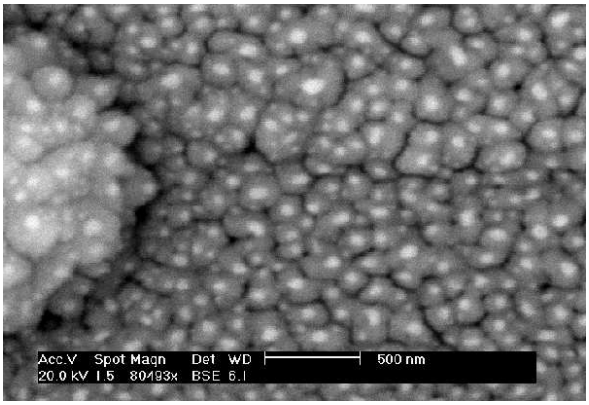

(b) Au-WO_3 on metallised region, taken with BSE detector.

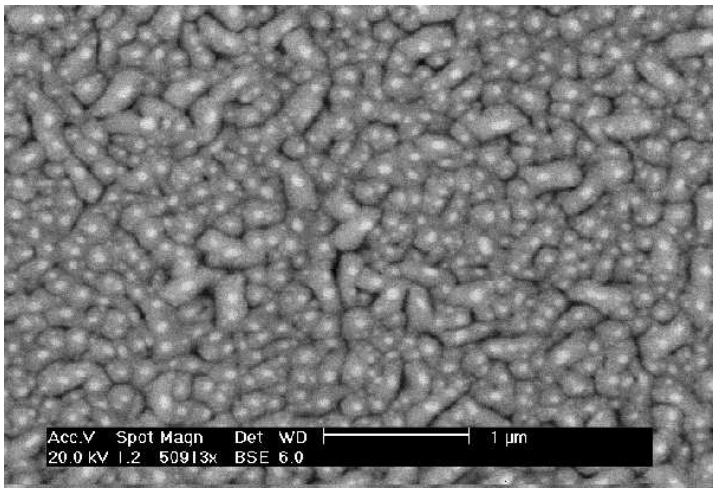

(c) Au-WO_3 on non-metallised ZnO/$LiTaO_3$ structure, taken with BSE detector.

Figure 6.19: SEM Micrograph of Au-WO_3 on ZnO/$LiTaO_3$ structure. Images taken with both SE and BSE detectors.

6.4 Summary

In this chapter, the material characterisation results of the InO_x/ZnO/X-cut $LiNbO_3$ and WO_3/ZnO/36° Y-cut $LiTaO_3$ layered structures were presented. The intermediate ZnO layer was also characterised on the respective substrates. AFM, SEM and XRD techniques were employed to investigate the material characteristics of each layer. To the best of the author's knowledge, this is the first time surface morphology of InO_x/ZnO/X-cut $LiNbO_3$ and WO_3/ZnO/36° Y-cut $LiTaO_3$ layered structures have been presented.

Micro-characterisation of the 1.2 µm thick ZnO intermediate layer by AFM and SEM showed different surface morphology on the metallised and non-metallised regions of $LiNbO_3$ and $LiTaO_3$ substrates. The underlying morphology of the intermediate ZnO

layer was found to highly influence the growth of the subsequent InO_x sensitive layer, directly affecting its grain size and surface area. The effect of prolonged operation at elevated temperature (∼300°C for 24 hours) on the ZnO and WO_3 surface morphology was also investigated by AFM. Additionally, XRD characterisation of the WO_3 and ZnO layer grown on $LiTaO_3$ confirmed that the ZnO grains grow mostly with the *c*-axis parallel to the substrate surface, and that the WO_3 pattern is characteristic to the deposition technique (i.e. RF sputtering).

Key outcomes for the ZnO, InO_x and WO_3 layers can be summarised by the following:

- **ZnO intermediate layer:**
  - The $LiNbO_3$ and $LiTaO_3$ substrates strongly influence the initial growth of the 1.2 µm thick ZnO intermediate layer, resulting in a significantly different surface morphology between the metallised and non-metallised regions of the respective substrate materials.
  - The average grain size of the ZnO layer on the ZnO/$LiTaO_3$ structure was shown to increase after thermal treatment. However, the RMS surface roughness was shown to increase in the non-metallised regions of the sample and slightly decreased in the metallised regions.
  - The surface morphology of the ZnO layer deposited on the X-cut $LiNbO_3$ substrate was observed to be more homogenous and compact on the non-metallised region, when compared to the metallised region of the sample. On the other hand, a more homogenous and compact ZnO surface morphology was observed in the metallised region of the 36° Y-cut $LiTaO_3$ substrate, as the ZnO was shown to grow with the *c*-axis parallel to the $LiTaO_3$ substrate surface.
- **InO_x sensitive layer:**
  - The 40 nm InO_x sensitive layer deposited over the ZnO/X-cut $LiNbO_3$ structure, exhibits surface morphology features with facets comparable with the rather rough topography of the underlying ZnO layer. This was confirmed by the vast differences in growth of InO_x sensitive layer on the ZnO/X-cut $LiNbO_3$ structure and silicon substrate.
  - For example, the RMS surface roughness of the InO_x layer on the silicon substrate was observed to be 0.610 nm. In comparison, the roughness of

the same 40 nm thick InO_x film deposited over the layered SAW structure was observed to be 10.12 and 27.03 nm for the non-metallised and metallised regions, respectively.

- After the InO_x sensitive layer deposition, the layered structures' surface morphology shows well defined grain boundaries in both the metallised and non-metallised regions of the samples. An increase in RMS roughness was observed in both the metallised and non-metallised regions after the 40 nm InO_x layer deposition. This suggests that the deposition of the InO_x layer and the thermal treatment process improved both the ZnO and InO_x layers' crystallinity.
- SEM characterisation revealed that the underlying ZnO grain boundaries also influence the 200 nm InO_x sensitive layer. The surface topography of the metallised region was observed to exhibit deeper, larger grain boundaries, while the non-metallised region exhibited a more compact, smoother texture.

- **WO_3 sensitive layer:**
  - The 'as deposited' WO_3 sensitive layer on the ZnO/36° Y-cut $LiTaO_3$ structure showed only a marginal difference in surface morphology features between the metallised and non-metallised regions of the sample. This demonstrated that the WO_3 layer is only marginally influenced by the underlying surface morphology of the ZnO layer.
  - After thermal treatment, a noticeable difference in the surface morphology of the WO_3 layer occurs between the non-metallised and metallised regions of the sample.
  - The average surface grain size of the WO_3/ZnO/36° Y-cut $LiTaO_3$ structure decreases in both the metallised and non-metallised regions of the sample after thermal treatment. However, in both the metallised and non-metallised regions, the RMS roughness was observed to increase after prolonged operation at elevated temperature.
  - AFM characterisation clearly shows that the shape of the WO_3 grains become well defined and an increase in surface area occurs after the thermal treatment, suggesting an improvement in WO_3 crystallinity.
  - The SEM micro-characterisation of the Au-WO_3/ZnO/36° Y-cut $LiTaO_3$ structure confirmed that the Au catalyst activator layer forms a non-continuous

film on the WO_3 surface.

It can be concluded that the surface morphology of the InO_x/ZnO/X-cut $LiNbO_3$ and WO_3/ZnO/36° Y-cut $LiTaO_3$ structures exhibit very different characteristics. AFM imaging shows the presence of well formed and well defined regular crystalline structures within the ZnO, InO_x and WO_3 layers. The prolonged operation at elevated temperature was found to cause surface morphology modifications in the ZnO, InO_x and WO_3 layers. Characteristics such as grain size, RMS surface roughness and the size of the surface features were influenced. Thermal treatment resulted in the sensitive layers' grain boundaries becoming more defined, which is particularly visible in the dramatic change in WO_3 grain shape, which suggests an improvement in surface crystallinity. The unique surface morphology effects observed can be attributed to the layered configuration. Effects of the device operating temperature regarding gas sensing properties of the InO_x and WO_3 sensitive layers will be further discussed in Chapter 8.

[This page is left blank intentionally.]

Chapter 7

Experimental Gas System Design

In this chapter, the measurement setup and testing procedures for the layered SAW gas sensing experiments are outlined. To test the performance of the designed multilayered SAW sensors, a custom built SAW test system was developed. The test system consisted of a gas chamber and amplifier assembly, which were both thermally and electrically shielded. Additionally, a computer controlled gas calibration setup with sequence control and data acquisition software was co-developed to automate the gas sensing experiments.

The gas calibration system and procedures presented herein were used by the author during the experimental gas sensing work conducted at both the Sensor Technology Laboratory at RMIT University, Australia and the Gas Sensing Labortory at The University of Brescia, Italy.

Section 7.1 introduces the measurement techniques employed to detect the change in SAW velocity during the gas sensing experiments. Both phase and frequency measurement techniques are discussed.

Section 7.2 describes the RF amplifier circuit designed and employed for the frequency measurement technique. The computer simulation and the measured frequency response of the RF amplifier circuit are presented.

Section 7.3 describes the computer controlled gas calibration system used to conduct the gas sensing experiments. The custom built SAW system consistes of a gas chamber, amplifier assembly and a computer controlled gas delivery system. Additionally, the gas pulse delivery and data acquisition software used in the gas sensing experiments are also outlined.

Section 7.4 provides a brief summary of this chapter.

7.1 SAW Measurement Techniques

Changes in SAW velocity can be measured by phase and frequency techniques. A common phase measurement technique involves applying an RF signal of fixed frequency to the input IDT of the SAW device and measuring the output signal with a vector voltmeter. The input signal is provided by a frequency generator and the vector voltmeter measures both the phase and magnitude of the transmission response. This technique has been well documented by Galipeau et al. [39] and offers high stability that can yield attenuation information at a given frequency; however specialised and expensive laboratory equipment is required.

An alternative phase measurement technique involves measuring the transfer function of the SAW device with a two port network analyser, as shown in figure 7.1. In this case, the network analyser functions as a combined source and vector voltmeter, measuring the amplitude and phase as a function of input frequency. Measurement of scattering

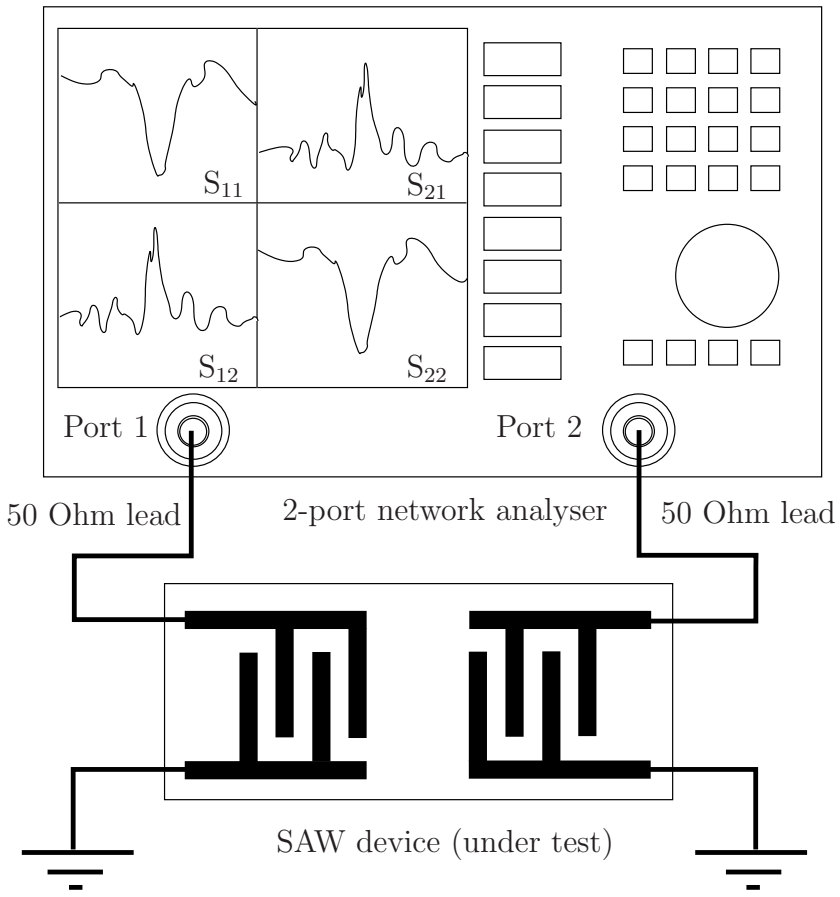

Figure 7.1: Experimental setup for measuring SAW phase velocity and attenuation using a network analyser.

parameters (s-parameters: S_{11}, S_{21}, S_{12}, S_{22}) allows determination of both phase velocity and attenuation of the SAW device over a given frequency range. A major advantage of this approach is that it allows a complete electrical analysis of the acoustic sensor under most conditions, including ones for which other methods like oscillator circuits and vector voltmeters have failed [44]. Frequency sweeps can be made periodically during the experiment to extract the sensor response as a function of time. Furthermore, results can be calculated to yield useful information such as device admittance, impedance and transmission loss at any chosen frequency. Similar to the first technique, it provides a stable platform for analysis, however it also requires a specialised and expensive network analyser setup. Examples of phase and amplitude (or attenuation) measurements include the original work of Wohltjen et al. [3] and Falconer et al. [172]. Further information can be found in textbooks such as [36]. Such measurements were made by the author during the fabrication process presented in Chapter 5 section 5.5 and during the experimental gas sensing procedures (under test conditions), presented in Chapter 8. All measurements were performed with a Rohde & Schwarz ZVRE network analyser using 50Ω calibrated leads.

The second method to measure changes in SAW velocity is via the frequency technique. For the frequency technique, the SAW device is used as the frequency control element in a closed loop oscillator circuit. The SAW device functions as a positive feedback element along with a RF amplifier as shown in figure 7.2. Initially, the small voltage appearing at the input of the RF amplifier is amplified and fed back through the SAW device. The SAW device transmits the signal with some delay (dependent on the substrate velocity, delay path length, IDT geometry, etc.) before it appears at the amplifier input. Subsequently, the signal is re-amplified and reappears at the SAW input terminal, resulting in an alternating signal that will be self-sustaining; thus forming an oscillator. The circuit will oscillate providing that the total loop-gain exceeds unity (under small signal conditions) and the phase of the loop-gain is an integer multiple of 2π [36]. Further discussion regarding oscillator principles will be discussed in section 7.2.

A major advantage of using the frequency technique to measure the change in SAW velocity is that it requires cheaper equipment when compared to phase measurement setups. Additionally, the measured frequency resolution is limited to that of the frequency counter, which is much higher than that of a network analyser. Furthermore, the system can be made completely independent from laboratory equipment (eg. network analysers, frequency generators, vector voltmeters and even the frequency counter), by

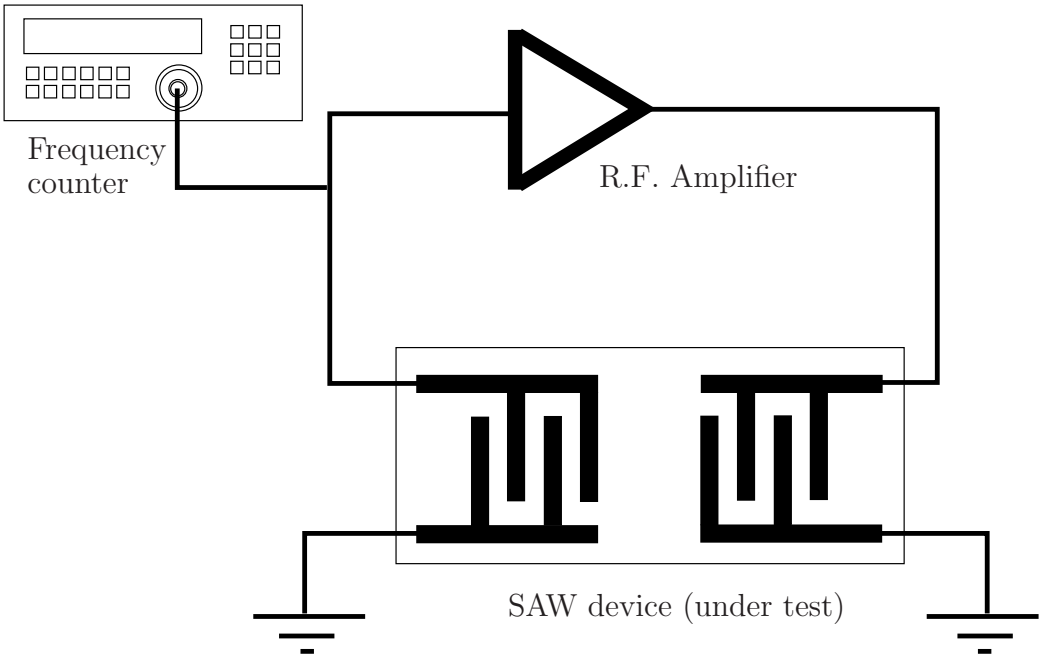

Figure 7.2: Experimental setup for (indirectly) measuring SAW phase velocity using a oscillator and frequency counter.

employing a simple microprocessor to measure the oscillation frequency – essential for commercialisation purposes and making the system a truly inexpensive and portable unit.

Frequency measurements for each of the layered SAW structures were made by the author during the experimental gas sensing procedures, presented in Chapter 8. A high-resolution, 10 digit counter (Fluke PM6680B) was used to measure the oscillation frequency.

7.2 Design and Implementation of the Amplifier

The main requirement of the RF amplifier is to obtain enough forward power gain to overcome the losses of the SAW delay line, whilst minimising noise. It should also be stable so that the amplifier does not self-oscillate. The system noise over the short term also needs to be minimised and kept well below the minimum frequency change induced by a sensing interaction. Furthermore, the input and output impedance of the amplifier should be closely matched to impedance of the SAW device, to maximise system efficiency.

The basic principles of the measuring system is well known [36, 173, 174]. The oscillation frequency of the system must satisfy the following relationship [175]:

$$\Phi_A + \Phi_c + 2\pi f\tau = 2\pi n \qquad , \tag{7.1}$$

where n is an integer and gives the number of the frequency mode, Φ_A and Φ_c are the phase shifts introduced by the amplifier and gas chamber electrical connections, respectively; and τ is the delay of the signal in the acoustic path of the SAW device. From equation (7.1), the oscillator frequency f must satisfy:

$$f = \frac{2\pi n - \Phi_e}{2\pi l}\, v \qquad , \tag{7.2}$$

where v is the velocity of propagation of the acoustic wave on the piezoelectric waveguide surface, l is the centre-to-centre spacing between the IDTs and the total loop phase given by $\Phi_e = \Phi_A + \Phi_c$. Φ_e can be considered constant if the amplifier is working in stable conditions, holding the following relationship plausible (assuming negligible dispersion):

$$\frac{\Delta f}{f_0} \cong \frac{\Delta v}{v_0} \qquad , \tag{7.3}$$

where Δv is the change in SAW velocity, f_0 and v_0 are the unperturbed oscillation frequency and SAW velocity, respectively. Although the advantages of the frequency technique include higher sensitivity with a less expensive setup and equipment, oscillator instability can be a problem [39]. This is further compounded by the physical and environmental issues associated with chemical sensing applications. Operation at elevated temperature upto 300°C and the non-ideal electrical terminations (impedance mismatch) imposed by the gas chamber significantly degrade system stability.

Depending on the thickness of each layer, the existence of higher order modes can pose both desired and undesired implications. The higher order modes may provide more sensitive, higher operating frequencies or the flexibility to choose an operating mode with desired characteristics for the particular sensing application. However, for an oscillator configuration, it is usually desirable to have a single operating frequency at which the system will reliably begin oscillation [37], reducing the chance of 'mode-hopping'. This can be achieved by ensuring that only one mode satisfies the oscillation condition of positive total gain when placed in line with the amplifier, and choosing the appropriate layer thicknesses during the design process.

Other considerations such as random noise effects are much more difficult to minimise, since the phenomena causing these fluctuations are still not well understood [37]. A

great deal of work has been done to characterise oscillator noise for applications such as communications and radar systems [176], however this work is focused on signal processing applications.

To overcome these difficulties the author found it necessary to design a flexible system that could be easily configured to accommodate the different layered SAW device structures investigated throughout the course of this research program. It was therefore necessary to design a high gain RF amplifier and a gas chamber allowing for RF electrical connections that could be easily configured with the appropriate total loop phase (Φ_e), for stable operation.

7.2.1 RF Amplifier Design and Simulation

The amplifier was designed and simulated using Agilent ADS computer software. The in-built *s*-parameter facility was utilised, thus ensuring that the respective input and output ports of the amplifier and SAW device were impedance matched. The amplifier consisted of three stages, as seen in figure 7.3. The first two stages provided the forward power gain (between 25 and 30dB), while the last stage functions as a buffer with a unity gain. The buffer stage was employed to increase the over all stability factor calculated by the Agilent ADS software.

Special low noise, high gain bipolar NPN RF transistors (Infineon BFS481) were employed for each stage. The BFS481 packages contained two balanced pair transistors, of which one IC package was used for each stage. The two high gain stages were biased using a common

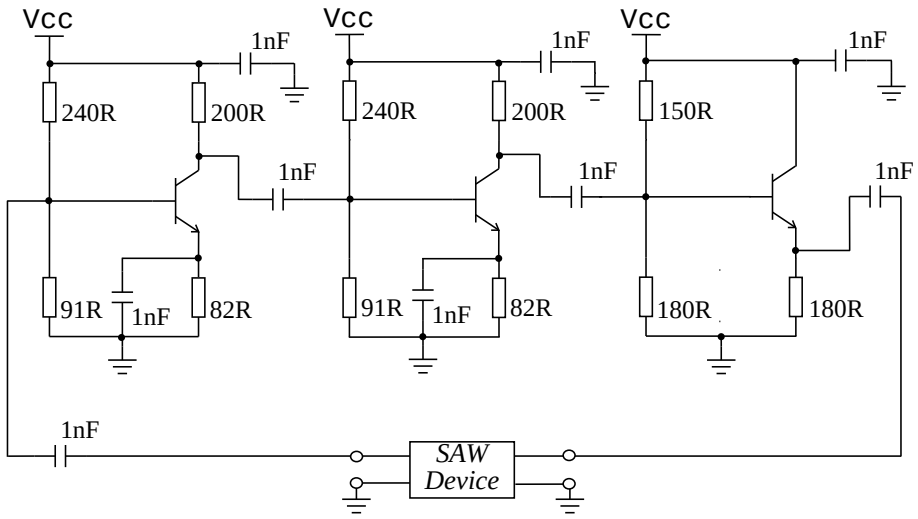

Figure 7.3: Three stage RF amplifier schematic.

emitter arrangement and a common collector (emitter follower) was used for the buffer stage. The remaining transistor in each of the three IC packages were used to form an identical amplifier circuit, thus allowing the system to be extended to facilitate differential measurements with nearly indistinguishable amplifier characteristics. Figure 7.4 shows both the back and front sides of the printed circuit board (PCB). The three Infineon packages are the small ICs shown on the right side in figure 7.4(b). The subsequent IC packages are the voltage regulator and the differential frequency mixer. The blue connectors provides the electrical connection between the layered SAW sensors and the amplifier circuit. The PCB allows two SAW sensors to be connected to the upper and lower row of connectors.

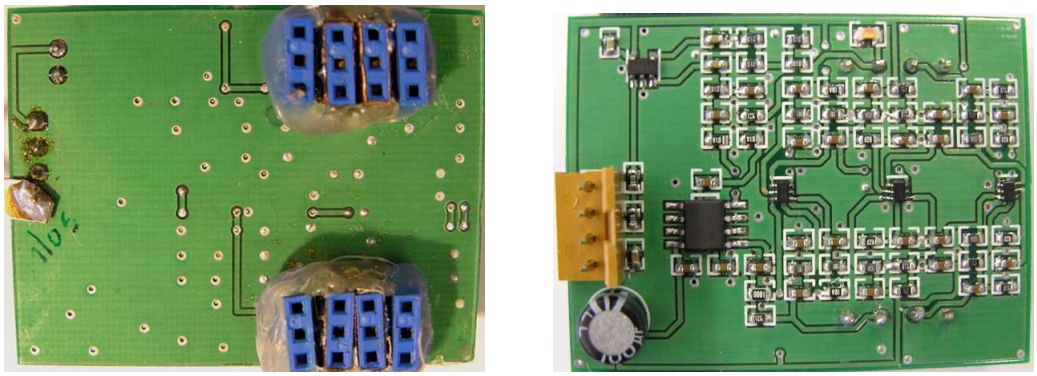

(a) Front (b) Back

Figure 7.4: Amplifier PCB.

Figure 7.5 shows the simulated and measured transmission response (S_{21}) of amplifier. The response was measured using the Rohde & Schwarz (ZVRE) network analyser using 50Ω leads. A specially made carrier board provided the electrical connection between the network analyser leads and the amplifier PCB. Good agreement between the measured and simulated results is shown over a 100 MHz range. The discrepancy in the gain can be attributed to loss induced by the carrier board used to make the measurements.

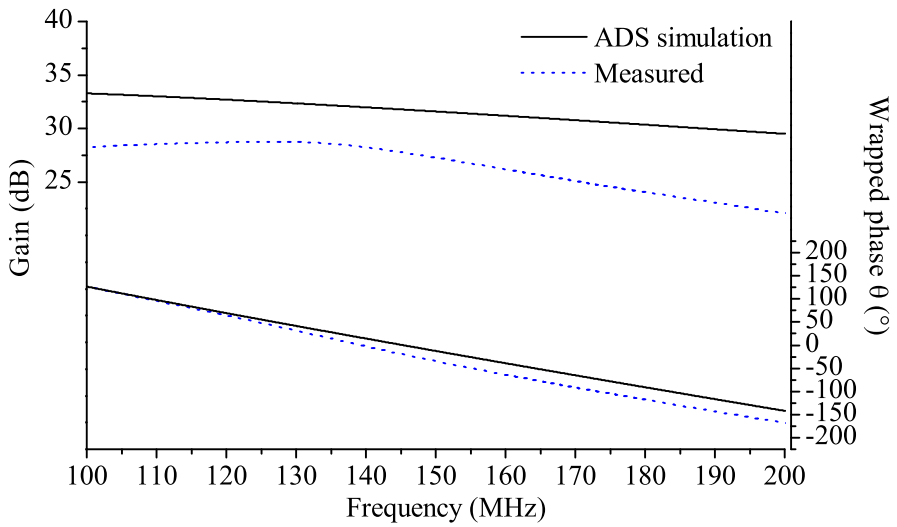

Figure 7.5: Comparison of measured and simulated RF amplifier.

7.3 Layered SAW Gas Calibration System

In parallel with the fabrication of the layered SAW sensors, which was described in Chapter 5, a custom built multi-channel gas calibration system was developed to facilitate the gas sensing experiments. The system was utilised to test the performance of the layered SAW sensors towards different gas analytes at various concentrations, operating temperatures and relative humidity (RH) levels. The experimental results for each of the investigated layered SAW structures are presented separately in Chapter 8.

7.3.1 Gas Delivery

To ensure the integrity of the gas sensing experiments, the SAW system and gas calibration setup were required to adjust environmental conditions essential to investigate the sensors' behaviour. The multi-channel gas calibration setup was based on volumetric mixing of gases with 4 mass flow controllers (MFCs). Certified gas cylinders of high purity synthetic air (zero-air) and low concentration analyte gas (balanced in synthetic air) were purchased. Each cylinder was connected to the computer controlled MFCs, which were used to produce a total constant flow of 200 SCCM (unless otherwise specified). By adjusting the flow rates of each MFC, the analyte gases could be further diluted in synthetic air, while maintaining a constant flow rate.

Figure 7.6 shows a diagram of the complete multi-channel gas calibration system. A MFC control processing unit, four MFCs, two computers, a temperature logger, a frequency

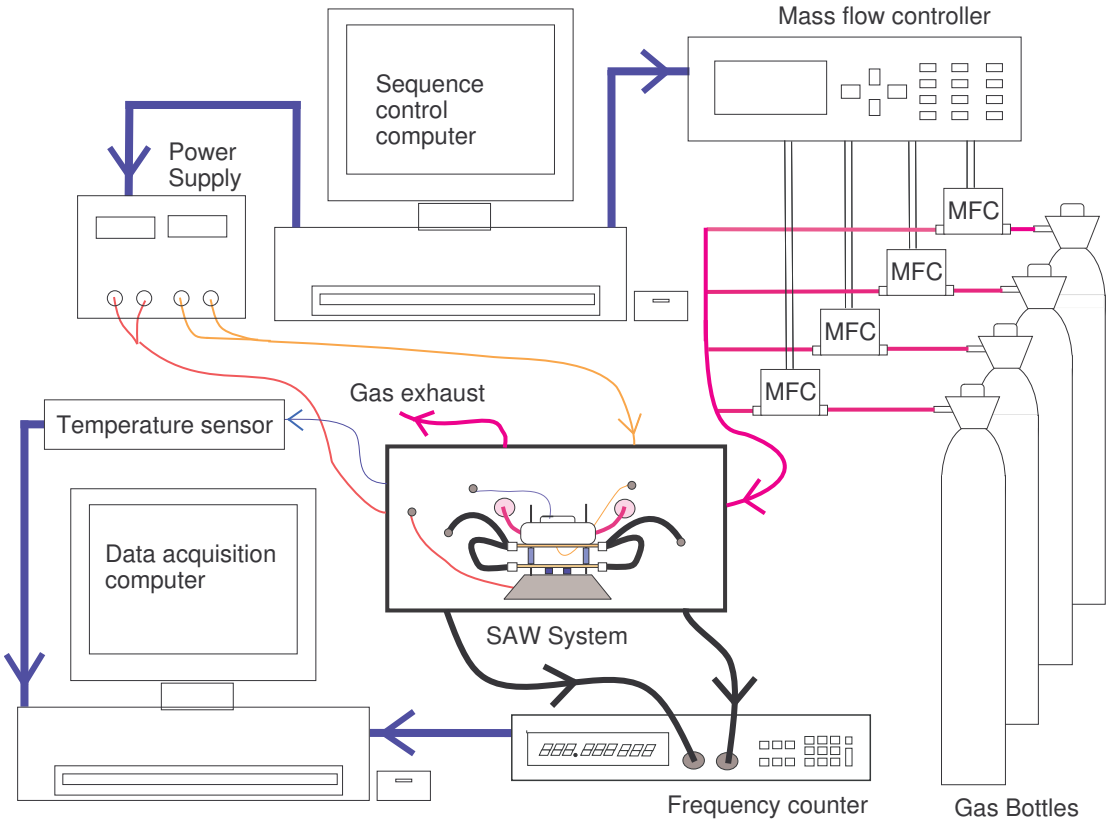

Figure 7.6: Diagram of layered SAW multi-channel gas calibration setup.

counter and a 2-channel DC power supply were employed. The custom built SAW system, used to integrate the gas chamber, layered SAW device and amplifier assembly is shown to be at the heart of the gas calibration setup.

7.3.2 The SAW System

As previously mentioned, the SAW system was required to be a flexible unit that could accommodate for the phase and gain requirements of each of the layered SAW structures investigated. Figure 7.7 shows the gas chamber and amplifier assembly inside a thermally shielded steel box. The steel box was especially chosen for its additional EMI shielding properties. During the actual experiments, further thermal stability was provided by placing the unit in an environmental chamber, holding the ambient temperature at 22°C. Figure 7.8 shows a close-up picture of the amplifier and gas chamber assembly. The amplifier PCB (not visible) is mounted in the machined aluminium block supporting the structure. Two carrier PCB boards (one for the gas chamber and the other for the amplifier) are shown to be connected by RF coaxial leads with different lengths. The

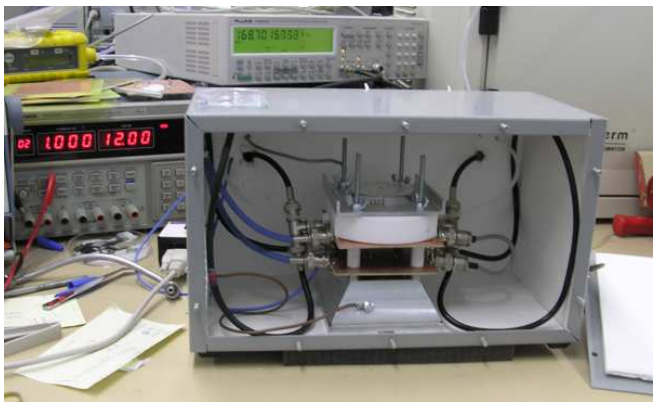

Figure 7.7: SAW test system used to integrate the gas chamber, layered SAW sensor and amplifier assembly with the multi-channel gas calibration setup. The insulated metal provides both thermal and EMI shielding.

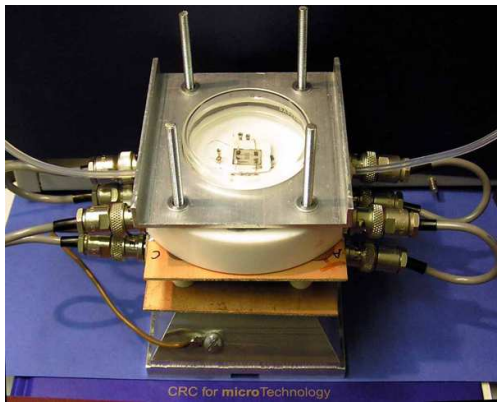

Figure 7.8: Custom built testing chamber and amplifier assembly.

different length coaxial leads were used to vary the total loop phase (Φ_e). Stable oscillation was achieved by choosing coaxial leads which satisfied the total loop-gain condition of unity or higher with a phase multiple of 2π. The author found that by measuring the SAW device in-suite with a network analyser reduced the uncertainly in choosing coaxial leads with the correct length.

7.3.3 The Gas Chamber

Figure 7.9 shows the 20mm thick machined Teflon block and fuzed quartz lid that form the gas chamber. The total chamber volume is approximately 30mm^2. A layered SAW sensor is shown inside, mounted on an planar alumina micro-heater. Operating temperature was controlled up to 300°C by the external regulated DC power supply. The aluminium mounting clamp, which is guided by the four metal posts, clamps the fuzed quartz lid onto a Viton O-ring to form an air-tight seal. The chamber is able to accommodate two, 2-port SAW device simultaneously, however this capability was not utilised in this work.

Figure 7.10 shows the two types of micro-heaters employed throughout this research program. The first was a platinum serpentine resistive element, formed on a 10×12mm sapphire substrate. Details of similar heating elements can be found in [19]. Unfortunately, due to the small size of the sapphire substrate, the SAW devices were found to fracture due to non-uniform heat distribution, thus limiting the operating temperature to approximately 270°C. To overcome this limitation a 25×25mm alumina substrate was used to form a larger heater. An evaporated composite Ni/Cr layer was used to form

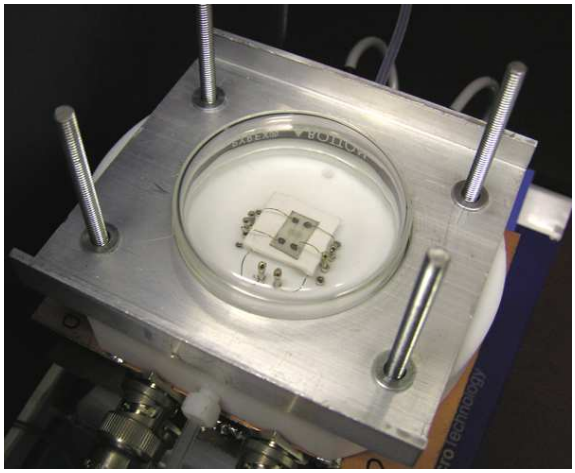

Figure 7.9: Teflon based gas chamber with fuzed quartz lid and aluminium clamp. Alumina heater and single delay line layered SAW device can be seen inside.

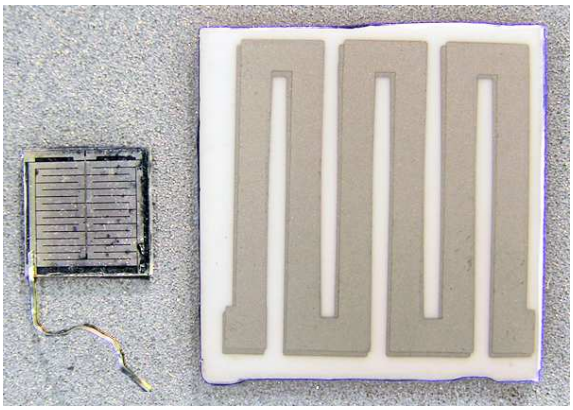

Figure 7.10: Substrate heaters. *Left* – sapphire substrate heater. *Right* – alumina substrate heater.

the serpentine resistive element (with a non-linear resistance of 150–220Ω). The larger alumina heater was found to have better heat distribution and provided a maximum operating temperature of approximately 330°C when 38V DC was applied.

7.3.4 Testing Procedure

Table 7.1 lists the analyte gas concentrations tested throughout this research program. Both reducing and oxidising gas species were used to characterise the performance of the layered SAW sensors' sensitivity towards conductivity based perturbations at the surface. Each layered SAW sensor was tested at several operating temperatures between room temperature and 300°C; typically in steps of 20 to 30°C. A sequence control computer was used automate both the operating temperature and the pulse sequence of varying analyte gas concentrations.

Table 7.1: Analyte gas pulse concentrations at 200 SCCM flow rate, balanced in synthetic air.

Analyte gas	Pulses					
	1^{st}	2^{nd}	3^{rd}	4^{th}	5^{th}	6^{th}
H_2	0.06%	0.12%	0.25%	0.50%	1.00%	0.12%
NO_2	510 ppb	1.06 ppm	2.12 ppm	4.25 ppm	8.50 ppm	1.06 ppm
Ethanol	10 ppm	25 ppm	50 ppm	250 ppm	500 ppm	–

The delivered NO_2 and H_2 gas concentration pulse sequences ranged from 500 ppb to 8.5 ppm and from 0.06 to 1.00% in synthetic air, respectively. Ethanol vapour balanced in synthetic air ranged from 10 to 500 ppm. The synthetic air composed of 20% oxygen

balanced in nitrogen (99.999% pure). At each operating temperature, the baseline gas was maintained for a minimum period of 90 minutes to allow the oscillation frequency to stabilise. The layered SAW sensors were then exposed to different concentrations (pulse) of the analyte gas. The sensors were repeatedly tested at each operating temperature for a minimum of 6 hours. This process was repeated for up to several weeks at a time. Figure 7.11 shows one typical pulse sequence used to deliver the NO_2 and H_2 gas concentration at each operating temperature. t_e and t_p are the exposure and purge time, respectively. During the purge time the gas chamber was flushed with synthetic air, allowing the sensitive layer to return to is baseline conductivity value (sometimes termed the 'recovery' period). For NO_2 and H_2 gas pulses, a typical exposure time of 180 to 240 seconds was utilised. The typical purge time was between 360 and 900 seconds. Longer exposure and purge times were used for sensors with slower response and recovery. For example, all ethanol vapour pulses had a 20-minute exposure and 40-minute purge time.

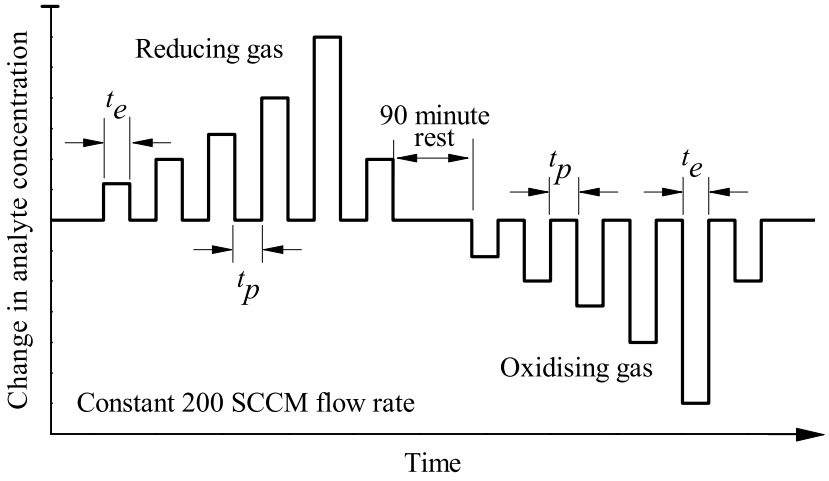

Figure 7.11: Analyte pulse sequence.

7.3.5 Relative Humidity System

The effects of different relative humidity (RH) conditions were investigated by the author during the research period conducted at The University of Brescia, Italy. A computer controlled gas calibration system similar to that created by the author was used in conjunction with a RH generator. All measurements regarding ethanol sensing and RH conditions were conducted with an ambient temperature of 20°C, however the layered SAW devices were operated at elevated temperatures between 100 and 300°C.

RH conditions were systematically changed between 0, 25 and 50% at each operating temperature. Figure 7.12 shows the basic diagram of the RH setup used. An air bubbler was employed to saturate the carrier gas with H_2O vapour. By adjusting MFC's flow rate, a partially saturated carrier gas was mixed with the analyte stream.

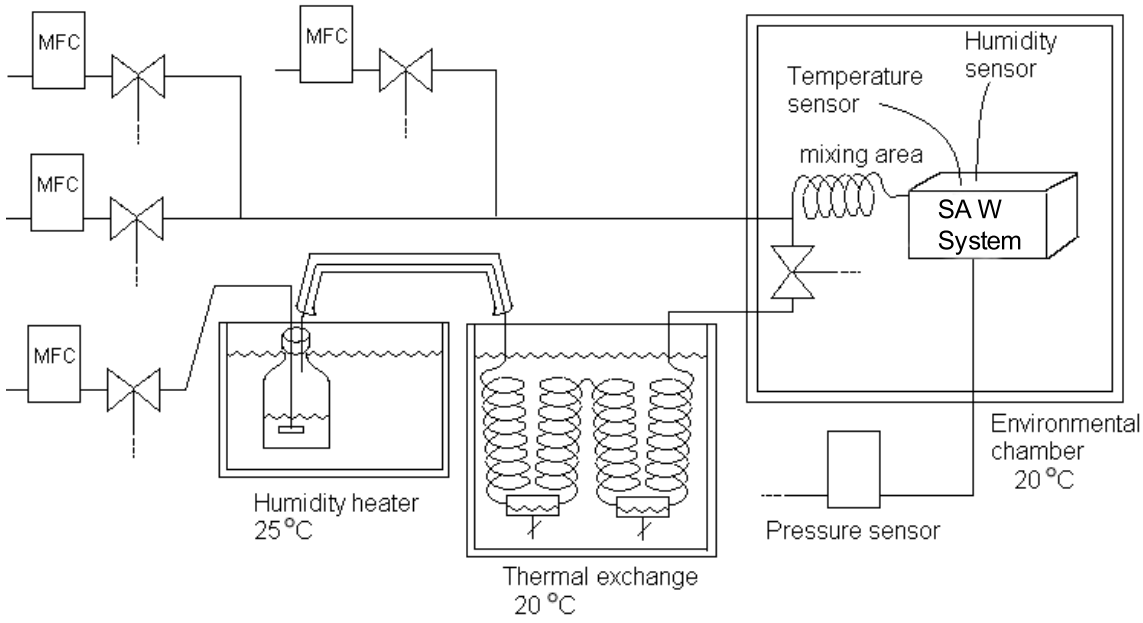

Figure 7.12: Block diagram of experimental setup used to provide the different RH conditions.

7.3.6 Data Acquisition

Custom written Labview 6.0 software was co-developed to log data from the Fluke (PM6680B) frequency counter. Data was collected by the computer via a GPIB IEEE-488 bus connection. Figure 7.13 shows a screen shot of the software. The program logged the oscillation frequency and displayed the acquired data in real time via a graphical user interface. The software enabled the author to control the data acquisition rate, frequency counter settings and graphical display options.

7.4 Summary

This chapter presented the measurement system and setup for the layered SAW gas sensing experiments conducted by the author at both RMIT University, Australia and The University of Brescia, Italy.

Both the phase and frequency measurement techniques used by the author to measure

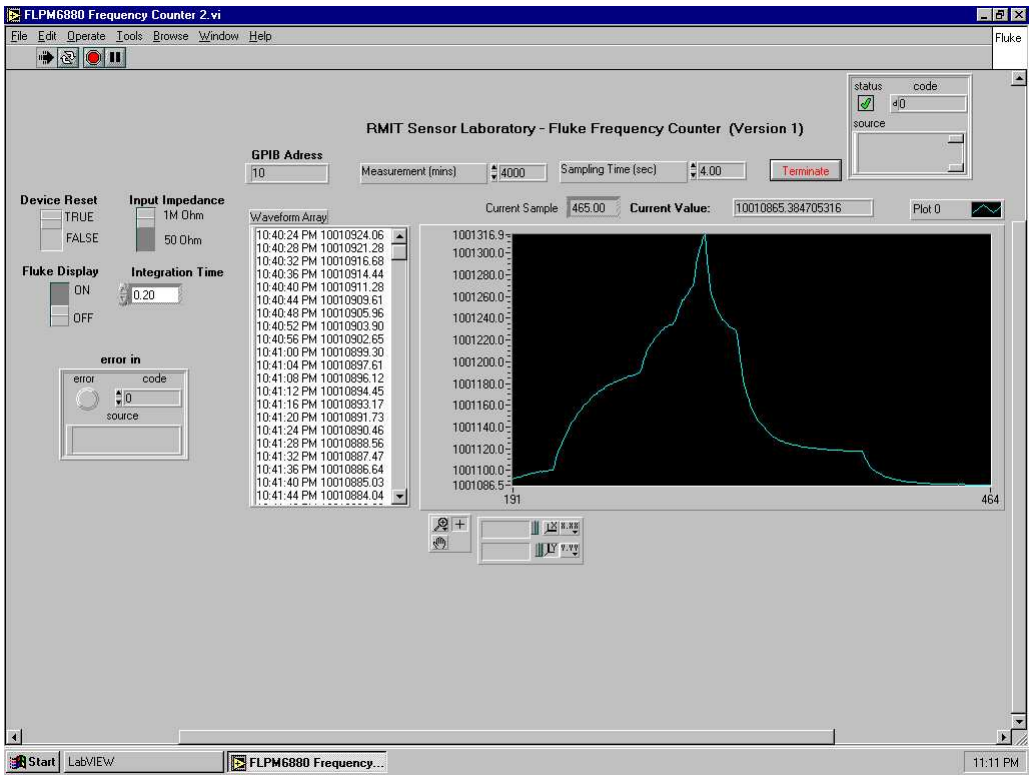

Figure 7.13: Screen shot of frequency counter acquisition software.

changes in SAW velocity were described. The design and simulation of an RF amplifier was also presented, which forms part of the closed loop oscillator circuit. Additionally, the custom built SAW test system, used to integrate the gas chamber, layered SAW device and amplifier assembly with the computer controlled gas calibration setup was detailed.

The testing procedures employed to characterise the layered SAW structures for conductivity based surface perturbations were also outlined. Furthermore, the RH system, sequence control and data acquisition software, as well as the gas pulse sequences used during the gas sensing experiments were also detailed.

The experimental results obtained using the system setup and procedures defined in this chapter will be presented in Chapter 8.

Chapter 8

Results – Experimental Gas Sensing

In this chapter, the gas sensing performance of the layered SAW device structures, proposed by the author in Chapter 4 are experimentally evaluated. The three primary layered SAW structures investigated are:

InO_x/ZnO/XY $LiNbO_3$
employing a 40 nm InO_x sensitive layer
and a 1.2 µm intermediate ZnO layer,

InO_x/ZnO/XZ $LiNbO_3$
employing 40 and 200 nm InO_x sensitive layers
with a 1.2 µm intermediate ZnO layer,

WO_3/ZnO/36° YX $LiTaO_3$
employing a 150 and 160 nm WO_3 sensitive layers
with a 1.2 µm intermediate ZnO layer. Furthermore,
160 nm WO_3 with non-continuous Pt and Au catalyst
activator layers will also be investigated.

Utilising the computer controlled gas calibration system and the experimental measurement setup outlined in Chapter 7, each of the above structures was tested towards different H_2 and NO_2 gas concentrations. In the case of the WO_3/ZnO/36° YX $LiTaO_3$ structure employing the 150 nm WO_3 sensitive layer, the author investigated its response towards ethanol vapour at different concentrations, operating temperatures and relative humidity (RH) conditions during the research fieldwork conducted at The University of Brescia, Italy.

This chapter outlines the phase and frequency measurement results obtained by the author in the experimental gas sensing component of this research program. The results highlight the high sensitivity provided by the multilayered configuration proposed by the author, compared to the structures discussed in Chapter 2 (table 2.1). Frequency measurements and perturbed transmission responses (S_{21}), when exposed to the gas analyte are presented for each of the proposed layered SAW structures.

Section 8.1 presents the preliminary experimental results verifying that the chosen intermediate ZnO layer thickness of 1.2 µm is justified. Results were obtained by using several WO_3/ZnO/36° YX $LiTaO_3$ layered SAW structures employing different intermediate ZnO layer thicknesses. The results correlate well with the calculations presented in Chapter 4.

Section 8.2 shows the experimental gas sensing results with the InO_x/ZnO/XY $LiNbO_3$ layered SAW structure exposed to different concentrations of H_2 and NO_2 gas. The structure was observed to exhibit highly repeatable responses towards H_2 gas concentrations below 1.00% in air. Both the frequency and phase measurement techniques are employed to evaluate the performance of the structure.

Section 8.3 presents the gas sensing results of the layered InO_x/ZnO/XZ $LiNbO_3$ SAW structures. These results highlight the different response magnitudes obtained for the 40 and 200 nm thick InO_x sensitive layers. Furthermore, the difference in sensitivity between the Rayleigh and SH-SAW modes supported by the ZnO/XZ $LiNbO_3$ structure is extensively discussed.

Section 8.4 shows the experimental gas sensing results of the WO_3/ZnO/36° YX $LiTaO_3$ SAW structure, employing the 160 nm WO_3 sensitive layer, towards H_2 and NO_2. Additionally a 150 nm thick WO_3 sensitive layer is investigated towards ethanol concentrations below 500 ppm in air. The effect of operating temperature and RH conditions is presented in section 8.4.4.

Finally, section 8.5 presents the sensitivity enhancements due to the addition of Pt and Au catalyst activator layers. The catalyst activator layers are studied on the WO_3/ZnO/36° YX $LiTaO_3$ layered SAW structure.

Section 8.6 provides a summary of the experimental findings presented in this chapter.

8.1 Intermediate ZnO Layer Thickness

As an important preliminary experiment, the effect of the intermediate ZnO layer thickness on response magnitude is investigated. As previously mentioned in Chapter 4, the ZnO intermediate layer affects SAW properties such as: phase velocity (v), electromechanical coupling (K^2), permittivity (ε_p) and polarisation (wave type). In section 4.4, theoretical calculations revealed that an optimal ZnO layer thickness is required to maximise the conductivity based sensitivity of each of the investigated layered SAW structures.

In this section, the author presents the experimental results, demonstrating that the response magnitude of the WO_3/ZnO/36° YX $LiTaO_3$ layered SAW structure can be optimised by adjusting the thickness of the intermediate ZnO layer, and hence the velocity-permittivity product of the supported SAW mode. Four similar SAW devices were fabricated with different ZnO intermediate layer thickness: 0.1, 0.5, 1.0 and 2 µm. Additionally, a fifth device was fabricated without the ZnO intermediate layer. All devices were deposited with a 160 nm thick WO_3 sensitive layer (as described in Chapter 5 section 5.4.2.1 and shown in figure 5.4(d)).

8.1.1 ZnO Layer Thickness vs. Device Sensitivity

A modified testing procedure (than the one described in Chapter 7), using a repetitive pulse sequence of 0.50 and 1.00% H_2 concentration was employed to test the performance of each structure. Each H_2 pulse had an exposure and purge time of 180 and 380 seconds, respectively. An example response to such a sequence is shown in figure 8.1, which is for the device with a 1.0 µm thick ZnO intermediate layer at an operating temperature of 330°C. Frequency shifts of 20.6 and 26.56 kHz were observed for 0.50 and 1.00% H_2 concentrations, respectively. At this operating temperature the device exhibited a non-linear response magnitude towards the 0.50 and 1.00% H_2 concentrations. Therefore, in order to test the 4 layered SAW devices at an operating temperature where the response is most linear, all tests thereafter were conducted at 225°C. The final results are presented in figure 8.2, which shows the observed frequency shifts against intermediate ZnO layer thickness. All structures were observed to exhibit an approximately linear response magnitude towards H_2 at the lower operating temperature. A maximum response magnitude towards 1.00% H_2 occurs when the ZnO layer thickness is 1.0 µm thick. Although the response magnitude towards 0.50% H_2 is largest for the structure without

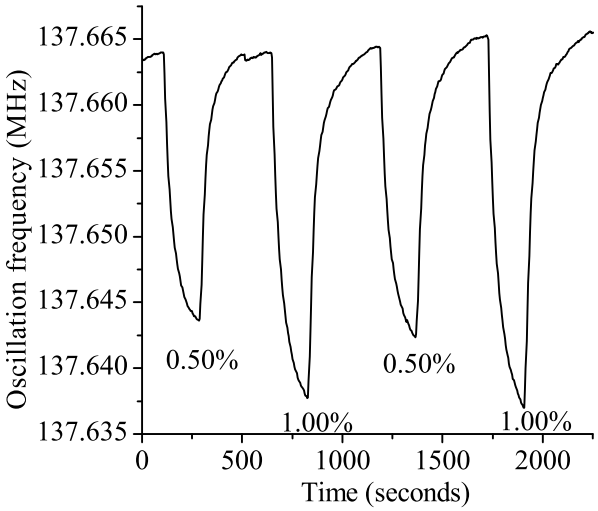

Figure 8.1: Oscillation frequency shift of layered SAW structure with 1.0 µm thick ZnO, towards 0.50 and 1.00% H_2 pulse sequence.

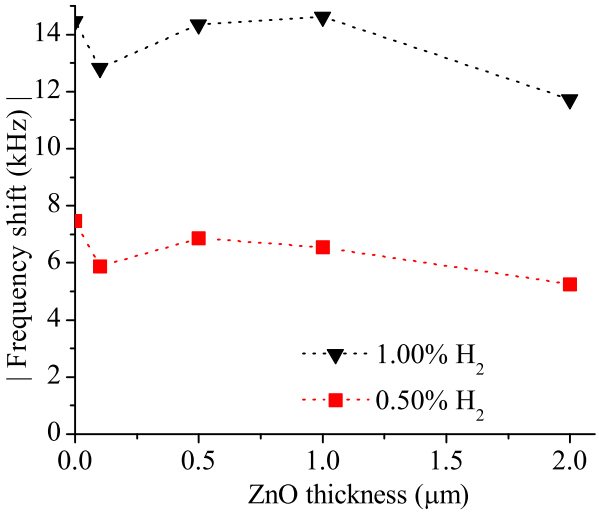

Figure 8.2: Oscillation frequency shift vs. ZnO intermediate layer thickness when exposed to H_2.

the ZnO intermediate layer, it does not fit with the general pattern of the layered devices. The most likely explanation is the different growth characteristics of the WO_3 sensitive layer on the polycrystalline ZnO as opposed to its growth on the polished single crystal $LiTaO_3$ substrate. Therefore, to make a meaningful comparison, only the layered devices are considered here.

The results presented in figure 8.2 demonstrate that the response magnitude is a function of ZnO thickness. This was earlier predicted by the theoretical sensitivity calculation of the layered ZnO/36° YX $LiTaO_3$ SAW structure shown in Chapter 4, figure 4.8. The experimental results confirm that the thickness of the intermediate layer directly affects the operating point of the SAW mode. The results provide experimental evidence that intermediate layer thickness can be used to match the velocity-permittivity product of the SAW mode to the conductivity of the metal oxide sensitive layer – thus, validating the method proposed by the author in Chapter 4, section 4.4.

The author suggests that the full potential of the multilayered SAW structure would become more evident when employing sensitive layers with higher sheet conductivity than the WO_3 metal oxide layer presented. Sensitive layers such as carbon nanotubes, metal oxide nano-wires and (Pt or Au) catalyst activated metal oxide layers have significantly higher sheet conductivity than the investigated WO_3 layer. If applied directly onto the substrate surface, these layers would most likely short circuit the IDT electrodes or introduce significant capacitive loading which reduces oscillation stability; in either case

impeding the SAW device's performance. Therefore, the intermediate layer properties can be utilised to match the velocity-permittivity as well as to chemically and electrically isolate the IDT electrodes from the sensitive layer.

According to the sensitivity calculations presented in Chapter 4, section 4.4.1, the ZnO thickness for maximum sensitivity differs for each of the investigated SAW modes. The calculations show that a ZnO layer thickness of 1.2 µm would to be a good compromise, providing near maximum sensitivity for all investigated SAW modes. In the subsequent sections, the author demonstrates that a 1.2 µm thick intermediate ZnO layer employed on XY $LiNbO_3$, XZ $LiNbO_3$ and 36° YX $LiTaO_3$ substrate orientations results in high performance conductivity-based gas sensors. In section 8.5, the dielectric properties of the intermediate ZnO layer are further demonstrated by loading the WO_3 surface with conductive Pt and Au catalyst activator films. The addition of the Pt and Au catalyst activators remarkably increases the structures' sensitivity towards H_2 gas when compared to non-activated (bare) WO_3 sensitive layers.

8.2 InO_x/ZnO/XY $LiNbO_3$ Experimental Results

In this section, the InO_x/ZnO/XY $LiNbO_3$ layered SAW structure is investigated towards different concentrations of H_2 and NO_2 gas in air. The structure employs the same substrate orientation, with a near normalised ZnO layer thickness (with regards to λ) as the finite-element simulation presented in Chapter 3. The sensor employs a 40 nm InO_x layer and was fabricated with the IDT pattern shown in Chapter 4, figure 4.3(c). The cross-section can be seen in Chapter 5, figure 5.4(b).

8.2.1 Response Towards H_2

Employing the experimental setup and procedure outlined in Chapter 7, the sensor was tested repeatedly towards sequential pulses of 0.06, 0.12, 0.25, 0.50 and 1.00% H_2 gas concentrations in air. The exposure and purge times used were 240 and 480 seconds, respectively. As H_2 is a reducing gas, it increases the conductivity of the InO_x sensitive layer by injecting electrons into the device surface. Therefore, the acoustic wave velocity decreases, resulting in a decrease in centre frequency f_0, when the device is exposed to H_2 gas.

8.2.1.1 Frequency Measurements

The sensor was tested at 14 different operating temperatures, ranging from room-temperature (22°C) to 308°C. Using the frequency measurement technique, the frequency was observed to decrease by up to 514.7 kHz when exposed to 1.00% H_2 at an operating temperature of 308°C. After the initial 'break in period', the sensor exhibited repeatable and stable responses towards the tested H_2 concentrations between operating temperatures of 221 and 308°C. The 'break in period' involved holding the sensor at the maximum tested operating temperature for approximately 24 hours, whilst repeatedly exposing it to the gas pulse sequence. The dynamic responses towards the H_2 gas pulse sequence is shown in figure 8.3. Two dynamic responses are shown (recorded ∼8 hours apart) for each operating temperatures of 263, 286 and 308°C.

The InO_x/ZnO/XY $LiNbO_3$ structure exhibited large response magnitude towards the tested H_2 gas concentrations with excellent dynamic performance. Figure 8.3 shows only small deviations between the two responses at each operating temperature, thus illustrating good dynamic response repeatability and baseline frequency stability. The sensor response returned back to baseline well within the allowed 480 second time period. Typical 90% recovery was achieved within 150 seconds at an operating temperature of 308°C. The observed oscillation frequency shift versus operating temperature is shown in figure 8.4. Although the largest responses for all tested H_2 concentrations were recorded at an operating temperature of 308°C, the sensor exhibited its greatest dynamic range at 263°C. This is clearly indicated by the circled data points in figure 8.4. The trends also suggest that sensitivity towards H_2 concentrations below 0.25% would be best at operating temperatures of 308°C or above. Similarly, sensitivity towards concentrations greater than 1.00% would be less likely to cause response saturation at operating temperatures between 220 and 263°C.

8.2.1.2 Phase and Insertion Loss Measurements

Figure 8.5 shows the perturbed transmission responses (S_{21}) of the sensor when exposed to 1.00% H_2, at an operating temperature of 308°C. The centre frequency changes from 144.5 MHz in air, to 143.95 MHz when exposed to 1.00% H_2. The corresponding insertion loss at the centre frequency changed from −15.16dB to −17.31dB. At a frequency of 144.5 MHz, the phase changed from −156.4° to −97.4° when exposed to 1.00% H_2. The red lines in figure 8.5 correspond to the oscillation frequency in figure 8.3(c) in air and

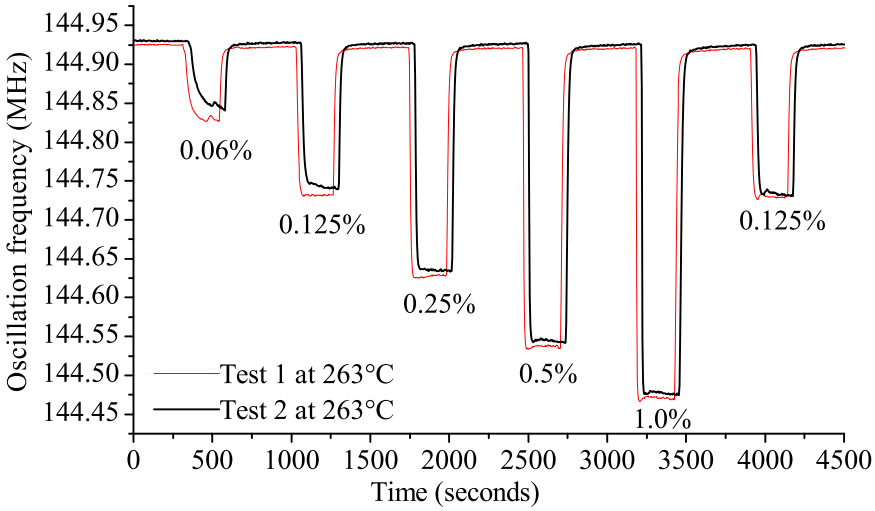

(a) Operating temperature of 263°C.

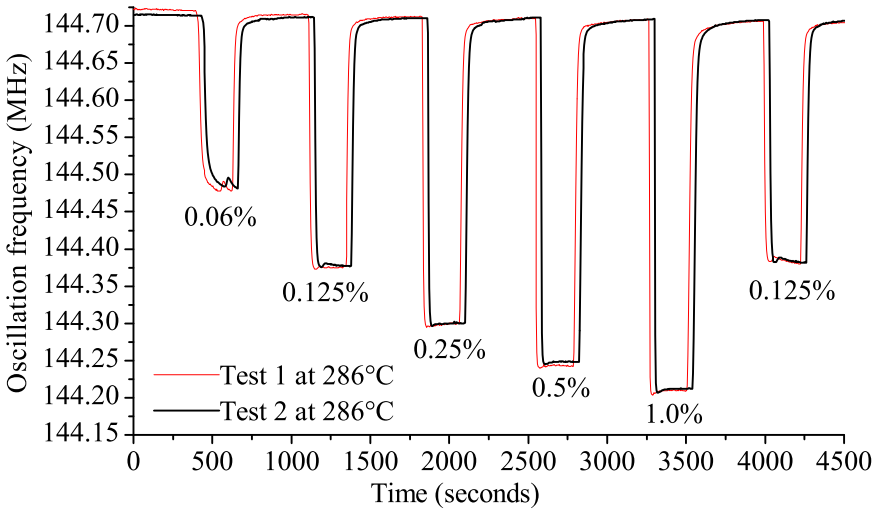

(b) Operating temperature of 286°C.

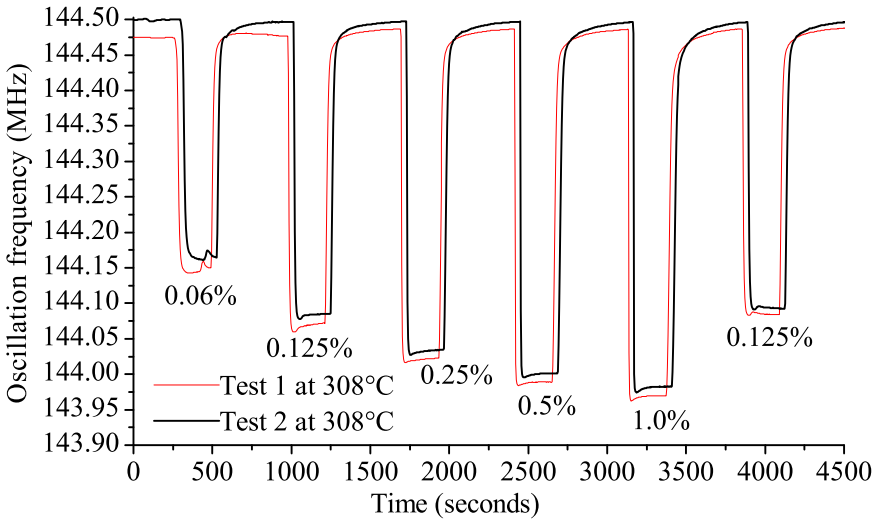

(c) Operating temperature of 308°C.

Figure 8.3: Dynamic response of 40 nm InO_x/ZnO/XY $LiNbO_3$ layered SAW sensor towards H_2 at different operating temperatures.

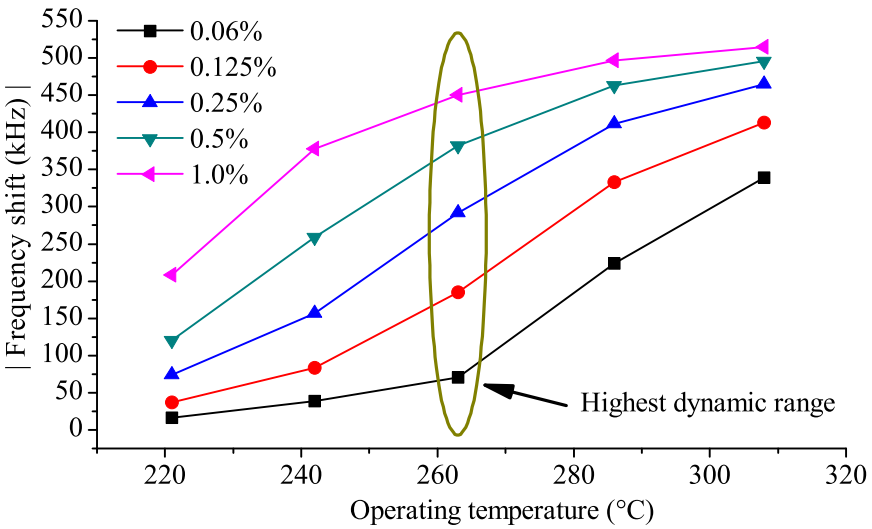

Figure 8.4: Oscillation frequency shift vs. operating temperature for 40 nm InO_x/ZnO/XY $LiNbO_3$ layered SAW sensor towards H_2.

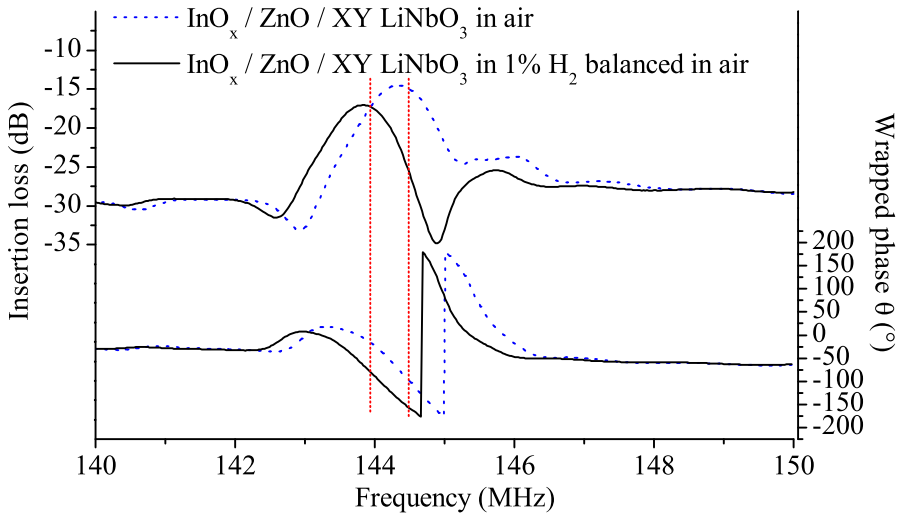

Figure 8.5: Comparison of frequency response and phase for 40 nm InO_x/ZnO/XY $LiNbO_3$ layered SAW sensor towards H_2 at an operating temperature of 308°C.

when exposed to the 1.00% H_2 concentration pulse.

8.2.2 Response Towards NO_2

Unlike hydrogen, NO_2 gas decreases the conductivity of the InO_x selective layer by stripping an electron from the conduction band; resulting in an increase in acoustic wave velocity and thus, in centre frequency. The InO_x/ZnO/XY $LiNbO_3$ sensor was tested repeatedly towards sequential pulses of 510 ppb, 1.06 ppm, 2.12 ppm, 4.25 ppm and 8.50 ppm of NO_2 gas concentrations in air. The exposure and purge times used were 240

and 480 seconds, respectively.

8.2.2.1 Frequency Measurements

The sensor was tested at the same 14 operating temperatures used during the H_2 gas testing described previously. The oscillation frequency was observed to change by a maximum of 13.0 kHz towards 8.5 ppm NO_2 at an operating temperature of 159°C. Figure 8.6 illustrates the dynamic performance of the sensor towards the NO_2 gas pulse sequence at operating temperatures of 159 and 179°C.

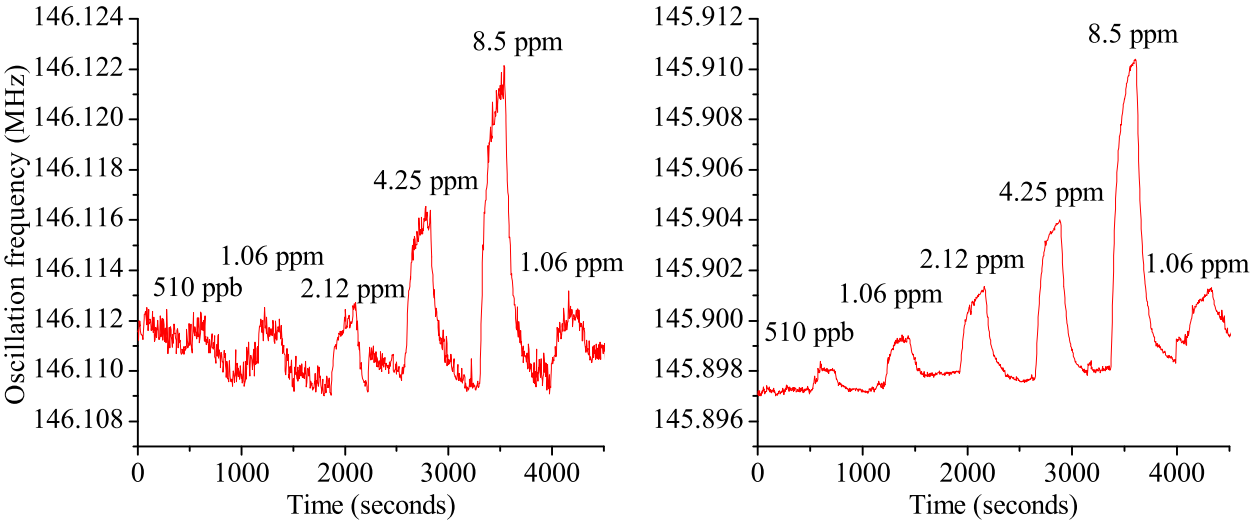

(a) Operating temperature of 159°C.

(b) Operating temperature of 179°C.

Figure 8.6: Dynamic response of 40 nm InO_x/ZnO/XY $LiNbO_3$ layered SAW sensor towards the NO_2 pulse sequence at different operating temperatures.

There was no distinguishable response towards NO_2 at operating temperatures below 94°C. The most stable response was observed at 179°C (as shown in figure 8.6(b)). Frequency shifts of 0.78, 1.78, 3.28, 6.1 and 12.5 kHz where observed for NO_2 concentrations of 510 ppb, 1.06 ppm, 2.12 ppm, 4.25 ppm and 8.50 ppm, respectively. The response towards NO_2 above 200°C became accumulative and thus, recovery to the baseline frequency between the successive NO_2 pulses did not occur. There were no responses towards NO_2 above 263°C. Table 8.1 lists the oscillation frequency shifts against operating temperature for 4.5 and 8.5 ppm NO_2 concentrations.

8.2.3 Discussion

The experimental gas sensing results of the layered InO_x/ZnO/XY $LiNbO_3$ SAW sensor showed good dynamic performance towards the tested H_2 concentrations. Frequency shifts

Table 8.1: Response magnitude of the 40 nm InO_x/ZnO/XY $LiNbO_3$ layered SAW sensor towards NO_2 in air.

Operating Temperature	8.5 ppm NO_2	4.25 ppm NO_2
94°C	8.5 kHz	5.9 kHz
120°C	10.7 kHz	5.7 kHz
140°C	11.8 kHz	6.5 kHz
159°C	13.0 kHz	6.2 kHz
179°C	12.5 kHz	6.1 kHz

of up to 514.7 kHz towards 1.00% H_2 were observed, while 13 kHz shifts were recorded for 8.5 ppm of NO_2. It is important to note that the sensor did not exhibit stable and repeatable responses towards the tested H_2 and NO_2 concentrations at the same operating temperatures. Stable H_2 responses were observed at operating temperatures between 221 and 308°C, while stable NO_2 responses occurred between 94 to 200°C.

Indium oxide films are known to exhibit a change in band-gap depending upon the oxygen concentration of the film [144, 145]. In its stoichiometric form (In_2O_3), indium oxide behaves as an insulator. In its non-stoichiometric form (InO_x) it may behave as an n-type semiconductor, due to intrinsic defects and oxygen vacancies [146]. The defects and oxygen vacancies provide 'active sites' where chemisorption between the oxide surface and the analyte gas can occur. During the interaction of H_2 and NO_2 gas species, the layer is assumed to be either reduced or oxidised, leading to a change in sheet-conductivity and as a result, perturbation of the propagating SAW occurs.

With regards to the H_2 interaction mechanism, it is postulated that in an oxidising environment, a reaction will occur between the adsorbed hydrogen and the adsorbed oxygen to produce water [98]:

$$H_{2,\ (gas)} \rightleftharpoons 2H_{\ (adsorbed)} \tag{8.1}$$

$$O_{2,\ (gas)} + 2H_{\ (adsorbed)} \rightleftharpoons 2OH_{\ (adsorbed)} \tag{8.2}$$

$$2OH_{\ (adsorbed)} + 2H_{\ (adsorbed)} \rightleftharpoons H_2O \quad . \tag{8.3}$$

These water forming reactions, which may occupy active sites on the sensitive layer surface, are presumably one of the reasons why H_2 gas responses were only observed at operating temperatures above 221°C. The ambient oxygen in the atmosphere results in an increased number of active oxygen sites on the surface of the metal oxide sensitive layer. Therefore, the primary response mechanism is assumed to be the dissociation of

H_2 gas molecules injecting electrons into the InO_x layer surface:

$$H_2 \rightarrow 2H^+_{(adsorbed)} + 2e^- \quad . \tag{8.4}$$

With regards to NO_2, the interaction mechanism is assumed to be the similar to the interaction between ozone (O_3) and other n-type metal oxides. According to Moseley et al. [177] and Galatsis [19], it is unlikely the NO_2 molecules interact with the oxygen atoms in the metal oxide sensitive layer. Instead, a direct chemisorption reaction occurs, such that:

$$NO_2 + e^- \leftrightharpoons {NO_2}^- \quad . \tag{8.5}$$

Therefore it is assumed that the NO_2 molecule strips an electron from the conduction band, which results in a decrease in film conductivity. This reaction is consistent with the experimental results, showing a decrease in the sensor's oscillation frequency upon exposure to NO_2 gas concentrations in air.

8.3 InO_x/ZnO/XZ $LiNbO_3$ Experimental Results

In this section, the InO_x/ZnO/XZ $LiNbO_3$ layered SAW structures is investigated towards different concentrations of H_2 and NO_2 gas in air. InO_x sensitive layers, 40 and 200 nm thick were employed on two separate ZnO/XZ $LiNbO_3$ layered SAW devices. Henceforth, each device will be referred by the sensitive layer type and thickness alone (i.e. 40 nm InO_x and 200 nm InO_x sensor). Both sensors were fabricated with the IDT pattern shown in figure 4.3(a) and the structural cross-section can be seen in Chapter 5, figure 5.4(c).

8.3.1 Response Towards H_2

Employing the test procedure detailed in Chapter 7, each sensor was tested over a 2 week period. Both the 40 and 200 nm InO_x sensors were tested separately. However, they were tested under the same conditions using the same computer controlled gas exposure sequence and operating temperatures.

8.3.1.1 Frequency Measurements

The oscillation frequencies for the 40 and 200 nm InO_x sensors at room temperature were 138.2 and 139.6 MHz, respectively. The pulse sequence consisted of 0.06, 0.12, 0.25, 0.50

and 1.00% H_2 concentrations balanced in synthetic air, and was exposed to the sensor at each operating temperature between room-temperature and 273°C (in 20 to 30°C steps). The exposure and purge times used were 240 and 480 seconds, respectively.

Frequency shifts towards H_2 gas concentrations of 0.06 to 1.00% were observed to be in the range of 78.5 to 319.4 kHz and 5.7 to 61.3 kHz for the 40 nm sensor and 200 nm sensor, respectively. The dynamic response of the 40 and 200 nm InO_x sensors towards the H_2 sequence, at an operating temperature of 246°C, is shown in figure 8.7. The 40 nm InO_x sensor is shown to exhibit a response overshoot for all H_2 concentrations above 0.12%, however this was not observed at operating temperatures below 218°C. The 200 nm InO_x sensor exhibited no response overshoot towards the tested concentration of H_2. As the response overshoot did not occur with the 200 nm InO_x sensor, it could be suggested that the hydrogen penetrates through the 40 nm InO_x layer and directly interacts with the intermediate ZnO layer. The SEM characterisation in figure 6.12 supports this hypothesis, as the texture of the 200 nm sensitive layer appears more dense, with a smoother surface texture. See Chapter 6, section 6.2 for more details.

Figure 8.8, shows the frequency shift observed at each operating temperature for all tested H_2 concentrations. The 40 nm InO_x sensor was observed to have the largest frequency shift of 319.4 kHz at 246°C towards 1.00% H_2. Figure 8.8(a) shows that response magnitude towards the different H_2 concentrations follows a common trend, where the largest frequency shift occurs at 246°C. Smaller response magnitudes were observed at the higher operating temperature of 273°C. In contrast to this, the oscillation frequency

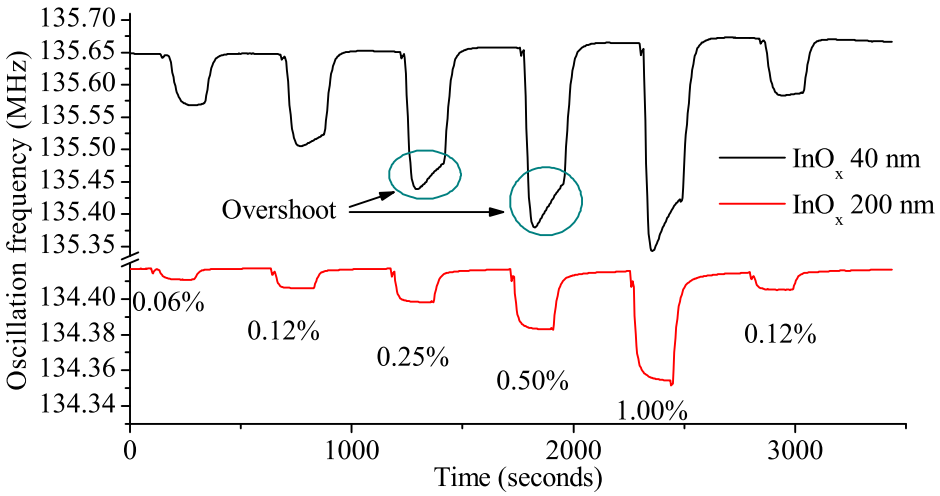

Figure 8.7: Dynamic response of 40 nm (top) and 200 nm (bottom) InO_x layered SAW sensors towards a sequence of H_2 pulses at an operating temperature of 246°C.

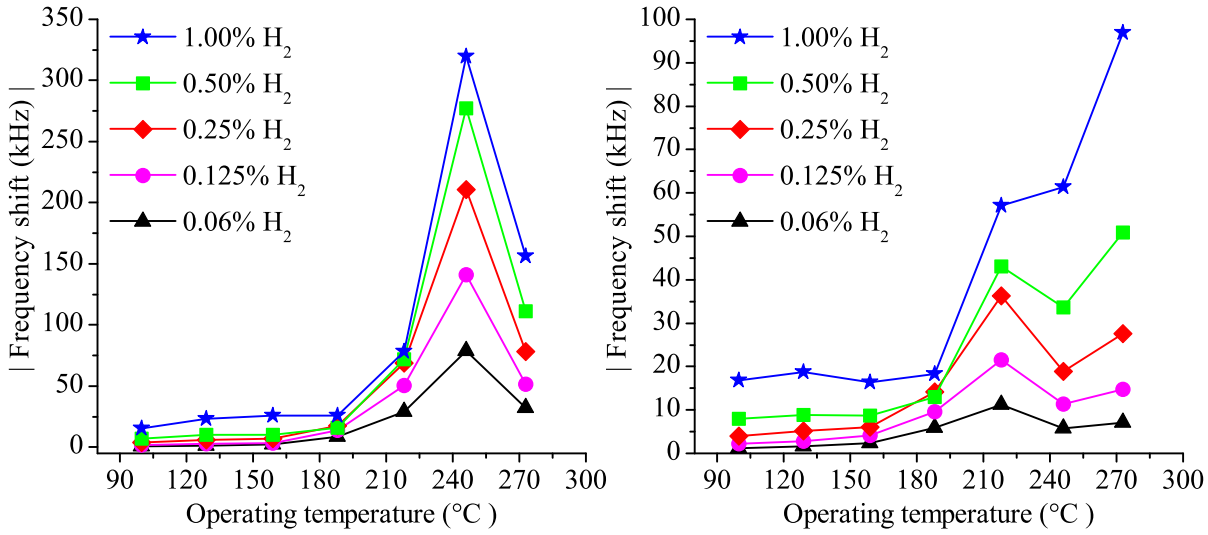

(a) 40 nm InO_x sensor.

(b) 200 nm InO_x sensor.

Figure 8.8: Oscillation frequency shift vs. operating temperature for 40 and 200 nm InO_x layered SAW sensors towards H_2.

shifts for the 200 nm InO_x sensor, presented in figure 8.8(b), increases at higher operating temperatures. The only exceptions occur at 246°C for H_2 concentrations below 0.50%. Following this trend, frequency shifts greater than 61.3 kHz would be predicted for 1.00% H_2 at operating temperatures above 273°C. Unfortunately, limitations in the experimental setup prevented testing above 273°C, due to the utilisation of the sapphire micro-heater shown in Chapter 7, figure 7.10.

The response magnitude of both the 40 and 200 nm InO_x sensors did not appear to saturate towards 1.00% H_2, leading the author to anticipate that the sensors would be suitable for H_2 concentrations above 1.00%. Furthermore, both sensors exhibited a large dynamic response over the tested H_2 concentration range and the sensor response returned to the baseline frequency well within the allowed recovery time. For the 1.00% H_2 concentration pulse, at an operating temperature of 246°C, 90% recovery was achieved within 125 and 140 seconds for the 40 and 200 nm InO_x sensors, respectively. The response time variation between the two sensors would also most likely be due to the different surface morphology of the 40 and 200 nm InO_x layers, as shown in the SEM characterisation presented in Chapter 6, section 6.2.3. Previous measurements for InO_x deposited on silicon and Corning glass substrates [178] showed that the film thickness has a strong influence on the film surface morphology, which plays an essential role in the gas sensing properties of the films.

8.3.1.2 Phase and Insertion Loss Measurements

Figure 8.9 shows the perturbed transmission response (S_{21}) of the 40 nm InO_x sensor when exposed to 1.00% H_2, at an operating temperature of 246°C. The centre frequency changes from 135.65 MHz in air, to 135.45 MHz when exposed to 1.00% H_2. The corresponding insertion loss at the centre frequency changed from −13.98dB to −16.63dB. At a frequency of 135.65 MHz, the phase changed from −79.6° to −93.8° when exposed to 1.00% H_2. The red lines in figure 8.9 correspond to the oscillation frequency in figure 8.7 in air and when exposed to the 1.00% H_2 concentration pulse.

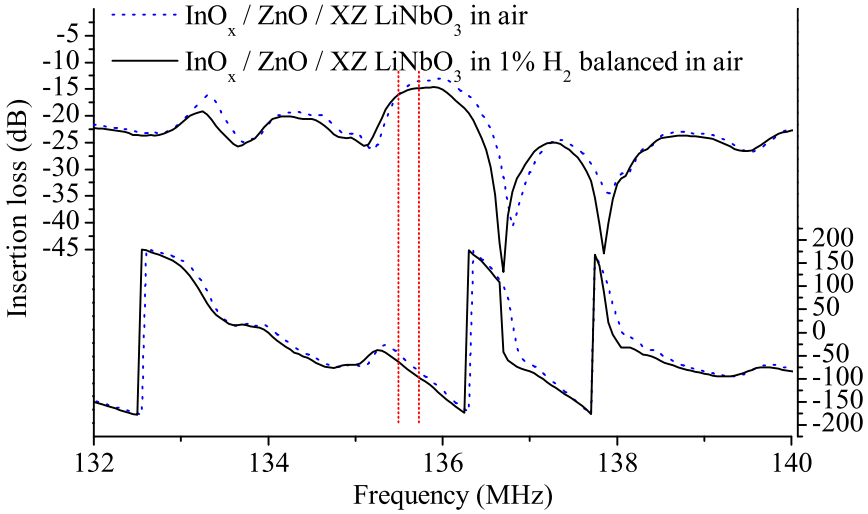

Figure 8.9: Comparison of frequency response and phase for the 40 nm InO_x/ZnO/XZ $LiNbO_3$ layered SAW sensor towards H_2 at an operating temperature of 246°C.

8.3.2 Response Towards NO_2

Both the 40 and 200 nm InO_x sensors were tested repeatedly towards sequential pulses of 510 ppb, 1.06 ppm, 2.12 ppm, 4.25 ppm and 8.50 ppm NO_2 gas concentrations. A second pulse of 1.06 ppm, in each sequence was used to confirm the sensors' repeatability. The exposure and purge times used were 180 and 360 seconds, respectively.

8.3.2.1 Frequency Measurements

Figure 8.10 illustrates the dynamic performance of the 40 and 200 nm InO_x sensors towards NO_2 at an operating temperature of 246°C. The frequency shift towards 2.12 ppm of NO_2 was observed to be in excess of 91 and 18 kHz for the 40 and 200 nm sensors, respectively. The response magnitude was observed to saturate for each sensor at an NO_2

concentration of 2.12 ppm. Increasing the NO_2 concentration above this level did not result in a significant increase in response magnitude.

Figure 8.11, shows the frequency shift observed at each operating temperature for all tested NO_2 concentrations. The largest frequency shift was recorded at 246°C and 218°C for the 40 and 200 nm InO_x sensors, respectively. It can be seen that the 40 nm InO_x sensor significantly outperforms the 200 nm sensor, with response magnitudes nearly 4 times larger. Figure 8.11(a) shows that at an operating temperature of 246°C, the 40 nm InO_x sensor exhibits distinguishable response magnitudes for NO_2 concentrations between 510 ppb and 1.06 ppm NO_2, however gives the same frequency shift for all concentrations above 2.12 ppm.

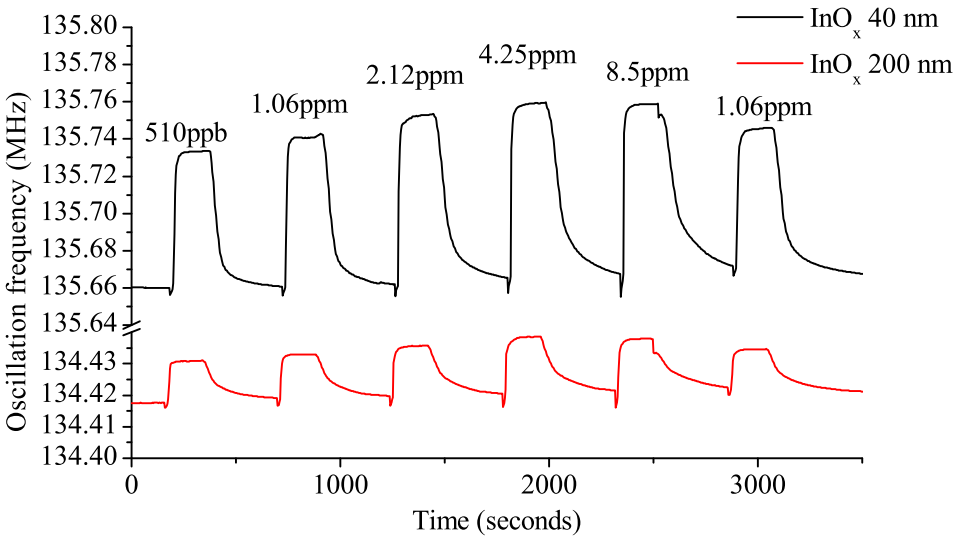

Figure 8.10: Dynamic response of 40 nm (top) and 200 nm (bottom) InO_x layered SAW sensors towards a sequence of NO_2 pulses at an operating temperature of 246°C.

Although figure 8.11(b) shows that the 200 nm sensor produced its largest response magnitude at 218°C, frequency shifts for all other NO_2 concentrations tested had approximately the same response magnitude. Therefore, the 200 nm sensor could only be used at an operating temperature of 246°C for NO_2 gas concentration below 4.25 ppm, for a meaningful correlation between response magnitude and NO_2 concentration.

8.3.3 Comparison between Rayleigh and SH-SAW modes

As previously mentioned in Chapter 4, section 4.3.2, the addition of the intermediate ZnO layer on the XZ $LiNbO_3$ substrate allows the structure to support Rayleigh and

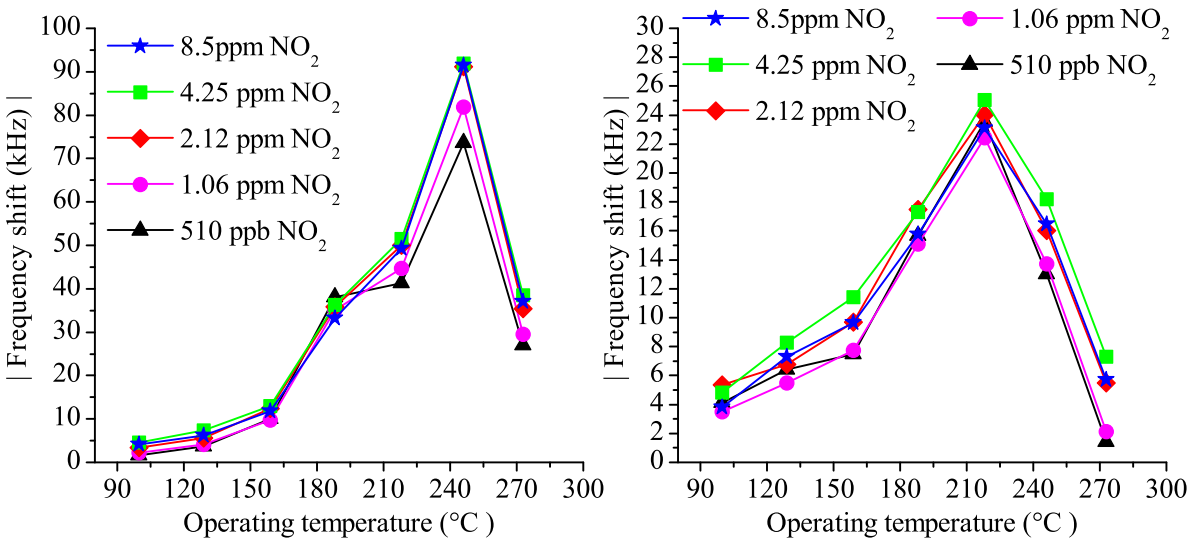

(a) 40 nm InO_x sensor.

(b) 200 nm InO_x sensor.

Figure 8.11: Oscillation frequency shift vs. operating temperature for 40 and 200 nm InO_x layered SAW sensors towards NO_2.

SH-SAW modes that can be utilised for conductometric gas sensing applications. The Rayleigh mode was employed for the H_2 and NO_2 gas sensing experiments presented in sections 8.3.1 and 8.3.2, respectively.

Without the ZnO layer, the supported SH-SAW has K^2 of 0% in the XZ $LiNbO_3$ substrate. Therefore in a non-layered configuration, it is not suitable for conductivity-based sensing applications and cannot be excited piezoelectrically by an IDT. However, due to the piezoelectric properties of the intermediate ZnO layer, the SH-SAWs K^2 value is increased by the presence of the piezoelectric intermediate ZnO layer. Hence, the overall K^2 of the ZnO/XZ $LiNbO_3$ layered structure is a function of the intermediate ZnO layer thickness. For a structure with an intermediate ZnO layer thickness of 1.2 µm, table 4.4 in Chapter 4 shows that the K^2 of the Rayleigh mode is 6.11% at the ZnO/substrate interface and 2.81% at the device surface. Using the same numerical method discussed in Chapter 4, the SH-SAW was calculated to have a K^2 of 0.27% at the ZnO/substrate interface and 0.15% at the surface. Therefore, the K^2 of the Rayleigh mode is as much as 22 times larger than the SH-SAW at the ZnO/substrate interface and 18 times larger at the device surface.

It is important to note that the separation of the two distinct modes in the frequency domain decreases with increasing ZnO layer thickness. Therefore, if the layered SAW sensor is used as the frequency determining element in an oscillator, the possibility of

'mode hopping' is substantially increased for ZnO layer thickness above 1.2 µm, when $\lambda_0 = 24$ µm. Figure 8.12 shows the transmission frequency response (S_{21}) of the 40 nm InO_x sensor at an operating temperature of 218°C. A 7.7 MHz frequency separation is shown between the Rayleigh and SH-SAW modes. By selecting the coaxial leads with the correct length, the author was able to adjust the total system phase, forcing stable oscillation to occur with either the Rayleigh or SH-SAW mode.

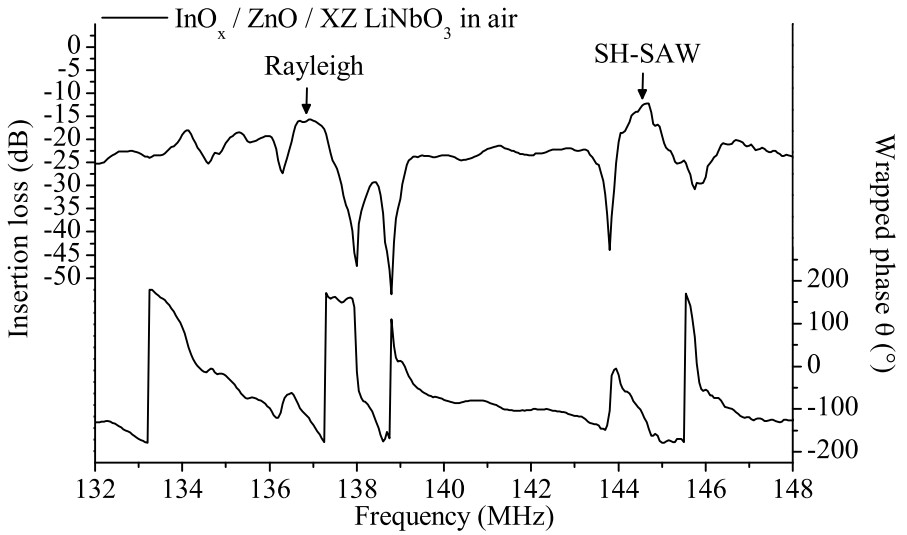

Figure 8.12: Frequency response and phase for 40 nm InO_x sensor in air at an operating temperature of 218°C.

Figure 8.13 illustrates the difference between the dynamic response of the Rayleigh and SH-SAW modes towards NO_2. The dynamics of both responses are similar, however the magnitude of the Rayleigh mode response is approximately 19 times larger than the SH-SAW towards 510 ppb of NO_2. By inspection of equation (4.4) in Chapter 4, the sensitivity of the two modes should have approximately the same ratio as their electromechanical coupling coefficients, which was calculated as 27.4. It should be noted that for NO_2 concentration of 1.06 and 2.12 ppm, the response magnitude ratios decrease to 14 and 11, respectively. Therefore, it is suggested that better agreement between calculations and measurements would be achieved at NO_2 concentrations lower than 510 ppb. Unfortunately, due to limitations with the experimental setup, it was not possible to test lower concentrations of NO_2. Further details regarding these calculations can be found in [179].

As the relationship between K^2 and the response magnitude of the Rayleigh and SH-SAW modes is not linear, it is proposed that the response saturation differs between the two

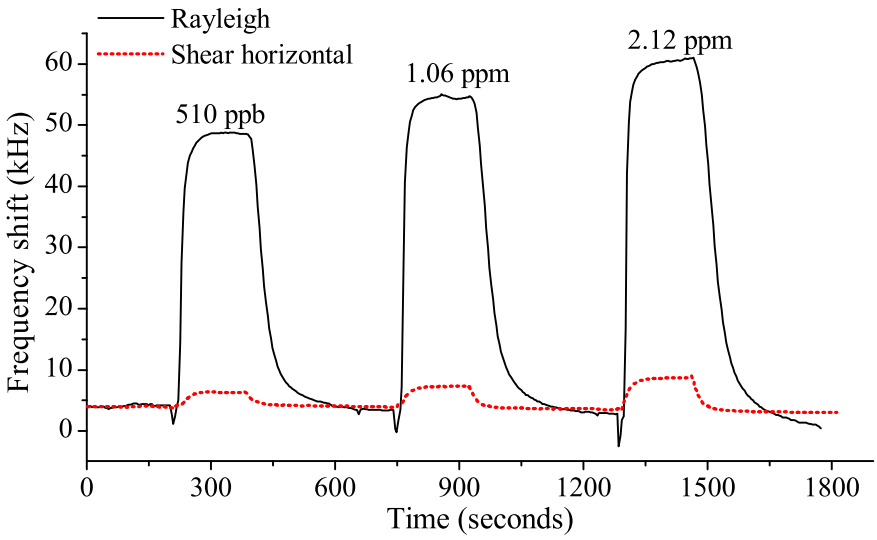

Figure 8.13: Comparison between the Rayleigh and SH-SAW modes: response towards 510 ppb, 1.06 ppm and 2.12 ppm NO_2 gas concentrations.

modes. Since the interaction kinetics are identical in both cases, the conductivity change experienced by the two modes is identical. Therefore the variation in conductometric sensitivity of the two modes results in the different response magnitude ratios. One possible explanation is the difference in the $v_f \varepsilon_p$ quantity of each mode; thus placing the operating region of the Rayleigh and SH-SAW mode at different points in figure 4.6. It should also be noted that equation (4.4) was derived assuming that the piezoelectric interaction between the SAW and the conductive layer is weak [72]. For highly piezoelectric materials such as XZ $LiNbO_3$, this assumption introduces error. The equation also neglects the dependence of the wave characteristics on the electrical boundary conditions [180] – particularly for non-Rayleigh modes, as well as the dispersion caused by the layer, which is dependant on the propagation mode. Therefore, a more accurate theoretical analysis or model would be expected to show a slightly different curve to the one presented in figure 4.6, and would be dependant on the mode of propagation [130].

8.3.4 Discussion

The experimental gas sensing results of the InO_x/ZnO/XZ $LiNbO_3$ layered SAW sensors showed excellent dynamic performance towards the tested NO_2 and H_2 gas concentrations. The results presented demonstrate that the 40 nm InO_x sensor largely outperforms the 200 nm InO_x device for the tested NO_2 and H_2 gas concentrations. Figure 8.14

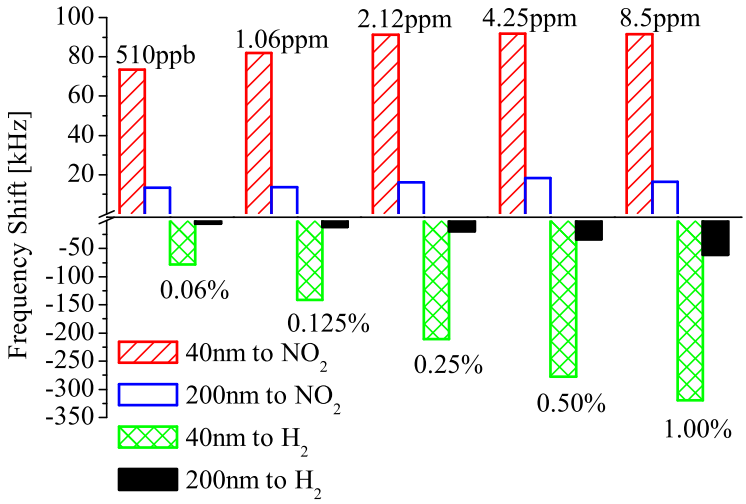

Figure 8.14: Frequency shift vs. concentration of NO_2 and H_2 gases for 40 and 200 nm InO_x layered SAW sensors at 246°C.

compares the response magnitude of both sensors at an operating temperature of 246°C. A large difference in response magnitude between the 40 and 200 nm sensors is shown. Furthermore, the saturation of NO_2 response for concentrations of 2.12 ppm and above is apparent.

The comparison of the Rayleigh and SH-SAW modes confirmed that the piezoelectric properties of the intermediate ZnO layer can be used advantageously for conductometric gas sensing applications. The direct comparison between the two modes demonstrated that response magnitude is approximately a linear function of K^2 and therefore, the interaction between the NO_2 gas and the InO_x sensitive layer is most definitely acousto-electric in nature.

Attempts to explain the interaction mechanism of H_2 and NO_2 with InO_x have been presented in the literature [181, 182] and in section 8.2.3. Based on previous experimental results for InO_x deposited on silicon and Corning glass substrates [178], it has been shown that the film thickness has strong influence on the film surface morphology. The lower sensitivity of the 200 nm InO_x layer is most likely attributed to its denser and smoother texture than the 40 nm InO_x layer, as shown in Chapter 6, figure 6.12. Together with the results presented in this section and the previously discussed surface characterisation of the 40 and 200 nm InO_x in Chapter 6, section 6.2, the author has shown that the surface morphology play an essential role on the InO_x film's gas sensing properties. The counter argument for this could be that the analyte gas interacts more with the ZnO than the

InO_x layer in the 40 nm sensor. However, upon review of ZnO thin film sensitivity results obtained by Kalantar-Zadeh [18], the author believes this to be most unlikely.

Consequently, the 40 nm InO_x sensor was found to exhibit high sensitivity towards low concentrations of NO_2 and medium concentrations of H_2 gas in air. Exceptionally strong frequency shifts of positive 91kHz for 2.12 ppm of NO_2 and negative 319kHz for 1.00% H_2 were observed for the 40 nm InO_x sensor. Due to the high sensitivity of the Rayleigh mode, the 40 nm InO_x sensor would be an excellent candidate for sub-ppm NO_2 gas sensing applications.

8.4 WO_3/ZnO/36° YX $LiTaO_3$ Experimental Results

In this section, the experimental gas sensing results of the WO_3/ZnO/36° YX $LiTaO_3$ layered SAW structures towards different concentrations of H_2 and NO_2 gas and ethanol vapour are investigated. WO_3 sensitive layer thicknesses of 150 and 160 nm were employed on a ZnO/36° YX $LiTaO_3$ layered SAW structure. The structure's cross-section was previously illustrated in Chapter 5, figure 5.4(d). Henceforth, each device will be referred by the sensitive layer type and thickness alone (i.e. 150 nm WO_3 or 160 nm WO_3 sensor).

8.4.1 Response Towards H_2

The 160 nm WO_3 sensor was fabricated with the IDT pattern shown in Chapter 4, figure 4.3(a). A modified testing procedure, using a repeated sequence of three 1.00% and two 0.50% H_2 pulses was employed to test the performance of the structure at different operating temperatures. An exposure time of 180 seconds and a purge time of 380 seconds was used for each H_2 pulse. The baseline oscillation frequency of the sensor was 164.070 MHz in air, at an operating temperature of 175°C. Figure 8.15(a) shows frequency shifts of 11 and 25.8 kHz towards H_2 concentrations of 0.50 and 1.00%, respectively. Operating temperatures exceeding 175°C were found to cause a drift in baseline stability. The drift was found to be approximately 8.5 kHz over a 50 minute period, which is approximately the same drift shown in figure 8.15(b). Response magnitudes of 12.3 and 24.7 kHz were observed towards 0.50 and 1.00% H_2 concentrations, respectively, at an operating temperature of 186°C.

The relationship between operating temperature and response magnitude, shown in figure 8.16, indicates that the response towards 0.50 and 1.00% H_2 is maximised at

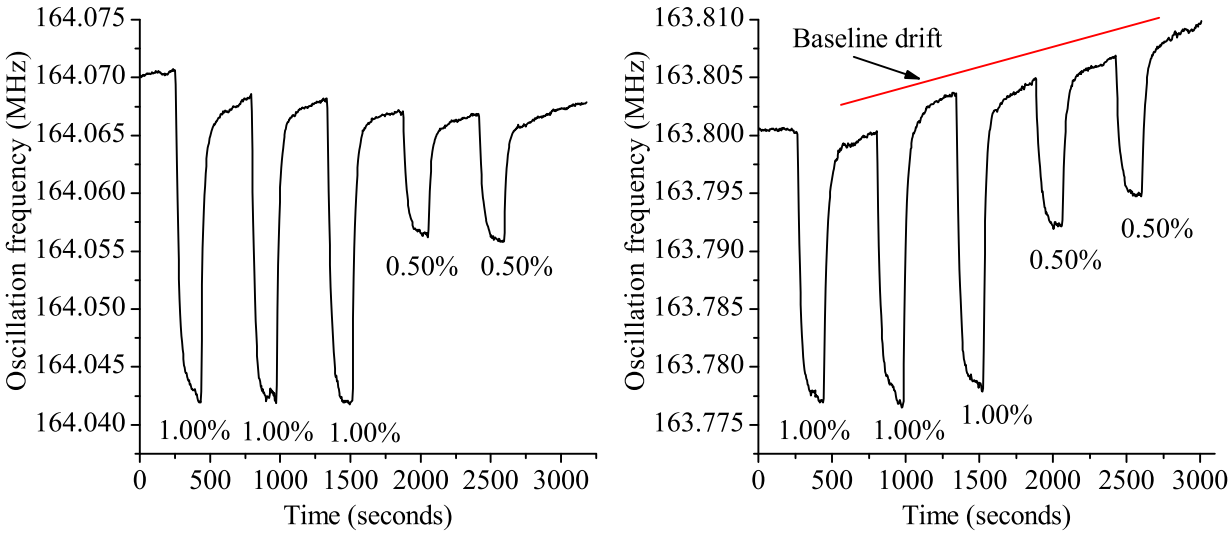

(a) Operating temperature: 175°C (b) Operating temperature: 186°C

Figure 8.15: Dynamic response of 160 nm WO_3 sensor towards H_2 concentrations of 0.50 and 1.00%.

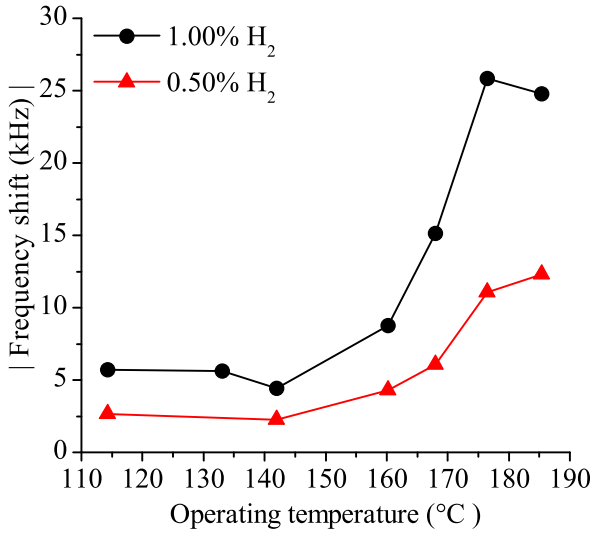

Figure 8.16: Oscillation frequency shift vs. operating temperature for 160 nm WO_3 sensor towards H_2.

operating temperatures of 186 and 175°C, respectively. It should be noted that the trade-off between the baseline drift and the 1.2kHz increase in response magnitude towards 0.50% H_2 would need to be considered before operating the sensor above 175°C.

8.4.2 Response Towards NO_2

In 1991, Akiyama et al. [183] observed that WO_3 layers were highly sensitive towards nitric oxide (NO) and NO_2. Preliminary experiments with the 160 nm WO_3 sensor, as described in section 8.4.1, showed it to exhibit good repeatability towards different NO_2 concentrations at an operating temperature of 100°C. Results were obtained using a higher flow rate of 300 SCCM to facilitate accurate mixing ratios to produce the 500 and 750 ppb NO_2 concentrations. The dynamic response of the sensor towards NO_2 gas pulses in the range of 500 ppb to 1.25 ppm are shown in figure 8.17.

The exposure time of each NO_2 pulse was for a 1260 second (21 minute) period. The sensor was allowed to recover during a 3600 second (1 hour) purge time in between NO_2 pulses. The associated frequency shifts for the 500 ppb, 750 ppb, 1 ppm and 1.25 ppm NO_2 concentrations were observed to be 30.22, 35.62, 39.45 and 43.86 kHz, respectively. The second pulse of 500 ppb (shown in figure 8.17), resulted in a 30.5 kHz frequency shift, demonstrating the repeatability of the sensor response. It should be noted that full response saturation was not achieved during the 1260 second exposure period.

Due to the longer response and recovery time required by the 160 nm WO_3 sensor towards NO_2, it was not tested at different operating temperatures. Optimisation of the thickness and deposition parameters of the WO_3 sensitive layer may improve the layer's surface morphology characteristics, resulting in higher sensitivity and quicker response towards

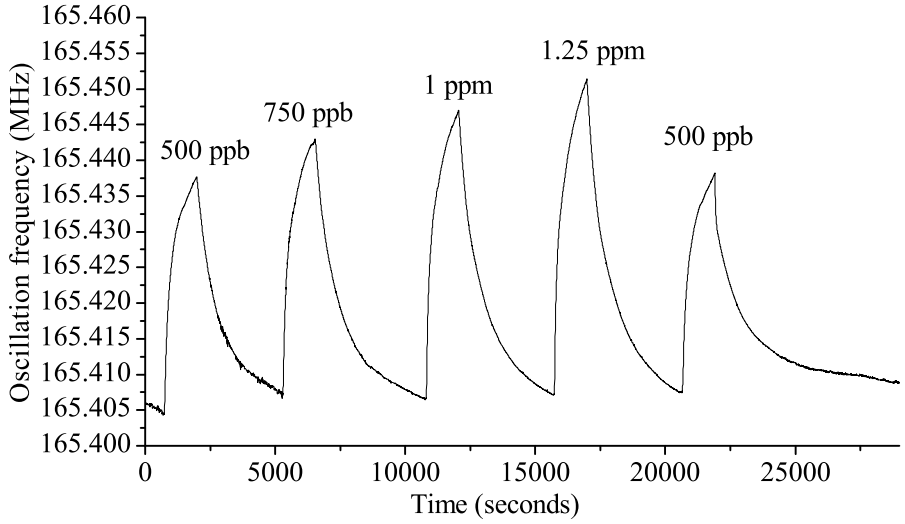

Figure 8.17: Dynamic response of the 160 nm WO_3/ZnO/36° YX $LiTaO_3$ layered SAW sensor towards different NO_2 concentrations at an operating temperature of 100°C. A gas flow rate of 300 SCCM was used.

NO_2. Nevertheless, it is important to note that by measuring the initial gradient of the sensor response, the NO_2 concentration could possible be extrapolated. However, the long recovery time required would impair any practical NO_2 gas sensing application of the structure.

8.4.3 Response Towards Ethanol Vapour

Ethanol vapour sensing experiments conducted during the author's stay in Brescia, Italy, utilised a 150 nm thick WO_3 sensitive layer deposited on the ZnO/36° YX $LiTaO_3$ structure. Two identical sensing structures were fabricated with the IDT pattern shown in Chapter 4, figure 4.3(b). The chamber and gas temperatures were held constant at 20°C for all ethanol sensing experiments – as opposed to the 22°C used for all H_2 and NO_2 experiments. Further experimental setup details can be found in Chapter 7, section 7.3.5. The 150 nm WO_3 sensors were exposed to 1200 second (20 minute) long pulses of ethanol. A 2400 second (40 minute) purge time of air was used to allow the oscillation frequency to return back to baseline. Both the 150 nm WO_3 sensors were tested at elevated operating temperatures between 100 and 300°C.

During the first 6 to 10 hours of operation at 300°C, both sensors showed very poor sensitivity towards the tested concentrations of ethanol vapour. After the initial 'break in' period, each sensor then responded towards the ethanol vapour with the same dynamic response characteristics. Figure 8.18 shows the dynamic response of the first sensor towards 10, 25, 50, 250 and 500 ppm pulse sequence of ethanol vapour. Due to experimental setup and small fabrication variations, each sensor operated with a slightly different fundamental frequency, however similar response magnitudes were observed for both sensors during each of the tested conditions. At an operating temperature of 300°C, frequency shifts of 119, 98, 65.7, 50, and 32.6 kHz were observed towards ethanol vapour concentrations of 500, 250, 50, 25 and 10 ppm, respectively.

8.4.4 Humidity effects on Ethanol Sensitivity

Employing the same ethanol pulse sequence, the effect of 25 and 50% RH levels on response magnitude were investigated at different operating temperatures. Although the 150 nm WO_3 sensors were observed to exhibit a response magnitude of 119 kHz at a 0% RH level, frequency shifts of 90 and 86 kHz were observed for 25 and 50% RH levels, respectively, towards 500 ppm of ehtanol at an operating temperature of 300°C. Figure 8.19 illustrates

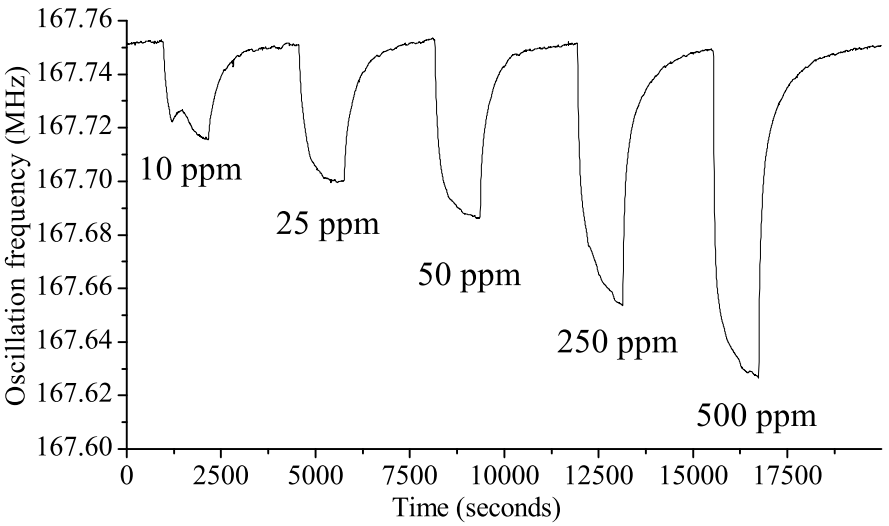

Figure 8.18: Response of a WO_3 layered SAW sensor towards ethanol pulse sequence at an operating temperature of 300°C. Relative humidity was 0% at 20°C.

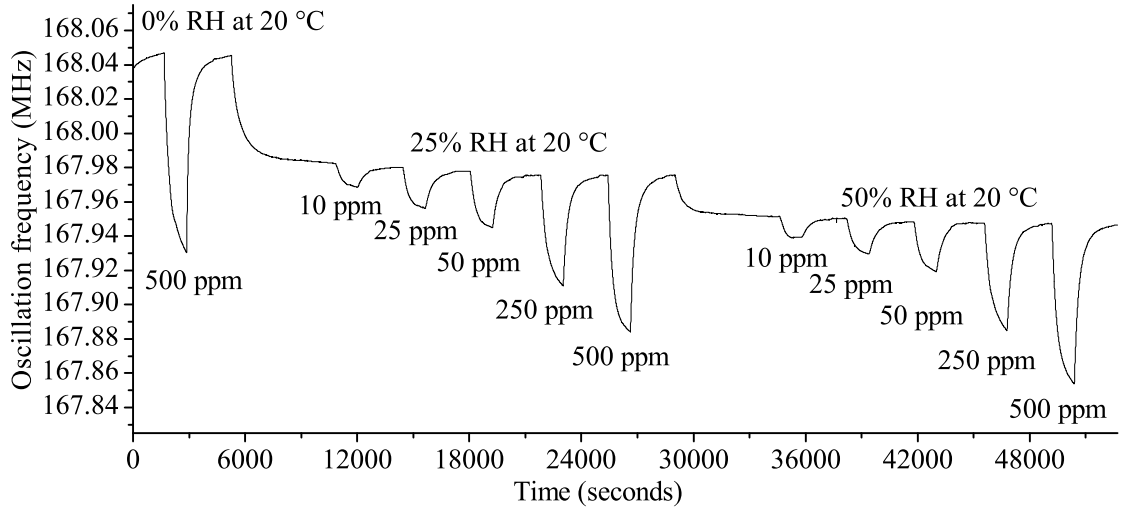

Figure 8.19: Dynamic response towards ethanol pulse sequence at an operating temperature of 300°C, with a RH of 0%, 25% and 50% (measured at 20°C), respectively.

the effect of 25 and 50% RH levels on the dynamic response of the 150 nm WO_3 sensor when operating at 300°C. It should be noted that all RH levels were measured at the ambient chamber and gas temperature of 20°C, which is not to be confused with the operating temperature of the 150 nm WO_3 sensors (ranging between 100 and 300°C).

Figure 8.19 also shows that the 25 and 50% RH levels produce a change in baseline frequency of approximately 200 kHz. The decrease in baseline frequency for an increase in RH can be attributed to H_2O molecules interacting with the WO_3 sensitive layer. Furthermore, the decrease in the response magnitude of each pulse during the ethanol

sequences at 0, 25 and 50% RH conditions is shown. It is thought that the H_2O molecules occupy some of the 'reactive sites' on the WO_3 sensitive layer, inhibiting the ethanol and WO_3 interaction process. The H_2O interaction may also increases the WO_3 layer conductivity, thus explaining the decrease in response magnitude, when compared to 0% RH conditions.

Figure 8.20 shows the oscillation frequency as a function of ethanol concentration for different RH levels at operating temperatures of 235, 256, 277 and 300°C. It can be seen that the response magnitude decreases with decreasing operating temperature. The response magnitude variation towards ethanol between the 0, 25 and 50% RH levels becomes more significant with decreasing operating temperature. No response towards ethanol concentrations below 25 ppm was observed at operating temperatures below 235°C with RH levels of 25 or 50%.

Operating temperature influences both physisorption and chemisorption. In most cases, physisorption monotonically decreases with increasing operating temperature. In the case presented, the dynamic response towards ethanol exhibits larger frequency shifts with increasing operating temperature. If the sensing mechanism towards ethanol vapour was due to gravimetric interaction, then it would more likely be temperature independent. Therefore, the response is most likely due to a chemisorption mechanism. Hence, ethanol is assumed to reduce the WO_3 layer, causing a negative frequency shift. Similarly, the decrease in response magnitude due to the RH level at each operating temperature can be attributed to the ethanol and H_2O competing for 'reactive sites' at the WO_3 sensitive layer surface.

8.4.5 Discussion

Unlike the generalised SAW or the Rayleigh modes supported by the layered structures presented in sections 8.2 and 8.3, the ZnO/36° YX $LiTaO_3$ structure supports a SH-SAW mode with a high K^2. The 160 and 150 nm WO_3 sensors exhibited good dynamic performance towards H_2, NO_2 and ethanol analytes. The 160 nm WO_3 sensor was shown to have a repeatable dynamic response towards the tested H_2 and NO_2 gas concentrations. Positive frequency shifts of 43.86 kHz towards 1.25 ppm of NO_2 was observed at an operating temperature of 100°C. Conversely, negative frequency shifts of up to 25.8 kHz were observed for 1.00% H_2 concentrations at an operating temperature of 175°C. Additionally, the 150 nm WO_3 sensors exhibited excellent repeatability towards

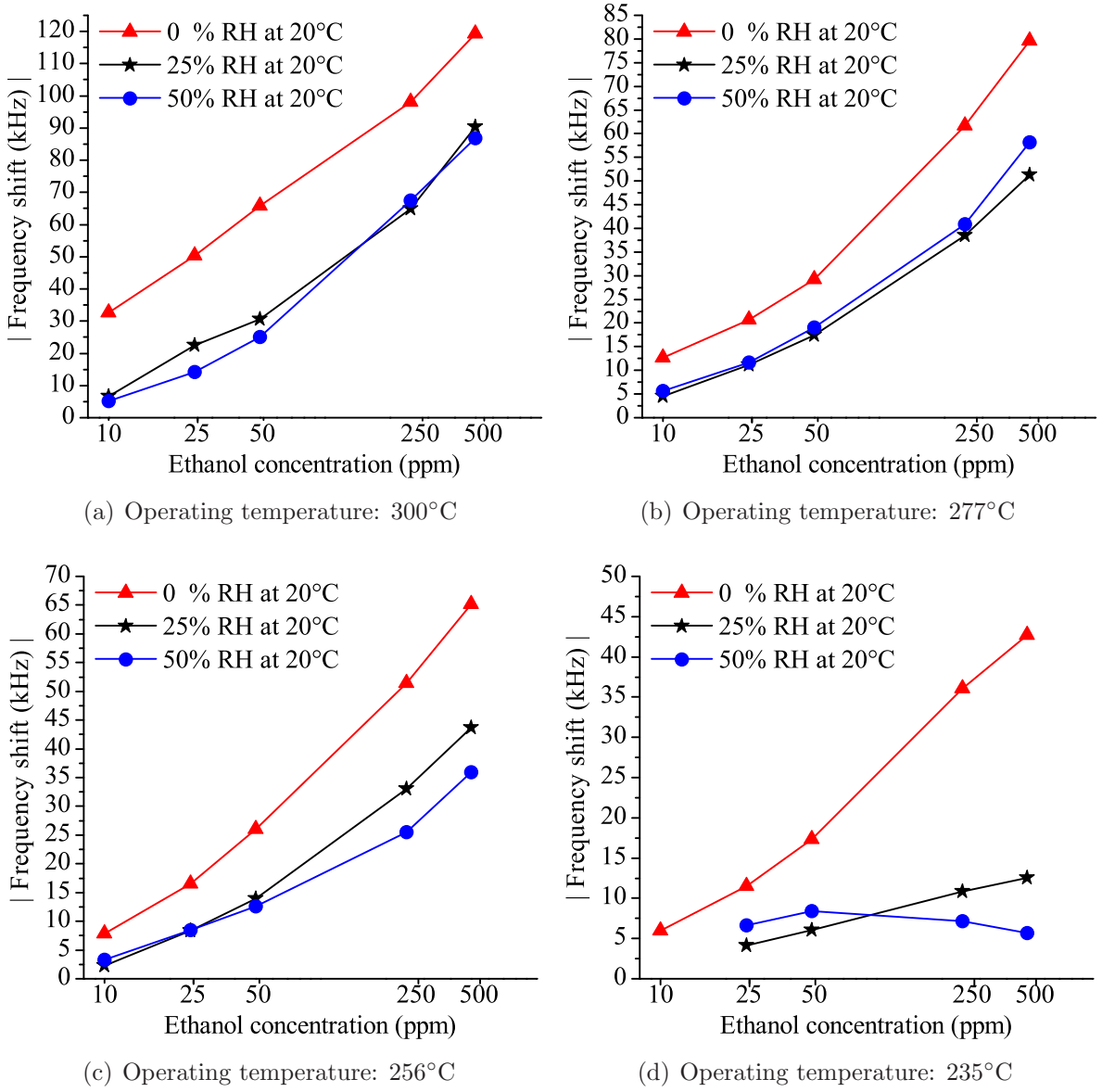

(a) Operating temperature: 300°C

(b) Operating temperature: 277°C

(c) Operating temperature: 256°C

(d) Operating temperature: 235°C

Figure 8.20: Frequency shift vs. ethanol concentration at 0%, 25% and 50% RH levels. RH measured at 20°C.

ethanol vapour concentrations below 500 ppm at operating temperatures between 235 and 300°C. The response magnitude towards each ethanol pulse was observed to decrease at RH levels of 25 and 50%. For example, at an operating temperature of 300°C, frequency shifts of 119, 90 and 86 kHz towards 500 ppm of ethanol vapour were observed for RH levels of 0, 25 and 50%, respectively.

Response saturation of the 160 nm WO_3 sensor towards H_2 was found to occur well within the 180 second exposure time. However, the 160 nm WO_3 sensor did not fully saturate towards any of the tested concentrations of NO_2 during the 1260 second exposure periods.

Furthermore, 3600 second purge periods were required between each pulse before the sensor response returned back to the baseline. In the case of ethanol vapour, exposure and purge times of 1200 and 2400 seconds, respectively were employed for the 150 nm WO_3 sensor. Fortunately, changes in the RH level were not found to significantly influence the response or recovery time. However, overall response time was found to be influenced by the operating temperature and the concentration of the analyte gas. Higher operating temperatures and analyte gas concentrations were generally found to result in a faster response.

The H_2 gas interaction with the WO_3 sensitive layer is similar to the mechanism associated with the InO_x layer presented in section 8.2.3. The introduction of low hydrogen concentrations in air induces a reaction with the WO_3 film, increasing its conductivity. The dissociation of the H_2 molecules at the surface of the WO_3 sensitive layer injects electrons into the device surface. Georg et al. [184] and Bludska et al. [185] recently proposed a model of oxygen deficiency based on the reaction of hydrogen and lattice oxygen. The disassociated hydrogen diffuses onto the WO_3 giving:

$$2x\mathrm{H}^{+}_{(adsorbed)} + \mathrm{WO_3} \rightarrow \mathrm{WO_{3-x}} \cdot x\mathrm{H_2O} \qquad . \tag{8.6}$$

This leads to an intermediate step, where H_2O and additional oxygen vacancies are created. The additional oxygen vacancies diffuse into the device surface, allowing some of the H_2O molecules to leave the WO_3 sensitive layer. The H_2O formation is important for the transport process of the H along the surface of the WO_3 layer, forming H_3O^+ and e^-, where the H becomes probable [184]. This may explain why the increased RH levels resulted in a decreased response magnitude towards ethanol, as the reactive sites occupied by the introduced H_2O molecules (humidity) inhibit the H_2O formation process in equation (8.6).

With regards to the interaction between the NO_2 or ethanol and the WO_3 sensitive layer, a direct chemisorption reaction is assumed to occur (see equation 8.5). As WO_3 is regarded as having a non-stoichiometric structure, free electrons originating from oxygen vacancies contribute to the conductivity of the thin film [186]:

$$\mathrm{O}_{(bulk)} = \mathrm{V}_o + 2e^- + \tfrac{1}{2}\mathrm{O}_{2\ (gas)} \qquad , \tag{8.7}$$

where V_o represents the oxygen vacancy and $O_{(bulk)}$ is oxygen present in the WO_3 lattice.

The n-type semiconductor properties of the WO_3 originate from the extra electron. As NO_2 is an oxidising agent, upon its interaction with the WO_3 surface a decrease in the layer's conductivity occurs, resulting in a positive frequency shift.

As the layered SAW sensors did not show a repeatable response until after the initial 'break in' period at elevated temperatures, it is suggested that the morphological modifications play an important role in the sensing properties of the WO_3 films. Surface characterisation work, presented in Chapter 6 section 6.3, clearly indicates that changes in the surface morphology occur when the sensor is exposed to an elevated temperature of 300°C for a period greater than 24 hours. The effect of elevated temperature on the structure's surface morphology, illustrated in figures 6.5 and 6.6, suggests that grain coalescence of the ZnO intermediate layer must be critical to the acousto-electric sensitivity of the sensor. The increase in the sensor's response magnitude could be further increased by the higher RMS roughness and improved crystallinity of the WO_3 sensitive layer after exposure to elevated temperatures. The results presented demonstrate that high sensitivity towards H_2, NO_2 and ethanol can be achieved utilising a SH-SAW mode with a WO_3 sensitive layer.

8.5 Effect of Catalyst Activated WO_3

In this section, Pt and Au catalyst activated WO_3/ZnO/36° YX $LiTaO_3$ layered SAW structures are investigated towards different concentrations of H_2. As early as 1967, Shaver [187] demonstrated that a Pt activated WO_3 based gas sensor possesses enhanced sensitivity towards airborne H_2 and other hydrogen containing gases, such as: H_2S, C_2H_4 and NH_3. Platinum is universally acknowledged as the most active catalyst for promoting reactions involving hydrogen. Work conducted by Triwahyono et al. [188] found that H_2 adsorption on Pt/WO_3-ZrO_2 is faster than that on WO_3-ZrO_2 . However, Au, Pd and Ag are also amongst the most common metal catalysts used to improve gas sensing properties of metal oxide based gas sensors [97].

To investigate the advantages associated with metal catalyst activators, a similar WO_3/ZnO/36° YX $LiTaO_3$ structure, to that presented in section 8.4 is employed. However, the surface of the 160 nm thick WO_3 sensitive layer is modified by sputtering a thin, non-continuous film of Pt or Au. Two near identical sensing structures were fabricated with the IDT pattern shown in figure 4.3(a). Each sensor was sputtered with either a 4–5 nm thick Pt or a 6–7 nm thick Au activator layer. The cross-section of each

structure is illustrated in Chapter 5, figures 5.4(e) and 5.4(f). Henceforth, each device will be referred to as the Pt–WO_3 or Au–WO_3 sensor.

Employing the experimental procedure outlined in Chapter 7, the Pt–WO_3 or Au–WO_3 sensors were tested repeatedly towards sequential pulses of 0.06, 0.12, 0.25, 0.50 and 1.00% H_2 gas concentrations in air. The sensors were tested using the frequency measurement technique at operating temperatures ranging from room-temperature (22°C) to 270°C and 287°C for the Pt–WO_3 and Au–WO_3 sensors, respectively.

8.5.1 Pt–WO_3/ZnO/36° YX $LiTaO_3$ Frequency Measurements

The dynamic performance of the layered WO_3/ZnO/36° YX $LiTaO_3$ SAW sensor was found to be greatly improved with the deposition of the Pt catalyst activator layer. The Pt–WO_3 sensor produced a frequency shift of up to 5 times larger than the (bare) 160 nm WO_3 sensor presented in section 8.4.1. At room-temperature the Pt–WO_3 sensors baseline oscillation frequency was approximately 168.66 MHz. It was found to exhibit maximum sensitivity at two distinct operating temperatures of 100 and 270°C. It was also found to respond and recover quicker at operating temperatures below 130°C. Figure 8.21(a) shows the dynamic response of the Pt–WO_3 sensor towards the H_2 pulse sequence, at an operating temperature of 100°C. Exposure time of 180 seconds and purge time of 360 seconds were used. Frequency shifts between 6.6 kHz and 95.4 kHz were observed for H_2 concentrations between 0.06% and 1.00%, respectively. At the higher operating temperature of 270°C, a response magnitude of 5.6 kHz and 118 kHz was observed for 0.06% and 1.00% concentrations, respectively. The dynamic response can be seen in figure 8.21(b), where and exposure time of 240 seconds and a purge time of 480 seconds were used.

Figure 8.22 shows the frequency shift observed for each tested H_2 concentration at the different operating temperatures. The lower operating temperature of 100°C exhibits a marginally larger response magnitude towards H_2 concentrations below 0.50%, when compared to the response observed at 270°C. This could be a considerable advantage of the Pt–WO_3 sensor for lower power consumption applications. The Pt–WO_3 sensor may have exhibited larger response magnitudes at operating temperatures above 270°C, however the experimental setup limited the operating temperature to below 270°C, due to the utilisation of the sapphire micro-heater shown in Chapter 7, figure 7.10.

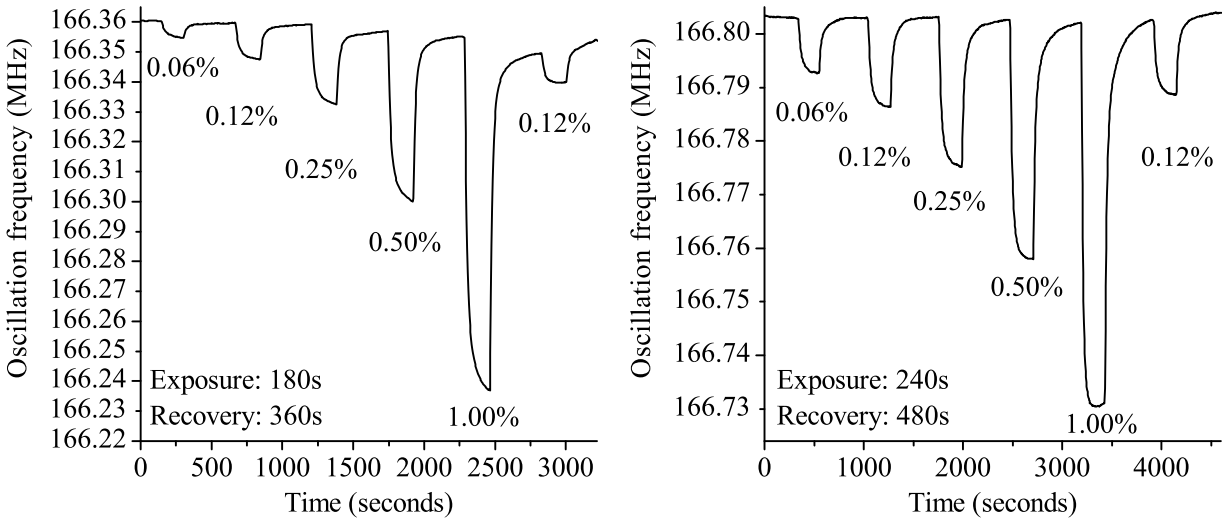

(a) Operating temperature: 270°C (b) Operating temperature: 100°C

Figure 8.21: Dynamic response of Pt–WO_3 sensor towards H_2 pulse sequence.

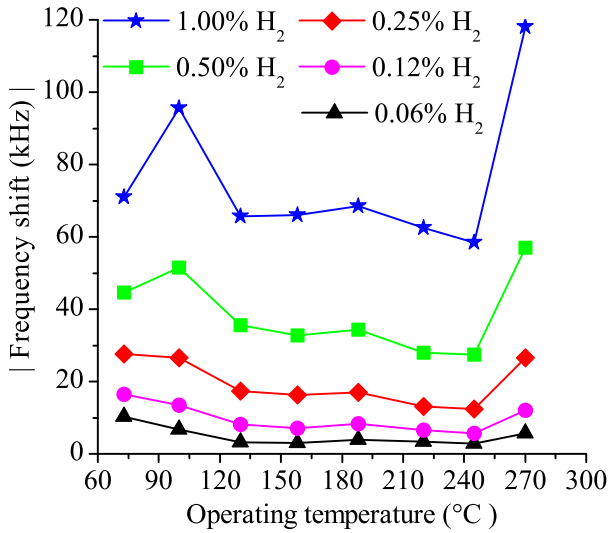

Figure 8.22: Frequency shift vs. operating temperature for the Pt–WO_3 sensor.

8.5.2 Au–WO_3/ZnO/36° YX $LiTaO_3$ Frequency Measurements

The Au–WO_3 sensor produced a maximum frequency shift approximately 50 times larger than the (bare) 160 nm WO_3 layer towards a hydrogen concentration of 0.50% in air. At room temperature, the Au–WO_3 sensor the had a baseline oscillation frequency of approximately 166.58 MHz. The sensor was tested at different operating temperatures, ranging from room-temperature to 287°C. Frequency shifts of up to 755 kHz were observed towards H_2 concentrations of 1.00% at an operating temperature of 245°C. Figure 8.23 shows the dynamic response of the Au–WO_3 sensor towards the H_2 pulse sequence

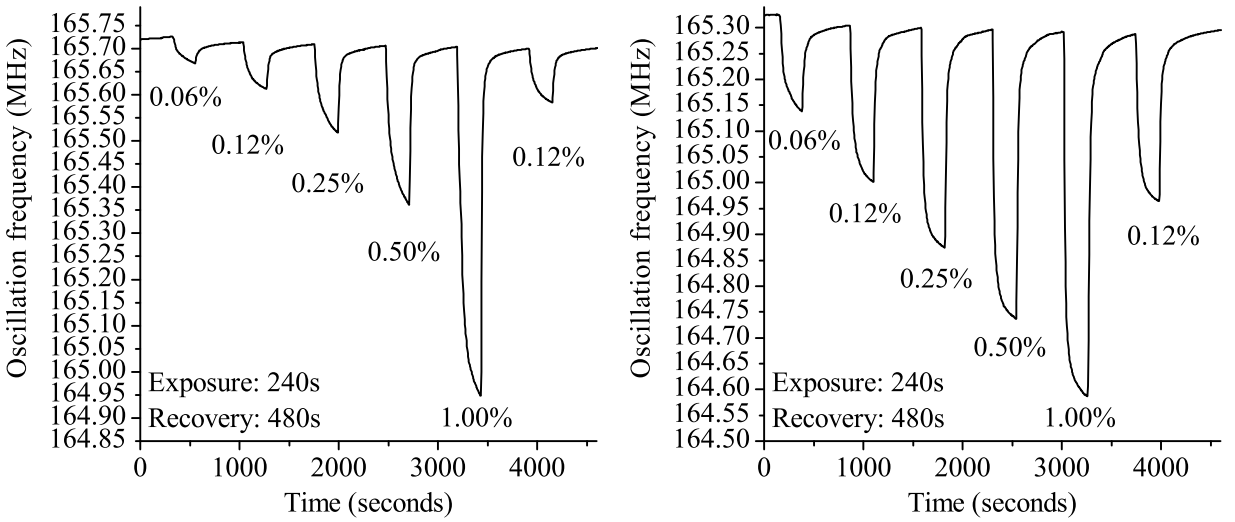

(a) Operating temperature: 245°C (b) Operating temperature: 270°C

Figure 8.23: Dynamic response of the Au–WO_3 sensor towards H_2 pulse sequence.

at operating temperatures of 245 and 270°C. Exposure and purge times of 240 and 480 seconds were used, respectively.

At an operating temperature of 245°C, frequency shifts of 55.4 and 755.0 kHz were observed towards H_2 concentrations of 0.06 and 1.00%, respectively. At the higher operating temperature of 270°C, response magnitudes of 187.0 and 705.1 kHz were observed for 0.06 and 1.00% H_2 concentrations, respectively. Figure 8.24 shows the frequency shift observed for each tested H_2 concentration at the different operating temperatures. It can be seen that an operating temperature of 270°C provides the best response magnitude for the majority of the tested H_2 concentrations.

8.5.2.1 Phase and Insertion Loss Measurements

Figure 8.25 shows the perturbed transmission response (S_{21}) of the Au–WO_3 sensor when exposed to 1.00% H_2, at an operating temperature of 270°C. The centre frequency changes from 165.3 MHz in air, to 164.5 MHz when exposed to 1.00% H_2. The corresponding insertion loss at the centre frequency changed from −16.17dB to −20.23dB. At a frequency of 165.3 MHz, the phase changed from 58.6° to −113.7° when exposed to 1.00% H_2. The red lines in figure 8.25 correspond to the oscillation frequency in figure 8.23(b) in air and when exposed to the 1.00% H_2 concentration pulse.

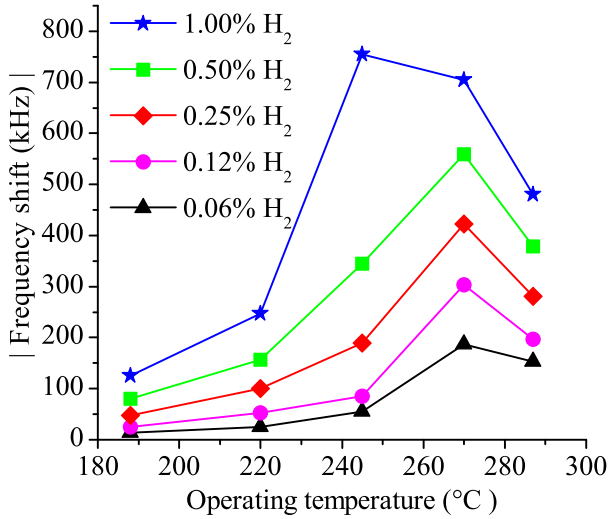

Figure 8.24: Frequency shift vs. operating temperature for the Au–WO_3 sensor.

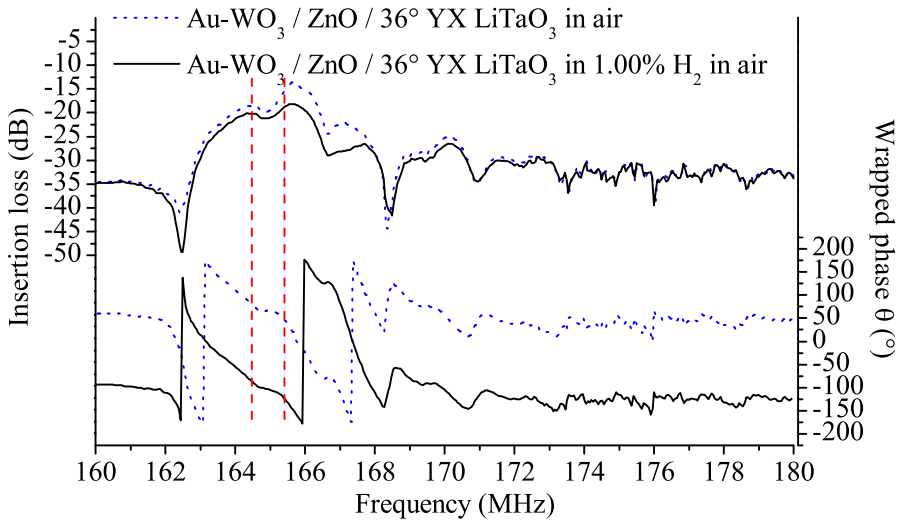

Figure 8.25: Comparison of frequency response and phase for the Au–WO_3/ZnO/36° YX $LiTaO_3$ layered SAW sensor towards 1.00% H_2, at an operating temperature of 270°C.

8.5.3 Discussion

The Pt and Au catalysts activators promote the reaction between the sensitive layer and H_2 molecules by reducing the required activation energy. The reduction of pure WO_3 by hydrogen begins above 400°C. However, it is understood that this reaction readily proceeds even at room temperature in the presence of noble metal catalyst activators, such as Pt or Pd [189]. It is well known that the amount of catalyst influences the sensitivity and the optimum operating temperature of a sensor structure [190]. In the case of the Pt–WO_3 sensor's low-temperature (100-130°C) response, H_2 molecules are

thought to dissociate on the Pt layer into hydrogen atoms in a 'spillover' process, to form tungsten bronze (H_xWO_3). Similar 'spillover' phenomenon on Pt–WO_3 sensitive layers has been reported in [191, 192]. In the case of H_2S interactions, formation of tungsten sulfide (WS_2), termed as 'sulfurization' over tungsten bronze has been suggested [193]. Such mechanisms for H_2 gas interaction on Au–WO_3 have not been clearly established in the literature. However, work conducted by Ando et al. [194] suggests that Pt films may lower the permeability of hydrogen to a greater extent than Au films. This, may explain why the Au–WO_3 sensor required a higher operating temperature before exhibiting larger response magnitudes towards the test H_2 concentrations.

The results of the Pt–WO_3 and Au–WO_3 sensors showed an increased sensitivity towards the tested H_2 concentrations, when compared with the bare 160 nm WO_3 device, which was presented in section 8.4.1. It was found that the Pt–WO_3 sensor generally responded and recovered faster than the Au–WO_3 sensor, however the difference was found to be marginal. The Pt–WO_3 sensor also exhibited large response magnitudes towards H_2 concentrations below 0.25% at operating temperatures below 130°C – presumably due to the 'spillover' phenomenon. In comparison, operating temperatures above 180°C were required before the Au–WO_3 sensor showed stable responses towards the tested H_2 concentrations. The Au–WO_3 sensor exhibited the largest response magnitude towards H_2 of all other layered SAW structures investigated in this research program. Table 8.2 summarises the maximum frequency shift observed for the 160 nm WO_3, Pt–WO_3 and Au–WO_3 sensors for each of the tested H_2 concentrations.

Table 8.2: Comparison of maximum frequency shift observed for the 160 nm WO_3, Pt–WO_3 and Au–WO_3 sensors for each of the tested H_2 concentrations.

Selective Layer	Operating temperature	Center frequency	Frequency shift (kHz)				
			0.06%	0.12%	0.25%	0.50%	1.00%
WO_3	175°C	164.0 MHz	-	-	-	11.0	25.8
Pt–WO_3	100°C	166.6 MHz	6.6	13.4	26.5	51.5	95.4
Pt–WO_3	270°C	166.3 MHz	5.6	12.0	26.5	57.0	118.0
Au–WO_3	270°C	165.3 MHz	187.0	302.9	422.7	559.6	705.1
Au–WO_3	245°C	165.7 MHz	55.4	85.2	189.5	344.9	755.0

The short-term stability of both the Pt–WO_3 and Au–WO_3 sensors' response magnitudes towards H_2 concentrations was found to be superior to that of the (bare) 160 nm WO_3 sensor. Due to the increase in response magnitude of the Pt–WO_3 and Au–WO_3 sensors, the short-term oscillation frequency stability is a much less significant problem (see figure 8.15(b)). Unfortunately, over the two-week testing period, the response magnitude

of the Pt–WO_3 and Au–WO_3 sensors was found to degrade. Long-term stability problems with Pt and Au doped WO_3 films due to ageing effects of the catalysts are well known [195]. Surface characterisation results presented Chapter 6 section 6.3.4 confirm that the Au layer forms a non-continuous film over the WO_3 sensitive layer. Since metal oxide sensitive layers operate at elevated temperatures (approximately 300°C or more), it is possible for the morphology of the metal (Pt or Au) particles to change with time. LeGore et al. [196] reported that gold particles on a WO_3 surface increase in size and decrease in number density over time, via accelerated aging. The aggregation into larger particles causes a significant decrease in device sensitivity, resulting in a decrease in response magnitude with the increase in size of the metal particles and the oxide grains. Continual testing and further work would be required to stabilise the metal particles on the WO_3 layer surface to resolve these issues.

8.6 Summary

In this chapter, the gas sensing performance of the InO_x/ZnO/XY $LiNbO_3$, InO_x/ZnO/XZ $LiNbO_3$ and WO_3/ZnO/36° YX $LiTaO_3$ layered SAW structures was presented. The utilisation of 0.1, 0.5, 1.0 and 2.0 µm thick intermediate ZnO layers experimentally verified the sensitivity calculations for the ZnO/36° YX $LiTaO_3$ structure presented in Chapter 4. The preliminary experimental results presented in section 8.1 clearly demonstrated that the ZnO intermediate layer thickness can be used to tailor the velocity-permittivity product of the propagating SAW mode. Following this, each of the investigated layered SAW structures, employing a 1.2 µm intermediate ZnO layer, were experimentally evaluated towards different concentrations of H_2 and NO_2 at various operating temperatures. Further evaluation of the WO_3/ZnO/36° YX $LiTaO_3$ layered SAW structure towards ethanol concentrations below 500 ppm, at operating temperatures between 200 to 300°C and RH levels of 0, 25 and 50%, was also conducted. Additionally, the effect of Pt and Au catalyst activator layers was investigated with respect to response magnitude and operating temperature, towards H_2 concentrations below 1.00%.

To the best of the author's knowledge, this is the first time that the experimental gas sensing performance of multilayered SAW structures employing a ZnO intermediate layer and a metal oxide sensitive layer have been presented. The results provide strong evidence that high sensitivity can be achieved utilising a layered SAW structure, with both Rayleigh and SH-SAW modes, for conductometric gas sensing applications. Key experimental

gas sensing outcomes for the InO_x/ZnO/XY $LiNbO_3$, InO_x/ZnO/XZ $LiNbO_3$ and WO_3/ZnO/36° YX $LiTaO_3$ layer SAW structures can be summarised as following:

- **InO_x/ZnO/XY $LiNbO_3$**
  - The InO_x/ZnO/XY $LiNbO_3$ sensor exhibited repeatable frequency shifts of 338.7 and 514.7 kHz towards H_2 concentrations between 0.06 and 1.00% in air, respectively with a stable baseline.
  - Frequency shifts of 0.78 and 12.5 kHz were observed towards NO_2 concentrations of 510 ppb and 8.5 ppm, respectively, at an operating temperature of 179°C.
- **InO_x/ZnO/XZ $LiNbO_3$**
  - The 40 nm InO_x sensor outperformed the 200 nm InO_x sensor for the tested concentrations of H_2 and NO_2 gas, with regards to response magnitude and response time.
  - A comparison between the supported Rayleigh and SH-SAW modes verified that the response magnitude is a function of K^2. Therefore, the sensor response caused by the interaction between NO_2 gas and the InO_x sensitive layer is based on an acousto-electric interaction. The Rayleigh mode was found to be up to 19 times more sensitive than the SH-SAW.
  - Saturation of response towards NO_2 was found to occur for both the 40 and 200 nm InO_x sensors at concentrations of 2.12 ppm and above.
  - It is the author's opinion that the 40 nm InO_x sensor is the best candidate for sub-ppm NO_2 sensing applications, when compared to all the other layered SAW structures investigated throughout this research program.
- **Pt–WO_3, Au–WO_3 and WO_3/ZnO/36° YX $LiTaO_3$**
  - The 160 nm WO_3 sensor required longer response and recovery periods towards NO_2 gas, when compared to the InO_x/ZnO/$LiNbO_3$ based structures.
  - The response magnitude of the catalyst activated Pt–WO_3 and Au–WO_3 sensors was approximately 5 and 50 times larger than the (bare) 160 nm WO_3 sensor, respectively.
  - The 160 nm WO_3, Pt–WO_3 and Au–WO_3 sensors exhibited different optimum operating temperature for H_2 sensing, which also depended on the gas concentration. In particular the Pt–WO_3 sensor was found to have two distinct

optimum operating temperatures of 100 and 270°C, while the Au–WO_3 and bare WO_3 sensors operated best at 270 and 175°C, respectively.

- The Au–WO_3 sensor's response magnitude was the largest of all investigated layered SAW structures, producing a 755 kHz frequency shift towards 1.00% H_2 at an operating temperature of 245°C.
- Although the short-term stability of the Pt–WO_3 and Au–WO_3 sensitive layers was superior to the non-activated (bare) 160 nm WO_3 sensor, their gas sensing performance was found to degrade over the two week testing period.

By conducting gas sensing experiments at both RMIT University and The University of Brescia, the results achieved by the author are shown to be independent of experimental setup and the gas calibration systems employed. The experimental gas sensing results presented in this chapter, combined with the surface characterisation presented in Chapter 6, have led the author to publish six referred journal articles and five articles in international conference proceedings. A full list of the author's publications can be found in Appendix C.

Chapter 9

Conclusions and Future Work

This PhD research program commenced with the aim of developing highly sensitive gas sensors using novel *multi*layered SAW structures. The structures developed by the author were shown to have unique surface morphological attributes and to exhibit excellent static and dynamic performance towards NO_2 and ethanol at ppb and ppm levels respectively, and H_2 concentrations below 1.00% in air. This thesis highlighted many of the advantages of employing a multilayered *sensitive-layer*/ZnO/*substrate* structure, which may lay the foundations for the next generation of SAW based conductometric gas sensors.

The high performance of the investigated layered SAW structures is achieved by adjusting the intermediate ZnO layer thickness for maximum sensitivity. By optimising the ZnO layer thickness, the velocity-permittivity product of the SAW mode can be matched to the conductivity of the sensitive layer. Furthermore, the high electromechanical coupling coefficient (K^2) of the X-cut $LiNbO_3$ and 36° Y-cut $LiTaO_3$ substrates, combined with the material properties of the piezoelectric intermediate ZnO layer, were shown to significantly improve the conductometric sensitivity of the investigated layered SAW structures, when compared to similar devices presented in the literature (see table 2.1). During the course of this research program, the author also developed 2D and 3D finite-element models to analyse the electromechanical phenomena occurring in the layered ZnO/XY $LiNbO_3$ SAW structure. To the best of the authors knowledge, this is the first time a layered *sensitive-layer*/ZnO/*substrate* SAW structure has been proposed and presented for gas sensing applications. Furthermore, this thesis presents the first full 3D finite-element model of a layered ZnO/XY $LiNbO_3$ SAW device with experimental verification. The finite-element model has recently gained significant interest from various independent research groups worldwide, where the author is currently collaborating with colleagues

with the aim of further developing and combining the modelling methods outlined within Chapters 3 and 4.

This thesis presented the evolution of the author's research, which can be summarised by the following points:

1. Simulation of the layered ZnO/XY $LiNbO_3$ SAW device utilising the 2D and 3D finite-element method, with experimental verification.
2. Design of multilayered SAW structures for conductivity based gas sensing applications, including:
   - InO_x/ZnO/XY $LiNbO_3$
   - InO_x/ZnO/XZ $LiNbO_3$
   - WO_3/ZnO/36° YX $LiTaO_3$
   - Pt–WO_3/ZnO/36° YX $LiTaO_3$
   - Au–WO_3/ZnO/36° YX $LiTaO_3$
3. Fabrication of the above mentioned multilayered SAW structures.
4. Material and surface morphology characterisation of:
   - The intermediate ZnO layer on X-cut $LiNbO_3$ and 36° Y-cut $LiTaO_3$ substrates.
   - The WO_3/ZnO/36° Y-cut $LiTaO_3$ structure.
   - The InO_x/ZnO/X-cut $LiNbO_3$ structure.
5. Electrical characterisation of the above mentioned multilayered SAW structures towards analyte gases which include: NO_2 and ethanol concentration of ppb and ppm levels respectively, and H_2 concentrations below 1.00% in air. Furthermore, the effect of RH levels on the dynamic response magnitude towards ethanol was investigated.

In the following sections, the author will briefly summarise the major findings of this research program and present his recommendations for future work.

9.1 Conclusions

Based on the results delivered in this thesis, the author has clearly demonstrated that the aims and objectives outlined in Chapter 1, section 1.2 have been satisfied. Major finding and outcomes derived from this research can be summarised by the following points:

- The 3D finite-element simulations of the layered ZnO/XY $LiNbO_3$ SAW structure showed higher acoustic energy confinement at the surface of the device when compared to its non-layered counterpart. The addition of the piezoelectric ZnO thin film was shown to make the layered structure more sensitive towards changes in the electrical boundary condition at the surface. Furthermore, the finite-element simulations demonstrated that by using the entire surface of the device as the active sensing area, a significantly larger frequency shift is achieved when compared to the conventional method of employing only the space in between the IDT ports.
- The modelling of the ZnO/substrate configuration by perturbation theory determined that sensitivity towards changes in conductivity at the device surface is maximised when the velocity-permittivity product of the SAW mode is matched to the conductivity of the sensitive layer. An intermediate ZnO layer thickness of 1.2 µm was determined to be the best tradeoff between device sensitivity and ZnO layer thickness for the investigated SAW modes.
- The development of a computer controlled gas calibration system, gas chamber and RF amplifier assembly was successfully undertaken by the author.
- The underlying surface morphology of the intermediate ZnO layer was shown to considerably influence the growth of the InO_x and WO_3 sensitive layers, influencing their grain size and surface to volume ratio. The unique surface morphology and grain formation of the InO_x and WO_3 sensitive layers can be directly attributed to the novel layered structure configuration. For example, the 40 nm InO_x layer deposited on a silicon substrate was calculated to have an RMS surface roughness of 0.610 nm with a mean grain radius of 19 nm. The same layer deposited over the layered ZnO/X-cut $LiNbO_3$ structure was calculated to have an RMS surface roughness of 10.12 nm with a mean grain radius of 70 nm.
- The AFM and SEM characterisation techniques revealed the presence of well formed and regularly defined crystalline structures within the ZnO, InO_x and WO_3 layers.
- The prolonged operation at elevated temperatures was found to cause surface morphology modifications in the ZnO, InO_x and WO_3 layers. Characteristics such as grain size, RMS surface roughness and the size of the surface features were modified. Thermal treatment resulted in the sensitive layers' grain boundaries becoming more defined, which is particularly evident in the dramatic change in WO_3 grain shape, suggesting an improvement in surface crystallinity. The grain

size in the non-metallised region decreased from 132 – 176 nm to 90 – 132 nm after thermal treatment.

- The preliminary gas sensing results, utilising 0.1, 0.5, 1.0 and 2.0 µm thick intermediate ZnO layers, clearly demonstrated that the intermediate layer thickness can be used to tailor the velocity-permittivity product of the propagating SAW mode for maximum conductometric sensitivity.
- The InO_x/ZnO/XY $LiNbO_3$, InO_x/ZnO/XZ $LiNbO_3$ and WO_3/ZnO/36° YX $LiTaO_3$ layered SAW structures exhibited good dynamic response magnitudes towards H_2, NO_2 and ethanol in air. Table 9.1 list a summary of the gas sensing results obtained by the author during the course of this research program.
- The gas sensing results provide strong evidence that high sensitivity can be achieved utilising a layered SAW structure, with both generalised SAW (ZnO/XY $LiNbO_3$) and SH-SAW modes (ZnO/36° YX $LiTaO_3$), for conductometric gas sensing applications. Experimental results obtained with the ZnO/XZ $LiNbO_3$

Table 9.1: Summary of experimental gas sensing results.

Sensitive layer	Structure	Operating Temperature	Analyte gas	Operating frequency (MHz)	Frequency shift	Section and reference
40 nm InO_x	ZnO/XY$LiNbO_3$	308°C	1.00% H_2 0.06% H_2	144.5	514.7kHz 338.7kHz	8.2.1
40 nm InO_x	ZnO/XY$LiNbO_3$	159°C	8.5ppm NO_2 4.25ppm NO_2	146.11	13kHz 6.2kHz	8.2.2
40 nm InO_x	ZnO/XZ$LiNbO_3$	246°C	1.00% H_2 0.06% H_2	135.65	319.4kHz 78.5kHz	8.3.1 [197]
40 nm InO_x	ZnO/XZ$LiNbO_3$	246°C	2.12ppm NO_2 510ppb NO_2	135.66	91kHz 73.5kHz	8.3.2 [197]
200 nm InO_x	ZnO/XZ$LiNbO_3$	246°C	1.00% H_2 0.06% H_2	134.42	61.3kHz 5.7kHz	8.3.1 [197]
200 nm InO_x	ZnO/XZ$LiNbO_3$	218°C	2.12ppm NO_2 510ppb NO_2	134.42	23kHz 22kHz	8.3.2 [197]
160 nm WO_3	ZnO/36° XY $LiTaO_3$	186°C	1.00% H_2 0.50% H_2	164.07	24.7kHz 12.3kHz	8.4.1 [198]
160 nm WO_3	ZnO/36° XY $LiTaO_3$	100°C	1.25ppm NO_2 500ppb NO_2	165.40	43.86kHz 30.22kHz	8.4.2 [169, 199]
150 nm WO_3	ZnO/36° XY $LiTaO_3$	300°C	500ppm ethanol 10ppm ethanol	167.75	119kHz 32.6kHz	8.4.3 [200, 201]
Pt–WO_3	ZnO/36° XY $LiTaO_3$	270°C	1.00% H_2 0.06% H_2	166.36	118kHz 5.6kHz	8.5.1 [202]
Au–WO_3	ZnO/36° XY $LiTaO_3$	245°C 275°C	1.00% H_2 1.00% H_2 0.06% H_2	165.7 165.3	755.0kHz 705.1kHz 187.0kHz	8.5.2 [202]

demonstrated that response magnitude is a function of K^2. For example, the Rayleigh mode in the ZnO/XZ $LiNbO_3$ structure was up to 19 times more sensitive than the supported SH-SAW mode, towards 510 ppb of NO_2.

- The sensor response and recovery times were found to be influenced by the operating temperature and the concentration of the analyte gas. Higher operating temperatures and analyte gas concentrations were generally found to result in faster dynamic response. Furthermore, relative humidity levels of 25 and 50% where found to reduce the response magnitude of the WO_3/ZnO/36° YX $LiTaO_3$ device towards ethanol at an operating temperature of 300°C.
- The gas sensing results of the catalyst activated Pt–WO_3 and Au–WO_3 sensors showed an increased response magnitude towards the tested H_2 concentrations, when compared to the bare WO_3 sensitive layer. It was found that the Pt–WO_3 sensor generally had a quicker response and recovery than the Au–WO_3 sensor, however the difference was found to be marginal. The Pt–WO_3 sensor was also observed to exhibit large response magnitudes towards H_2 concentrations below 0.25% at operating temperatures below 130°C. Overall, the largest response magnitude of 755kHz was obtained by the Au–WO_3 sensor towards 1.00% H_2 at an operating temperature of 245°C.

In summary, this PhD research program has resulted in a number of novel and significant contributions to the field of layered SAW device modelling and gas sensor technology. Various accomplishments and achievements have have been made by the author as a result of the work conducted. Research papers resulting from this PhD program have been published in refereed journals and presented at various international conferences. These include eight first author refereed manuscripts and sixteen conference proceedings, published in: *Sensors and Actuators:B Chemical*, *Smart Material Substructures*, *Chiang Mai Journal of Science IEEE COMMAD*, *IEEE Sensors*, *IEEE Ultrasonics*, *IEEE Frequency control*, *SPIE* and *Sensor Letters*, etc. Additionally, the author had the opportunity to co-author a chapter in the '*Encyclopedia of Sensors*', entitled '*Layered Surface Acoustic Wave Chemical and Bio-Sensors*'. A complete list of publications by the author can be found in Appendix C. Furthermore, the author was asked to be a referee for the journal of *Solid-State Electronics*.

9.2 Suggestions for Future Work

Throughout the course of this PhD program several areas of interest, which have tremendous research potential, have been identified by the author. These areas of interest can be subdivided as follows:

1. **Fundamental research on multilayered SAW structures**

   - The investigation of other piezoelectric intermediate layer materials, such as aluminium nitride or lead zirconate titanate (PZT), to determine suitable velocity-permittivity properties for matching a SAW mode to a given sensitive layer conductivity range.
   - The investigation of layered SAW resonators and different IDT structures for gas sensing applications.
   - The extension of the sensitivity calculations presented in Chapter 4, section 4.4, to include sensitive layer material parameters. This would enable better matching of the velocity-permittivity product of the SAW device to the sheet conductivity of a given sensitive layer.
   - The extension of the 3D finite-element models:
     - To develop acoustic absorber elements for ANSYS to enable reduced model size and computation time.
     - To include mass loading effects caused by the IDT metallisation layer.
     - To increase the capability of the model for a larger number of IDT electrode finger pairs.
     - To model the effect of nanomaterials, with regards to their arrangement (ordered vs. random placement) and their influence on the underlying SAW propagation.
     - To investigate the gas interaction occurring in sensitive the layer (via both mass and electrical perturbations) by exploring the changes in structural and material properties of the finite-element model during the sensing process.

   The knowledge gained by such models will aid in understanding the sensing mechanism and improving sensor design and optimisation.

2. **Development of gas sensitive layers**

   - The investigation of the response overshoot phenomena observed with the 40 nm InO_x sensor.
   - The investigation of other sensitive layer materials (e.g. binary metal oxides, polymers) and quasi-one dimensional structures (e.g. nanorods, nanobelts and carbon nanotubes) for improved selectivity and sensitivity to specific gas analytes.
   - The investigation of nanocrystalline materials and different deposition techniques, which results in sensitive layers with higher porosity and larger surface area. For example WO_3 synthesised by gas-evaporation results in a mean grain size of 10 nm and has been shown to exhibit higher sensitivity towards H_2S, when compared to polycrystalline WO_3 thin films [190].
   - The tailoring of the intermediate layers' surface morphology to increase the surface to volume ratio of a given sensitive layer material.
   - The further investigation of catalyst activated sensitive layers with the objective of increasing response magnitude, long-term stability and reducing aging effects.
   - Material characterisation of the sensitive layer, with the aim of improving sensitivity, response and recovery of the structure towards different gas analytes.

It is the author's opinion that if the layered SAW structures presented in this thesis were further optimised, their gas sensing performance would make them highly suitable for applications in sensor arrays and for commercialisation purposes.

[This page is left blank intentionally.]

Appendix A

Material Properties

A.1 $LiNbO_3$ material properties for ANSYS

Density = 4700 kg/m^3

Sonic Velocity = 3769 m/s

Anisotropic Elastic Matrix:

$$D_{IJ} = \begin{bmatrix} 2.03 \times 10^{11} & 5.3 \times 10^{10} & 7.5 \times 10^{10} & 9 \times 10^{9} & 0 & 0 \\ & 2.03 \times 10^{11} & 7.5 \times 10^{10} & -9 \times 10^{9} & 0 & 0 \\ & & 2.45 \times 10^{11} & 0 & 0 & 0 \\ & & & 6 \times 10^{10} & 0 & 0 \\ & & & & 6 \times 10^{10} & 9 \times 10^{9} \\ & & & & & 7.5 \times 10^{10} \end{bmatrix} \tag{A.1}$$

Relative Permittivity:

$$[\varepsilon] = \begin{bmatrix} 38.9 & 0 & 0 \\ 0 & 38.9 & 0 \\ 0 & 0 & 25.7 \end{bmatrix} \tag{A.2}$$

Piezoelectric Matrix:

$$[e] = \begin{array}{c} \\ x \\ y \\ z \\ xy \\ yz \\ xz \end{array} \begin{array}{c} \begin{array}{ccc} x & y & z \end{array} \\ \begin{bmatrix} 0 & -2.5 & 0.2 \\ 0 & 2.5 & 0.2 \\ 0 & 0 & 1.3 \\ -2.5 & 0 & 0 \\ 0 & 3.7 & 0 \\ 3.7 & 0 & 0 \end{bmatrix} \end{array} \tag{A.3}$$

A.2 ZnO material properties for ANSYS

Density = 5680 kg/m^3

Sonic Velocity = 2634 m/s

Anisotropic Elastic Matrix:

$$D_{IJ} = \begin{bmatrix} 2.097 \times 10^{11} & 1.051 \times 10^{11} & 1.21 \times 10^{10} & 0 & 0 & 0 \\ & 2.097 \times 10^{11} & 1.051 \times 10^{11} & 0 & 0 & 0 \\ & & 2.097 \times 10^{11} & 0 & 0 & 0 \\ & & & 4.247 \times 10^{10} & 0 & 0 \\ & & & & 4.247 \times 10^{10} & 0 \\ & & & & & 4.3 \times 10^{10} \end{bmatrix} \tag{A.4}$$

Relative Permittivity:

$$[\varepsilon] = \begin{bmatrix} 7.5702 & 0 & 0 \\ 0 & 9.0311 & 0 \\ 0 & 0 & 7.5702 \end{bmatrix} \tag{A.5}$$

Piezoelectric Matrix:

$$[e] = \begin{array}{c} \\ x \\ y \\ z \\ xy \\ yz \\ xz \end{array} \begin{array}{c} \begin{array}{ccc} x & y & z \end{array} \\ \begin{bmatrix} 0 & 0.573 & 0 \\ 0 & -1.23 & 0 \\ 0 & 0.573 & 0 \\ 0.48 & 0 & 0 \\ 0 & 0 & 0.48 \\ 0 & 0 & 0 \end{bmatrix} \end{array} \tag{A.6}$$

Appendix B

Electromechanical Coupling Coefficient, (K^2)

Table B.1 lists the estimated K^2 values for the ZnO/XY $LiNbO_3$, ZnO/XZ $LiNbO_3$ and ZnO/36° YX $LiTaO_3$ structures. The K^2 values calculated by equation (4.1) are shown to lie between the value produced by equations (4.3) and (4.2) for all cases. Values differing by more than 1 order of magnitude are highlighted in a **bold** font. The results show that the ZnO/XZ $LiNbO_3$ structure conforms remarkably well. However, the ZnO/XY $LiNbO_3$ structure is shown to conform only for ZnO thickness less than 2 µm. The ZnO/36° YX $LiTaO_3$ structure is only shown to conform with the ZnO layer for reasons presented in section 4.2.1.3.

Table B.1: Theoretical determination of K^2 for $\lambda = 24$ µm.

ZnO thickness	Γ_f	Λ_m	ε_∞	K^2_{free}	$K^2_{metalised}$	$K^2_{equation\ (4.1)}$
	ZnO/XY $LiNbO_3$					
0 µm	-1.2451×10^7	1.8147×10^{-11}	7.2099×10^{-10}	1.79×10^{-2}	5.03×10^{-2}	3.06×10^{-2}
0.5 µm	-1.0639×10^7	1.9775×10^{-11}	7.0693×10^{-10}	1.50×10^{-2}	5.59×10^{-2}	2.98×10^{-2}
1.2 µm	-8.4845×10^6	2.4438×10^{-11}	7.0613×10^{-10}	1.19×10^{-2}	6.92×10^{-2}	3.04×10^{-2}
1.5 µm	-7.7044×10^6	2.8193×10^{-11}	7.0613×10^{-10}	1.08×10^{-2}	7.98×10^{-2}	3.19×10^{-2}
2.0 µm	-6.5612×10^6	3.8776×10^{-11}	7.0613×10^{-10}	**9.26×10^{-3}**	**0.1098**	**3.76×10^{-2}**
2.5 µm	-5.5660×10^6	5.4161×10^{-11}	7.0613×10^{-10}	**7.86×10^{-3}**	**0.1534**	**5.03×10^{-2}**
	ZnO/XZ $LiNbO_3$					
0 µm	-5.1659×10^7	1.0039×10^{-11}	4.1773×10^{-10}	4.31×10^{-2}	4.80×10^{-2}	4.54×10^{-2}
0.5 µm	-5.9207×10^7	1.1867×10^{-11}	4.7783×10^{-10}	5.65×10^{-2}	4.96×10^{-2}	5.27×10^{-2}
1.0 µm	-6.4144×10^7	1.3615×10^{-11}	4.7657×10^{-10}	6.11×10^{-2}	5.71×10^{-2}	5.90×10^{-2}
1.5 µm	-6.5341×10^7	1.5210×10^{-11}	4.7657×10^{-10}	6.22×10^{-2}	6.38×10^{-2}	6.37×10^{-2}
2.0 µm	-5.9419×10^7	1.6603×10^{-11}	4.7657×10^{-10}	5.66×10^{-2}	6.96×10^{-2}	6.60×10^{-2}
2.5 µm	-3.8828×10^7	1.7781×10^{-11}	4.7657×10^{-10}	3.70×10^{-2}	7.46×10^{-2}	6.38×10^{-2}
3.0 µm	-1.1775×10^7	1.8764×10^{-11}	4.7657×10^{-10}	1.12×10^{-2}	7.87×10^{-2}	5.32×10^{-2}
	ZnO/36° YX $LiTaO_3$					
0 µm	-7.8897×10^6	1.7244×10^{-11}	4.4499×10^{-10}	**7.02×10^{-3}**	**7.75×10^{-2}**	**5.56×10^{-2}**
0.5 µm	-6.1861×10^7	1.9444×10^{-11}	5.1459×10^{-10}	6.36×10^{-2}	7.55×10^{-2}	7.46×10^{-2}
1.0 µm	-8.5291×10^7	2.0599×10^{-11}	5.1437×10^{-10}	8.77×10^{-2}	8.01×10^{-2}	8.41×10^{-2}
1.5 µm	-9.1947×10^7	2.0683×10^{-11}	5.1437×10^{-10}	9.45×10^{-2}	8.04×10^{-2}	8.59×10^{-2}
2.0 µm	-8.7579×10^7	1.9783×10^{-11}	5.1437×10^{-10}	9.00×10^{-2}	7.69×10^{-2}	8.17×10^{-2}
2.5 µm	-7.7288×10^7	1.8139×10^{-11}	5.1437×10^{-10}	7.95×10^{-2}	7.05×10^{-2}	7.35×10^{-2}

Appendix C

List of Author's Publications

C.1 Book Chapter

1. David A. Powell, Kourosh Kalantar-zadeh, Wojtek Wlodarski, and **Samuel J. Ippolito**, "Layered surface acoustic wave chemical and bio-sensors," in *Encyclopedia of Sensors*, Craig A. Grimes, Elizabeth C. Dickey, and Michael V. Pishko, Eds., vol. 5, pp. 245–262. American Scientific Publishers, 25650 North Lewis Way, Stevenson Ranch, California 91381-1439, USA, 2006.

C.2 Refereed Manuscripts

1. **S. J. Ippolito**, A. Ponzoni, K. Kalantar-zadeh, W. Wlodarski, E. Comini, G. Faglia, and G. Sberveglier, "Layered WO_3/ZnO/36° $LiTaO_3$ SAW gas sensor sensitive towards ethanol vapour and humidity," *Sensors and Actuators B: Chemical*, vol. 117, pp. 442–450, 2006.

2. **Samuel. J. Ippolito**, Sasikaran Kandasamy, Kourosh Kalantar-zadeh, Wojtek Wlodarski, and Anthony Holland, "Comparison between conductometric and layered SAW hydrogen gas sensor," *Smart Mater. Struct.*, vol. 15, pp. S131–S136, 2006.

3. **S. J. Ippolito**, S. Kandasamy, K. Kalantar-zadeh, W. Wlodarski, K. Galatsis, G. Kiriakidis, N. Katsarakis, and M. Suchea, "Highly sensitive layered ZnO/$LiNbO_3$ SAW device with InO_x selective layer for NO_2 and H_2 gas sensing," *Sensors and Actuators B: Chemical*, vol. 111-112, pp. 207–212, 2005.

4. LiLin Li, Wojtek Wlodarski, and **Samuel J. Ippolito**, "Platinum resistive film CO sensor without selective layer," *Sensors and Actuators B: Chemical*, vol. 111-112, pp. 130–134, 2005.

5. David A. Powell, Kourosh Kalantar-zadeh, **Samuel J. Ippolito**, and Wojtek Wlodarski, "Comparison of conductometric gas sensitivity of surface acoustic wave modes in layered structures," *Sensor Letters*, pp. 66–70, 2005.

6. **S. J. Ippolito**, S. Kandasamy, K. Kalantar-zadeh, and W. Wlodarski, "Layered SAW hydrogen sensor with modified tungsten trioxide selective layer," *Sensors and Actuators B: Chemical*, vol. 108, pp. 553–557, 2005.

7. **S. J. Ippolito**, S. Kandasamy, K. Kalantar-zadeh, and W. Wlodarski, "Hydrogen sensing characteristics of WO_3 thin film conductometric sensors activated by Pt and Au catalysts," *Sensors and Actuators B: Chemical*, vol. 108, pp. 154–158, 2005.

8. A. C. Fechete, **S. J. Ippolito**, W. Wlodarski, K. Kalantar-zadeh, A. S. Holland, and A. Wisitsora-at, "Layered $InO_x/Si_3N_4/36°$ YX $LiTaO_3$ surface acoustic wave based hydrogen sensor," *Chiang Mai Journal of Science*, vol. 32, pp. 465–470, 2005.

9. G. I. Matthews, **S. J. Ippolito**, K. Kalantar-zadeh, W. Wlodarski, and A. Holland, "Finite element modeling of flexural plate device," *Conference on Optoelectronic and Microelectronic Materials and Devices*, pp. 145–148, 2004.

10. A. Trinchi, W. Wlodarski, S. Santucci, D. Di Claudio, M. Passacantando, C. Cantalini, B. Rout, **S. J. Ippolito**, K. Kalantar-zadeh, and G. Sberveglieri, "Microstructural characterisation of RF magnetron sputtered ZnO thin films on SiC," *Functional Nanomaterials for Optoelectronics and other Applications: Diffusion and Defect Data Pt.B: Solid State Phenomena*, vol. 99-100, pp. 123–126, 2004.

11. **S. J. Ippolito**, S. Kandasamy, K. Kalantar-zadeh, A. Trinchi, and W. Wlodarski, "A layered surface acoustic wave ZnO/ $LiTaO_3$ structure with a WO_3 selective layer for hydrogen sensing," *Sensor Letters*, vol. 1, pp. 33–36, 2003.

12. K. Kalantar-zadeh, D. A. Powell, W. Wlodarski, **S. J. Ippolito**, and K. Galatsis, "Comparison of layered based SAW sensors," *Sensors and Actuators B: Chemical*, vol. 91, pp. 303–308, 2003.

13. **S. J. Ippolito**, K. Kalantar-zadeh, D. A. Powell, and W. Wlodarski, "A finite element approach for 3-dimensional simulation of layered acoustic wave transducers," *Conference on Optoelectronic and Microelectronic Materials and Devices*, pp. 541–544, Dec. 2002.

14. **S. J. Ippolito**, K. Kalantar-zadeh, W. Wlodarski, K. Galatsis, W. J. Fischer, O. Berger, and H. Stab, "A layered SAW based NO_2 sensor with a copper phthalocyanine selective layer," *Conference on Optoelectronic and Microelectronic Materials and Devices*, pp. 165–168, 2002.

C.3 Conference Papers

1. Massood Z. Atashbar, Kourosh Kalantar-zadeh, **Samuel J. Ippolito**, and Wojtek Wlodarski, "Palladium nanowire hydrogen sensor based on a SAW transducer," *Proceedings of IEEE Sensors*, pp. 1363–1365, 2005.

2. **S. J. Ippolito**, A. Ponzoni, K. Kalantar-zadeh, W. Wlodarski, E. Comini, G. Faglia, and G. Sberveglier, "Ethanol sensor based on layered WO_3/ZnO/36° $LiTaO_3$ SAW devices," *TRANSDUCERS '05 Digest of Technical Papers, presented at the 13th International Conference on Solid-State Sensors, Actuators and Microsystems*, vol. 2, pp. 1915–1918, 2005.

3. Alexandru C. Fechete, **Samuel J. Ippolito**, Kourosh Kalantar-zadeh, Wojtek Wlodarski, and Anthony S. Holland, "Surface acoustic wave based ozone sensor with a InO_x/Si_3N_4/36° YX $LiTaO_3$ structure," in *Micro- and Nanotechnology: Materials, Processes, Packaging, and Systems II*, Jung-Chih Chiao, David N. Jamieson, Lorenzo Faraone, and Andrew S. Dzurak, Eds. 2005, vol. 5650, pp. 268–275, Proceedings of SPIE.

4. Vijay P. Sivan, **S.J. Ippolito**, S. Kandasamy, K. Kalantar-Zadeh, W. Wlodarski, and A. Holland, "Investigation of layered SAW sensors based on a WO_3/ZnO/64°YX $LiNbO_3$ structure with gold catalytic layer," in *Micro- and Nanotechnology: Materials, Processes, Packaging, and Systems II*, Jung-Chih Chiao, David N. Jamieson, Lorenzo Faraone, and Andrew S. Dzurak, Eds. 2005, vol. 5650, pp. 276–284, Proceedings of SPIE.

5. A. C. Fechete, **S. J. Ippolito**, K. Kalantar-zadeh, W. Wlodarski, A. S. Holland, K. Galatsis, G. Kiriakidis, N. Katsarakis, and M. Katharakis, "The study of

InO_x/ZnO/XZ $LiNbO_3$ layered SAW devices for ozone sensing," *Proceedings of IEEE Sensors*, vol. 3, pp. 1510–1513, 2004.

6. K. Kalantar-zadeh, D. A. Powell, **S. J. Ippolito**, and W. Wlodarski, "Study of layered SAW devices operating at different modes for gas sensing applications," *Proceedings of the IEEE Ultrasonics Symposium*, pp. 191–194, 2004.

7. A. Trinchi, **S.J. Ippolito**, S. Kandasamy, W. Wlodarski, K. Kalantar-Zadeh, S. Kaciulis, L. Pandolfi, S.Viticoli, "Hydrogen sensing by WO_3/SiC based solid state structures," Proceedings of the 9th Italian conference on Sensors and Microsystems, The Italian Association of Sensors and Microsystems (AISEM), Ferrara, Italy, February, 2004

8. **S. J. Ippolito**, Sasikaran Kandasamy, Kourosh Kalantar-zadeh, Wojtek Wlodarski, and Anthony Holland, "Comparison between conductometric and layered SAW hydrogen gas sensor," in *Microelectronics: Design, Technology and Packaging*, Derek Abbott, Kamran Eshraghian, Edith Cowan, Charles A. Musca, Dimitris Pavlidis, and Neil Weste, Eds. 2004, vol. 5274, pp. 416–424, Proceedings of SPIE.

9. **S. J. Ippolito**, K. Kalantar-zadeh, A. Trinchi, D. A. Powell, and W. Wlodarski, "Layered SAW nitrogen dioxide sensor with WO_3 selective layer," in *Smart Sensors, Actuators and MEMS*, Jung-Chih Chiao, Vijay K. Varadan, and Carles Cane, Eds. 2003, vol. 5116, pp. 904–911, Proceedings of SPIE.

10. **S. J. Ippolito**, K. Kalantar-zadeh, W. Wlodarski, and G. I. Matthews, "The study of ZnO/XY $LiNbO_3$ layered SAW devices for sensing applications," *Proceedings of IEEE Sensors*, vol. 2, pp. 539–542, 2003.

11. **S. J. Ippolito**, K. Kalantar-zadeh, D. A. Powell, and W. Wlodarski, "A 3-dimensional finite element approach for simulating acoustic wave propagation in layered SAW devices," *Proceedings of the IEEE Ultrasonics Symposium*, vol. 1, pp. 303–306, 2003.

12. **S. J. Ippolito**, K. Kalantar-zadeh, A. Trinchi, W. Wlodarski, and M. Tobar, "Layered SAW nitrogen dioxide sensor based on a ZnO/ 36° YX $LiTaO_3$ structure with WO_3 selective layer," *Proceedings of the IEEE International Frequency Control Symposium and PDA Exhibition*, pp. 931–934, 2003.

13. D. A. Powell, K. Kalantar-Zadeh, **S. J. Ippolito**, and W. Wlodarski, "A layered SAW device based on ZnO/ $LiTaO_3$ for liquid media sensing applications," *Proceedings of the IEEE Ultrasonics Symposium*, vol. 1, pp. 493–496, 2002.

14. **S. J. Ippolito**, K. Kalantar, W. Wlodarski, and D. A. Powell, "Finite-element analysis for simulation of layered SAW devices with XY $LiNbO_3$ substrate," in *Smart Structures, Devices, and Systems*, Erol C. Harvey, Derek Abbott, and Vijay K. Varadan, Eds. 2002, vol. 4935, pp. 120–131, Proceedings of SPIE.

[This page is left blank intentionally.]

Bibliography

[1] T. Grandke and J. Hesse, "Introduction," in *Sensors, A Comprehensive Survey*, W. Göpel, J. Hesse, and J.N. Zemel, Eds., vol. 1, pp. 1–16. VCH Publishers, Weinheim Germany, 1989.

[2] K. S. Lion, "Transducers: Problems and prospects," *IEEE Transactions on Industrial Electronics and Control Instrumentation*, vol. IECI-16, pp. 2–7, 1969.

[3] Henry Wohltjen and Raymond Dessy, "Surface acoustic wave probe for chemical analysis. Part I: Introduction and instrument description," *Analytical Chemistry*, vol. 51, no. 9, pp. 1458–1475, August 1979.

[4] Massood Zandi Atashbar, *Surface Acoustic Wave (SAW) Oxygen Sensor Based on Nanosized TiO_2 Thin Films*, Ph.D. thesis, Royal Melbourne Institute of Technology, 1998.

[5] F. Schmidt and G. Scholl, "Wireless SAW identification and sensor systems," In Ruppel and Fjeldly [203], pp. 34–34.

[6] F. S Hickernell and E. L. Adler, "Pseudo-SAW propagation on layered piezo-substrates:experiments and theory including film viscosity," *Proceedings of the IEEE Ultrasonics Symposium*, pp. 87–90, 1996.

[7] T. Kikuchi and T. Moriizumi, "Effects of liquid viscosity on ultrasonic propagation in liquid/solid structure," *Journal of Applied Physics*, vol. Supplement 25-1, pp. 43–45, 1986.

[8] S. Furukawa, H. Furukawa, T. Nomura, T. Yasuda, and M. Tamura, "Precise estimation of viscosity of liquid using leaky surface acoustic waves propagating along liquid/polymer/$LiNbO_3$ structures," *Proceedings of the IEEE Ultrasonics Symposium*, pp. 303–306, 1992.

[9] G. Kovacs, M. J. Vellekoop, R. Haueis, G. W. Lubking, and A. Venema, "A Love wave sensor for (bio)chemical sensing in liquids," *Sensors and Actuators A: Physical*, vol. 43, pp. 38–43, 1994.

[10] S. Furukawa, R. Nishimura, M. Obana, T. Nomura, and T. Yasuda, "Characteristic of leaky surface acoustic wave propagating along liquid/polymer/$LiNbO_3$ and its application to liquid sensor," *IEEE MTT-S Digest*, pp. 517–520, 1994.

[11] D. A. Powell, K. Kalantar-Zadeh, S. J. Ippolito, and W. Wlodarski, "A layered SAW device based on ZnO/ $LiTaO_3$ for liquid media sensing applications," *Proceedings of the IEEE Ultrasonics Symposium*, vol. 1, pp. 493–496, 2002.

[12] Jun Kondoh, Yoshikazu Matsui, and Showko Shiokawa, "New biosensor using shear horizontal surface acoustic wave device," *Japanese Journal of Applied Physics*, vol. 32, pp. 2376–2379, 1993.

[13] Gizeli Electra, Goddard Nicholas, Lowe Christopher, and Stevenson Adrian, "Love plate biosensor utilising a polymer layer," *Sensors and Actuators B: Chemical*, vol. 6, pp. 131–137, 1992.

[14] Jia Du and Geoffrey L. Harding, "A multilayer structure for love-mode acoustic sensors," *Sensors and Actuators A: Physical*, vol. 65, pp. 152–159, 1998.

[15] G. L. Harding, J. Du, P. R. Dencher, D. Barnett, and E. Howe, "Love wave acoustic immunosensor operating in liquid," *Sensors and Actuators A: Physical*, vol. 61, pp. 279–286, 1997.

[16] Kourosh Kalantar-zadeh, Yuen Yuen Chen, Benjamin N. Fry, Adrian Trinchi, and Wojtek Wlodarski, "A novel love mode SAW sensor with ZnO layer operating in gas and liquid media," *Proceedings of the IEEE Ultrasonics Symposium*, pp. 353–356, 2001.

[17] Kourosh Kalantar-zadeh, Adrian Trinchi, Wojtek Wlodarski, and Anthony Holland, "A love-mode device based on a ZnO/ST-cut quartz crystal structure for sensing applications," *Sensors and Actuators A: Physical*, vol. 100, pp. 135–143, January 2002.

[18] Kourosh Kalantar-Zadeh, *Investigation of a Love Mode Acoustic Wave Transducer for Bio-sensing Applications*, Ph.D. thesis, RMIT University, Nov. 2001.

[19] Kosmas Galatsis, *Investigation of nanosized molybdenum oxide - titanium oxide and tungsten oxide thin films for gas sensing*, Ph.D. thesis, RMIT University, 2002.

[20] M. Rapp, J. Reibel, S. Stier, A. Voigt, and J. Bahlo, "SAGAS: Gas analyzing sensor system based on surface acoustic wave devices - an issue of commercialization of SAW sensor technology," *IEEE International Frequency Control Symposium*, pp. 129–132, 1997.

[21] C. Christofides and A. Mandelis, "Solid-state sensors for trace hydrogen gas detection," *Journal of Applied Physics*, vol. 68, pp. R1–R30, 1990.

[22] Sasikaran Kandasamy, "Investigation of SAW devices with sol-gel deposited selective layeres for gas-sensing applications," Minor M.Eng. thesis, Royal Melbourne Institute of Technology, June 2003.

[23] Vijay Prasad Sivan, "Investigation of layered SAW sensors based on WO_3/ZnO/64° YX $LiNbO_3$ structure," Minor M.Eng. thesis, Royal Melbourne Institute of Technology, June 2004.

[24] Colin K. Campbell, *Surface Acoustic Wave Devices for Mobile and Wireless Communications*, Academic Press, San Diego, 1998.

[25] Arthur Ballato, "Piezoelectricity: History and new thrusts," *IEEE Transactions on Ultrasonics Ferroelectrics & Frequency Control*, vol. 42, no. 5, pp. 916–926, 1995.

[26] Arthur Ballato, "Piezoelectricity: History and new thrusts," *Proceedings of the IEEE Ultrasonics Symposium*, pp. 575–583, 1996.

[27] Robert Peach, "On the existence of surface acoustic waves on piezoelectric substrates," *IEEE Transactions on Ultrasonics Ferroelectrics & Frequency Control*, vol. 48, no. 5, pp. 1308–1320, 2001.

[28] David. P. Morgan, "History of SAW devices," *IEEE International Frequency Control Symposium*, pp. 439–460, 1998.

[29] Fred S. Hickernell, "Surface acoustic wave devices: A rewarding past, a significant present, and a promising future," *Proceedings 12th International Conference on Microwaves and Radar*, vol. 4, pp. 159–168, 1998.

[30] J. David N. Cheeke, *Fundamentals and Applications of Ultrasonics Waves*, CRC Press, Boca Raton, Florida, 2001.

[31] David P. Morgan, *Surface-Wave Devices for Signal Processing*, Elsevier, Amsterdam, 1991.

[32] D. S. Ballantine, R. M. White, S. J. Martin, A. J. Ricco, G. C. Frye, E. T. Zellers, and H. Wohtltjen, *Acoustic Wave Sensors: theory, design and Physico-Chemical Applications*, Academic Press, New York, 1997.

[33] B. A. Auld, *Acoustic Fields and Waves in Solids*, John Wiley, New York, 1973.

[34] Andrew J. Slobodnik, "Surface acoustic waves and SAW materials," *Proceedings of IEEE*, vol. 64, no. 5, pp. 581–595, 1976.

[35] F. S. Hickernell, "Thin films for SAW devices," In Ruppel and Fjeldly [203], p. 34.

[36] Michael Thompson and David C. Stone; edited by J. D. Winefordner, *Surface-Launched Acoustic Wave Sensors. Chemical Sensing and Thin-Film Characterization*, vol. 144 in Chemical Analysis:A series of monographs on analytical chemistry and its applications, John Wiley & sons, inc., New York, 1997.

[37] David A. Powell, Kourosh Kalantar-Zadeh, Wojtek Wlodarski, and Samuel J. Ippolito, "Layered surface acoustic wave chemical and bio-sensors," in *Encyclopedia of Sensors*, Craig A. Grimes, Elizabeth C. Dickey, and Michael V. Pishko, Eds., vol. 5, pp. 245–262. American Scientific Publishers, 25650 North Lewis Way, Stevenson Ranch, California 91381-1439, USA, 2006.

[38] A. J. Ricco and S. J. Martin, "Thin metal film characterization and chemical sensors: monitoring electronic conductivity, mass loading and mechanical properties with surface acoustic wave devices," *Thin Solid Films*, vol. 206, pp. 94–101, 1991.

[39] David W. Galipeau, Patrick R. Story, Kevin A. Vetelino, and Russell D. Mileham, "Surface acoustic wave microsensors and applications," in *Smart Mater Structure*, Brookings, SD 57006 USA, July 1997, Microconversion Technologies Company, vol. 6, pp. 658–667, IOP Pulishing Ltd.

[40] Holger Becker, Manfred von Schickfus, and Siegfried Hunklinger, "A new sensor principle based on the reflection of surface acoustic waves," *Sensors and Actuators A: Physical*, vol. 54, pp. 618–621, 1996.

[41] A. R ugemer, S. Reiss, A. Geyer, M.v. Schickfus, and S. Hunklinger, "Surface acoustic wave NO_2 sensing using attenuation as the measured quantity," *Sensors and Actuators B: Chemical*, vol. 56, pp. 45–49, 1999.

[42] S. J. Martin and A. J. Ricco, "Effective utilization of acoustic wave sensor responses: simultaneous measurements of velocity and attenuation," *Proceedings of the IEEE Ultrasonics Symposium*, pp. 621–625, 1989.

[43] Henry Wohltjen and Raymond Dessy, "Surface acoustic wave probe for chemical analysis. Part II: Gas chromatography detector," *Analytical Chemistry*, vol. 51, no. 9, pp. 1465–1470, August 1979.

[44] Jay. W. Grate, Stephan J. Martin, and Richard M. White, "Acoustic wave microsensors," *Analytical Chemistry*, vol. 65, pp. 940A–948A, 1993.

[45] A. D'Amico, A. Palma, and E. Verona, "Surface acoustic wave hydrogen sensor," *Sensors and Actuators*, vol. 3, pp. 31–39, 1982/83.

[46] A. D'Amico, A. Palma, and E. Verona, "Hydrogen sensor using a palladium coated surface acoustic wave delay-line," *Proceedings of the IEEE Ultrasonics Symposium*, pp. 308–311, 1982.

[47] M.S. Nieuwenhuizen and A.J. Nederlof, "A SAW gas sensor for carbon dioxide and water. preliminary experiments," *Sensors and Actuators*, vol. B2, pp. 97–101, 1990.

[48] J. D. Galipeau, R. S. Falconer, J. F. Vetelino, J. J. Caron, E. L. Wittman, M. G. Schweyer, and J. C. Andle, "Theory, design and operation of a surface acoustic wave hydrogen sulfide microsensor," *Sensors and Actuators B: Chemical*, vol. 24-25, pp. 49–53, 1995.

[49] M. Penza and L. Vasanelli, "SAW NO_x gas sensor using WO_3 thin-film sensitive coating," *Sensors and Actuators B: Chemical*, vol. 41, pp. 31–36, 1997.

[50] M. Rapp, R. Stanzel, M. v. Schickfus, and S. Hunklinger, "Gas detection in the ppb-range with a high frequency, high sensitivity acoustic wave device," *Thin Solid Films*, vol. 210-211, pp. 474–476, 1992.

[51] Dominique Rebiere, Corinne Dejous, Jacques Pistre, Jean-Francois Lipskier, and Roger Planade, "Synthesis and evaluation of fluoropolyol isomers as SAW microsensor coatings: role of humidity and temperature," *SAB*, vol. 49, pp. 139–145, 1998.

[52] Hank Wohltjen, "Mechanism of operation and design considerations for surface acoustic wave device vapour sensors," *Sensors and Actuators*, vol. 5, pp. 1307–325, May 1984.

[53] A. D'Amico and E. Verona, "SAW sensors," *Sensors and Actuators*, vol. 17, pp. 55–66, 1989.

[54] D. S. Ballantine and Hank Wohltjen, "Surface acoustic wave devices for chemical analysis," *Analytical Chemistry*, vol. 61, pp. 704A–715A, 1989.

[55] Jay. W. Grate, Stephan J. Martin, and Richard M. White, "Acoustic wave microsensors . part ii," *Analytical Chemistry*, vol. 65, pp. 987A–996A, 1993.

[56] S. J. Martin, G. C. Frye, J. J. Spates, and M. A. Butler, "Gas sensing with acoustic devices," *Proceedings of the IEEE Ultrasonics Symposium*, pp. 423–433, 1996.

[57] J. D. N. Cheeke and Z. Wang, "Acoustic wave gas sensors," *Sensors and Actuators B: Chemical*, vol. 59, pp. 146–153, 1999.

[58] Michael J. Vellekoop, "Acoustic wave sensors and their technology," *Proceedings of the IEEE Ultrasonics Symposium*, vol. 36, pp. 7–14, 1998.

[59] Bill Drafts, "Acoustic wave technology sensors," *IEEE Transactions on microwave theory and techniques*, vol. 49, pp. 795–802, 2001.

[60] V. I. Anisimkin, Yu. V. Gulyaev, and I. V. Anisimkin, "Surface acoustic waves method: New analytical capabilities," *Surface Investigation*, vol. 16, pp. 1213–1224, 2001.

[61] R. Ionescu, A. Hoel, C. G. Granqvist, E. Llobert, and P. Haszler, "Ethanol and H_2S gas detection in air and in reducing and oxidising ambience: application of pattern recognition to analyse the output from temperature-modulated nanoparticulate WO_3 gas sensors," *Sensors and Actuators B: Chemical*, vol. 104, pp. 124–131, 2005.

[62] Corrado Di Natale, Fabrizio A. M. Davide, and Arnaldo D'Amico, "A self-organizing system for pattern classification: time varying statistics and sensor drift effects," *Sensors and Actuators B: Chemical*, vol. 27, pp. 237–241, 1995.

[63] Andrew Paul Campitelli, *Investigation of Shear Horizontal Surface Acoustic Wave Sensor System for Liquid Media*, Ph.D. thesis, Royal Melbourne Institute of Technology, Oct. 1997.

[64] V. I. Anisimkin, I. M. Kotelyanskii, P. Verardi, and E. Verona, "Elastic properties of thin-film palladium for surface acoustic wave (SAW) sensors," *Sensors and Actuators B: Chemical*, vol. 23, pp. 203–208, 1995.

[65] J. Du, G. L. Harding, J. A. Ogilvy, P. R. Dencher, and M. Lake, "A study of Love-wave acoustic sensors," *Sensors and Actuators A: Physical*, vol. 55, pp. 211–219, 1996.

[66] B. Jakoby, G. M. Ismail, M. P. Byfield, and M. J. Vellekoop, "A novel molecularly imprinted thin film applied to a love wave gas sensor," *Sensors and Actuators A: Physical*, vol. 76, pp. 93–97, 1999.

[67] C. Zimmermann, D. Reiere, C. Dejous, J. Pistre, E. Chastaing, and R. Planade, "A love wave gas sensor coated with functionalized polysiloxane for sensing organophosphorus compounds," *Sensors and Actuators B: Chemical*, vol. 76, pp. 86–94, 2001.

[68] M. Penza, F. Antolini, and M. Vittori-Antisari, "Carbon nanotubes as SAW chemical sensors materials," *Sensors and Actuators B: Chemical*, vol. 100, pp. 47–59, 2004.

[69] Geoffrey L. Harding, "Mass sensitivity of love-mode acoustic sensors incorporating silicon dioxide and silicon-oxy-fluoride guiding layers," *Sensors and Actuators A: Physical*, vol. 88, pp. 20–28, 2001.

[70] Ren-Chuan Chang, Sheng-Yuan Chu, Cheng-Shong Hong, and Yu-Ting Chuang, "A study of love wave devices in ZnO/Quartz and ZnO/$LiTaO_3$ structures," *Thin Solid Films*, vol. 498, pp. 146–151, 2006.

[71] Ren-Chuan Chang, Sheng-Yuan Chu, Cheng-Shong Hong, and Yu-Ting Chuang, "An investigation of preferred orientation of doped ZnO films on the 36° YX $LiTaO_3$ substrates and fabrications of Love–mode devices," *Surface and Coatings Technology*, vol. 200, pp. 3235–3240, 2006.

[72] A. J. Ricco, S. J. Martin, and T. E. Zipperian, "Surface acoustic wave gas sensor based on film conductivity changes," *Sensors and Actuators*, vol. 8, pp. 319–333, 1985.

[73] M.S. Nieuwenhuizen and A.J. Nederlof, "A silicon-based SAW chemical sensor for NO_2 by applying a silicon nitride passivation layer," *Sensors and Actuators B: Chemical*, vol. 9, pp. 171–176, 1992.

[74] Wieslaw P. Jakubik, Marian W. Urbanczyk, Stanislaw Kochowski, and Jerzy Bodzenta, "Bilayer structure for hydrogen detection in a surface acoustic wave sensor system," *Sensors and Actuators B: Chemical*, vol. 82, pp. 265–271, 2002.

[75] Wieslaw P. Jakubik, Marian W. Urbanczyk, Stanislaw Kochowski, and Jerzy Bodzenta, "Palladium and phthalocyanine bilayer films for hydrogen detection in a surface acoustic wave sensor system," *Sensors and Actuators B: Chemical*, vol. 96, pp. 321–328, 2003.

[76] Wieslaw P. Jakubik and Marian W. Urbanczyk, "SAW hydrogen sensor with a bilayer structure based on interaction speed," *Sensors and Actuators B: Chemical*, vol. 106, pp. 602–608, 2005.

[77] K. Kalantar-Zadeh, Y. X. Li, W. Wlodarksi, and F. Brennan, "A layered structure surface acoustic wave for oxygen sensing," *Proceedings Conference on Optoelectronic and Microelectronic Materials and Devices, COMMAD 2000*, pp. 202–205, 2000.

[78] S. J. Ippolito, K. Kalantar-zadeh, W. Wlodarski, K. Galatsis, W. J. Fischer, O. Berger, and H. Stab, "A layered SAW based NO_2 sensor with a copper phthalocyanine selective layer," *Conference on Optoelectronic and Microelectronic Materials and Devices*, pp. 165–168, 2002.

[79] Joshua J. Caron, Thomas D. Kenny, L. Jay LeGore, Derek G. Liby, Carl J. Freeman, and John F. Vetelino, "A surface acoustic wave nitric oxide sensor," *IEEE International Frequency Control Symposium*, pp. 156–162, 1997.

[80] R. Lec, J. F. Vetelino, R. S. Falconer, and Z. Xu, "Macroscopic theory of surface acoustic wave gas micosensors," *Proceedings of the IEEE Ultrasonics Symposium*, pp. 585–589, 1988.

[81] B. Holcroft and G. G. Roberts, "Surface acoustic wave sensors incorporating langmuir-blodgett films," *Thin Solid Films*, vol. 160, pp. 445–452, 1988.

[82] W. Jakubik, M. Urba/'nczyk, and A. Opilski, "Sensor properties of lead phthalocyanine in a surface acoustic wave system," *Elsevier - Ultrasonics*, vol. 39, pp. 227–232, 2001.

[83] J. D. Galipeau, L. J. LeGore, K. Snow, J. J. Caron, J. F. Vetelino, and J. C. Andle, "The integration of a chemiresistive film overlay with a surface acoustic wave microsensor," *Sensors and Actuators B: Chemical*, vol. 35-36, pp. 158–163, 1996.

[84] J. A. Thiele and M. Pereira da Cunha, "High temperature LGS SAW devices with Pt/WO_3 and Pd sensing films," *Proceedings of the IEEE Ultrasonics Symposium*, pp. 1750–1753, 2003.

[85] Kourosh Kalantar-zadeh, Adrian Trinchi, Wojtek Wlodarski, Anthony Holland, and Massood Z. Atashar, "A novel love mode device with nanocrystalline ZnO film for gas sensing applications," *IEEE-NANO*, pp. 556–561, 2001.

[86] T. Shoji, K. Nakamura, and D. Yamazaki, "Propagation characteristics of the SH-SAW on $(110)ZnO/(012)LiTaO_3$," *Proceedings of the IEEE Ultrasonics Symposium*, pp. 215–219, 2001.

[87] Florain Bender, Reiner Dahint, and fabien Josse, "Surface acoustic wave-based sensors using mode conversion in an array of periodic gratings," *IEEE International Frequency Control Symposium*, pp. 973–977, 1999.

[88] A. M. Azad, S. A. Akbar, S. G. Mhaisalkar, L. D. Birkefeld, and K. S. Goto, "Solid-state gas sensors: A review," *J. Electrochemical. Soc.*, vol. 139, no. 12, pp. 3690–3703, 1992.

[89] T. Seiyama, A. Kato, K. Fujiishi, and M. Nagatani, "A new detector for gaseous components using semiconductive thin films," *Analytical Chemistry*, vol. 34, pp. 1502, 1962.

[90] P. K. Clifford and D. T. Tuma, "Characteristics of semiconductor gas sensors i. steady state gas response," *Sensors and Actuators*, vol. 3, pp. 233–254, 1982/83.

[91] Nobo Yamazoe and Norio Miura, "Environmental gas sensing," *Sensors and Actuators B: Chemical*, vol. 20, pp. 95–102, 1994.

[92] S. Roy Morrison, "Selectivity in semiconductor gas sensors," *Sensors and Actuators B: Chemical*, vol. 12, pp. 425–440, 1987.

[93] S. Roy Morrison, "Mechanism of semiconductor gas sensor operation," *Sensors and Actuators B: Chemical*, vol. 11, pp. 283–287, 1987.

[94] K. Zakrzewska, "Mixed oxides as gas sensors," *Thin Solid Films*, vol. 391, pp. 229–238, 2001.

[95] C. Baratto, E. Comini, G. Faglia, G. Sberveglieri, M. Zha, and A. Zappettini, "Metal oxide nanocrystals for gas sensing," *Sensors and Actuators B: Chemical*, vol. 109, pp. 2–6, 2005.

[96] Elisabetta Comini, "Metal oxide nano-crystals for gas sensing," *Analytica Chimica Acta*, vol. 568, pp. 28–40, 2006.

[97] J. Mizsei, P. sipila, and V. Lantto, "Structural studies of sputtered noble metal catalysts on oxide surfaces," *Sensors and Actuators B: Chemical*, vol. 47, pp. 139–144, 1998.

[98] Adrian Trinchi, *Investigation of Metal Reactive Insulator Silicon Carbide (MRISiC) Devices and Semiconduction Metal oxide thin films for gas sensing applications*, Ph.D. thesis, RMIT University, 2004.

[99] Reinhard Lerch, "Finite element analysis of piezoelectric transducers," *Proceedings of the IEEE Ultrasonics Symposium*, pp. 643–654, 1988.

[100] S. J. Ippolito, K. Kalantar, W. Wlodarski, and D. A. Powell, "Finite-element analysis for simulation of layered SAW devices with XY $LiNbO_3$ substrate," in *Smart Structures, Devices, and Systems*, Erol C. Harvey, Derek Abbott, and Vijay K. Varadan, Eds. 2002, vol. 4935, pp. 120–131, Proceedings of SPIE.

[101] S. J. Ippolito, K. Kalantar-zadeh, D. A. Powell, and W. Wlodarski, "A finite element approach for 3-dimensional simulation of layered acoustic wave transducers," *Conference on Optoelectronic and Microelectronic Materials and Devices*, pp. 541–544, Dec. 2002.

[102] S. J. Ippolito, K. Kalantar-zadeh, D. A. Powell, and W. Wlodarski, "A 3-Dimensional finite element approach for simulating acoustic wave propagation in layered SAW devices," *Proceedings of the IEEE Ultrasonics Symposium*, vol. 1, pp. 303–306, 2003.

[103] S. J. Ippolito, K. Kalantar-zadeh, W. Wlodarski, and G. I. Matthews, "The study of ZnO/XY $LiNbO_3$ layered saw devices for sensing applications," *Proceedings of IEEE Sensors*, vol. 2, pp. 539–542, 2003.

[104] M. Z. Atashbar, B. J. Bazuin, M. Simpeh, and S. Krishnamurthy, "3-D finite-element simulation model of SAW palladium thin film hydrogen sensor," *Proceedings of the IEEE International Frequency Control Symposium and Exposition*, pp. 549–553, 2004.

[105] M. Z. Atashbar, B. J. Bazuin, M. Simpeh, and S. Krishnamurthy, "3-D FE simulation of H_2 SAW gas sensor," *Sensors and Actuators B: Chemical*, vol. 111-112, pp. 213–218, 2005.

[106] G. I. Matthews, S. J. Ippolito, K. Kalantar-zadeh, W. Wlodarski, and A. Holland, "Finite element modeling of flexural plate device," *Conference on Optoelectronic and Microelectronic Materials and Devices*, pp. 145–148, 2004.

[107] R. Lerch, M. Kaltenbacher, H. Landes, J. Hoffelner, M. Rausch, and M. Schinnerl, "Advanced transducer modelling using the finite element method," *International Journal of Applied Electromagnetics and Mechanics*, vol. 17, pp. 59–73, 2003.

[108] Jun Lan and Stephen G. Boucher, "Improvement in accuracy of finite modeling for ultrasonic transducers," *Proceedings of the IEEE Ultrasonics Symposium*, pp. 1051–1055, 1998.

[109] R. Lerch, "Simulation of piezoelectric devices by Two- and Three-dimensional finite elements," *IEEE Transactions on Ultrasonics Ferroelectrics & Frequency Control*, vol. 37, no. 2, pp. 233–247, 1990.

[110] R. Simkovics, H. Landes, M. Kaltenbacher, and R. Lerch, "Nonlinear finite element analysis of piezoelectric transducers," *Proceedings of the IEEE Ultrasonics Symposium*, vol. 2, pp. 1057–1060, 1999.

[111] Jun Lan, Michael J. Simoneau, Robert K. Jeffers, and Stephen G. Boucher, "A complete finite element model," *Proceedings of the IEEE Ultrasonics Symposium*, pp. 999–1003, 1994.

[112] A. Gachagan, J. T. Bennett, and G. Hayward, "A finite element modelling approach into the influence of mechanical matching and damping in 1-3 piezocomposites," *Proceedings of the IEEE Ultrasonics Symposium*, pp. 995–998, 1994.

[113] J. T. Stewart, "Finite element modeling of resonant microelectromechanical structures for sensing applications," *Proceedings of the IEEE Ultrasonics Symposium*, pp. 643–646, 1994.

[114] Masanori Koshiba, Koji Hasegawa, and Michio Suzuki, "Finite-element solution of horizontally polarized shear wave scattering in an elastic plate," *IEEE Transactions on Ultrasonics Ferroelectrics & Frequency Control*, vol. 34, no. 4, pp. 461–466, 1987.

[115] W. Li, J. M. Gilmore, and F. J. Bennett, "3D finite element modeling of obliquely oriented piezocomposite materials and transducer arrays," *Proceedings of the IEEE Ultrasonics Symposium*, pp. 1666–1669, 2004.

[116] Jiri Maryška, Josef Novák, Jirina Královcová, Jan Fousek, and Petr Rálek, "FEM modeling of electro-elastic field in ferroelectric crystal with domain boundaries," *IEEEInternational Symposium on Applications of Ferroelectrics*, pp. 106–109, 2004.

[117] Yukio Kagawa and Tasuo Yamabuchi, "A finite-element approach to electromechanical problems with an applications to energy-trapped and surface-wave devices," *IEEE Transactions on Sonics & Ultrasonics*, vol. SU-23, no. 4, pp. 263–272, July 1976.

[118] Guanshui Xu, "Direct finite-element analysis of the frequency response of a Y-Z lithium niobate SAW filter," *Smart Mater. Struct.*, vol. 9, pp. 973–980, 2000.

[119] Reinhard Lerch, "Finite element analysis of SAW-transducers," *ISCAS'88 IEEE*, pp. 1399–1403, 1988.

[120] Peter-Christian Eccardt, Hermann Landes, and Richard Lerch, "Finite element simulation of acoustic wave propagation within flowing media," *Proceedings of the IEEE Ultrasonics Symposium*, pp. 991–994, 1996.

[121] Koji Hasegawa and Masanori Koshiba, "Finite-element solution of rayleigh-wave scattering from reflective gratings on a piezoelectric substrate," *IEEE Transactions on Ultrasonics Ferroelectrics & Frequency Control*, vol. 37, no. 2, pp. 99–105, 1990.

[122] Guanshui Xu, "Finite-element analysis of second order effects on the frequency response of a SAW device," *Proceedings of the IEEE Ultrasonics Symposium*, pp. 187–190, 2000.

[123] Werner Friedrich, Reinhard Lerch, K. Prestele, and R. Soldner, "Simulations of piezoelectric lamb wave delay lines using a finite element method," *IEEE Transactions on Ultrasonics Ferroelectrics & Frequency Control*, vol. 37, pp. 248–254, May 1990.

[124] Masanori Koshiba, Naoki Shichishima, Kazuhiro Ohbuchi, and Yasuhide Tsuji, "Software for a multilayered surface acoustic wave device based on the finite element method and coupling-of-modes theory," *Japanese Journal of Applied Physics*, vol. 36, no. Pt1 5B, pp. 3060–3063, 1997.

[125] Saeed Moaveni, *Finite Elements Analysis: Theory and Application with ANSYS*, Prentice Hall, Upper Saddle River, New Jersey 07458, 1999.

[126] "ANSYS 8.0 documentation," *Copyright, 2003 SAS IP*, 2003.

[127] E. L. Adler, J. K. Slaboszewicz, G. W. Farnell, and C. K. Jen, "PC software for SAW propagation in anisotropic multilayers," *IEEE Transactions on Ultrasonics Ferroelectrics & Frequency Control*, vol. 37, no. 2, pp. 215–223, 1990.

[128] D. A. Smith and J. J. Johnson, "Low drive-power integrated acoustooptic filter on X-cut Y-propagating $LiNbO_3$," *IEEE Photonics Technology Letters*, vol. 3, no. 10, pp. 923–925, 1991.

[129] F. Chagla, C. Cabani, and P. M. Smith, "Perfectly matched layer for FDTD computations in piezoelectric crystals," *Proceedings of the IEEE Ultrasonics Symposium*, pp. 517–520, 2004.

[130] David A. Powell, Kourosh Kalantar-zadeh, Samuel J. Ippolito, and Wojtek Wlodarski, "Comparison of conductometric gas sensitivity of surface acoustic wave modes in layered structures," *Sensor Letters*, vol. 3, pp. 66–70, 2005.

[131] David A. Powell, Kourosh Kalantar-zadeh, and Wojtek Wlodarski, "Numerical calculation of SAW sensitivity: Application to $ZnO/LiTaO_3$ transducers," *Sensors and Actuators A: Physical*, vol. 115, pp. 456–461, 2004.

[132] M. Austin, "Wideband lithium niobate integrated optical modulators," in *OECC/IOOC incorporating ACOFT*, Sydney, Australia, 2001, pp. 256–257.

[133] H. Mendis, A. Mitchell, I. Belski, M. Austin, and O.A. Peverini, "Design, realisation and analysis of an apodised, film-loaded acousto-optic tunable filter," *Applied Physics B (Lasers and Optics)*, vol. B73, no. 5-6, pp. 489–493, 2001.

[134] F.C.M. Van De Pol, "Thin-film ZnO-properties and applications," *American Ceramic Society Bulletin*, vol. 69, pp. 1959–1965, 1990.

[135] X. Bévenot, A. Trouillet, C. Veillas, H. Gagnaire, and M. Clément, "Hydrogen leak detection using an optical fibre sensor for aerospace applications," *Sensors and Actuators B: Chemical*, vol. 67, pp. 57–67, Jan. 2000.

[136] Th. Becker, L. Tomasi, Chr. Bosch-v.Braunmuhl, G. Muller, G. Sberveglieri, G. Fagli, and E. Comini, "Ozone detection using low-power-consumption metal-oxide gas sensors," *Sensors and Actuators B: Chemical*, vol. 64, pp. 229–232, 1999.

[137] I. Stambolva, K. Konstantinov, S. Vassilev, P. Peshev, and Ts. Tsacheva, "Lanthanum doped SnO_2 and ZnO thin films sensitive to ethanol and humidity," *Materials Chemistry and Physics*, vol. 63, pp. 104–108, 2000.

[138] J. Hubálek, K. Malysz, J. Prášek, X. Vilanova, P. Ivanov, E. Llobet, J. Brezmes, X. Correig, and Z. Svěrák, "Pt-loaded Al_2O_3 catalytic filters for screen-printed WO_3 sensors highly selective to benzene," *Sensors and Actuators B: Chemical*, vol. 101, pp. 277–283, 2004.

[139] Tadashi Takada, "A new method for gas identification using a single semiconductor sensor," *Sensors and Actuators B: Chemical*, vol. 52, pp. 45–52, May 1998.

[140] A. Jones, T. A. Jones, B. Mann, and J. G. Firth, "The effect of the physical form of the oxide on the conductivity changes produced by CH_4 and CO and H_2O on ZnO," *Sensors and Actuators B: Chemical*, vol. 5, pp. 75–88, 1984.

[141] B. Bhooloka Rao, "Zinc oxide ceramic semi-conductor gas sensor for ethanol vapour," *Materials Chemistry and Physics*, vol. 64, pp. 62–65, 2000.

[142] D. F. Paraguay, M. Miki-Yoshida, J. Morales, J. Solis, and L. W. Estrada, "Influence of Al, In, Cu, Fe and Sn dopants on the response of thin film ZnO gas sensor to ethanol vapour," *Thin Solid Films*, vol. 373, pp. 137–140, 2000.

[143] F.C.M. Van De Pol, "Thin-film ZnO-properties and applications," *American Ceramic Society Bulletin*, vol. 69, pp. 1959–1965, 1990.

[144] P. Thilakan and J. Kumar, "Oxidation dependent crystallization behavior of IO and ITO thin films deposited by reactive thermal deposition technique," *Materials Science and Engineering B*, vol. 55, pp. 195–200, 1998.

[145] P. Thilakan and J. Kumar, "Studies on the preferred orientation changes and its influenced properties on ITO thin films," *Vacuum*, vol. 48, pp. 463–466, 1997.

[146] M. Bender, N. Katsarakis, E. Gagaoudakis, E. Hourdakis, E. Douloufakis, V. Cimalla, and G. Kiriakidis, "Dependence of the photoreduction and oxidation behavior of indium oxide films on substrate temperature and film thickness," *Journal of Applied Physics*, vol. 90, no. 10, pp. 5382–5387, November 2001.

[147] H. Fritzsche, B. Pashmakov, and B. Clafin, "Reversible changes of the optical and electrical properties of amorphous InO_x by photoreduction and oxidation," *Solar Energy Materials & Solar Cells*, vol. 32, no. 4, pp. 383–393, April 1994.

[148] G. Kiriakidis, H. Ouacha, N. Katsarakis, K. Galatsis, and W. Wlodarski, "Low temperature InO_x thin films for O_3 and NO_2 gas sensing," *Proceedings of SPIE*, vol. 5116, pp. 84–91, 2003.

[149] C. Cantalini, W. Wlodarski, Y. Li, M. Passacantando, S. Santucci, E. Comini, G. Faglia, and G. Sberveglieri, "Investigation on the O_3 sensitivity properties of WO_3 thin films prepared by sol-gel, thermal evaporation and r.f. sputtering techniques," *Sensors and Actuators B: Chemical*, vol. 64, pp. 182–188, 2000.

[150] M. Penza, M. A. Tagliente, L. Mirenghi, C. Gerardi, C. Martucci, and G. Cassano, "Tungsten trioxide (WO_3) sputtered thin films for a NO_x gas sensor," *Sensors and Actuators B: Chemical*, vol. 50, pp. 9–18, 1998.

[151] W.R. Smith, H.M. Gerard, J.H. Collins, T.M. Reeder, and H.J. Shaw, "Analysis of interdigital surface wave transducers by use of an equivalent circuit model," *IEEE Transactions on Microwave Theory and Techniques*, vol. MTT-17, pp. 856–864, 1969.

[152] W.R. Smith, H.J. Shaw, T.M. Reeder, H.M. Gerard, and J.H. Collins, "Analysis and design of interdigital surface-wave transducers by use of an equivalent circuit model," *IEEE Transactions on Sonics and Ultrasonics*, vol. SU17, pp. 55, 1970.

[153] G. Tobolka, "Mixed matrix representation of SAW transducers," *IEEE Transactions on Sonics and Ultrasonics*, vol. SU-26, pp. 426–428, 1979.

[154] D.-P. Chen and H.A. Haus, "Analysis of metal-strip SAW gratings and transducers," *IEEE Transactions on Sonics and Ultrasonics*, vol. SU-32, pp. 395–408, 1985.

[155] L. Boyer, J. Desbois, Y. Zhang, and J. M. Hodé, "Theoretical determination of the pseudo surface acoustic wave characteristic parameters," *Proceedings of the IEEE Ultrasonics Symposium*, pp. 353–358, 1991.

[156] R. F. Milson, N. H. C. Reilly, and M. Redwood, "Analysis of generation and detection of surface and bulk acoustic waves by interdigital transducer," *IEEE Transactions on Sonics & Ultrasonics*, pp. 147–166, 1977.

[157] D. L. Lee, "A green's fuction formulation for analyzing excitation of surface skiming bulk waves," *IEEE Transactions on Sonics & Ultrasonics*, vol. SU-27, pp. 77–81, 1980.

[158] A. Grisel and V. Demarne, "Fabrication of integrated thin film semiconductor gas sensors," in *Chemical Sensor Technology 2*, T. Seiyama, Ed., pp. 44—57. Elsevier, Amsterdam, 1988.

[159] E. Gagaoudakis, M. Bender, E. Douloufakis, E. Natsakou, V. Cimalla, and G. Kiriakidis, "The influence of deposition parameters on room temperature ozone sensing properties of InO_x films," *Sensors and Actuators B: Chemical*, vol. 80, pp. 155–161, July 2001.

[160] G. Kiriakidis, "Nanostructured holograhic recording utilizing InO_x photorefractive thin films," *Proceedings of SPIE*, vol. 5118, pp. 117–124, 2003.

[161] S. J. Ippolito, S. Kandasamy, K. Kalantar-zadeh, and W. Wlodarski, "Hydrogen sensing characteristics of WO_3 thin film conductometric sensors activated by Pt and Au catalysts," *Sensors and Actuators B: Chemical*, vol. 108, pp. 154–158, 2005.

[162] Samuel. J. Ippolito, Sasikaran Kandasamy, Kourosh Kalantar-zadeh, Wojtek Wlodarski, and Anthony Holland, "Comparison between conductometric and layered SAW hydrogen gas sensor," in *Microelectronics: Design, Technology and Packaging*, Derek Abbott, Kamran Eshraghian, Edith Cowan, Charles A. Musca, Dimitris Pavlidis, and Neil Weste, Eds. 2004, vol. 5274, pp. 416–424, Proceedings of SPIE.

[163] Kjell Blϕtekjær, Kjell A. Ingebrigtsen, and Halvor Skeie, "A method of analyzing waves in structures consisting of metal strips on dispersive media," *IEEE Transactions on Electron Devices*, vol. ED-20, no. 12, pp. 1133–1138, 1973.

[164] M. Stankova, X. Vilanova, E. Llobet, J. Calderer, C. Bittencourt, J. J. Pireaux, and X. Correig, "Influence of the annealing and operating temperatures on the gas-sensing properties of rf sputtered WO_3 thin-film sensors," *Sensors and Actuators B: Chemical*, vol. 105, pp. 271–277, 2005.

[165] A. Al Mohammmad and M. Gillet, "Phase transformations in WO_3 thin films during annealing," *Thin Solid Films*, vol. 408, pp. 302–309, February 2002.

[166] K. Wasa and S. Hayakawa, *Handbook of Sputter Deposition Technology: Principals, Technology and Applications*, Noyes Publications, New Jersey, 1992.

[167] D.P. Norton, M. Ivill, Y. Li, Y.W. Kwon, J.M. Erie, H.S. Kim, K. Ip, S.J. Pearton, Y.W. Heo, S. Kim, B.S. Kang, F. Ren, A.F. Hebard, and J. Kelly, "Charge carrier and spin doping in ZnO thin films," *Thin Solid Films*, vol. 496, pp. 160–168, 2006.

[168] F. Chaabouni, M. Abaab, and B. Rezig, "Effects of the substrate temperature on the properties of ZnO films grown by RF magnetron sputtering," *Materials Science and Engineering B*, pp. 236–240, 2004.

[169] S. J. Ippolito, K. Kalantar-zadeh, A. Trinchi, W. Wlodarski, and M. Tobar, "Layered SAW nitrogen dioxide sensor based on a ZnO/ 36° YX $LiTaO_3$structure with WO_3 selective layer," *Proceedings of the IEEE International Frequency Control Symposium and PDA Exhibition*, pp. 931–934, 2003.

[170] D. Kohl, "The role of noble metals in the chemistry of the solid-state gas sensor," *Sensors and Actuators B: Chemical*, vol. 1, pp. 158–165, 1990.

[171] D. Kohl, "Catalytic reactions and electronic processes relevant in gas sensing. an extended abstract," *Sensors and Actuators*, vol. 17, pp. 309–311, 1989.

[172] R. S. Falconer, J. F. Vetelino, D. J. Smith, and M. J. Osborn, "An activation process for increased sensitivity of a saw gas microsensor," *Proceedings of the IEEE Ultrasonics Symposium*, pp. 315–318, 1990.

[173] A. Bryant, M. Poirier, G. Riley, D. L. Lee, and J. F. Vetelino, "Gas detection using surface acoustic wave delay lines," *Sensors and Actuators*, vol. 4, pp. 105–111, 1983.

[174] M. F. Lewis, "Surface acoustic wave devices and applications: Oscillators - the next successful surface acoustic wave device?," *Ultrasonics*, pp. 115–123, May 1974.

[175] Meirion Lewis, "The surface acoustic wave oscillator - a natural and timely development of the quartz crystal oscillator," *Proceedings of the 28th Annual Frequency Control Symposium*, pp. 304–314, 1974.

[176] T.E. Parker and G.K. Montress, "Precision surface-acoustic-wave (SAW) oscillators," *IEEE Transactions on Ultrasonics, Ferroelectrics and Frequency Control*, vol. 35, pp. 342–364, 1988.

[177] P. T. Moseley and A. J. Crocker, *Sensor Materials*, Institute of Physics Publishing, Bristol and Philadelphia, 1996.

[178] M. Suchea and G. Kiriakidis, "Atomic force microscopy analysis of polycrystalline indium oxide thin films," poster presented in XIX National Conference in Solid State and Material Science, Tessaloniki Greece, 21-24 September 2003.

[179] K. Kalantar-zadeh, D. A. Powell, S. J. Ippolito, and W. Wlodarski, "Study of layered SAW devices operating at different modes for gas sensing applications," *Proceedings of the IEEE Ultrasonics Symposium*, pp. 191–194, 2004.

[180] Th. Pastureaud, V. Laude, and S. Ballandras, "Stable scattering-matrix method for surface acoustic waves in piezoelectric multilayers," *Applied Physics Letters*, vol. 80, pp. 2544, 2002.

[181] G. Korotcenkov, V. Brinzari, A. Cerneavschi, M. Ivanov, A. Cornet, J. Morante, A. Cabot, and J. Arbiol, "In_2O_3 films deposited by spray pyrolysis: gas response to reducing (CO, H_2) gases," *Sensors and Actuators B: Chemical*, vol. 98, pp. 122–129, 2004.

[182] M. Ivanovskaya, A. Gurlo, and P. Bogdanov, "Mechanism of O_3 and NO_2 detection and selectivity of In_2O_3 sensors," *Sensors and Actuators B: Chemical*, vol. 77, pp. 264–267, 2001.

[183] M. Akiyama, J. Tamaki, N. Miura, and N. Yamazoe, "Tungsten oxide-based semiconductor sensors highly sensitive to NO and NO_2," *Chem. Lett.*, vol. 9, pp. 1611, 1991.

[184] A. Georg, W. Graf, R. Neumann, and V. Wittwer, "The role of water in gasochromic WO_3 films," *Thin Solid Films*, vol. 384, pp. 269–275, 2001.

[185] Jana Bludska, Jiri Vondrak, Ivo Jakubec, and Petr Krtil, "The accelerating role of water in hydrogen insertion into tungsten trioxide," *Solar Energy Materials & Solar Cells*, vol. 56, pp. 231–235, 1999.

[186] Yong-Keun Chung, Mi-Hyang Kim, Woo-Sik Um, Hee-Soo Lee, Jun-Kwang Song, Sung-Churl Choi, Kang-Myung Yi, Myung-Jin Lee, and jyung Won Chung, "Gas sensing properties of WO_3 thick film for NO_2 gas dependent on process condition," *Sensors and Actuators B: Chemical*, vol. 60, pp. 49–56, 1999.

[187] P. J. Shaver, "Activated tungsten oxide gas detectors," *Applied Physics Letters*, vol. 11, pp. 255–257, 1967.

[188] Sugeng Triwahyono, Takashi Yamada, and Hideshi Hattori, "Kinetic study of hydrogen adsorption on Pt/WO_3-ZrO_2 and WO_3-ZrO_2," *Analytical Chemistry*, vol. General 250, pp. 65–73, 2003.

[189] S. Okazaki, H. Nakagawa, S. Asakura, Y. Tomiuchi, N. Tsuji, H. Murayama, and M. Washiya, "Sensing characteristics of an optical fiber sensor for hydrogen leak," *Sensors and Actuators B: Chemical*, vol. 93, pp. 142–147, 2003.

[190] Hong-Ming Lin, Chi-Ming Hsu, Huey-Yih Yang, and Pee-Yew Lee, "Nanocrystalline WO_3-based H_2S sensors," *Sensors and Actuators B: Chemical*, vol. 22, pp. 63–68, 1994.

[191] N. yamazoe, Y. kurokawa, and T. Seiyama, "Effects of additives on semiconductor gas sensors," *Sensors and Actuators*, vol. 4, pp. 283–289, 1983.

[192] D. S. Vlachos, C. A Papadopoulos, and J. N. Avaritsiotis, "Characterisation of the catalyst-semiconductor interaction mechanism in metal-oxide gas sensors," *Sensors and Actuators B: Chemical*, vol. 44, pp. 458–461, 1997.

[193] B. Fr uhberger, M. Grunze, and D. J. Dwyer, "Surface chemistry of H_2S-sensitive tungsten oxide films," *Sensors and Actuators B: Chemical*, vol. 31, pp. 167–174, 1996.

[194] Masanori Ando, Rupert Chabicovsky, and Masatake Haruta, "Optical hydrogen sensitivity of noble metal-tungsten oxide composite films prepared by sputtering deposition," *Sensors and Actuators B: Chemical*, vol. 76, pp. 13–17, 2001.

[195] M. Penza, C. Martucci, and G. Cassano, "NO_x gas sensing characteristics of WO_3 thin films activated by noble metals (Pd, Pt, Au) layers," *Sensors and Actuators B: Chemical*, vol. 50, pp. 52–59, 1998.

[196] L.J. Legore, R. J. Lad, J. F Vetelino, B. G. Frederick, and E.A Kenik, "Aggregation and sticking probability of gold on tungsten trioxide films," *Sensors and Actuators B: Chemical*, vol. 76, pp. 373–379, 2001.

[197] S. J. Ippolito, S. Kandasamy, K. Kalantar-zadeh, W. Wlodarski, K. Galatsis, G. Kiriakidis, N. Katsarakis, and M. Suchea, "Highly sensitive layered ZnO/$LiNbO_3$ SAW device with InO_x selective layer for NO_2 and H_2 gas sensing," *Sensors and Actuators B: Chemical*, vol. 111-112, pp. 207–212, 2005.

[198] S. J. Ippolito, S. Kandasamy, K. Kalantar-zadeh, A. Trinchi, and W. Wlodarski, "A layered surface acoustic wave ZnO/$LiTaO_3$ structure with a WO_3 selective layer for hydrogen sensing," *Sensor Letters*, vol. 1, pp. 33–36, 2003.

[199] S. J. Ippolito, K. Kalantar-zadeh, A. Trinchi, D. A. Powell, and W. Wlodarski, "Layered SAW nitrogen dioxide sensor with WO_3 selective layer," in *Smart Sensors, Actuators and MEMS*, Jung-Chih Chiao, Vijay K. Varadan, and Carles Cane, Eds. 2003, vol. 5116, pp. 904–911, Proceedings of SPIE.

[200] S. J. Ippolito, A. Ponzoni, K. Kalantar-zadeh, W. Wlodarski, E. Comini, G. Faglia, and G. Sberveglier, "Ethanol sensor based on layered WO_3/ZnO/36° $LiTaO_3$ SAW devices," *TRANSDUCERS '05 Digest of Technical Papers, presented at the 13th International Conference on Solid-State Sensors, Actuators and Microsystems*, vol. 2, pp. 1915–1918, 2005.

[201] S. J. Ippolito, A. Ponzoni, K. Kalantar-zadeh, W. Wlodarski, E. Comini, G. Faglia, and G. Sberveglier, "Layered WO_3/ZnO/36° $LiTaO_3$ SAW gas sensor sensitive towards ethanol vapour and humidity," *Sensors and Actuators B: Chemical*, vol. 117, pp. 442–450, 2006.

[202] S. J. Ippolito, S. Kandasamy, K. Kalantar-zadeh, and W. Wlodarski, "Layered SAW hydrogen sensor with modified tungsten trioxide selective layer," *Sensors and Actuators B: Chemical*, vol. 108, pp. 553–557, 2005.

[203] C.W. Ruppel and T.A. Fjeldly, Eds., *Advances in Surface Acoustic Wave Technology Systems and Applications*, World Scientific Publishing, Singapore, 2000.